THE UNIVERSITY OF CHICAGO

MOLECULAR MATERIAL DESIGN OF NANOSCALE METAL-ORGANIC FRAMEWORKS FOR CANCER THERAPY

A DISSERTATION SUBMITTED TO

THE FACULTY OF THE DIVISION OF THE PHYSICAL SCIENCES

IN CANDIDACY FOR THE DEGREE OF

DOCTOR OF PHILOSOPHY

DEPARTMENT OF CHEMISTRY

BY

GEOFFREY TRISTRAM NASH

CHICAGO, ILLINOIS

DECEMBER 2023

Table of Contents

List of Figures

List of Tables

List of Schemes

List of Abbreviations

°C	degrees Celsius
$^1O_2$	singlet oxygen
2D	two-dimensional
3D	three-dimensional
Å	angstrom
AcOH	acetic acid
AFM	atomic force microscopy
AIQ	aggregation-induced quenching
BDC	1,4,-benzenedicarboxylic acid
CLSM	confocal laser scanning microscopy
CRT	calreticulin
DBB	4,4'-di(4-benzoato)-2,2'-bipyridine
DBU	1,8-diazabicyclo[5.4.0]undec-7-ene
DCF-DA	2′,7′-dichlorodihydrofluorescein diacetate
dF(CF_3)ppy	2-(2,4-difluorophenyl)-5-(trifluoromethyl)pyridine
DLS	dynamic light scattering
DMEM	Dulbecco's Modified Eagle Medium
DMF	*N*,*N*-dimethylformamide
DPBS	Dulbecco's phosphate-buffered saline
ESI-MS	electrospray ionization mass spectrometry
EtOH	ethanol

FFT	fast Fourier transform
FRET	Förster resonance energy transfer
FT-IR	Fourier transform infrared spectroscopy
H&E	hematoxylin-eosin
H_2DBB-Ir-F	Ir(DBB)[dF(CF_3)-ppy]$_2^+$
H_2DBP	5,15-di(*p*-benzoato)porphyrin
H_2QC	2″,3′-dinitro-[1,1’:4′,1”;4″,1’”-quaterphenyl]-4,4’”-dicarboxylate
H_3BTB	1,3,5-tris(4-carboxyphenyl)benzene
H_4TBC	5,10,15,20-tetra-(*p*-benzoato)chlorin
H_4TBP	5,10,15,20-tetra(*p*-benzoato)porphyrin
H_4ZnTBIPc	*N*-propyl zinc(II) tetra(*p*-benzoato)imidazophthalocyanine
HIFU	high-intensity focused ultrasound
HR-TEM	high-resolution transmission electron microscopy
IC	internal conversion
IC_{50}	half maximal inhibitory concentration
ICD	immunogenic cell death
ICP-MS	inductively coupled plasma mass spectrometry
ISC	intersystem crossing
K_3PO_4	potassium phosphate tribasic
LED	light-emitting diode
MALDI-TOF HR-MS	matrix-assisted laser desorption/ionization-time of flight high-resolution mass spectrometry
Me	methyl (CH_3)

MeOH	methanol
MOF	metal-organic framework
MOL	metal-organic layer
MPS	mononuclear phagocyte system
MRgFUS	magnetic resonance imaging guided focused ultrasound surgery
nMOF	nanoscale metal-organic framework
nMOL	nanoscale metal-organic layer
NMR	nuclear magnetic resonance
PBS	phosphate buffered saline
$Pd(OAc)_2$	palladium(II) acetate
PDT	photodynamic therapy
Pe	pentyl (C_5H_{11})
PEG	polyethylene glycol
PeOH	1-pentanol
Pe_4ZnTBIPc	*N*-propyl zinc(II) tetra(*p*-pentyl-benzoato)imidazophthalocyanine
PI	propidium iodide
PS	photosensitizer
PSM	postsynthetic modification
PXRD	powder x-ray diffraction
RCF	relative centrifugal force
RDT	radiodynamic therapy
ROS	reactive oxygen species

RPS	reticuloendothelial phagocytic system
rt	room temperature
RT	radiotherapy
S_0	ground state
S_1	singlet excited state
SBU	secondary building unit
SDT	sonodynamic therapy
SOSG	Singlet Oxygen Sensor Green
SPhos	2-dicyclohexylphosphino-2',6'-dimethoxybiphenyl
SS	sonosensitizer
T_1	triplet excited state
TA	transient absorption
t-BuOK	potassium *tert*-butoxide
TCSPC	time-correlated single photon counting
TEA	triethylamine
TEM	transmission electron microscopy
TFA	trifluoroacetic acid
TGA	thermogravimetric analysis
THF	tetrahydrofuran
TTET	triplet-triplet energy transfer
US	ultrasound
UV-Vis	ultraviolet-visible

VR	vibrational relaxation
wt %	weight percent
$Zn(OAc)_2$	zinc(II) acetate
ZnOPPc	zinc(II) 2,3,9,10,16,17,23,24-octa(4-carboxyphenyl)phthalocyanine

Abstract

Molecular Material Design of Nanoscale Metal-Organic Frameworks for Cancer Therapy

Geoffrey Tristram Nash

Under the Direction of Professor Wenbin Lin

Metal-organic frameworks (MOFs) are a class of hybrid inorganic-organic crystalline porous materials composed of inorganic cluster and organic linker building units. MOFs can combine the advantages of material properties and molecular design into a single multifunctional platform. With functional capabilities possible at each discrete building unit and in the framework architecture as a whole, the tunability of the MOF platform has emerged as an attractive property that can be harnessed to design novel nanomedicines. This dissertation focuses on the exploration of molecular design to enhance the anticancer efficacy of various multifunctional nanoscale MOFs (nMOFs) in combination with localized cancer therapeutic modalities, including photodynamic therapy (PDT), sonodynamic therapy (SDT), and radiotherapy (RT).

Chapter 1 of this thesis introduces the general concept, history, advantages, and research directions of nMOFs. The synthetic strategies and postsynthetic molecular functionalization approaches are also discussed. Additionally, to put nMOFs' utility in nanomedicine into context, the advantages and disadvantages of various local cancer therapeutic modalities are weighed.

Chapter 2 describes the PDT enhancement of surface-anchored zinc-phthalocyanine (ZnOPPc) photosensitizers (PSs) on a 2D Hf_{12}-based MOF, also known as a metal-organic layer

(MOL). Typically, PSs are loaded into a 3D MOF as the bridging linkers, but in this chapter we find that surface-anchoring the PS to the secondary building units (SBUs) of a MOL changes its local environment and makes it more accessible to ground state oxygen ($^3O_2$) for enhanced production of cytotoxic singlet oxygen ($^1O_2$). The ZnOPPc@MOL assembly demonstrates highly effective anticancer efficacy *in vitro* and *in vivo* on mouse models.

Chapter 3 presents another PDT design strategy by loading the ZnOPPc PSs into MOF pores. The MOF pores act as cages to isolate hydrophobic ZnOPPc PSs and prevent their aggregation-induced quenching. Non-covalent trapping of ZnOPPc PSs does not adversely affect the photophysical properties of ZnOPPc. As a result, ZnOPPc@MOF significantly enhances the $^1O_2$ generation efficiency compared to previous MOFs, thus allowing the highly potent ZnOPPc PSs to reach their full potential in PDT. ZnOPPc@MOF exhibited extremely effective *in vitro* and *in vivo* anticancer efficacy, with >99% tumor growth inhibition and 80% cure rates on two murine colon cancer models.

Chapter 4 describes the synthesis of the first 3D Zr- and Hf-nMOFs with Pc-based bridging ligands. Due to the synthetic challenges, poor solubility, and inflexible/incompatible symmetry of phthalocyanines, Pc-based MOFs have been extremely elusive to the MOF community, with no 3D Pc-based MOFs reported to date. In this chapter we report the first example of using an *N*-alkylated tetraimidazophthalocyanine to grow 3D nMOFs with Zr or Hf SBUs and a cubic PCN-221 structure.

Chapter 5 demonstrates the SDT performance of surface-anchored sensitizers on a Hf_{12} SBU- and iridium PS linker-based nMOL platform and investigates its mechanism of $^1O_2$ generation. The TBP@MOL (TBP = 5,10,15,20-tetra(*p*-benzoato)porphyrin) assembly efficiently captures broad-spectrum sonoluminescence through both the Ir-PS linker and anchored porphyrin

sensitizers, where the excited Ir-PS linkers (donors) can then transfer energy directly to the porphyrin units (acceptors). The energy transfer synergizes with the highly flexible and accessible sensitizers to significantly enhance $^1O_2$ generation and *in vivo* SDT anticancer efficacy.

Acknowledgements

"I enjoy talking to you. Your mind appeals to me. It resembles my own mind except that you happen to be insane." – O'Brien in *1984* by George Orwell (an example of a typical academic interaction)

Although my time at the University of Chicago has been rife with personal struggles – beyond the grueling pursuit of academic success – the cathartic process of writing this thesis and acknowledgements section gave me the clarity to consider myself extremely fortunate to have been able to experience it all. To me, the chapters of this thesis are not only a recount of my research, but a memorial of my personal and academic growth in spite of the vicissitudes of life and science. To all the following people who inspired, motivated, educated, and nurtured me, your brilliance and humanity were paramount to my success and my survival through difficult times.

First and foremost, I would like to express my deepest gratitude toward my PhD advisor, Professor Wenbin Lin, who not only provided me with immense chemistry and biomedical knowledge but also a model for how to conduct myself as a professional scientist. Wenbin gave me the opportunity to explore various areas of chemistry, including inorganic, organic, physical, and materials, enabling me to become a well-rounded scientist capable of driving scientific advancements towards practical applications. I'm truly grateful that he gave me so much trust and support, especially when I felt lost at times trying to reach my research goals. Wenbin's high work ethic, rigorous scrutiny of data, and fervent ambition to effect transformative change in the world of science and medicine have all left a strong impression on me and will be the foundation upon which I will build my endeavors in the next chapters of my life. I shall forever be grateful of the knowledge acquired under his tutelage, as his unwavering convictions and scientific tenacity epitomize the traits befitting a true scholar and professor.

I'm privileged to have had the honor of selecting Professor John Anderson and Professor Bozhi Tian as my thesis committee members. Although still early in their careers, they have both been tremendous in their success as scientists and possess a sort of radiant humanity that lifted me up during this difficult endeavor. I will always reminisce on the days of playing softball with John on Team Beer or jokingly catcalling him from my car whenever I saw him jogging around Hyde Park. I'll also fondly remember how kind Bozhi was, always checking up on me in the elevator or near the coffee machine, making sure I was doing well. While those moments might seem small, he had an uncanny ability to always catch me when I was feeling demotivated and bring me back up.

I would have never reached this moment without the early guidance and foundation built by many of the teachers I've had along the way. In particular, I am indebted to my high school chemistry teacher, James Galinski, for pulling me away from being a troublemaker and instilling me with a passion for chemistry that provided me with direction and momentum when I lacked any. I also cannot truly express the gratitude that I have for the many professors and teachers that I had the pleasure of learning from at the University of Sussex: Professor Hazel Cox, Dr. Shane Lo Fan Hin, Professor John Spencer, Professor Mark Bagley, Dr. John Turner, Dr. Eddy Viseux and Professor Geoff Cloke, among others. They not only imparted me with a wide breadth of chemical knowledge that culminated in this interdisciplinary work but also did so with such elegance, eccentricity, and mastery that it profoundly shaped me as a person, scientist, and mentor.

There have been countless unbelievably brilliant people in the Lin Lab that I've had the chance to collaborate with, and it was only with their knowledge, creativity, and hard work that my projects found any form of success. I would like to first thank Professor Guangxu Lan, as he trained and guided me on MOF synthesis and design from my first day at the University of Chicago

and allowed me to work with him and learn from him on several projects during the first few years of my PhD. Without his friendship and mentorship, I would have undoubtedly been lost during the early years of my PhD. My colleague and best friend in the lab, Taokun Luo, was indispensable to the success of all of my projects and ideas throughout my PhD. I'm truly grateful that Taokun and I have spent 5 years in the lab together as I was not only able to see just how talented and creative he is as a scientist but also how compassionate he is as a friend. I will always be beholden to him for all of his hard work in our collaborations and the plethora of advice he gave me over the years. I'm also glad to have worked with a truly top-notch undergraduate, Tomas Germanas, whose ambition and hard work helped push me through the final challenges of my PhD. Although a few unexpected events led us to work together, he joined me when I needed him the most, making my final year unbelievably productive and surprisingly enjoyable. I'm truly grateful that he allowed me to be his mentor and that we had so many funny and interesting conversations between experiments.

The Lin Lab allowed me to work with, learn from, and become friends with so many amazing people over the years. I would like to thank the following members of the lab for their contributions to me: my 5th year cohort colleagues, Dr. Ziwan Xu and Dr. Xiaomin Jiang, for their expansive scientific advice and friendship; Dr. Yang Song and Dr. Xuanyu Feng for their guidance on inorganic chemistry, air-free synthesis and MOF characterization techniques; Dr. Haifeng Zheng, Dr. Yuanyuan Zhu and Dr. Yangjian Quan for teaching me synthetic organic and inorganic techniques; Dr. Christina Chan and Dr. Daniel Micheroni for guiding me through PhD life in my early years. I also want to thank the following current and previous graduate students and postdoctoral scholars for their support over the years (in no particular order): Yingjie Fan, Dr. Wenyao Zhen, Dr. Luciana Albano, Youyou Li, Dr. Yingying Li, Jinhong Li, Dr. Dong-Won

Kang, Zitong Wang, Dr. Qingyun Guo, Dr. Kuangda Lu, Langston Tillman, Dr. Pengfei Ji, Dr. Nining Guo, Dr. Wenbo Han, Dr. Chunbai He, Yibin Mao, Dr. Jing Liu. I consider myself extremely lucky to have met, worked with and mentored so many intelligent, ambitious and energetic undergraduate students, who made my time here truly enjoyable. So, I have to thank Pierce Yeary, Callie McCleary, Michael Kaufmann, Morten Lee, Steven Labalme, Abbie Blenko, Eric Yuan, Sam Veroneau, Megan Rodriguez, August Culbert and Eric You.

When the COVID-19 pandemic caused the city of Chicago (and indeed the rest of the world) to go into lockdown in 2020, it became extremely difficult to motivate myself and I found it somewhat paralyzing to work and socialize in the years after the lockdown was lifted. As such, I could not have been more fortunate to have already met my great friend, colleague and collaborator, Siddhartha Sohoni, in the years prior. Sid let me vent a lot of my academic and social frustrations and eventually helped me solve them by providing me with brilliant ideas, data, and research as well as a community in Professor Greg Engel's research group. Without Sid, I would not have had met two other incredible friends and collaborators, Indranil Ghosh and Olivia Wedig, who have provided me with too many opportunities and laughs to count. I also want to thank all the other members of the Engel group who let me frequent their office space for coffee and bounce ideas off of them: Lawson Lloyd, Qijie Shen, Coco Li, Eric Wu, Caitlin Bellora, Ainsley Iwanicki, Claire Jones, Katelyn Feuling, Emma McNesby, Keerthi Vaasan, and Rachel Leech.

The facility and staff at the University of Chicago have been astonishingly supportive, knowledgeable, and patient with me and were critical to my development during these years. In particular I have to thank Dr. Qiti Guo, who not only gave me technical training on AFM and other instruments in the MRSEC facilities but is also a great family friend and insightful mentor. It was an incredible honor to have been trained by him and celebrate his retirement and great success

with my dad, as they have been friends and collaborators ever since I was a young child. Secondly, I want to thank Dr. Vera Dragisich for her support through several difficult times during my PhD. Vera was always empathetic and gave me insightful perspectives on academic affairs and life in general, which really helped me to maintain a healthy frame of reference on myself and my research when things were not going well. I also owe much to the following facility staff members for their kind-hearted nature, masterful teaching, and swift instrument maintenance: Dr. Alexander Filatov for sharing his knowledge of crystallography and help with X-ray diffraction facilities; Dr. Yimei Chen, Dr. Joe Austin and Dr. Tera Lavoie for their help with electron microscopy; Dr. Jin Qin for his help with mass spectrometry; Dr. Josh Kurutz for his help with the nuclear magnetic resonance facilities; Dr. Justin Jureller for his help with MRSEC facilities.

To all the friends that I've made during my time at the University of Chicago, I can't thank you all enough for the positive encouragement, endless coffee runs, summer softball on Team Beer, strange yet hilarious conversations, and all the other good times. There are too many to list here, but I have to give particular thanks to the following people for being there for me during my hardest times: Joseph Schneider, Aritrajit Gupta, Dr. Nikita Onizhuk, Dr. Colin Swenson, Sean Sutyak, Adarsh Suresh, Sofi Maltseva, Nathaniel Durfee, Greg Rassolov, Maia Czaikowski, Olivia Laxton, Julia Dalrymple, Justin Ngai, Russell Kielawa, Julia Noel, Ethan Hyland, Lauren McNamara, Alex Crolais, Spela Kunstelj, Patrick Kelly, and Joseph Sifakis.

I was also lucky enough to have Dr. Dan Micheroni introduce me to the Midway Football pickup group. Playing touch/flag American football with this group for the last few years led to some of the best moments of my time at the University of Chicago. All the incredible plays, funny conversations, and elaborate game recap emails really gave me something to look forward to every Saturday. In particular I have to thank Dr. Seth Darling, who has been organizing this group for

25 years, for all of his throws that made me look so good and for the opportunity to run the group in my last year here. It goes without saying that I owe too much to all the Midway Football players I've had the honor of playing with: Isaac Darling, Olivier Menager, Sarah Collins, Demetric Wilson, Jovany Trujillo-Avila, Elgin Johnson, Eivan Johnson, Tyler Brazil, Deep Patel, Rylan Miyat, Monty Kakadia, Abhay Shah, Prentice Bradford, and Dan Harris.

One of the best decisions I ever made was attending the University of Sussex for my undergraduate degree, where I forged lifelong friendships. Late-night problem set sessions, navigating the eccentricities of our professors, and going out to the beachfront clubs in Brighton are just a few cherished memories. In my final year, I was lucky enough to have lived with some of my best friends: Ilyaas New, Jordan Doyle, Harry Morrissey, and Sam Snowden. I enjoyed too many hilarious moments with them blasting music in the tiny "living room" closet, braving "bucket-heated" pool parties and gym sessions in the concrete backyard, and having bonfire barbecues in the Moulsecoomb woods. I want to thank them and all of my other friends for all the good memories and support that helped me get to this point: Molly Jakes, Michael Vitiello, Daniel Maclean, Amino Yusuf, Anthony Lunn, Eirin Aegenes, Harry Watson, David Attlee and Zach Smythe.

I would be remiss to not express my deepest gratitude to my best friend, Esteban Perez, for being such an integral part of my life and growing alongside me since our early childhood. From the days of calling each other on landlines after school to share early internet memes and creating YouTube videos with early 2000s vibes, to supporting each other through the challenges of adulthood and creating a video game, Esteban has been an invaluable source of friendship and support. In the same vein, I want to extend my heartfelt thanks Derrick Kimura, Calvin Rudy, Daniel Romero, Tony Chen, Aron Tan, Robert Cao, Ivan Ng, and Ivan Chen. Their unwavering

friendship has been the lifeblood of my success, and they are a huge reason why I hold my upbringing in Chicago so dearly. Over the past three years, I've also had the privilege of living with one of my closest friends, Sander Peterman. During that time, we've been through some truly wild and spontaneous experiences, essentially becoming Costco royalty and boat pirates of the Chicago harbors. Thank you for the countless hilarious moments and for tolerating my annoying habit of spontaneously inviting all sorts of people over.

Without a doubt, my family has been the most important part of my life and words can never be enough to describe my fortune and appreciation for them for instilling me with a treasure trove of wisdom and character. First and foremost, I obviously would not be writing this without my parents, Drs. Philip and Guiru Nash. Without their unconditional love and support (and believe me when I say unconditional, because I can be a real pain sometimes) through all of my failings and successes, I would not have had such a rich and happy life. I'm grateful for all the years with my dad where he embedded a frustrating yet charismatic English personality within me, filled with a cheeky eagerness to wind people up, a proclivity for getting into bizarre situations, and a strangely apathetic yet fervent nature. However, I'm perhaps even more grateful for the balance my mom gave me in a rather amusing dichotomy by teaching me to be brutally logical even to a fault, to be stoic in the face of adversity, and to be virtuous and compassionate to others (all while being a Michelin level chef). While parent-child relationships can be tumultuous at times, those moments made me ever more appreciative of my siblings: Stephen Huang, Caroline Nash and Alex Nash. Stephen was not only my role model but best friend when I was growing up and he had a profound impact on all my favorite passions in music, sports and video games that still burn strong today. Although Caroline grew up far away from me, I was always in awe of my elder sister as she was and still is the embodiment of charm, perseverance, and courageous defiance. My eldest

brother Alex has consistently been a beacon of wisdom, providing enlightening conversations, and has always looked out for me and inspired my passions. Thank you all for everything.

Amidst the countless hours spent buried in research, the most precious gift that this academic pursuit bestowed upon me was the serendipitous alignment of circumstances that led me to meet my girlfriend and soulmate, Jessica Ng. It still amazes me how our paths intertwined in the most improbable way imaginable. Yet, all the memories and wildly unpredictable adventures we've been on together make even that seem ordinary. From the preposterous gondola ride in The Venetian wearing bridal sashes, to the daring moped trip in Mallorca where we dodged a minefield of jellyfish at a secluded beach, to discovering a golden ticket for free items in the Amsterdam Rituals store that not even the staff had ever seen before. Jess' vibrant spirit, spontaneity and curiosity is a sharp contrast to my annoyingly cynical and apathetic outlook, and I can't thank her enough for putting up with me and teaching me that there is so much more to cherish and explore in life. Although this chapter of my academic journey is coming to a close, I'm filled with immense joy and anticipation for all the memories I will continue to make with my partner and best friend, Jess.

Chapter 1: Introduction

1.1 Nanoscale metal-organic frameworks

1.1.1. Structure and history

As we look toward new molecular materials to provide increasingly more complex capabilities and functionality in the pursuit of evermore effective cancer treatment methods, structural and molecular stability, variety and tunability become paramount to reach any form of clinical success. Considering this, reticular chemistry – the study of geometry-guided linking of discrete molecular entities with strong bonds to form an extended periodic network – has drawn significant attention as a developing field within nanomedicine for its potential to establish a valuable multifaceted platform.[1-5]

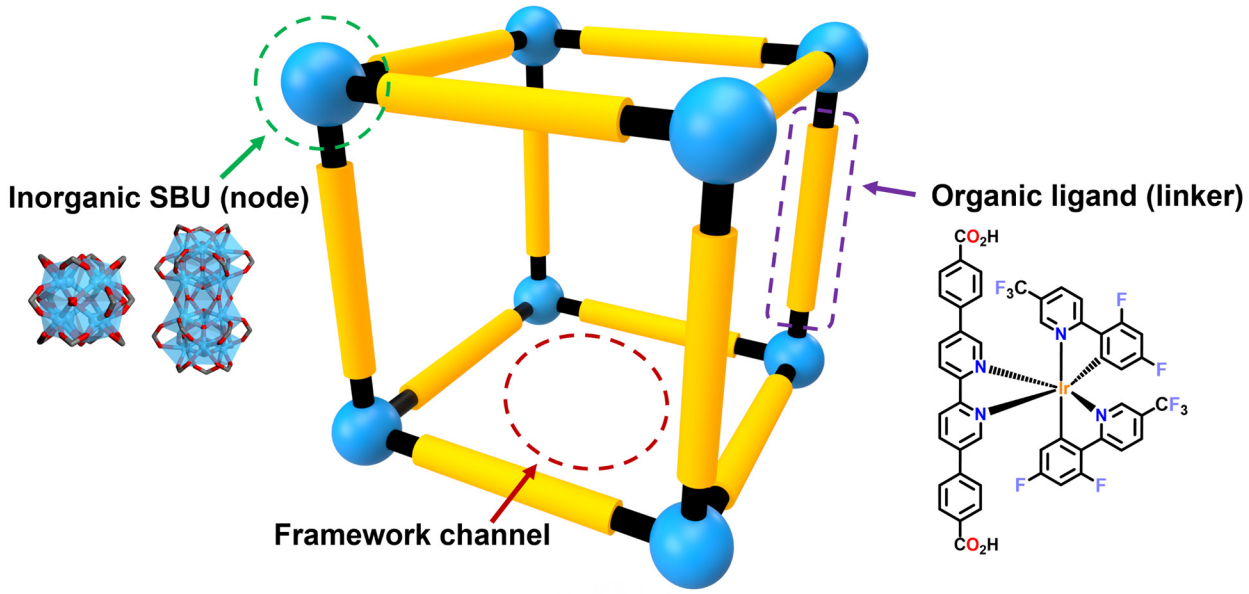

Figure 1-1. Illustration of a general MOF architecture with its fundamental building units.

One such class of porous crystalline networks is metal-organic frameworks (MOFs), also known as porous coordination polymers (PCPs), which are hybrid organic-inorganic molecular materials composed of a network of multidentate organic ligands (linkers) coordinated to inorganic

clusters (nodes) (**Figure 1-1**). Accordingly, the expansive structural variety of MOFs is a result of the following: (1) precise synthetic manipulation and modular behavior of the organic linkers; (2) geometric and compositional diversity possible with inorganic clusters; (3) assortment of ancillary ligands (e.g. H_2O, OH^-, AcO^- among others); (4) mesoscopic architecture, topology and porosity; (5) postsynthetic modification (PSM) of each of the previous points; (6) linker defect sites.[6-10]

Reticular chemistry and hybrid organic-inorganic molecular materials resulted from a culmination of many centuries of work and serendipitous discoveries on the synthesis and characterization of coordination compounds. It is generally agreed that the oldest reported synthesis of a coordination compound was the pigment Prussian blue by Johann J. Diesbach in 1706, although the chemical composition and structure was not known until much later.[11] It was not until the conceptual foundation of coordination chemistry was built by Nobel Prize-winner Alfred Werner (awarded in 1913), for elucidating the geometric linkage of coordination complexes, that the field could blossom and dimensionally extend these structures.[12] One example of an extended structure that came shortly after is the Hofmann clathrate, with the formula $[Ni(CN)_2(L)](C_6H_6)$ ($L = NH_3$), published by Karl A. Hofmann and later found to be composed of 2D layers with linked Ni^{2+} and CN^- ions with adjacently alternating octahedral and tetrahedral nickel center geometries and trapped benzene solvent molecules that assist in templating the material.[13-14] Structure elucidation through X-ray crystallography sparked an influx of modifications to the clathrate that would eventually lead to metal ions linked to longer and more elaborate multidentate organic ligands to form 3D materials with extended crystalline networks.

While the synthesis of these new class of higher dimension materials would become more advanced, the topological classification of these networks would be concurrently developed by Alexander F. Wells who proposed a system to break the crystal structures into nets composed of

linkers and nodes.[15] It was from this crystal engineering perspective that Richard Robson and Bernard Hoskins would apply these principles in their 1989 seminal work to demonstrate that the material structures can be predicted and designed based on the geometries and connectivities of the discrete molecule building units to yield a variety of structure types.[16-17] The resulting ability to synthetically control the material structures ignited a surge of work on these extended 3D coordination networks.[18-20] These coordination networks would later be coined metal-organic frameworks by Omar M. Yaghi in 1995,[21] and both the field of reticular chemistry and the library of MOFs would experience an incredible growth in the following decades by research from the following scientists and their coworkers: Omar M. Yaghi, Makoto Fujita, Susumu Kitagawa, Michael J. Zaworotko, Gerard Ferrey, Wenbin Lin, Jeffrey R. Long, Hong-Cai Zhou, Karl P. Lillerud and many others.

Early works in the MOF field used charge neutral organic linkers to try and form non-interpenetrated 3D networks, such as $[(en)Pd(bpy)(NO_3)_8]_4$ (en = ethylenediamine; bpy = 4,4'-bipyridine) with single metal-ion nodes that sustain well-defined molecular dimension pores and channels, similar to those found in zeolites.[22-24] However, these charge neutral materials have relatively weak coordination bonds and require charge-balancing counter ions within the pores, leading to poor structural and chemical stability. As a result, research efforts quickly moved to using charged carboxylate linkers and polynuclear inorganic clusters (commonly referred to as secondary building units or SBUs) to increase the bond strengths, structural rigidity and chemical stability with $Co(BTC)(Py)_2$ (BTC = benzene tricarboxylate; Py = pyridine) in 1995, $Zn(BDC)(H_2O)$ in 1998, and $Zn_4O(BDC)_3$ in 1999.[25-27] However, the issues of stability in aqueous environments and at higher temperatures severely limited the potential applications of the growing library of early MOFs until the seminal work by Karl P. Lillerud and coworkers in 2008, which

demonstrated the isoreticular synthesis of a 12-connected Zr_6-cluster MOF family (denoted as UiO) with exceptional stability (**Figure 1-2**).[28] This family of MOFs, with the general formula $Zr_6O_4(OH)_4(R)_6$ (where R = linear dicarboxylate ligand), utilizes the highly symmetric SBU and strong bonds between Group IV metals and oxygen to afford a versatile and stable MOF platform.[29-30] Although over 100,000 MOF structures have been reported to date,[31] a large majority of them incorporate relatively labile coordination bonds or soluble ligands. While this confers intrinsic biodegradability, these MOFs consequently lack the overall structural stability to be fully effective in some industrial and clinical applications. The search for more MOFs with functionality and adequate stability for applications in aqueous environments, such as in nanomedicine, remains ongoing.

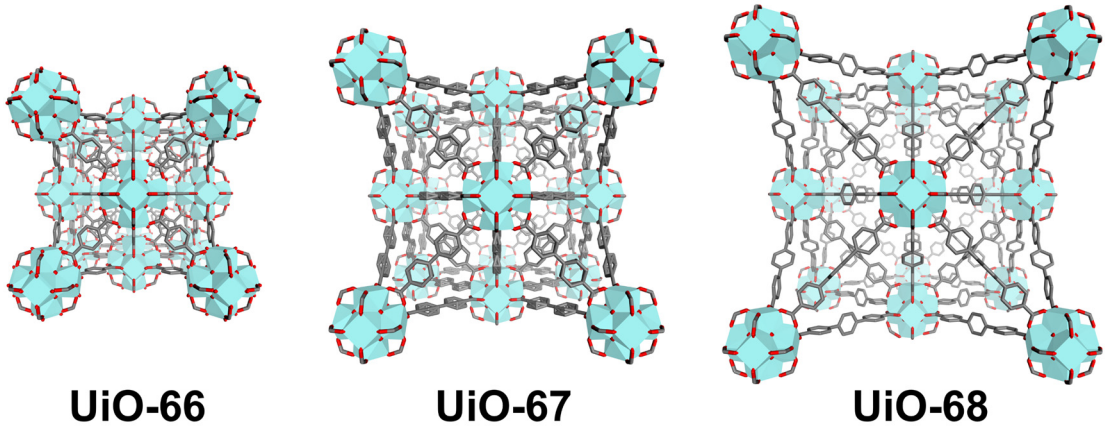

Figure 1-2. Isoreticular synthesis of the Zr_6 cluster-based UiO MOFs.

1.1.2. Synthetic strategy and structural design

The synthesis of crystalline nMOFs occurs through the self-assembly of metal ions, modulators [e.g. acetic acid (AcOH), formic acid (HCOOH), benzoic acid (BA), trifluoroacetic acid (TFA)], and multidentate bridging organic ligands, driven by the minimization of the system free energy (**Figure 1-3**).[32] This process typically proceeds solvothermally through first forming metastable SBUs in solution, which are then interlinked by the bridging organic ligands – in

competition with the modulators present – to generate the MOF structure.[33-35] Consequently, there are several factors that can be modified to manipulate the overall structure and properties of the resulting MOF, which have resulted in the extensive library of different structures.[36] Perhaps the most important aspect in the solution-based crystallization of MOFs is the solubility of the metal precursors and organic ligands, which is determined by time, temperature and pH of the solution. The solvent typically used in MOF synthesis is *N,N*-dimethylformamide (DMF), which upon exposure to water and higher temperatures progressively undergoes hydrolysis to produce formic acid and dimethylamine.[37-38] The latter is a base and proceeds to deprotonate the carboxylic acid groups of the organic ligands, which can then coordinate to the formed SBUs. Thus, the crystallization kinetics can be finely controlled by the rate of linker deprotonation and coordination competition to the SBU.

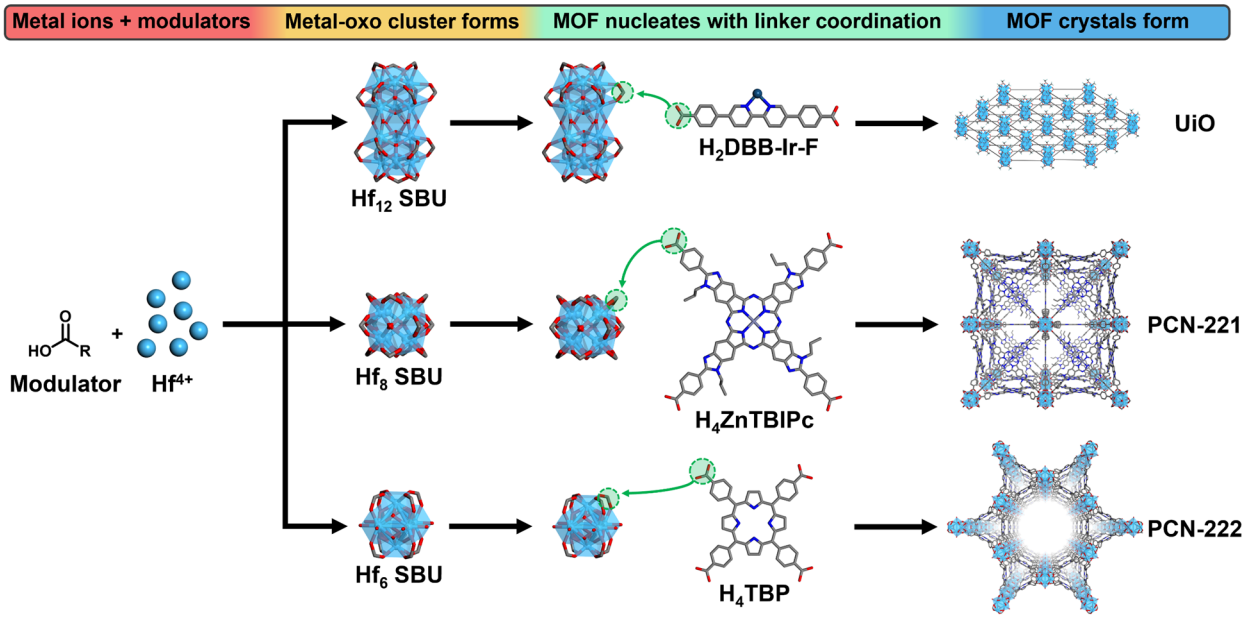

Figure 1-3. Schematic of the synthetic mechanism for MOF crystallization and growth.

Varying the amounts of water and modulator strongly influence the SBU structure as well as the MOF's particle size, crystallinity, and morphology.[30, 39-41] In general, lower temperatures

and modulator concentrations tend to result in faster nucleation and smaller particle sizes, thus reaction conditions can be optimized to yield nanoscale metal-organic frameworks (nMOFs).[42]

The concept of isoreticular chemistry describes the modular nature of the discrete MOF building blocks, as the same network and topology can be used with interchangeable components within certain limitations. For example, a simple organic ligand like 1,4-benzenedicarboxylic acid (BDC) can be functionalized at any of the positions ortho to the carboxylic acid groups and still result in a MOF with the same topology.[43] Accordingly, organic ligands which are structurally or functionally different but contain very similar lengths and denticity can also form mixed-ligand MOFs during the solvothermal process.[44-46] However, this method is typically limited to linear dicarboxylate organic ligands, and often cannot be extended to bridging ligands of higher denticities and different geometries. Although MOFs have high tunability, the specific inorganic cluster and its connectivities impose geometric restraints that limit the types of organic ligands that can be used as linkers during MOF synthesis. Typically, the ligands must be rigid and the coordinating functional groups must have a specific orientation relative to each other to form crystalline phases. Thus, the inclusion of organic ligands with lower symmetry or restrictive geometries either require substantial synthetic effort to overcome or a different loading method altogether.[47]

1.1.3. Postsynthetic modification

The structural tunability of MOFs can be extended by the ability to postsynthetically modify each of the discrete building units in a variety of ways while retaining its crystallinity and porosity. These postsynthetic modifications (PSM) can be broadly classified into three categories: (1) functionalization at the organic linker site;[48-51] (2) functionalization at the SBU site;[52-54] (3)

encapsulation of various species (e.g. small molecule drugs, biomolecules, sensitizers) in the pores and channels (**Figure 1-4**).[55-58] PSM provides an alternative method to functionalize the MOF, as the same functionalization during the initial solvothermal synthesis may become complicated or fail entirely. For example, organic ligands with functional groups that are either thermally labile or can coordinate to the metal ions will be unsuitable to incorporate using conventional synthetic conditions. However, optimizing reaction conditions for MOF synthesis using a modified ligand can be a challenging and time-consuming task.

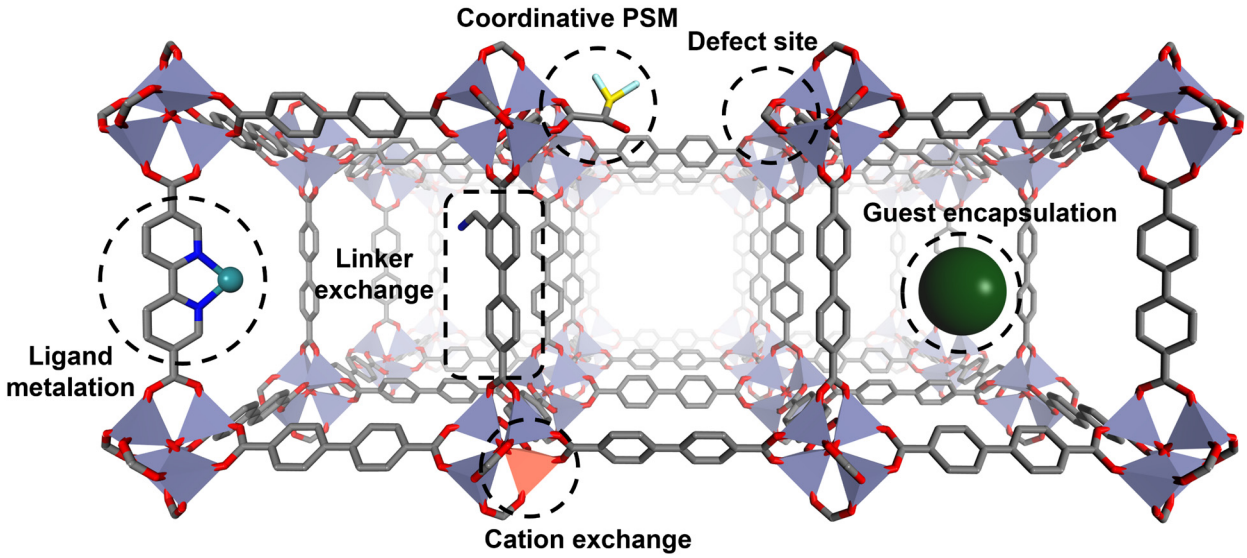

Figure 1-4. Illustration of different PSM strategies for MOF functionalization.

As we look toward nanomaterials with progressively complex functionalities, their synthesis becomes exponentially difficult. Therefore, it is often a streamlined approach to build the MOF as a stable scaffold which can then be functionalized further through PSM. This strategy provides several advantages: (1) functional groups or entire ligands that are unsuitable presynthetically can be introduced; (2) the organic ligand is open to a vast array of organic chemistry transformations; (3) other metal ions can be inserted into or between SBUs or even coordinated to the organic linker through dative bonds (e.g. 2,2'-bipyridine moiety); (4) other

molecular species unsuitable for use as a bridging ligand can be loaded physically into the MOF pores or onto its surface.[59] Multiple PSMs can then be combined to afford even more complex or multifunctional MOFs.

1.2 Nanoscale metal-organic layers

Although MOFs are typically synthesized as 3D materials with permanent porosity and large channels, metal-organic layers (MOLs) – a 2D analogue of MOFs – have recently demonstrated potential in catalysis, photocatalysis and nanomedicine.[54, 60-65] MOLs retain many of the properties and advantages of MOFs over discrete molecular species but replace the permanent porosity for higher surface area and capacity for surface modification. Reducing the dimensionality eliminates diffusion barriers and allows other molecular species in solution to easily access and form the necessary encounter complexes with the SBUs or organic ligands, resulting in enhanced activity.[66] The SBUs typically have coordinating monocarboxylate capping ligands (e.g. TFA, HCOOH, BA, AcOH) whose pKa values can be leveraged to postsynthetically exchange with other carboxylate-based ligands under relatively mild conditions. Surface PSM is especially advantageous for loading larger and geometrically challenging or unstable compounds unsuitable for solvothermal MOL synthesis. Additionally, the surface isolation of the organic ligands (e.g. sensitizers, catalysts, sensors) prevents aggregation, results in a different local environment, and spatially restricts their movement relative to the bridging ligands.[67-68] This loading method often results in a synergistic effect as efficacy is increased relative to the molecular species and additional functionality can be built in by energy transfer mechanisms (e.g. Förster, Dexter) between the bridging and capping ligands, which are typically within 0.5-1 nm of each other.[69-70]

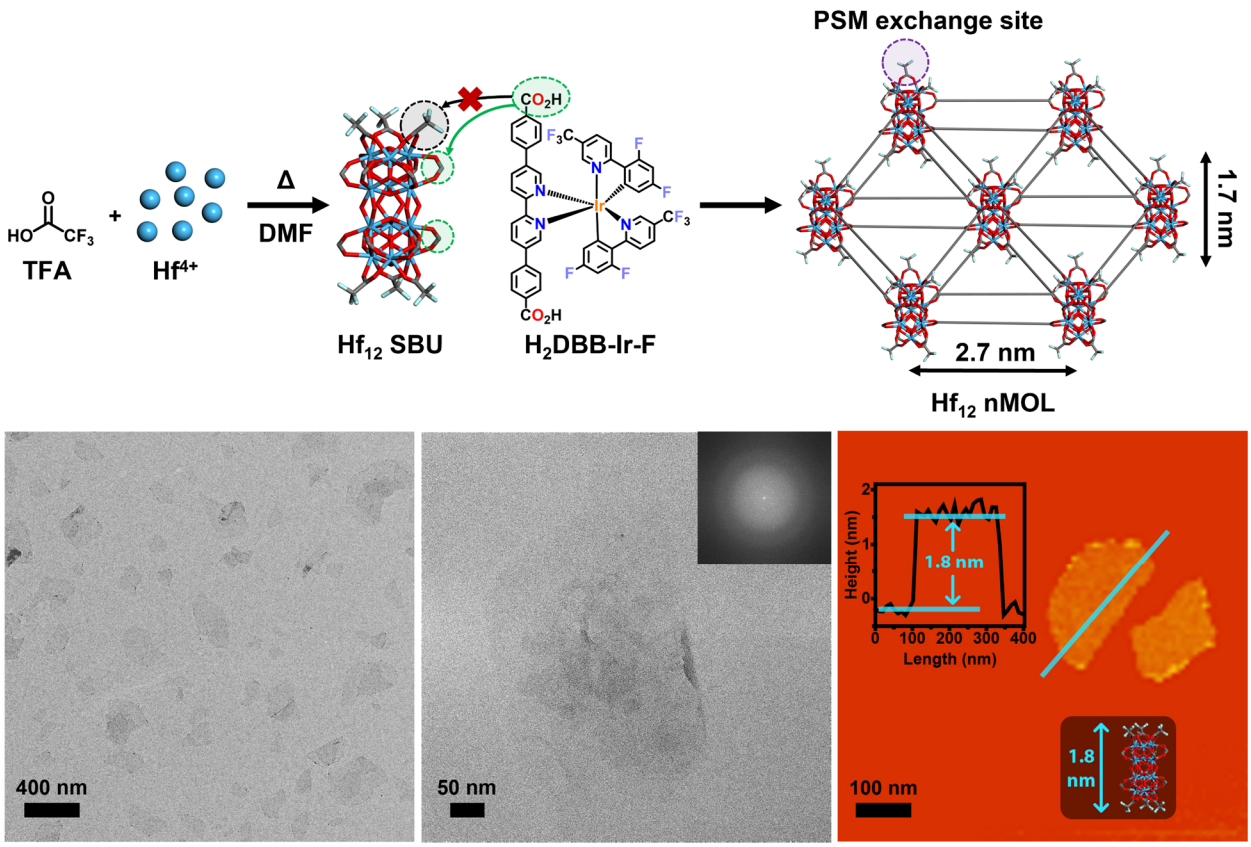

Figure 1-5. Schematic showing the synthetic route to Hf_{12} nMOLs. TFA capping ligands on the nMOL can be postsynthetically exchanged with other carboxylic acid-functionalized molecules under mild conditions. Hf_{12} nMOLs have a nanoplate morphology, shown by high-resolution transmission electron microscopy (HR-TEM) and atomic force microscopy (AFM).

Despite their advantages, only a handful of MOL platforms have been synthesized as the organic ligands and modulators must be precisely chosen and controlled to afford the monolayers. Through several MOLs reported from our group, we postulate that directing lateral growth and preventing vertical growth can be facilitated using the following design principles: (1) certain modulators and capping ligands can reduce the surface energy; (2) the variation in binding energy of the vertical and lateral coordination sites of the SBU; (3) favorable charge distribution across the laterally coordinating metal ions of the SBU; (4) weakly coordinating electron-deficient organic ligands that only replace the favorable lateral sites. The resulting monolayers are typically

several hundred nanometers in width and only a few nanometers in height depending on the size of the SBU and the capping ligands.

1.3 Nanoscale metal-organic frameworks for localized cancer therapy

Cancer encompasses a group of complex diseases characterized by abnormal cell proliferation, which can invade or metastasize to different regions of the body. It is one of the world's largest public health problems and remains a leading cause of death. With the rapid advancement in medicine and healthcare accessibility, cancer death rates have been declining since the early 1990s despite an increase in new cancer cases annually in higher income countries, with ~1.9 million new cases diagnosed in the United States in 2022.[71] However, even with increasingly positive prognosis rates, there is still a need for more effective, less toxic and cheaper innovations in cancer therapy in order to relieve the economic pressures that prevent many patients from receiving treatment.[72] This point is becoming progressively more important as low- and middle-income countries are expected to bear the majority of the global cancer burden within the next 50 years, with approximately three-quarters of all cancer deaths occurring in these countries.[73]

Cancer treatment modalities can be generally categorized into surgery, radiation therapy, chemotherapy, hormonal therapy and immunotherapy. Surgery is the oldest and most effective treatment for localized primary tumors and their associated regional lymph nodes as it operates by zero-order kinetics, eliminating 100% of excised tumor cells.[74-75] However, it is not without its downsides as it requires large excision margins, can result in collateral damage of adjacent structures depending on the location, and lacks efficiency in resecting certain metastases.[76-77] It is estimated that somewhere between half and two-thirds of all new cancer patients will receive radiotherapy (RT), and is responsible for about 40% of cancer cure rates.[78-79] Overall, RT is an

extremely cost-effective treatment and, when combined with surgery and chemotherapy (CT), results in an effective modality of palliative care for local and metastatic disease. Nevertheless, advances in RT and CT technologies have yet to fully solve the issue of toxicity, as the techniques lead to either local or systemic collateral tissue/organ damage.[80-83]

Several potential localized cancer modalities look to compliment the library of options available to oncologists: photodynamic therapy (PDT), sonodynamic therapy (SDT), radiotherapy (RT) and radiodynamic therapy (RDT) (**Figure 1-6**).

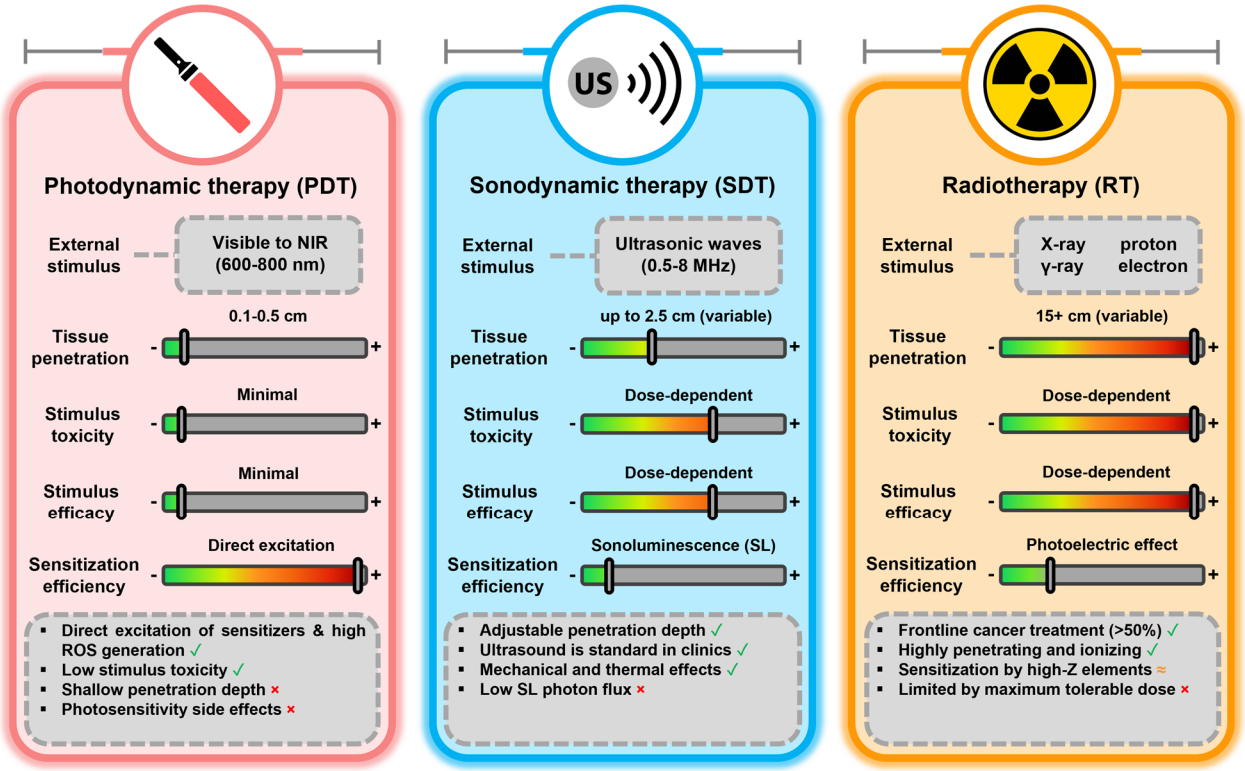

Figure 1-6. Illustration comparing the various externally stimulated local cancer modalities.

These methods seek to irradiate sensitizers that have accumulated at the tumor with visible to near-infrared (NIR) light,[84-85] ultrasound,[86] or X-rays,[87] respectively, to produce cytotoxic reactive oxygen species (ROS) that can destroy tumor cells. The sensitizers provide a unique advantage as they are non-toxic to healthy cells without irradiation and their antitumor efficacy

can be activated using non-damaging irradiation or with lower irradiation doses (in the case of X-rays).[67, 88] The specific mechanisms of action as well as advantages and disadvantages of these modalities will be discussed in the following sections.

Traditionally, sensitizers have been macrocyclic organic compounds or metal-based nanoparticles, but these can suffer from low solubility, poor pharmacokinetics, low tumor uptake, and toxicity. nMOFs and nMOLs have recently shown promising results in applications as a multifunctional nanosensitizer platform.[4, 68, 89-91] The nanoscale particle utilizes the advantageous enhanced permeability and retention (EPR) effect, which exploits the abnormalities in tumor vasculature to increase the uptake of intravenously administered drugs with diameters less than 200 nm.[92-93] Additionally, the tunable and porous framework allows insoluble sensitizers and drugs to be loaded with high-capacity as a bridging linker or physically loaded in the pores in a multifunctional platform. In the following sections the advantages of nMOFs and nMOLs will be discussed relative to the specific therapeutic modality.

1.3.1. Photodynamic therapy

Photodynamic therapy (PDT) is one of the localized therapeutic modalities that utilizes a photosensitizer (PS), usually an organic dye, a visible or NIR light source, and oxygen to produce cytotoxic ROS that can damage or eradicate tumors (**Figure 1-6**).[94] The mechanism of PDT is illustrated in **Figure 1-7**. In PDT, the PS absorbs a photon of sufficient energy and causes the PS to be excited from the ground state (S_0) to one of its singlet excited states (S_n), where it undergoes internal conversion (IC) to its lowest excited state (S_1). From this point there are several general non-radiative or radiative transitions that can occur: fluorescence (radiative) back to S_0, vibrational relaxation (non-radiative) back to S_0, intersystem crossing (ISC; non-radiative) to the triplet

excited state (T_1). Only the ISC pathway will result in PDT efficacy, as the triplet excited organic PS is required to undergo triplet-triplet annihilation with ground state oxygen ($^3O_2$) to generate the highly reactive singlet oxygen ($^1O_2$), known as a type II PDT pathway.[95] However, depending on the type of PS used, the triplet excited PS can undergo an alternative type I pathway which involves either proton or electron transfer to form reactive radicals and other ROS such as superoxide (O_2^-), hydrogen peroxide (H_2O_2), hydroxyl radical ($^{\bullet}OH$).[96] These two pathways occur simultaneously to varying degrees depending on the PS and oxygen concentration. Of the various ROS produced in PDT, $^1O_2$ is perhaps the most effective as it is highly reactive and can oxidize nearby tumor cells, has a lifetime of ~3.5 μs in water or ~3 μs in cell nuclei, and a diffusion radius of ~200 nm.[97-98] Ultimately, PDT can lead to localized destruction of diseased tissue (apoptosis and necrosis) and acute inflammation, which stimulates the innate immune system to combat the primary tumor and any distant tumor cells.[99-100]

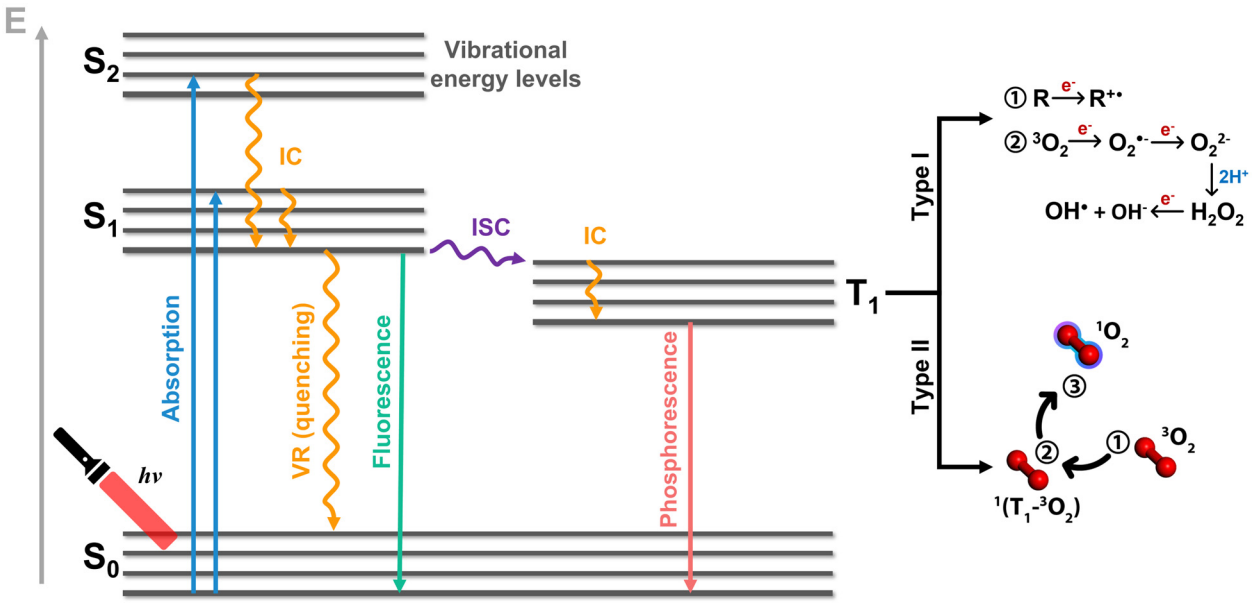

Figure 1-7. Jablonski diagram illustrating the photophysical processes and chemical consequences of photoexcitation and PDT. (VR = vibrational relaxation; IC = internal conversion; ISC = intersystem crossing)

The chemical structure and photophysical properties of the PS are of critical importance to the PDT efficacy. An ideal photosensitizer must possess the following properties: (1) absorption wavelength in the phototherapeutic window (650-850 nm) to optimize the tissue penetration depth of visible light; (2) high molar absorption coefficient, ε, to maximize the efficiency of absorbing incident photons that reach the PS; (3) aqueous solubility to prevent aggregation-induced quenching (AIQ) of the excited PS.[101] Porphyrins are macrocyclic molecules commonly found in naturally occurring pigments such as hemoglobin and chlorophyll and are a staple of PDT as they feature high ISC efficiency and high triplet quantum yield due to low radiative relaxation rates.[102] However, their most intense absorption is the Soret band around 400 nm, while the PDT-relevant Q-bands from 500-700 nm have very low ε values (~6800 M^{-1} cm^{-1}) (**Figure 1-8**).[103] Synthetic analogues of porphyrin, such as chlorin, bacteriochlorin, have reduced molecular symmetry and display a red shift of the Q-band to around 740 nm in addition to a significantly higher oscillator strength.[104-105] Despite these improvements, chlorins and bacteriochlorins suffer from photoinstability and are therefore mostly unsuitable for PDT.[106-107]

Phthalocyanines are a structural analogue of porphyrins except they are composed of four isoindole subunits, as opposed to pyrrole subunits, linked together in a ring by nitrogen atoms at the four *meso* positions.[108] They are synthesized by reductive cyclotetramerization of phthalonitriles, typically at high temperatures and in the presence of a metal salt as a templating agent and a strong base (e.g. 1,8-diazabicyclo(5.4.0)undec-7-ene; DBU).[109-111] Consequently, however, this synthetic methodology is notoriously inflexible compared to their porphyrin counterparts,[112-114] as phthalocyanines cannot be built stepwise and often form regioisomeric mixtures with asymmetric phthalonitriles.[106, 115]

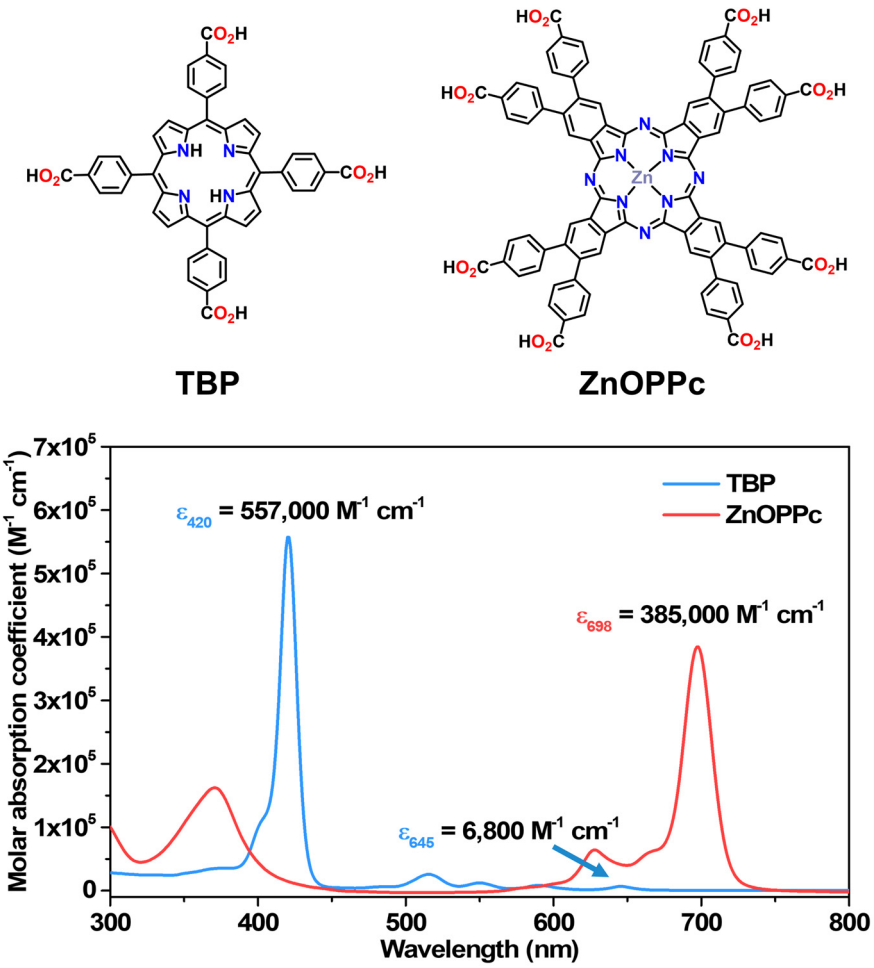

Figure 1-8. Structures and UV-visible absorption spectra comparing the general PS properties of porphyrin and phthalocyanine.

The extended conjugation and delocalization of the π-electrons imparts a strong propensity for cofacial aggregation but also affords a sensitizer with a Q-band between 650-750 nm (depending on functionalization) and an ε value several orders of magnitude greater than that of porphyrin (~385,000 M^{-1} cm^{-1}) (**Figure 1-8**).[116] Additionally, unsubstituted phthalocyanines possess tremendous thermal, chemical and photostability, but suffer from severe aggregation even in organic solvents.[117-119] Metalated phthalocyanines can be substituted axially depending on the metal center (e.g. Si or Al) or peripherally on the phthalocyanine precursor, which can confer higher solubility but lower stability than its unsubstituted version. With aqueous solubility

imparted through axial and peripheral substitutions, phthalocyanines have even shown promise in clinical trials (phase 1).[120-121]

However, even with high stability and an ideal photophysical profile, synthetically designing these organic PSs to also have the desired pharmacokinetic behavior and tumor accumulation is an arduous if not impossible task. Multifunctional platforms such as nMOFs and nMOLs have shown great potential in photodynamic therapy for their dispersibility, tunability, and capacity to densely load insoluble PSs while restricting their aggregation and preventing the loss of PDT efficacy. Therefore, it is of great interest to design and optimize the loading and performance of these sensitizers within the MOF systems to unlock their full potential in PDT.

1.3.2. Sonodynamic therapy

Although PDT is extremely efficient at transferring energy from visible light to produce tumor-killing ROS, it has two major drawbacks: visible and NIR light penetration through tissue and patient photosensitivity. Light attenuation varies with different tissues but visible and NIR light flux generally decrease exponentially over depth ranges of 1-30 mm, with photons reaching their maximum penetration depth around 700-800 nm due to increasing attenuation by water in the IR region (**Figure 1-6**).[122-124] As a consequence of the penetration depth, PDT is often tested for the treatment of skin cancers, but retention of PSs after treatment lead to undesirable phototoxicity.[125]

Sonodynamic therapy (SDT) is an alternative localized modality that potentially addresses these issues as it utilizes the interactions between ultrasonic waves, cavitation in aqueous solutions and sonosensitizers to locally destroy tumor cells at larger depths (**Figure 1-6**). SDT attempts to branch off the success of magnetic resonance imaging guided focused ultrasound surgery

(MRgFUS) in clinics, which was FDA-approved in 2016 for treating medically-refractory essential tremors by ablating the ventral intermediate nucleus of the thalamus.[126-128] However, the drawback of MRgFUS is that it requires magnetic resonance imaging (MRI), as many medical devices (e.g. pacemakers) are MRI incompatible and the ultrasound transducer instrument itself or any implanted metallic devices can cause image artifacts.[129-131] It has been shown that SDT can elicit a general cancer killing effect at low US energy doses without precise imaging guidance and may avoid these issues.[132-133] Therefore, sonosensitizers are being developed as an intravenously administered and externally activated drug to provide extra flexibility in ultrasound-based cancer therapy.[134]

Ultrasound (US) is a mechanical wave that propagates through particles in a medium from continuous compression (high pressure) and rarefaction (low pressure), which is generally produced by the expansion and contraction of a piezoelectric transducer crystal.[135] The efficiency of energy propagation through tissue depends on the acoustic impedance – a measure of the medium's compressibility – which is composed of several phenomena: reflection, refraction, scattering and attenuation.[136] The intensity loss is tissue and frequency (f) dependent, making it a critical component of SDT as it defines the maximum effective depth of the treatment. US intensity can be expressed in decibels (dB) and the attenuation coefficient, μ, in soft tissues can be approximated as 0.5 dB/cm × f (MHz), which means that higher frequency US will have rapidly reduced penetration depths.[136] Therapeutic US, such as in high-intensity focused ultrasound (HIFU) treatments, typically uses frequencies between 0.5-8 MHz, depending on the depth of treatment.[137-138] With lower frequencies (0.5-1 MHz) the effective therapeutic penetration depth can reach up to 10 cm. However, the initial US intensity required to evoke a therapeutic effect depends on the modality (e.g. HIFU ablation or SDT) and its required intensity threshold at the

treatment site; the threshold to thermally induce a lesion is ~1700 W/cm^2,[139] while the threshold for cavitation-induced sonoluminescence in SDT is ~0.25 W/cm^2.[140]

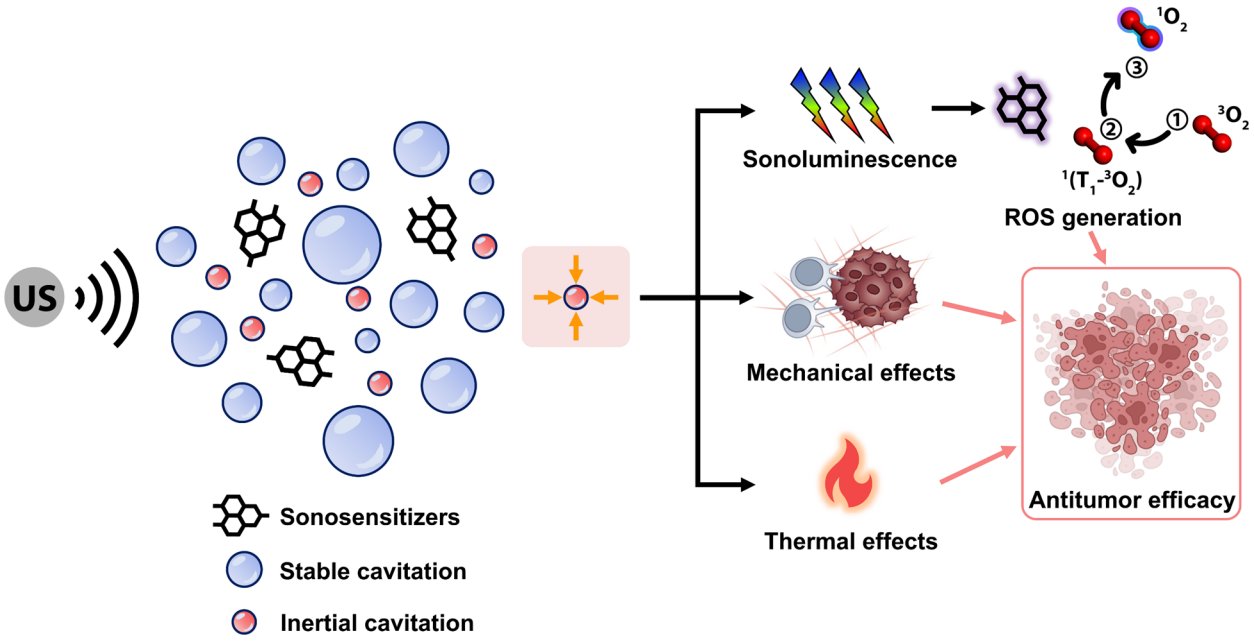

Figure 1-9. Illustration of the *in vivo* effects of US cavitation leading to SDT antitumor efficacy.

The mechanism of SDT is complex and multifaceted and is still being discussed. Currently, there are three widely accepted biological consequences: (1) generation of ROS through a sonosensitizer; (2) US cavitation effects; (3) thermal damage from US attenuation as previously discussed (**Figure 1-9**).[134] The most contentious is the mechanism of ROS generation, with sonoluminescence (SL)[141] and pyrolysis[142] being the two prominent theories. Recent work has provided strong evidence that SL is the dominant mechanism, especially with porphyrin sonosensitizers.[143] SL is produced upon the collapse of US-induced cavitation bubbles (inertial cavitation), where high temperatures and pressures of the densely compressed gases within the bubble lead to thermal ionization and subsequent bremsstrahlung emission.[144-145] This emission produces continuous spectrum radiation in the ultraviolet (UV) and visible spectral regions (200-800 nm) that can excite sonosensitizers to the S_1 state and ultimately produce ROS in a similar

manner to PDT.[146] However, US cavitation itself can produce therapeutically relevant non-thermal and thermal effects.[147] Non-thermally it has been suggested to damage tumor vasculature, disturb cell membranes, and increase permeability, accelerating the intracellular uptake of sonosensitizers or other drugs.[148-149] Unstable cavitation can also produce microjets that can cause thermal damage to tumor architecture.[150] Thermal effects are believed to be primarily responsible for the only FDA-approved US treatment of cancer – the high intensity focused ultrasound (HIFU) treatment of prostate cancer.

1.3.3. Radiotherapy-radiodynamic therapy

Radiotherapy (RT) has evolved in the last century to become an integral part of the frontline clinical defense against and palliative care of many cancers and their metastases. Its therapeutic efficacy arises from the interactions of highly penetrating ionizing radiation, such as X-rays, with water in cancerous tissue and cells to produce highly reactive hydroxyl radicals through radiolytic cleavage (**Figure 1-6**). The generated hydroxyl radicals can then diffuse and cause DNA double-strand breaks leading to cell death, but this process does not differentiate between healthy or cancerous cells.[151] Although RT is a highly effective local therapeutic modality, it is limited by the maximum tolerable radiation dose that optimizes the balance between cancer killing efficacy and collateral damage to healthy tissues and organs (**Figure 1-6**).[152]

To shift the balance further in favor of the patient, modern strategies have focused on using radiotherapy in lower doses or with greater spatial control to avoid undesired tissue damage and also in combination with immunotherapy to combat recurrence and radioresistance.[153-156] One strategy is to use a radiosensitizer that can attenuate X-rays at lower and safer doses while exerting the same therapeutic effect as full dose treatments. Although organic radiosensitizers have been

studied for decades, they have often shown poor efficacy in preclinical or clinical trials.[157-158] Heavy metal-based nanoparticles (e.g. Au or HfO_2) on the other hand have shown promising results as a radiosensitizer because their high atomic number (Z) enhances the photoelectric effect and pair production, leading to electron emission and secondary water radiolysis.[159-162] Recently, our group has demonstrated that nMOFs and nMOLs can have even stronger radioenhancing effects – by the generation of ROS from high Z SBUs and sensitizing organic linkers in a process called radiotherapy-radiodynamic therapy (RT-RDT) – while providing a multifunctional platform that can deliver chemo- or immune-therapy drugs.[88, 91, 163-165] The RDT effect has been suggested to arise due to energy transfer from the high Z SBUs to the sensitizing ligands. Despite these advances, with a Hf-based nMOF even showing very promising results in phase 1 clinical trials using RT-RDT,[166] we believe the tunability of nMOFs offer the potential to vastly improve the radioenhancement effect, pharmacokinetics of intravenous administration and tumor accumulation.

1.6 References

1. Yaghi, O. M.; O'Keeffe, M.; Ockwig, N. W.; Chae, H. K.; Eddaoudi, M.; Kim, J., Reticular synthesis and the design of new materials. *Nature* **2003,** *423* (6941), 705-714.

2. Della Rocca, J.; Liu, D.; Lin, W., Nanoscale Metal–Organic Frameworks for Biomedical Imaging and Drug Delivery. *Accounts of Chemical Research* **2011,** *44* (10), 957-968.

3. Lan, G.; Ni, K.; Lin, W., Nanoscale metal–organic frameworks for phototherapy of cancer. *Coordination Chemistry Reviews* **2019,** *379*, 65-81.

4. Ni, K.; Luo, T.; Nash, G. T.; Lin, W., Nanoscale Metal–Organic Frameworks for Cancer Immunotherapy. *Accounts of Chemical Research* **2020,** *53* (9), 1739-1748.

5. Wu, M.-X.; Yang, Y.-W., Metal–Organic Framework (MOF)-Based Drug/Cargo Delivery and Cancer Therapy. *Advanced Materials* **2017,** *29* (23), 1606134.

6. Kim, J.; Chen, B.; Reineke, T. M.; Li, H.; Eddaoudi, M.; Moler, D. B.; O'Keeffe, M.; Yaghi, O. M., Assembly of Metal−Organic Frameworks from Large Organic and Inorganic Secondary

Building Units: New Examples and Simplifying Principles for Complex Structures. *Journal of the American Chemical Society* **2001,** *123* (34), 8239-8247.

7. Zhao, D.; Timmons, D. J.; Yuan, D.; Zhou, H.-C., Tuning the Topology and Functionality of Metal−Organic Frameworks by Ligand Design. *Accounts of Chemical Research* **2011,** *44* (2), 123-133.

8. Lu, W.; Wei, Z.; Gu, Z.-Y.; Liu, T.-F.; Park, J.; Park, J.; Tian, J.; Zhang, M.; Zhang, Q.; Gentle Iii, T.; Bosch, M.; Zhou, H.-C., Tuning the structure and function of metal–organic frameworks via linker design. *Chemical Society Reviews* **2014,** *43* (16), 5561-5593.

9. Ma, L.; Falkowski, J. M.; Abney, C.; Lin, W., A series of isoreticular chiral metal–organic frameworks as a tunable platform for asymmetric catalysis. *Nature Chemistry* **2010,** *2* (10), 838-846.

10. Furukawa, H.; Müller, U.; Yaghi, O. M., "Heterogeneity within Order" in Metal–Organic Frameworks. *Angewandte Chemie International Edition* **2015,** *54* (11), 3417-3430.

11. Yaghi, O. M.; Kalmutzki, M. J.; Diercks, C. S., Emergence of Metal-Organic Frameworks. In *Introduction to Reticular Chemistry*, 2019; pp 1-27.

12. Werner, H., Alfred Werner: a forerunner to modern inorganic chemistry. *Angewandte Chemie International Edition* **2013,** *52* (24), 6146-6153.

13. Hofmann, K.; Küspert, F., Verbindungen von kohlenwasserstoffen mit metallsalzen. *Zeitschrift für anorganische Chemie* **1897,** *15* (1), 204-207.

14. Rayner, J.; Powell, H. M., 67. Structure of molecular compounds. Part X. Crystal structure of the compound of benzene with an ammonia–nickel cyanide complex. *Journal of the Chemical Society (Resumed)* **1952**, 319-328.

15. Wells, A. F., The geometrical basis of crystal chemistry. Part 1. *Acta Crystallographica* **1954,** *7* (8-9), 535-544.

16. Hoskins, B. F.; Robson, R., Infinite polymeric frameworks consisting of three dimensionally linked rod-like segments. *Journal of the American Chemical Society* **1989,** *111* (15), 5962-5964.

17. Hoskins, B. F.; Robson, R., Design and construction of a new class of scaffolding-like materials comprising infinite polymeric frameworks of 3D-linked molecular rods. A reappraisal of the zinc cyanide and cadmium cyanide structures and the synthesis and structure of the diamond-related frameworks [N (CH3) 4][CuIZnII (CN) 4] and CuI [4, 4', 4'', 4'''-tetracyanotetraphenylmethane] BF4. xC6H5NO2. *Journal of the American Chemical Society* **1990,** *112* (4), 1546-1554.

18. Gable, R. W.; Hoskins, B. F.; Robson, R., Synthesis and structure of [NMe 4][CuPt (CN) 4]: an infinite three-dimensional framework related to PtS which generates intersecting hexagonal channels of large cross section. *Journal of the Chemical Society, Chemical Communications* **1990,** (10), 762-763.

19. Zaworotko, M. J., Crystal engineering of diamondoid networks. *Chemical Society Reviews* **1994,** *23* (4), 283-288.

20. Abrahams, B.; Hoskins, B.; Michail, D.; Robson, R., Assembly of porphyrin building blocks into network structures with large channels. *Nature* **1994,** *369* (6483), 727-729.

21. Yaghi, O.; Li, H., Hydrothermal synthesis of a metal-organic framework containing large rectangular channels. *Journal of the American Chemical Society* **1995,** *117* (41), 10401-10402.

22. Fujita, M.; Yazaki, J.; Ogura, K., Preparation of a macrocyclic polynuclear complex,[(en) Pd (4, 4'-bpy)] 4 (NO3) 8 (en= ethylenediamine, bpy= bipyridine), which recognizes an organic molecule in aqueous media. *Journal of the American Chemical Society* **1990,** *112* (14), 5645-5647.

23. Fujita, M.; Kwon, Y. J.; Washizu, S.; Ogura, K., Preparation, clathration ability, and catalysis of a two-dimensional square network material composed of cadmium (II) and 4, 4'-bipyridine. *Journal of the American Chemical Society* **1994,** *116* (3), 1151-1152.

24. Subramanian, S.; Zaworotko, M. J., Porous solids by design:[Zn (4, 4′-bpy) 2 (SiF6)] n· xDMF, a single framework octahedral coordination polymer with large square channels. *Angewandte Chemie International Edition in English* **1995,** *34* (19), 2127-2129.

25. Yaghi, O. M.; Li, G.; Li, H., Selective binding and removal of guests in a microporous metal–organic framework. *Nature* **1995,** *378* (6558), 703-706.

26. Li, H.; Eddaoudi, M.; Groy, T. L.; Yaghi, O., Establishing microporosity in open metal-organic frameworks: Gas sorption isotherms for Zn (BDC)(BDC= 1, 4-benzenedicarboxylate)[28]. *Journal of the American Chemical Society* **1998,** *120* (33), 8571-8572.

27. Li, H.; Eddaoudi, M.; O'Keeffe, M.; Yaghi, O. M., Design and synthesis of an exceptionally stable and highly porous metal-organic framework. *nature* **1999,** *402* (6759), 276-279.

28. Cavka, J. H.; Jakobsen, S.; Olsbye, U.; Guillou, N.; Lamberti, C.; Bordiga, S.; Lillerud, K. P., A New Zirconium Inorganic Building Brick Forming Metal Organic Frameworks with Exceptional Stability. *Journal of the American Chemical Society* **2008,** *130* (42), 13850-13851.

29. Kandiah, M.; Usseglio, S.; Svelle, S.; Olsbye, U.; Lillerud, K. P.; Tilset, M., Post-synthetic modification of the metal–organic framework compound UiO-66. *Journal of Materials Chemistry* **2010,** *20* (44), 9848-9851.

30. Shearer, G. C.; Chavan, S.; Bordiga, S.; Svelle, S.; Olsbye, U.; Lillerud, K. P., Defect Engineering: Tuning the Porosity and Composition of the Metal–Organic Framework UiO-66 via Modulated Synthesis. *Chemistry of Materials* **2016,** *28* (11), 3749-3761.

31. Moosavi, S. M.; Nandy, A.; Jablonka, K. M.; Ongari, D.; Janet, J. P.; Boyd, P. G.; Lee, Y.; Smit, B.; Kulik, H. J., Understanding the diversity of the metal-organic framework ecosystem. *Nature Communications* **2020,** *11* (1), 4068.

32. Boles, M. A.; Engel, M.; Talapin, D. V., Self-Assembly of Colloidal Nanocrystals: From Intricate Structures to Functional Materials. *Chemical Reviews* **2016,** *116* (18), 11220-11289.

33. Eddaoudi, M.; Moler, D. B.; Li, H.; Chen, B.; Reineke, T. M.; O'keeffe, M.; Yaghi, O. M., Modular chemistry: secondary building units as a basis for the design of highly porous and robust metal− organic carboxylate frameworks. *Accounts of chemical research* **2001,** *34* (4), 319-330.

34. Rood, J. A.; Boggess, W. C.; Noll, B. C.; Henderson, K. W., Assembly of a Homochiral, Body-Centered Cubic Network Composed of Vertex-Shared Mg12 Cages: Use of Electrospray Ionization Mass Spectrometry to Monitor Metal Carboxylate Nucleation. *Journal of the American Chemical Society* **2007,** *129* (44), 13675-13682.

35. Deng, H.; Doonan, C. J.; Furukawa, H.; Ferreira, R. B.; Towne, J.; Knobler, C. B.; Wang, B.; Yaghi, O. M., Multiple Functional Groups of Varying Ratios in Metal-Organic Frameworks. *Science* **2010,** *327* (5967), 846-850.

36. Furukawa, H.; Cordova, K. E.; O'Keeffe, M.; Yaghi, O. M., The Chemistry and Applications of Metal-Organic Frameworks. *Science* **2013,** *341* (6149), 1230444.

37. Noel, N. K.; Congiu, M.; Ramadan, A. J.; Fearn, S.; McMeekin, D. P.; Patel, J. B.; Johnston, M. B.; Wenger, B.; Snaith, H. J., Unveiling the Influence of pH on the Crystallization of Hybrid Perovskites, Delivering Low Voltage Loss Photovoltaics. *Joule* **2017,** *1* (2), 328-343.

38. Yaghi, O. M., Reticular Chemistry: Molecular Precision in Infinite 2D and 3D. *Molecular Frontiers Journal* **2019,** *03* (01), 66-83.

39. Vermoortele, F.; Bueken, B.; Le Bars, G.; Van de Voorde, B.; Vandichel, M.; Houthoofd, K.; Vimont, A.; Daturi, M.; Waroquier, M.; Van Speybroeck, V., Synthesis modulation as a tool to increase the catalytic activity of metal–organic frameworks: the unique case of UiO-66 (Zr). *Journal of the American Chemical Society* **2013,** *135* (31), 11465-11468.

40. Taylor, J. M.; Dekura, S.; Ikeda, R.; Kitagawa, H., Defect control to enhance proton conductivity in a metal–organic framework. *Chemistry of Materials* **2015,** *27* (7), 2286-2289.

41. Forgan, R. S., Modulated self-assembly of metal–organic frameworks. *Chemical science* **2020,** *11* (18), 4546-4562.

42. Marshall, C. R.; Staudhammer, S. A.; Brozek, C. K., Size control over metal–organic framework porous nanocrystals. *Chemical Science* **2019,** *10* (41), 9396-9408.

43. Kandiah, M.; Nilsen, M. H.; Usseglio, S.; Jakobsen, S.; Olsbye, U.; Tilset, M.; Larabi, C.; Quadrelli, E. A.; Bonino, F.; Lillerud, K. P., Synthesis and Stability of Tagged UiO-66 Zr-MOFs. *Chemistry of Materials* **2010,** *22* (24), 6632-6640.

44. Chun, H.; Dybtsev, D. N.; Kim, H.; Kim, K., Synthesis, X-ray Crystal Structures, and Gas Sorption Properties of Pillared Square Grid Nets Based on Paddle-Wheel Motifs: Implications for Hydrogen Storage in Porous Materials. *Chemistry – A European Journal* **2005,** *11* (12), 3521-3529.

45. Chavan, S. M.; Shearer, G. C.; Svelle, S.; Olsbye, U.; Bonino, F.; Ethiraj, J.; Lillerud, K. P.; Bordiga, S., Synthesis and Characterization of Amine-Functionalized Mixed-Ligand Metal–Organic Frameworks of UiO-66 Topology. *Inorganic Chemistry* **2014,** *53* (18), 9509-9515.

46. Lee, Y.; Kim, S.; Kang, J. K.; Cohen, S. M., Photocatalytic CO2 reduction by a mixed metal (Zr/Ti), mixed ligand metal–organic framework under visible light irradiation. *Chemical Communications* **2015,** *51* (26), 5735-5738.

47. Guillerm, V.; Maspoch, D., Geometry Mismatch and Reticular Chemistry: Strategies To Assemble Metal–Organic Frameworks with Non-default Topologies. *Journal of the American Chemical Society* **2019,** *141* (42), 16517-16538.

48. Wu, C.-D.; Hu, A.; Zhang, L.; Lin, W., A Homochiral Porous Metal−Organic Framework for Highly Enantioselective Heterogeneous Asymmetric Catalysis. *Journal of the American Chemical Society* **2005,** *127* (25), 8940-8941.

49. Wang, Z.; Cohen, S. M., Postsynthetic Covalent Modification of a Neutral Metal−Organic Framework. *Journal of the American Chemical Society* **2007,** *129* (41), 12368-12369.

50. Burrows, A. D.; Frost, C. G.; Mahon, M. F.; Richardson, C., Post-Synthetic Modification of Tagged Metal–Organic Frameworks. *Angewandte Chemie International Edition* **2008,** *47* (44), 8482-8486.

51. Taylor-Pashow, K. M. L.; Della Rocca, J.; Xie, Z.; Tran, S.; Lin, W., Postsynthetic Modifications of Iron-Carboxylate Nanoscale Metal−Organic Frameworks for Imaging and Drug Delivery. *Journal of the American Chemical Society* **2009,** *131* (40), 14261-14263.

52. Shearer, G. C.; Vitillo, J. G.; Bordiga, S.; Svelle, S.; Olsbye, U.; Lillerud, K. P., Functionalizing the Defects: Postsynthetic Ligand Exchange in the Metal Organic Framework UiO-66. *Chemistry of Materials* **2016,** *28* (20), 7190-7193.

53. Ji, P.; Feng, X.; Oliveres, P.; Li, Z.; Murakami, A.; Wang, C.; Lin, W., Strongly Lewis Acidic Metal–Organic Frameworks for Continuous Flow Catalysis. *Journal of the American Chemical Society* **2019,** *141* (37), 14878-14888.

54. Lan, G.; Quan, Y.; Wang, M.; Nash, G. T.; You, E.; Song, Y.; Veroneau, S. S.; Jiang, X.; Lin, W., Metal–Organic Layers as Multifunctional Two-Dimensional Nanomaterials for Enhanced Photoredox Catalysis. *Journal of the American Chemical Society* **2019,** *141* (40), 15767-15772.

55. He, C.; Lu, K.; Liu, D.; Lin, W., Nanoscale Metal–Organic Frameworks for the Co-Delivery of Cisplatin and Pooled siRNAs to Enhance Therapeutic Efficacy in Drug-Resistant Ovarian Cancer Cells. *Journal of the American Chemical Society* **2014,** *136* (14), 5181-5184.

56. Luo, T.; Nash, G. T.; Xu, Z.; Jiang, X.; Liu, J.; Lin, W., Nanoscale Metal–Organic Framework Confines Zinc-Phthalocyanine Photosensitizers for Enhanced Photodynamic Therapy. *Journal of the American Chemical Society* **2021,** *143* (34), 13519-13524.

57. Ikezoe, Y.; Fang, J.; Wasik, T. L.; Uemura, T.; Zheng, Y.; Kitagawa, S.; Matsui, H., Peptide Assembly-Driven Metal–Organic Framework (MOF) Motors for Micro Electric Generators. *Advanced Materials* **2015,** *27* (2), 288-291.

58. Huxford, R. C.; Della Rocca, J.; Lin, W., Metal–organic frameworks as potential drug carriers. *Current opinion in chemical biology* **2010,** *14* (2), 262-268.

59. Cohen, S. M., Postsynthetic Methods for the Functionalization of Metal–Organic Frameworks. *Chemical Reviews* **2012,** *112* (2), 970-1000.

60. Lin, Z.; Thacker, N. C.; Sawano, T.; Drake, T.; Ji, P.; Lan, G.; Cao, L.; Liu, S.; Wang, C.; Lin, W., Metal–organic layers stabilize earth-abundant metal–terpyridine diradical complexes for catalytic C–H activation. *Chemical Science* **2018,** *9* (1), 143-151.

61. Cao, L.; Lin, Z.; Peng, F.; Wang, W.; Huang, R.; Wang, C.; Yan, J.; Liang, J.; Zhang, Z.; Zhang, T.; Long, L.; Sun, J.; Lin, W., Self-Supporting Metal–Organic Layers as Single-Site Solid Catalysts. *Angewandte Chemie International Edition* **2016,** *55* (16), 4962-4966.

62. Lan, G.; Ni, K.; Xu, R.; Lu, K.; Lin, Z.; Chan, C.; Lin, W., Nanoscale metal–organic layers for deeply penetrating X-ray-induced photodynamic therapy. *Angewandte Chemie* **2017,** *129* (40), 12270-12274.

63. Lan, G.; Ni, K.; Veroneau, S. S.; Song, Y.; Lin, W., Nanoscale metal–organic layers for radiotherapy–radiodynamic therapy. *Journal of the American Chemical Society* **2018,** *140* (49), 16971-16975.

64. Lan, G.; Li, Z.; Veroneau, S. S.; Zhu, Y.-Y.; Xu, Z.; Wang, C.; Lin, W., Photosensitizing metal–organic layers for efficient sunlight-driven carbon dioxide reduction. *Journal of the American Chemical Society* **2018,** *140* (39), 12369-12373.

65. Ni, K.; Lan, G.; Chan, C.; Duan, X.; Guo, N.; Veroneau, S. S.; Weichselbaum, R. R.; Lin, W., Ultrathin metal-organic-layer mediated radiotherapy-radiodynamic therapy. *Matter* **2019,** *1* (5), 1331-1353.

66. Luo, T.; Fan, Y.; Mao, J.; Yuan, E.; You, E.; Xu, Z.; Lin, W., Dimensional Reduction Enhances Photodynamic Therapy of Metal–Organic Nanophotosensitizers. *Journal of the American Chemical Society* **2022,** *144* (12), 5241-5246.

67. Nash, G. T.; Luo, T.; Lan, G.; Ni, K.; Kaufmann, M.; Lin, W., Nanoscale Metal–Organic Layer Isolates Phthalocyanines for Efficient Mitochondria-Targeted Photodynamic Therapy. *Journal of the American Chemical Society* **2021,** *143* (5), 2194-2199.

68. Lan, G.; Ni, K.; You, E.; Wang, M.; Culbert, A.; Jiang, X.; Lin, W., Multifunctional Nanoscale Metal–Organic Layers for Ratiometric pH and Oxygen Sensing. *Journal of the American Chemical Society* **2019,** *141* (48), 18964-18969.

69. Lin, G.; Nash, G. T.; Luo, T.; Ghosh, I.; Sohoni, S.; Christofferson, A. J.; Liu, G.; Engel, G. S.; Lin, W., 2D Nano-Sonosensitizers Facilitate Energy Transfer to Enhance Sonodynamic Therapy. *Advanced Materials* **2023,** *35* (19), 2212069.

70. Quan, Y.; Lan, G.; Shi, W.; Xu, Z.; Fan, Y.; You, E.; Jiang, X.; Wang, C.; Lin, W., Metal–organic layers hierarchically integrate three synergistic active sites for tandem catalysis. *Angewandte Chemie* **2021,** *133* (6), 3152-3157.

71. Siegel, R. L.; Miller, K. D.; Fuchs, H. E.; Jemal, A., Cancer statistics, 2021. *Ca Cancer J Clin* **2021,** *71* (1), 7-33.

72. Sullivan, R.; Peppercorn, J.; Sikora, K.; Zalcberg, J.; Meropol, N. J.; Amir, E.; Khayat, D.; Boyle, P.; Autier, P.; Tannock, I. F.; Fojo, T.; Siderov, J.; Williamson, S.; Camporesi, S.; McVie, J. G.; Purushotham, A. D.; Naredi, P.; Eggermont, A.; Brennan, M. F.; Steinberg, M. L.; De Ridder, M.; McCloskey, S. A.; Verellen, D.; Roberts, T.; Storme, G.; Hicks, R. J.; Ell, P. J.; Hirsch, B. R.; Carbone, D. P.; Schulman, K. A.; Catchpole, P.; Taylor, D.; Geissler, J.; Brinker, N. G.; Meltzer, D.; Kerr, D.; Aapro, M., Delivering affordable cancer care in high-income countries. *The Lancet Oncology* **2011,** *12* (10), 933-980.

73. Pramesh, C. S.; Badwe, R. A.; Bhoo-Pathy, N.; Booth, C. M.; Chinnaswamy, G.; Dare, A. J.; de Andrade, V. P.; Hunter, D. J.; Gopal, S.; Gospodarowicz, M.; Gunasekera, S.; Ilbawi, A.; Kapambwe, S.; Kingham, P.; Kutluk, T.; Lamichhane, N.; Mutebi, M.; Orem, J.; Parham, G.; Ranganathan, P.; Sengar, M.; Sullivan, R.; Swaminathan, S.; Tannock, I. F.; Tomar, V.; Vanderpuye, V.; Varghese, C.; Weiderpass, E., Priorities for cancer research in low- and middle-income countries: a global perspective. *Nature Medicine* **2022,** *28* (4), 649-657.

74. Urruticoechea, A.; Alemany, R.; Balart, J.; Villanueva, A.; Vinals, F.; Capella, G., Recent advances in cancer therapy: an overview. *Current pharmaceutical design* **2010,** *16* (1), 3-10.

75. Figueras, J.; Torras, J.; Valls, C.; Llado, L.; Ramos, E.; Marti-Ragué, J.; Serrano, T.; Fabregat, J., Surgical resection of colorectal liver metastases in patients with expanded indications: a single-center experience with 501 patients. *Diseases of the colon & rectum* **2007,** *50*, 478-488.

76. Ohlsson, B.; Stenram, U.; Tranberg, K.-G., Resection of colorectal liver metastases: 25-year experience. *World journal of surgery* **1998,** *22*, 268-277.

77. Kaifi, J. T.; Gusani, N. J.; Deshaies, I.; Kimchi, E. T.; Reed, M. F.; Mahraj, R. P.; Staveley-O'Carroll, K. F., Indications and approach to surgical resection of lung metastases. *Journal of Surgical Oncology* **2010,** *102* (2), 187-195.

78. Baskar, R.; Lee, K. A.; Yeo, R.; Yeoh, K. W., Cancer and radiation therapy: current advances and future directions. *International journal of medical sciences* **2012,** *9* (3), 193-9.

79. Delaney, G.; Jacob, S.; Featherstone, C.; Barton, M., The role of radiotherapy in cancer treatment: estimating optimal utilization from a review of evidence-based clinical guidelines. *Cancer: Interdisciplinary International Journal of the American Cancer Society* **2005,** *104* (6), 1129-1137.

80. Sauer, R.; Becker, H.; Hohenberger, W.; Rödel, C.; Wittekind, C.; Fietkau, R.; Martus, P.; Tschmelitsch, J.; Hager, E.; Hess, C. F., Preoperative versus postoperative chemoradiotherapy for rectal cancer. *New England Journal of Medicine* **2004,** *351* (17), 1731-1740.

81. Stupp, R.; Hegi, M. E.; Gilbert, M. R.; Chakravarti, A., Chemoradiotherapy in malignant glioma: standard of care and future directions. *Journal of Clinical Oncology* **2007,** *25* (26), 4127-4136.

82. Milas, L.; Mason, K. A.; Liao, Z.; Ang, K. K., Chemoradiotherapy: emerging treatment improvement strategies. *Head & Neck: Journal for the Sciences and Specialties of the Head and Neck* **2003,** *25* (2), 152-167.

83. Sioka, C.; Kyritsis, A. P., Central and peripheral nervous system toxicity of common chemotherapeutic agents. *Cancer chemotherapy and pharmacology* **2009,** *63*, 761-767.

84. Ormond, A. B.; Freeman, H. S., Dye sensitizers for photodynamic therapy. *Materials* **2013,** *6* (3), 817-840.

85. De Rosa, F. S.; Bentley, M. V. L., Photodynamic therapy of skin cancers: sensitizers, clinical studies and future directives. *Pharmaceutical research* **2000,** *17*, 1447-1455.

86. Son, S.; Kim, J. H.; Wang, X.; Zhang, C.; Yoon, S. A.; Shin, J.; Sharma, A.; Lee, M. H.; Cheng, L.; Wu, J., Multifunctional sonosensitizers in sonodynamic cancer therapy. *Chemical Society Reviews* **2020,** *49* (11), 3244-3261.

87. Wang, H.; Mu, X.; He, H.; Zhang, X.-D., Cancer radiosensitizers. *Trends in pharmacological sciences* **2018,** *39* (1), 24-48.

88. Lu, K.; He, C.; Guo, N.; Chan, C.; Ni, K.; Lan, G.; Tang, H.; Pelizzari, C.; Fu, Y.-X.; Spiotto, M. T.; Weichselbaum, R. R.; Lin, W., Low-dose X-ray radiotherapy–radiodynamic therapy via nanoscale metal–organic frameworks enhances checkpoint blockade immunotherapy. *Nature Biomedical Engineering* **2018,** *2* (8), 600-610.

89. Lan, G.; Ni, K.; Veroneau, S. S.; Feng, X.; Nash, G. T.; Luo, T.; Xu, Z.; Lin, W., Titanium-Based Nanoscale Metal–Organic Framework for Type I Photodynamic Therapy. *Journal of the American Chemical Society* **2019,** *141* (10), 4204-4208.

90. Luo, T.; Nash, G. T.; Jiang, X.; Feng, X.; Mao, J.; Liu, J.; Juloori, A.; Pearson, A. T.; Lin, W., A 2D Nanoradiosensitizer Enhances Radiotherapy and Delivers STING Agonists to Potentiate Cancer Immunotherapy. *Advanced Materials* **2022,** *34* (39), 2110588.

91. Lan, G.; Ni, K.; Veroneau, S. S.; Luo, T.; You, E.; Lin, W., Nanoscale Metal–Organic Framework Hierarchically Combines High-Z Components for Multifarious Radio-Enhancement. *Journal of the American Chemical Society* **2019,** *141* (17), 6859-6863.

92. Iyer, A. K.; Khaled, G.; Fang, J.; Maeda, H., Exploiting the enhanced permeability and retention effect for tumor targeting. *Drug discovery today* **2006,** *11* (17-18), 812-818.

93. Wong, A. D.; Ye, M.; Ulmschneider, M. B.; Searson, P. C., Quantitative analysis of the enhanced permeation and retention (EPR) effect. *PloS one* **2015,** *10* (5), e0123461.

94. Dougherty, T. J.; Gomer, C. J.; Henderson, B. W.; Jori, G.; Kessel, D.; Korbelik, M.; Moan, J.; Peng, Q., Photodynamic therapy. *Journal of National Cancer Institute* **1998,** *90* (12), 889-905.

95. Dolmans, D. E.; Fukumura, D.; Jain, R. K., Photodynamic therapy for cancer. *Nature reviews cancer* **2003,** *3* (5), 380-387.

96. Castano, A. P.; Demidova, T. N.; Hamblin, M. R., Mechanisms in photodynamic therapy: part one-photosensitizers, photochemistry and cellular localization. *Photodiagnosis and photodynamic therapy* **2004,** *1* (4), 279-93.

97. Skovsen, E.; Snyder, J. W.; Lambert, J. D. C.; Ogilby, P. R., Lifetime and Diffusion of Singlet Oxygen in a Cell. *The Journal of Physical Chemistry B* **2005,** *109* (18), 8570-8573.

98. Snyder, J. W.; Skovsen, E.; Lambert, J. D. C.; Ogilby, P. R., Subcellular, Time-Resolved Studies of Singlet Oxygen in Single Cells. *Journal of the American Chemical Society* **2005,** *127* (42), 14558-14559.

99. Mroz, P.; Hashmi, J. T.; Huang, Y.-Y.; Lange, N.; Hamblin, M. R., Stimulation of anti-tumor immunity by photodynamic therapy. *Expert review of clinical immunology* **2011,** *7* (1), 75-91.

100. Barton, G. M., A calculated response: control of inflammation by the innate immune system. *The Journal of clinical investigation* **2008,** *118* (2), 413-420.

101. Lismont, M.; Dreesen, L.; Wuttke, S., Metal-Organic Framework Nanoparticles in Photodynamic Therapy: Current Status and Perspectives. *Advanced Functional Materials* **2017,** *27* (14), 1606314.

102. Perun, S.; Tatchen, J.; Marian, C. M., Singlet and triplet excited states and intersystem crossing in free-base porphyrin: TDDFT and DFT/MRCI study. *ChemPhysChem* **2008,** *9* (2), 282-292.

103. Rio, Y.; Rodriguez-Morgade, M. S.; Torres, T., Modulating the electronic properties of porphyrinoids: a voyage from the violet to the infrared regions of the electromagnetic spectrum. *Organic & biomolecular chemistry* **2008,** *6* (11), 1877-1894.

104. Chen, Y.; Li, G.; Pandey, R. K., Synthesis of bacteriochlorins and their potential utility in photodynamic therapy (PDT). *Current Organic Chemistry* **2004,** *8* (12), 1105-1134.

105. Nyman, E. S.; Hynninen, P. H., Research advances in the use of tetrapyrrolic photosensitizers for photodynamic therapy. *Journal of Photochemistry and Photobiology B: Biology* **2004,** *73* (1), 1-28.

106. Bonnett, R., Photosensitizers of the porphyrin and phthalocyanine series for photodynamic therapy. *Chemical Society Reviews* **1995,** *24* (1), 19-33.

107. Luo, T.; Ni, K.; Culbert, A.; Lan, G.; Li, Z.; Jiang, X.; Kaufmann, M.; Lin, W., Nanoscale Metal–Organic Frameworks Stabilize Bacteriochlorins for Type I and Type II Photodynamic Therapy. *Journal of the American Chemical Society* **2020,** *142* (16), 7334-7339.

108. Rodríguez-Morgade, M. S.; Stuzhin, P. A., The chemistry of porphyrazines: an overview. *Journal of Porphyrins and Phthalocyanines* **2004,** *08* (09), 1129-1165.

109. Tomoda, H.; Saito, S.; Ogawa, S.; Shiraishi, S., Synthesis of phthalocyanines from phthalonitrile with organic strong bases. *Chemistry Letters* **1980,** *9* (10), 1277-1280.

110. Tomoda, H.; Saito, S.; Shiraishi, S., Synthesis of metallophthalocyanines from phthalonitrile with strong organic bases. *Chemistry Letters* **1983,** *12* (3), 313-316.

111. Wöhrle, D.; Schnurpfeil, G.; Knothe, G., Efficient synthesis of phthalocyanines and related macrocyclic compounds in the presence of organic bases. *Dyes and Pigments* **1992,** *18* (2), 91-102.

112. Rothemund, P., A new porphyrin synthesis. The synthesis of porphin1. *Journal of the American Chemical Society* **1936,** *58* (4), 625-627.

113. Lindsey, J. S.; Schreiman, I. C.; Hsu, H. C.; Kearney, P. C.; Marguerettaz, A. M., Rothemund and Adler-Longo reactions revisited: synthesis of tetraphenylporphyrins under equilibrium conditions. *The Journal of Organic Chemistry* **1987,** *52* (5), 827-836.

114. Hiroto, S.; Miyake, Y.; Shinokubo, H., Synthesis and Functionalization of Porphyrins through Organometallic Methodologies. *Chemical Reviews* **2017,** *117* (4), 2910-3043.

115. McKeown, N. B., Chapter 98: The Synthesis of Symmetrical Phthalocyanines. In *The Porphyrin Handbook*, Kadish, K. M.; Smith, K. M.; Guilard, R., Eds. Academic Press: Amsterdam, 2003; pp 61-124.

116. Ghani, F.; Kristen, J.; Riegler, H., Solubility Properties of Unsubstituted Metal Phthalocyanines in Different Types of Solvents. *Journal of Chemical & Engineering Data* **2012,** *57* (2), 439-449.

117. Lawton, E. A., The thermal stability of copper phthalocyanine. *The Journal of Physical Chemistry* **1958,** *62* (3), 384-384.

118. Kuznetsova, N. A.; Kaliya, O. L., Oxidative photobleaching of phthalocyanines in solution. *Journal of Porphyrins and Phthalocyanines* **2012,** *16* (07n08), 705-712.

119. Słota, R.; Dyrda, G., UV Photostability of Metal Phthalocyanines in Organic Solvents. *Inorganic Chemistry* **2003,** *42* (18), 5743-5750.

120. Li, Y.-S.; Zaidi, S. I. A.; Rodgers, M. A. J.; Mukhtar, H.; Kenney, M. E.; Oleinick, N. L.; He, J.; Larkin, H. E.; Rihter, B. D., The Synthesis, Photophysical and Photobiological Properties and in vitro Structure-Activity Relationships of a Set of Silicon Phthalocyanine PDT Photosensitizers. *Photochemistry and Photobiology* **1997,** *65* (3), 581-586.

121. Baron, E. D.; Malbasa, C. L.; Santo-Domingo, D.; Fu, P.; Miller, J. D.; Hanneman, K. K.; Hsia, A. H.; Oleinick, N. L.; Colussi, V. C.; Cooper, K. D., Silicon phthalocyanine (pc 4) photodynamic therapy is a safe modality for cutaneous neoplasms: results of a phase 1 clinical trial. *Lasers in Surgery and Medicine* **2010,** *42* (10), 888-895.

122. Wilson, B. C.; Jeeves, W. P.; Lowe, D. M., IN VIVO and POST MORTEM MEASUREMENTS OF THE ATTENUATION SPECTRA OF LIGHT IN MAMMALIAN TISSUES. *Photochemistry and Photobiology* **1985,** *42* (2), 153-162.

123. Arnfield, M. R.; Tulip, J.; Chetner, M.; McPhee, M. S., Optical dosimetry for interstitial photodynamic therapy. *Medical physics* **1989,** *16* (4), 602-8.

124. Mahmoud, B. H.; Hexsel, C. L.; Hamzavi, I. H.; Lim, H. W., Effects of Visible Light on the Skin†. *Photochemistry and Photobiology* **2008,** *84* (2), 450-462.

125. Gould, J. W.; Mercurio, M. G.; Elmets, C. A., Cutaneous photosensitivity diseases induced by exogenous agents. *Journal of the American Academy of Dermatology* **1995,** *33* (4), 551-573.

126. Fishman, P. S., Thalamotomy for essential tremor: FDA approval brings brain treatment with FUS to the clinic. *Journal of therapeutic ultrasound* **2017,** *5*, 19.

127. Jolesz, F. A.; McDannold, N., Current status and future potential of MRI-guided focused ultrasound surgery. *Journal of Magnetic Resonance Imaging* **2008,** *27* (2), 391-399.

128. Lynn, J. G.; Zwemer, R. L.; Chick, A. J., The Biological Application of Focused Ultrasonic Waves. *Science* **1942,** *96* (2483), 119-120.

129. Koch, K. M.; Hargreaves, B. A.; Pauly, K. B.; Chen, W.; Gold, G. E.; King, K. F., Magnetic resonance imaging near metal implants. *Journal of Magnetic Resonance Imaging* **2010,** *32* (4), 773-787.

130. Bennett, L. H.; Wang, P. S.; Donahue, M. J., Artifacts in magnetic resonance imaging from metals. *Journal of Applied Physics* **1996,** *79* (8), 4712-4714.

131. Yiallouras, C.; Damianou, C., Review of MRI positioning devices for guiding focused ultrasound systems. *The International Journal of Medical Robotics and Computer Assisted Surgery* **2015,** *11* (2), 247-255.

132. Costley, D.; Mc Ewan, C.; Fowley, C.; McHale, A. P.; Atchison, J.; Nomikou, N.; Callan, J. F., Treating cancer with sonodynamic therapy: A review. *International Journal of Hyperthermia* **2015,** *31* (2), 107-117.

133. Choi, V.; Rajora, M. A.; Zheng, G., Activating Drugs with Sound: Mechanisms Behind Sonodynamic Therapy and the Role of Nanomedicine. *Bioconjugate Chemistry* **2020,** *31* (4), 967-989.

134. Li, D.; Yang, Y.; Li, D.; Pan, J.; Chu, C.; Liu, G., Organic Sonosensitizers for Sonodynamic Therapy: From Small Molecules and Nanoparticles toward Clinical Development. *Small* **2021,** *17* (42), 2101976.

135. Leighton, T. G., What is ultrasound? *Progress in Biophysics and Molecular Biology* **2007,** *93* (1), 3-83.

136. Seibert, J. A., Physics of Ultrasound. *Fundamentals of Emergency Ultrasound* **2019**, 1.

137. ter Haar, G.; Coussios, C., High intensity focused ultrasound: Physical principles and devices. *International Journal of Hyperthermia* **2007,** *23* (2), 89-104.

138. Zhou, Y. F., High intensity focused ultrasound in clinical tumor ablation. *World journal of clinical oncology* **2011,** *2* (1), 8-27.

139. Köhrmann, K. U.; Michel, M. S.; Steidler, A.; Marlinghaus, E.; Kraut, O.; Alken, P., Technical characterization of an ultrasound source for noninvasive thermoablation by high-intensity focused ultrasound. *BJU International* **2002,** *90* (3), 248-252.

140. Pickworth, M. J. W.; Dendy, P. P.; Leighton, T. G.; Walton, A. J., Studies of the cavitational effects of clinical ultrasound by sonoluminescence: 2. Thresholds for sonoluminescence from a therapeutic ultrasound beam and the effect of temperature and duty cycle. *Physics in Medicine & Biology* **1988,** *33* (11), 1249.

141. Umemura, S.-i.; Yumita, N.; Nishigaki, R.; Umemura, K., Mechanism of Cell Damage by Ultrasound in Combination with Hematoporphyrin. *Japanese Journal of Cancer Research* **1990,** *81* (9), 962-966.

142. Miŝík, V.; Riesz, P., Free Radical Intermediates in Sonodynamic Therapy. *Annals of the New York Academy of Sciences* **2000,** *899* (1), 335-348.

143. Beguin, E.; Shrivastava, S.; Dezhkunov, N. V.; McHale, A. P.; Callan, J. F.; Stride, E., Direct Evidence of Multibubble Sonoluminescence Using Therapeutic Ultrasound and Microbubbles. *ACS Applied Materials & Interfaces* **2019,** *11* (22), 19913-19919.

144. Flannigan, D. J.; Suslick, K. S., Plasma formation and temperature measurement during single-bubble cavitation. *Nature* **2005,** *434* (7029), 52-55.

145. Yasui, K., Multibubble Sonoluminescence from a Theoretical Perspective. *Molecules* **2021,** *26* (15), 4624.

146. Didenko, Y. T.; McNamara Iii, W. B.; Suslick, K. S., Molecular emission from single-bubble sonoluminescence. *Nature* **2000,** *407* (6806), 877-879.

147. Wood, A. K.; Sehgal, C. M., A review of low-intensity ultrasound for cancer therapy. *Ultrasound in medicine & biology* **2015,** *41* (4), 905-928.

148. Rapoport, N.; Gao, Z.; Kennedy, A., Multifunctional nanoparticles for combining ultrasonic tumor imaging and targeted chemotherapy. *Journal of the National Cancer Institute* **2007,** *99* (14), 1095-1106.

149. Rapoport, N., Ultrasound-mediated micellar drug delivery. *International Journal of Hyperthermia* **2012,** *28* (4), 374-385.

150. Suslick, K. S., Sonochemistry. *Science* **1990,** *247* (4949), 1439-1445.

151. Lomax, M.; Folkes, L.; O'neill, P., Biological consequences of radiation-induced DNA damage: relevance to radiotherapy. *Clinical oncology* **2013,** *25* (10), 578-585.

152. Thariat, J.; Hannoun-Levi, J.-M.; Sun Myint, A.; Vuong, T.; Gérard, J.-P., Past, present, and future of radiotherapy for the benefit of patients. *Nature reviews Clinical oncology* **2013,** *10* (1), 52-60.

153. Schaue, D.; McBride, W. H., Opportunities and challenges of radiotherapy for treating cancer. *Nature reviews Clinical oncology* **2015,** *12* (9), 527-540.

154. Barker, H. E.; Paget, J. T. E.; Khan, A. A.; Harrington, K. J., The tumour microenvironment after radiotherapy: mechanisms of resistance and recurrence. *Nature Reviews Cancer* **2015,** *15* (7), 409-425.

155. Demaria, S.; Bhardwaj, N.; McBride, W. H.; Formenti, S. C., Combining radiotherapy and immunotherapy: A revived partnership. *International Journal of Radiation Oncology*Biology*Physics* **2005,** *63* (3), 655-666.

156. Barcellos-Hoff, M. H.; Park, C.; Wright, E. G., Radiation and the microenvironment – tumorigenesis and therapy. *Nature Reviews Cancer* **2005,** *5* (11), 867-875.

157. Wardman, P., Chemical Radiosensitizers for Use in Radiotherapy. *Clinical Oncology* **2007,** *19* (6), 397-417.

158. Saunders, M.; Dische, S., Clinical results of hypoxic cell radiosensitisation from hyperbaric oxygen to accelerated radiotherapy, carbogen and nicotinamide. *The British journal of cancer. Supplement* **1996,** *27*, S271-8.

159. Hainfeld, J. F.; Dilmanian, F. A.; Slatkin, D. N.; Smilowitz, H. M., Radiotherapy enhancement with gold nanoparticles. *Journal of pharmacy and pharmacology* **2008,** *60* (8), 977-985.

160. Retif, P.; Pinel, S.; Toussaint, M.; Frochot, C.; Chouikrat, R.; Bastogne, T.; Barberi-Heyob, M., Nanoparticles for radiation therapy enhancement: the key parameters. *Theranostics* **2015,** *5* (9), 1030.

161. Misawa, M.; Takahashi, J., Generation of reactive oxygen species induced by gold nanoparticles under x-ray and UV Irradiations. *Nanomedicine: Nanotechnology, Biology and Medicine* **2011,** *7* (5), 604-614.

162. Mesbahi, A., A review on gold nanoparticles radiosensitization effect in radiation therapy of cancer. *Reports of Practical Oncology & Radiotherapy* **2010,** *15* (6), 176-180.

163. Xu, Z.; Luo, T.; Mao, J.; McCleary, C.; Yuan, E.; Lin, W., Monte Carlo Simulation-Guided Design of a Thorium-Based Metal–Organic Framework for Efficient Radiotherapy-Radiodynamic Therapy. *Angewandte Chemie International Edition* **2022,** *61* (46), e202208685.

164. Xu, Z.; Ni, K.; Mao, J.; Luo, T.; Lin, W., Monte Carlo Simulations Reveal New Design Principles for Efficient Nanoradiosensitizers Based on Nanoscale Metal–Organic Frameworks. *Advanced Materials* **2021,** *33* (40), 2104249.

165. Ni, K.; Lan, G.; Veroneau, S. S.; Duan, X.; Song, Y.; Lin, W., Nanoscale metal-organic frameworks for mitochondria-targeted radiotherapy-radiodynamic therapy. *Nature Communications* **2018,** *9* (1), 4321.

166. Koshy, M.; Spiotto, M.; Feldman, L. E.; Luke, J. J.; Fleming, G. F.; Olson, D.; Moroney, J. W.; Nanda, R.; Rosenberg, A.; Pearson, A. T.; Juloori, A.; Weinberg, F.; Ray, C.; Gaba, R. C.; Chang, P. J.; Janisch, L. A.; Xu, Z.-Q.; Lin, W.; Weichselbaum, R. R.; Chmura, S. J., A phase 1 dose-escalation study of RiMO-301 with palliative radiation in advanced tumors. *Journal of Clinical Oncology* **2023,** *41* (16_suppl), 2527-2527.

Chapter 2: Nanoscale Metal–Organic Layer Isolates Phthalocyanines for Efficient Mitochondria-Targeted Photodynamic Therapy

2.1 Introduction

Although PDT is an effective localized anticancer treatment – with minimal collateral damage and systemic toxicity compared to RT and chemotherapy, respectively – its clinical utility is limited by the photophysical and pharmacokinetic properties of the PS, patient photosensitivity after administration, and the short tissue penetration depth of visible light.[1-8] Although phthalocyanines possess several ideal chemical and photophysical properties as a PS, few molecular phthalocyanines have reached clinical testing for PDT as their large extended pi system confers poor solubility and strong cofacial aggregation in aqueous environments.[9-11] The excited PSs then undergo aggregation-induced quenching back to the ground state before they can transfer energy to $^3O_2$, which significantly reduces their PDT efficacy. However, even the most promising clinical candidates, which have solubilizing axial and peripheral functional groups, still suffer from poor tumor accumulation and require extensive functionalization to enhance their *in vivo* efficacy.[12-13]

With the rapid development of nanotechnology and nanomedicine, nMOFs have emerged as a promising platform to load and deliver poorly soluble PSs, while also allowing additional modification and functionality for effective PDT.[14-18] With structural and compositional tunability, crystallinity, framework rigidity, high porosity, and biodegradability, nMOFs have been used to incorporate PSs for PDT.[19-22] The crystalline and rigid frameworks prevent photobleaching and self-quenching of excited PSs to significantly increase PDT efficacy.[23-24] The physical dimensions of typical 3D nMOFs can also be reduced to afford nMOLs with monolayer thickness, which bear

fully accessible PSs and allow facile ROS diffusion for enhanced tumor cell cytotoxicity.[25-27] The therapeutic efficacy of PDT can also be improved by targeting PS delivery to subcellular organelles, such as mitochondria. Generation of cytotoxic ROS in mitochondria disrupts key biological processes, such as energy production, and activates apoptotic pathways via caspase activation.[28-30] nMOF tunability allows the modification of bridging linkers to bestow sufficient lipophilicity and positive charge can target mitochondria without relying on auxiliary triphenylphosphonium moieties.[31-35] However, although the design of mixed linker nMOFs to load both ideal PSs and targeting species is flexible, it not only requires similar linker connectivity, length and geometry, but also significant time and effort to synthesize the ligands and optimize their nanoparticle growth.

In this chapter, we report the design and post-synthetic modification of a highly modular, mitochondria-targeting Hf_{12}-Ir nMOL platform for highly effective PDT. ZnOPPc@nMOL is composed of a monolayer of Hf_{12} SBUs and H_2DBB-Ir-F horizontally bridging linkers with either trifluoroacetic acid (TFA) or ZnOPPc PSs vertically capping the Hf SBUs (**Figure 2-1**). ZnOPPc was postsynthetically incorporated on the SBUs of the nMOL via carboxylate exchange with TFA capping ligands. Upon light irradiation, SBU-bound ZnOPPc PSs absorb light and undergo intersystem crossing (ISC) to the triplet excited state, which, in the presence of $^3O_2$, efficiently generates cytotoxic $^1O_2$ through a type II PDT process.[36-37] The rigid, ultrathin and cationic nMOL isolates ZnOPPc PSs to prevent self-quenching, while allowing efficient ROS diffusion and translocation of the nMOL into mitochondria to afford a highly effective PDT treatment of colorectal cancer.[38-42]

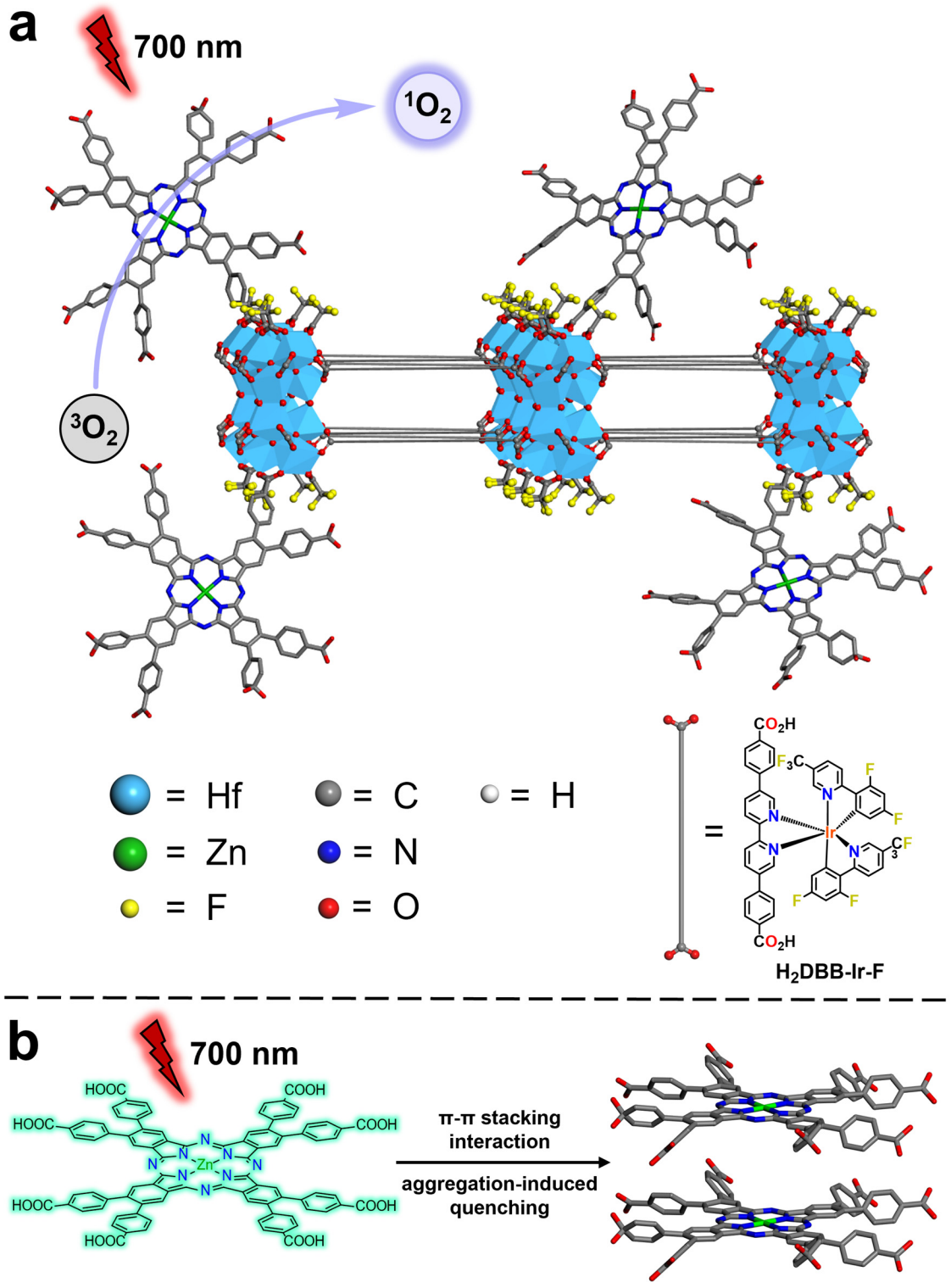

Figure 2-1. Illustration of using the ZnOPPc@nMOL platform to enhance $^1O_2$ generation for effective PDT. (a) Modeled structure of ZnOPPc@nMOL showing its efficient $^1O_2$ generation from vertically capped and spatially isolated ZnOPPc PSs on the SBUs. (b) Schematic showing the π–π stacking of two ZnOPPc PSs in aqueous solution leading to self-quenching of excited states.

2.2 Results and discussion

2.2.1 Synthesis and characterization

The phthalocyanine precursor, 4,5-bis(4-methoxycarbonylphenyl)phthalonitrile, was synthesized via a Suzuki-Miyaura cross coupling using 4,5-dichlorophthalonitrile, 4-(methoxycarbonylphenyl)-boronic acid, K_3PO_4 as base, and $Pd(OAc)_2$/SPhos as catalysts. The ZnOPPc ester was synthesized by refluxing 4,5-bis(4-methoxycarbonylphenyl)phthalonitrile, $Zn(OAc)_2$ and 1,8-diazabicyclo[5.4.0]undec-7-ene (DBU) in 1-pentanol for 36 h (**Scheme 2-1**). Matrix-assisted laser desorption/ionization-time of flight high-resolution mass spectrometry (MALDI-TOF HR-MS) revealed the product contained a mixture of methyl and pentyl esters in the product due to transesterification with 1-pentanol (**Figure 2-16**). Hydrolysis of the ZnOPPc ester yielded the desired octa-carboxylic acid form, ZnOPPc, and MALDI-TOF HR-MS of the product showed a single molecular ion peak with isotope peaks matching that of ZnOPPc (**Figure 2-17**).

The UV−visible spectrum of ZnOPPc in dimethyl sulfoxide (DMSO) exhibited three peaks that are characteristic of zinc phthalocyanines (**Figure 2-3**).[43] The Soret band peak at λ_{max} = 370 nm is assigned to a $\pi \rightarrow \pi^*$ transition with a molar extinction coefficient of ε_{370} = 147,200 M^{-1} cm^{-1}, which is 2−3 times lower than the Soret band maximum of 5,10,15,20-tetra(*p*-benzoato)porphyrin (H_4TBP)[44] and 5,10,15,20-tetra-(*p*-benzoato)chlorin (H_4TBC).[14] This difference may alleviate some photosensitivity side effects for ZnOPPc, as this region is not in the therapeutic window of PDT.[45-47] The Q_{02}-band peak at λ_{max} = 628 nm is assigned to an $n \rightarrow \pi^*$ transition with ε_{628} = 61,000 M^{-1} cm^{-1}, and the Q_{01}-band peak at λ_{max} = 697 nm is a $\pi \rightarrow \pi^*$ (HOMO−LUMO) transition with ε_{697} = 343,600 M^{-1} cm^{-1}.[48] The Q_{01} band has a 72 times larger ε value than the longest wavelength Q-band absorption of H_4TBP (ε_{646} = 4,800 M^{-1} cm^{-1}), which is

the absorption peak typically used for PDT. Compared to H_4TBP, the Q_{01}-band peak of ZnOPPc not only has a longer absorption wavelength for deeper tissue penetration, but also has an order of magnitude greater ε value that makes ZnOPPc significantly more light efficient. This band appears because phthalocyanines lack the near-degeneracy of the a_{1u} and a_{2u} orbitals and mixing of the associated electronic configurations that lead to cancellation of transition dipole moments in porphyrins.[49]

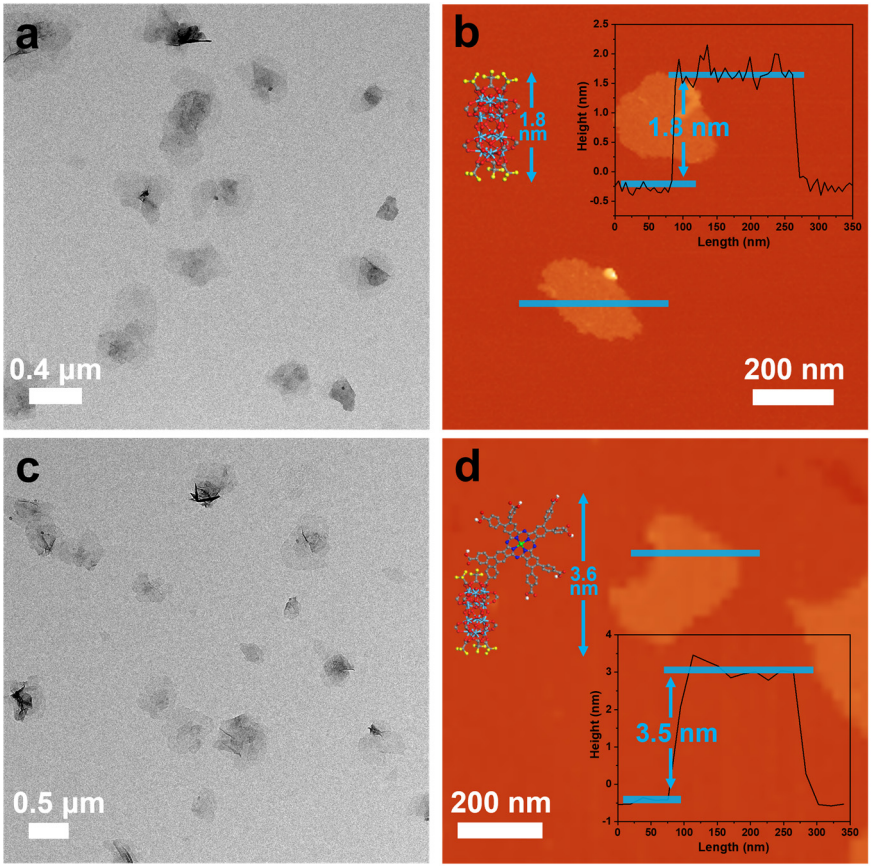

Figure 2-2. TEM and AFM images of Hf_{12}-Ir nMOL and ZnOPPc@nMOL. (a) Large area TEM image of Hf_{12}-Ir nMOL. (b) AFM topographic image of Hf_{12}-Ir nMOL with its selected area (blue bar), height profile (inset, right), and modeled SBU/capping ligand height (inset, left). (c) Large area TEM image of ZnOPPc@nMOL. (d) AFM topographic image of ZnOPPc@nMOL with its selected area (blue bar), height profile (inset, right), and modeled SBU/capping ligand height (inset, left).

Hf_{12}-Ir nMOL was synthesized through a solvothermal reaction between $HfCl_4$ and H_2DBB-Ir-F in *N*,*N*-dimethylformamide (DMF) at 80 °C with TFA and water as modulators

(**Scheme 2-3**).[50] Hf_{12}-Ir nMOL forms an infinite 2D network with **kgd** topology and each SBU is vertically capped with TFA groups to afford an ideal molecular formula of $Hf_{12}(\mu_3\text{-}O)_8(\mu_3\text{-}OH)_8(\mu_2\text{-}OH)_6$(DBB-Ir-F)$_6(TFA)_6$. ZnOPPc@nMOL was synthesized by vigorously stirring a mixture of ZnOPPc in DMF and Hf_{12}-Ir nMOL in ethanol, with a final solvent ratio of DMF/ethanol (2:1), at room temperature (**Scheme 2-3**). The ZnOPPc loading was determined to be 14.9 wt% based on inductively coupled plasma-mass spectrometry (ICP-MS) analysis and UV−visible absorption spectroscopy of digested ZnOPPc@nMOL, which corresponded to a 1.1 : 1.0 ratio of ZnOPPc : Hf_{12} SBU. Additionally, the TFA peak integral decreased in the ^{19}F NMR spectra of digested ZnOPPc@nMOL compared to the bare Hf_{12}-Ir nMOL, supporting the loading values and confirming the successful exchange of ZnOPPc with TFA capping ligands (**Figure 2-24**, **Figure 2-26**). Based on these results, the molecular formula of ZnOPPc@nMOL was determined to be $(ZnOPPc)_{1.1}@Hf_{12}(\mu_3\text{-}O)_8(\mu_3\text{-}OH)_8(\mu_2\text{-}OH)_6$(DBB-Ir-F)$_6(TFA)_{4.9}$.

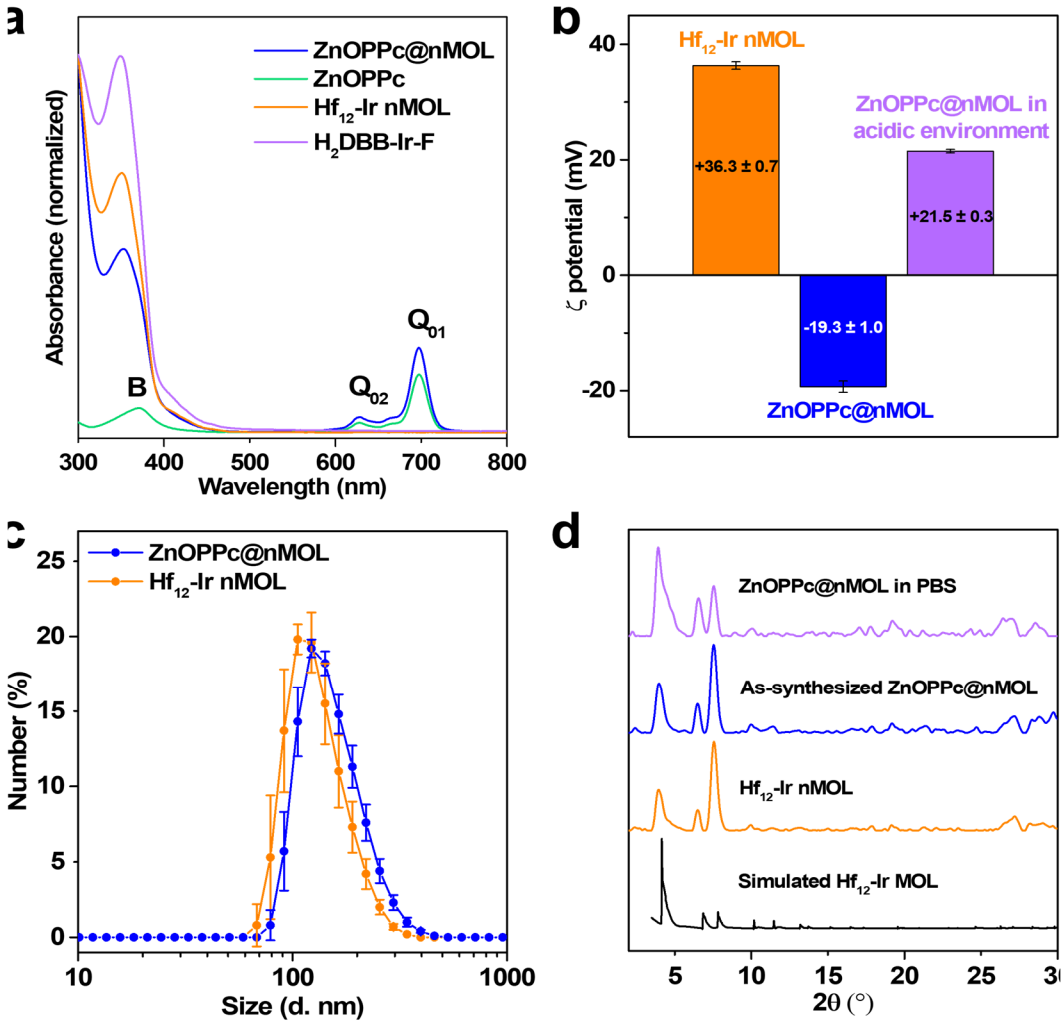

Figure 2-3. Characterization of Hf_{12}-Ir nMOL and ZnOPPc@nMOL. (a) Normalized UV-Vis spectra of ZnOPPc@nMOL, ZnOPPc, Hf_{12}-Ir nMOL and H_2DBB-Ir-F in DMSO. (b) Zeta potentials of Hf_{12}-Ir nMOL in water (pH = 7), ZnOPPc@nMOL in water (pH = 7), and ZnOPPc@nMOL in aqueous acidic buffer (pH = 4).

Transmission electron microscopy (TEM) imaging showed that ZnOPPc@nMOL maintained the same particle size and monolayer morphology as Hf_{12}-Ir nMOL (**Figure 2-2**). Atomic force microscopy (AFM) analysis confirmed the monolayer structure of Hf_{12}-Ir and postsynthetic surface loading in ZnOPPc@nMOL with average thicknesses of 1.8 and 3.5 nm, respectively, which are consistent with the modeled heights of Hf_{12} SBUs capped with only TFA ligands or Hf_{12} SBUs capped with both ZnOPPc and TFA (**Figure 2-2**). The UV−visible spectrum

of ZnOPPc@nMOL showed characteristic peaks from ZnOPPc and Hf_{12}-Ir even after several washes with DMF, further confirming successful loading (**Figure 2-3**). Dynamic light scattering (DLS) particle size distribution analysis of ZnOPPc@nMOL revealed a number-averaged size of 156.2 ± 6.4 nm with a polydispersity index of 0.10 (**Figure 2-3**), which is slightly larger than that of Hf_{12}-Ir nMOL at 133.2 ± 8.0 nm and is concordant with the surface loading of a large hydrophobic molecule. The Hf_{12}-Ir cationic framework showed a highly positive zeta potential of +36.3 ± 0.7 mV, while ZnOPPc@nMOL showed a negative zeta potential of −19.3 ± 1.0 mV, consistent with the surface installation of partially deprotonated ZnOPPc (**Figure 2-3**). The powder X-ray diffraction (PXRD) pattern of ZnOPPc@nMOL matched well with the experimental and simulated PXRD patterns of the Hf_{12}-Ir nMOL (**Figure 2-3**). ZnOPPc@MOL was found to be stable in phosphate-buffered saline (PBS) at physiological pH, either at 37 °C or with 700 nm LED irradiation (100 mW/cm^2), by PXRD (**Figure 2-3**) and DLS (**Figure 2-4**) analysis after incubation.

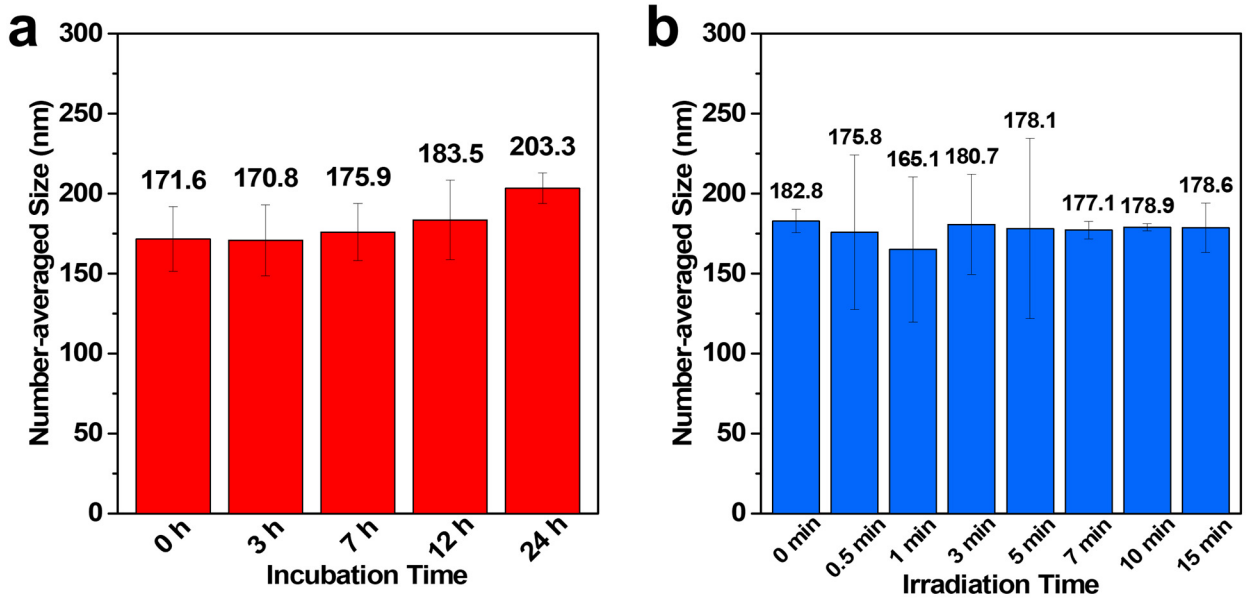

Figure 2-4. Stability studies of ZnOPPc@nMOL. (a) DLS measurements at different time points of number-averaged sizes of ZnOPPc@nMOL samples incubated in PBS at 37 °C. (b) DLS measurements at different time points of number-averaged sizes of ZnOPPc@nMOL in PBS after 700 nm LED irradiation (100 mW/cm^2).

2.2.2. *In vitro* mitochondria targeting

Confocal laser scanning microscopy (CLSM) imaging revealed time-dependent enrichment of mitochondria with Hf_{12}-Ir nMOL in murine colorectal cancer MC38 cells. Mitochondria were labeled by MitoTracker Red CMXROS and Hf_{12}-Ir nMOL was detected through fluorescence of the bridging DBB-Ir-F linkers. Most of the Hf_{12}-Ir nMOL fluorescence was detected outside of mitochondria 15 min after nMOL incubation, likely being captured and trapped in endo/lysosomes (**Figure 2-5**). From 30 min to 2 h (**Figure 2-5**), the fluorescence of Hf_{12}-Ir nMOL outside of mitochondria decreased while colocalization between mitochondria and Hf_{12}-Ir nMOL signals increased, which is consistent with previous reports of mitochondria targeting by cationic nanoparticles.[31, 38-42] Surprisingly, we observed the colocalization of ZnOPPc@nMOL with MitoTracker 30 min post-incubation despite its measured negative surface charge after ZnOPPc loading (**Figure 2-5**, **Figure 2-3**).

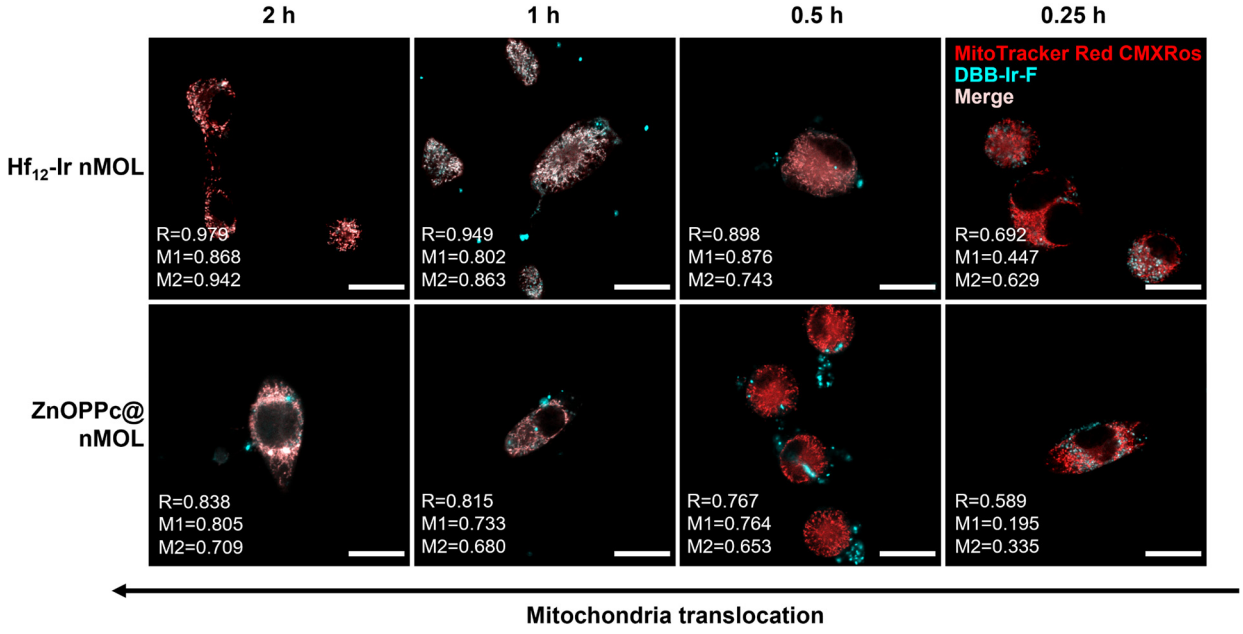

Figure 2-5. Mitochondria translocation. Colocalization of mitochondria and ZnOPPc@nMOl or Hf_{12}-Ir nMOL visualized by CLSM after incubation with MC38 cells at various time points with Pearson's coefficients (R) and overlapping coefficients (M1, M2) of the signals calculated in ImageJ. Scale bars = 20 μm.

This phenomenon is likely due to the reversal of surface charge for ZnOPPc@nMOL after protonation of ZnOPPc to its neutral form in the endo/lysosome, and not due to partial release of ZnOPPc (**Figure 2-7**). This hypothesis was supported by a positive zeta potential of +21.5 ± 0.3 mV for ZnOPPc@nMOL measured in an acidic buffer (pH = 4), which mimics the acidic environment of the endo/lysosome (**Figure 2-3**). At 2 h, the Pearson's coefficients of colocalization of ZnOPPc@nMOL and Hf_{12}-Ir nMOL with MitoTracker reached 0.838 and 0.979, respectively, indicating successful translocation (**Figure 2-5**). Efficient translocation of nMOLs into mitochondria was further supported by ICP-MS analysis of Hf concentrations. 8 h after PDT treatment with ZnOPPc@ nMOL (100 mW/cm^2 , 10 min; "+" and "–" denote with and without light irradiation, respectively), depolarization of mitochondria membrane potential and release of cytochrome c were observed by CLSM (**Figure 2-6**), which are indicative of mitochondria disruption.

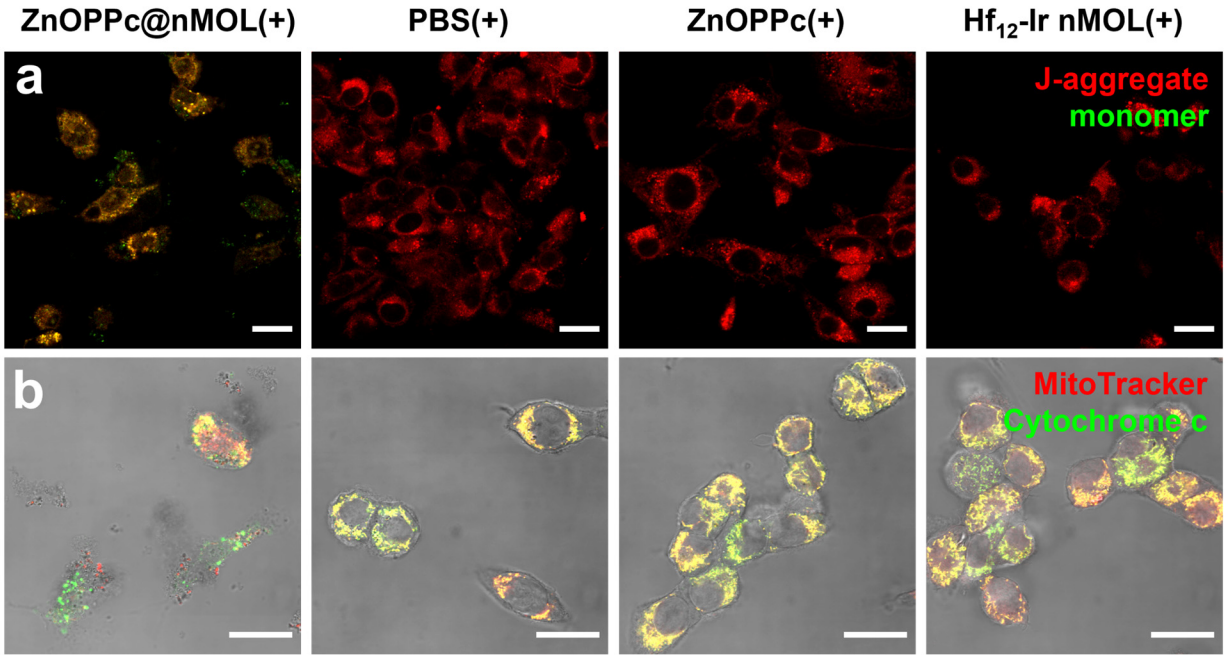

Figure 2-6. Mitochondria disruption. CLSM images of (a) loss of mitochondria membrane potential by JC-1 assay and (b) release of cytochrome *c* from mitochondria. Scale bars = 20 μm.

2.2.3. *In vitro* PDT anticancer efficacy

We then examined whether the surface isolation of ZnOPPc PSs on the Hf_{12}-Ir nMOL SBUs can facilitate ROS generation/diffusion and enhance cellular uptake to elicit stronger cytotoxic effects than the molecular PS alone. Singlet Oxygen Sensor Green (SOSG) assays revealed that ZnOPPc@nMOL significantly enhanced $^1O_2$ generation compared to ZnOPPc in test tube (**Figure 2-7**) and *in vitro* experiments (**Figure 2-8**), indicating that surface isolation of ZnOPPc PSs on the nMOL eliminates aggregation-induced quenching and recovers its ROS generation efficacy. As expected, ZnOPPc was sparingly soluble and suffered from severe cofacial aggregation in serum-containing media, which ultimately led ZnOPPc@nMOL to have 12 times higher cellular uptake than ZnOPPc (**Figure 2-7**). ZnOPPc@nMOL(+) displayed high cytotoxicity with an IC_{50} of 0.11 μM, resulting from the combination of enhanced $^1O_2$ generation/diffusion, high cellular uptake, and strong mitochondria translocation effect (**Figure 2-7**). In contrast, ZnOPPc(+) did not inhibit proliferation or cause morphology changes at concentrations up to 10 μM (**Figure 2-7**).

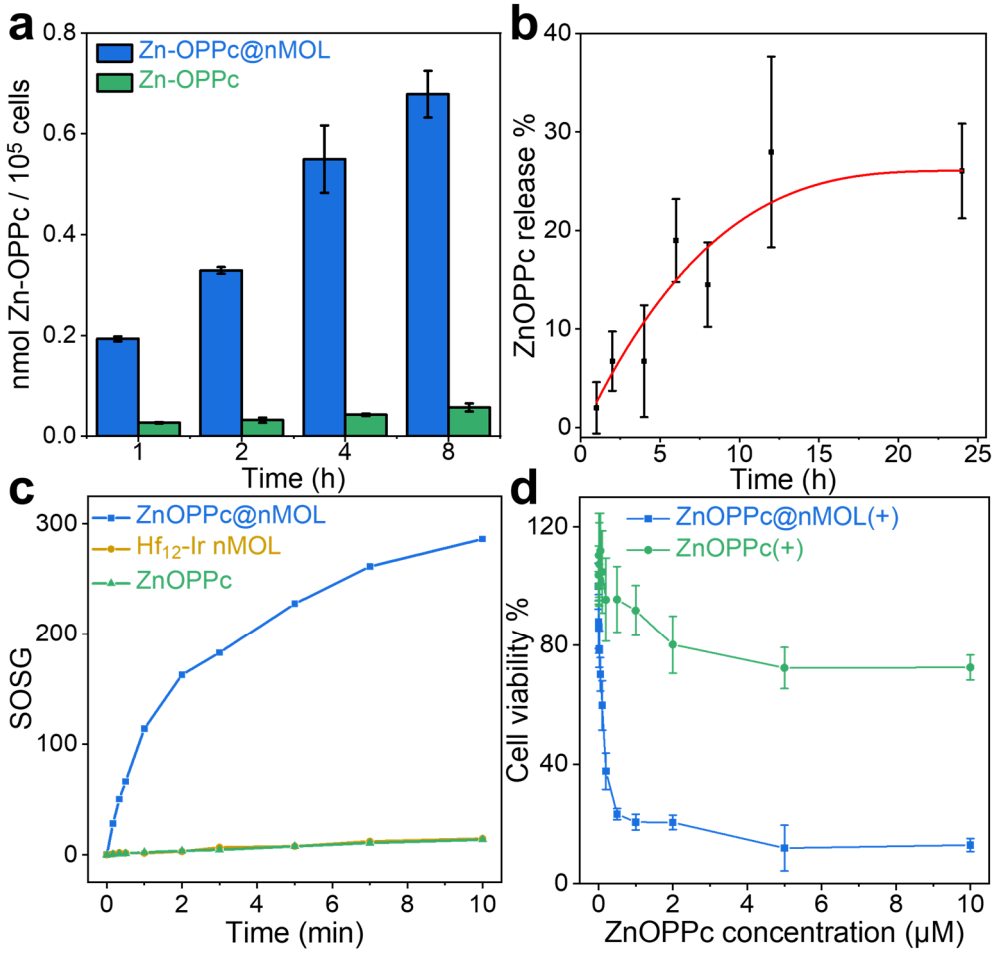

Figure 2-7. Test tube and *in vitro* anticancer efficacy. (a) Cellular uptake of ZnOPPc@nMOL and ZnOPPc in MC38 cells quantified by UV-visible spectroscopy (n = 3). (b) Release profile of ZnOPPc loaded in ZnOPPc@nMOL in PBS (n = 3). (c) Test tube $^1O_2$ generation of ZnOPPc@nMOL, Hf_{12}-Ir nMOL and ZnOPPc after 700 nm irradiation, detected by SOSG assay. (d) MTS assay of PDT treatment with ZnOPPc or ZnOPPc@nMOL on MC38 cells (n = 6).

PDT-induced apoptosis and immunogenic cell death (ICD) were evaluated on MC38 cells by flow cytometry and CLSM. Annexin V and propidium iodine (PI) staining revealed ZnOPPc@nMOL(+) had more severe apoptotic cell death than both Hf_{12}-Ir nMOL(+) and ZnOPPc(+) (**Figure 2-8**, **Figure 2-9**). The ZnOPPc@ nMOL(+) group also showed stronger surface translocation of calreticulin (**Figure 2-8**, **Figure 2-10**), an "eat-me" signal during ICD that can attract myeloid cells for phagocytosis and antigen presentation to facilitate immune responses.

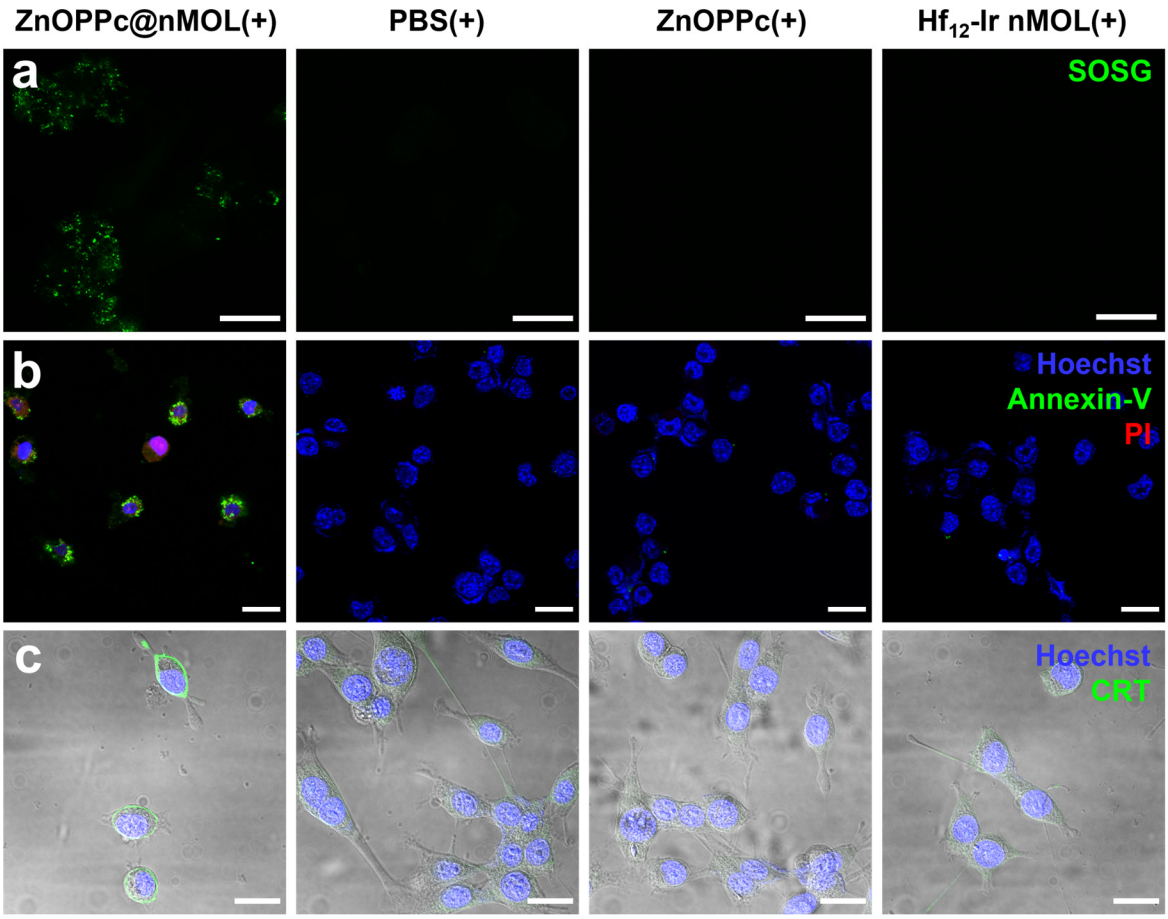

Figure 2-8. *In vitro* PDT-induced $^1O_2$ generation, apoptosis, and immunogenic cell death. (a) $^1O_2$ generation detected by SOSG assay. (b) Cell apoptosis visualized by annexin-V and PI staining. (c) ICD detected by CRT expression on the cell surface. Cell nuclei were stained by Hoechst 33342 in (d) and (e). MC38 cells were used for all experiments. Scale bars = 20 μm.

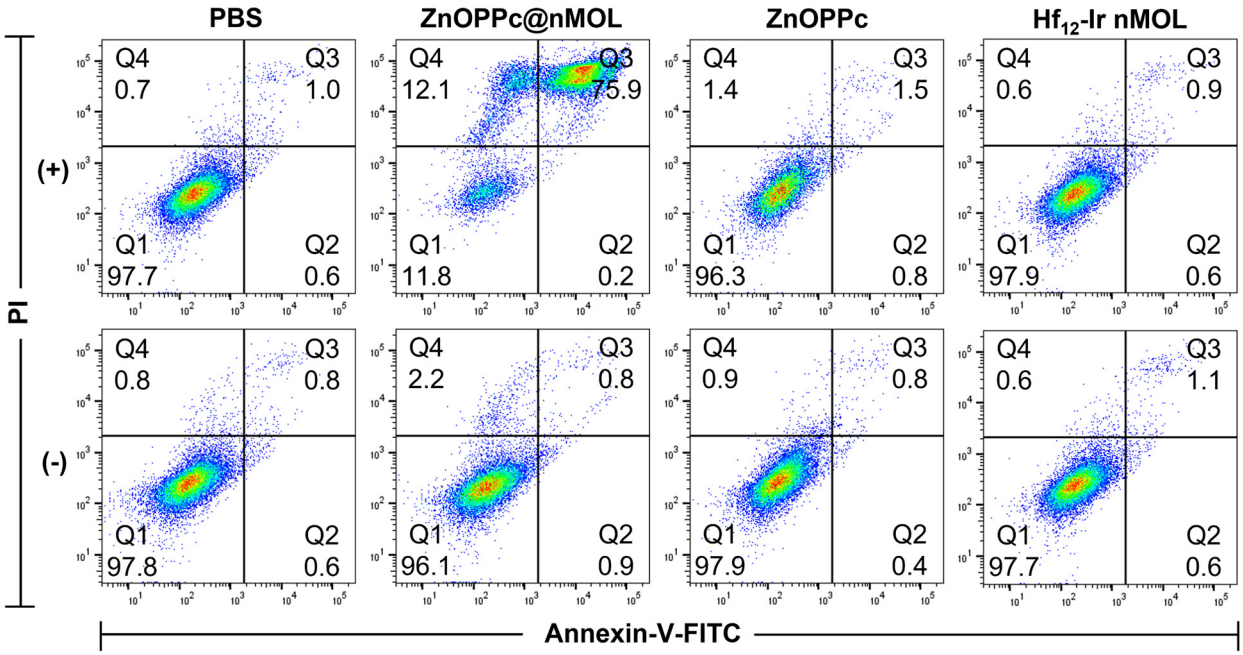

Figure 2-9. Flow cytometry analysis of PDT-induced apoptosis. Analysis was performed 24 hours after PDT treatment on MC38 cells. Q1, Q2, Q3 and Q4 indicate normal, early apoptotic, late apoptotic, necrotic populations among MC38 cells, respectively. The percentages of each population are shown in each quadrant.

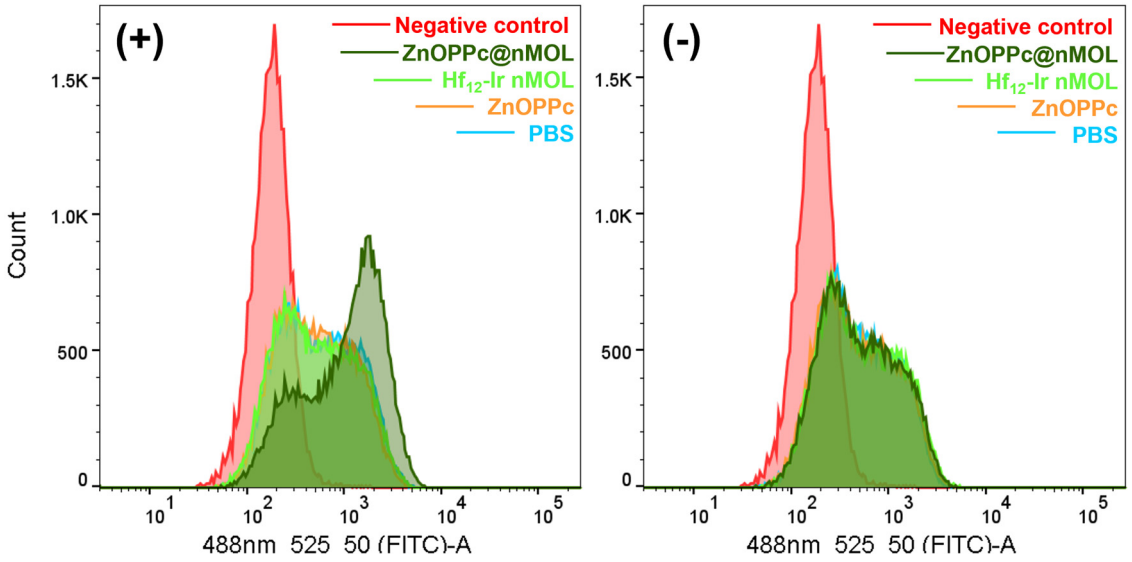

Figure 2-10. Flow cytometry analysis of PDT-induced CRT expression. Analysis was performed 24 hours after PDT treatment on MC38 cells. The negative control without staining is shown in red.

2.2.4. *In vivo* PDT anticancer efficacy

The *in vivo* PDT efficacy of ZnOPPc@nMOL was evaluated on subcutaneous MC38 tumor-bearing C57BL/6 mice and CT26 tumor-bearing BALB/c mice. Hf_{12}-Ir nMOL and ZnOPPc@nMOL were PEGylated before administration to protect against proteolytic degradation, avoid clearance from the reticuloendothelial phagocytic system (RPS) and the mononuclear phagocyte system (MPS), and improve overall blood circulation time. ZnOPPc, Hf_{12}-Ir, and ZnOPPc@nMOL were intravenously injected into mouse tail veins at an equivalent ZnOPPc dose of 0.1 μmol (equivalent DBB-Ir-F dose of 0.5 μmol) followed by 700 nm LED irradiation at the tumor site, with a total light dose of 90 J/cm^2 (100 mW, 15 min).

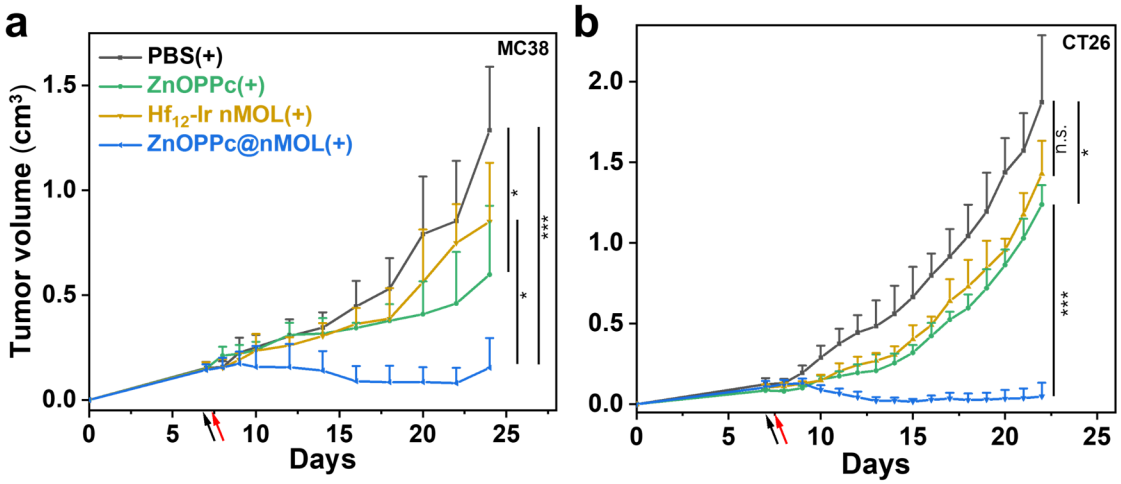

Figure 2-11. *In vivo* PDT anticancer efficacy. Tumor growth curves of (a) MC38 tumor-bearing C57BL/6 mice and (b) CT26 tumor-bearing BALB/c mice (n = 5). *P < 0.05 and ***P < 0.001 by ANOVA test.

The ZnOPPc@nMOL(+) group showed superior anticancer efficacy with tumor growth inhibition (TGI) values of TGI_{MC38} = 85.6% and TGI_{CT26} = 96.7%, as well as 2 out of 5 mice and 3 out of 5 mice being tumor free for MC38- and CT26-tumor-bearing mice, respectively (**Figure 2-11**). ZnOPPc(+) moderately inhibited tumor growth with TGI_{MC38} = 59.6% and TGI_{CT26} =

37.7%, whereas Hf_{12}-Ir(+) had a minimal effect on tumor growth with statistically insignificant TGI_{MC38} = 35.6% and TGI_{CT26} = 10.0%.

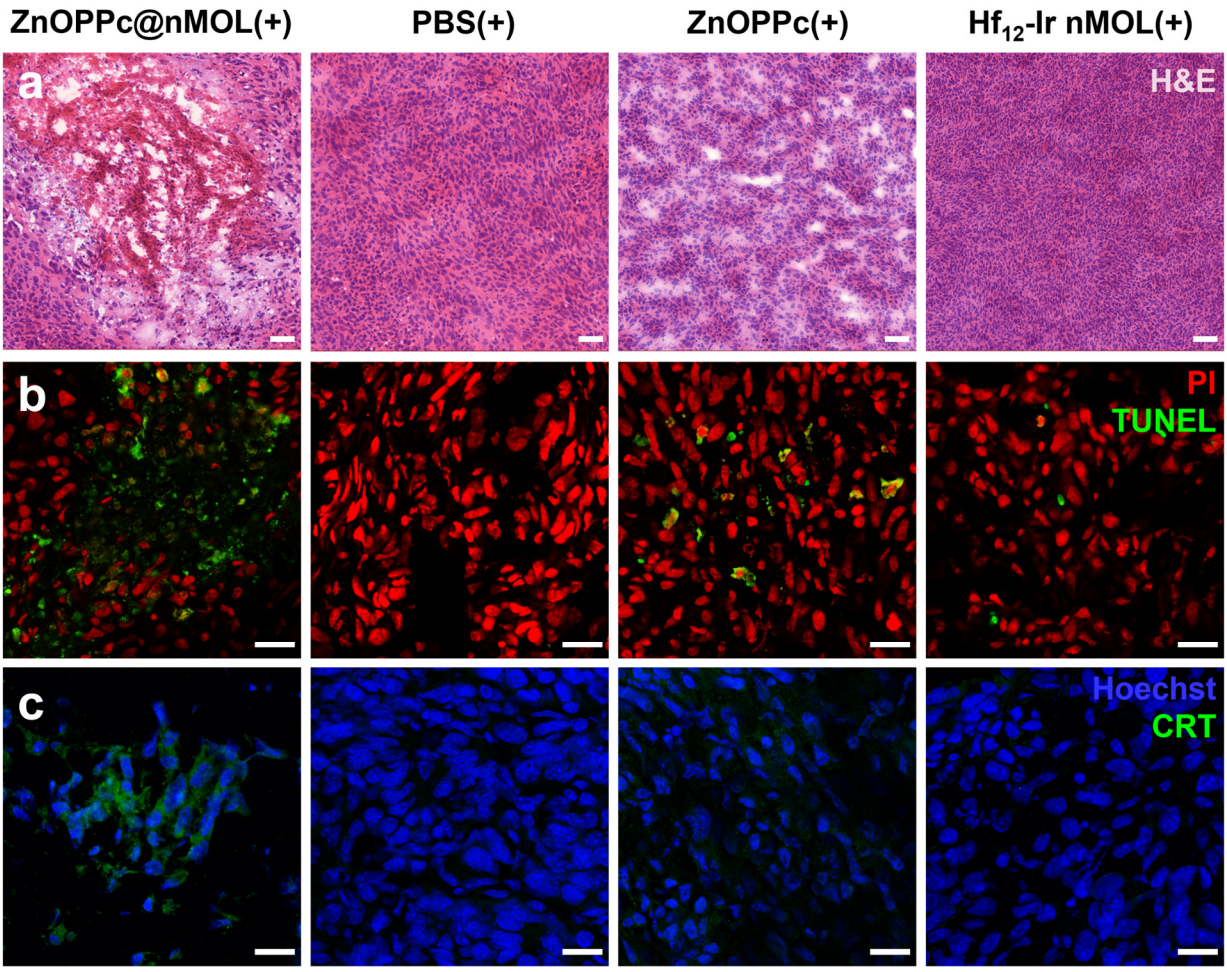

Figure 2-12. *In vivo* PDT-induced necrosis, apoptosis, and immunogenic cell death. (a) H&E staining, (b) TUNEL assay, (c) and CRT staining of excised tumors from treated C57BL/6 mice. Scale bars are 50 μm for H&E staining and 20 μm for the others.

Terminal deoxynucleotidyl transferase dUTP nick end labeling (TUNEL) and calreticulin (CRT) staining revealed severe apoptosis and obvious CRT surface translocation in the ZnOPPc@nMOL(+) tumors, respectively (**Figure 2-12**). Hematoxylin-eosin (H&E) staining of tumor sections also showed that ZnOPPc@nMOL(+) treatment caused severe necrosis (**Figure 2-12**). ZnOPPc@nMOL(+) thus exhibited remarkable antitumor activity and produced strong ICD, which yielded excellent PDT efficacy. All treatment groups showed a lack of general dark toxicity,

with steady trends in mouse body weights (**Figure 2-13**) and minimal aberration in major organ sections. Thus, Hf_{12}-Ir nMOL is a biocompatible and modular nano-delivery platform for PSs that can significantly enhance their therapeutic effects.

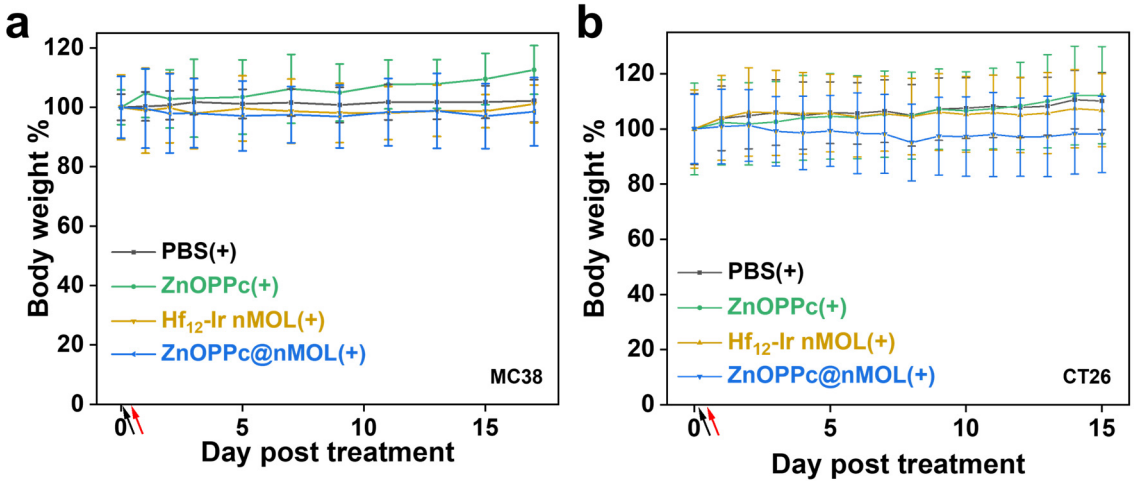

Figure 2-13. Body weight percentage curves. Mouse body weight percentages of (a) MC38- and (b) CT26-tumor-bearing mice over the treatment period.

2.3 Conclusion

In this chapter, we report the surface isolation of ZnOPPc PSs on cationic Hf_{12}-Ir nMOLs to prevent aggregation-induced quenching of the photoexcited ZnOPPc macrocycles and to enable mitochondria translocation. As a result, ZnOPPc@nMOL showed significantly enhanced $^1O_2$ generation and superb anticancer efficacy over the molecular ZnOPPc species. This work demonstrates the potential of using nMOLs to deliver highly potent PSs with nonideal physicochemical and pharmacokinetic properties for effective PDT treatment of cancers.

2.4 Experimental section

2.4.1. Materials and methods

All chemical reagents were purchased from commercial sources and used without further purification as follows: 4,5-dichlorophthalonitrile (Tokyo Chemical Industry), 4-

(methoxycarbonylphenyl)-boronic acid (Boron Molecular), palladium(II) acetate ($Pd(OAc)_2$; Thermo Scientific Chemicals), 2-dicyclohexylphosphino-2',6'-dimethoxybiphenyl (SPhos; Sigma-Aldrich), 1,8-diazabicyclo[5.4.0]undec-7-ene (DBU; Oakwood Chemical).

TEM images were collected on a TECNAI Spirit TEM (120 kV). PXRD data was collected on a Bruker D8 Venture diffractometer using a Cu Kα radiation source (λ = 1.54178 Å) and processed with PowderX software. AFM images were collected on a Bruker Multimode 8-HR AFM, and images were processed using NanoScope Analysis 1.40 software. Dynamic light scattering (DLS) and zeta-potential measurements were obtained on a Malvern Zetasizer Nano ZS instrument. UV-Vis spectra were collected on a Shimadzu UV-2600 UV-Vis spectrophotometer. Fluorescence excitation/emission spectra were obtained using a Shimadzu RF-5301PC spectrofluorophotometer. ICP-MS data was collected using an Agilent 7700x ICP-MS and analyzed using ICP-MS Mass Hunter version B01.03. Samples were diluted in a 2% HNO_3 matrix and analyzed with ^{159}Tb and ^{115}In internal standards against 10-point standard curves over the range from 1 ppb to 500 ppb. The correlation was >0.999 for all analyses of interest. Data collection was performed in Spectrum Mode with three replicates per sample and 100 sweeps per replicate. ^{1}H, ^{13}C, and ^{19}F NMR spectra were recorded on a Bruker NMR 500 DRX spectrometer (^{1}H NMR: 500 MHz, ^{19}F NMR: 377 MHz) or a Bruker NMR 400 DRX spectrometer (^{1}H NMR: 400 MHz, ^{13}C NMR: 101 MHz) and referenced to the proton resonance resulting from incomplete deuteration of $CDCl_3$ (^{1}H NMR: δ 7.26; ^{13}C NMR: δ 77.16) or DMSO-*d*$_6$ (^{1}H NMR: δ 2.50; ^{13}C NMR: δ 39.52). MALDI-TOF HR-MS data was collected on a Bruker Ultraflextreme MALDI-TOF/TOF using negative-ion reflectron mode. Thermogravimetric analysis (TGA) was performed in air using a Shimadzu TGA-50 equipped with an alumina crucible and heated at a rate of 1 °C per min.

Flow cytometry data was collected on an LSR-Fortessa 4-15 (BD Biosciences, USA) and analyzed by FlowJo software (Tree Star, USA). Confocal laser scanning microscope images were collected on a Leica SP8. Imaging was performed at the University of Chicago Integrated Light Microscopy Facility and analysis was done with LAS X (Leica) and ImageJ software (NIH, USA). Cell morphology and proliferation were captured and analyzed by IncuCyte S3 with standard mode. Protein electrophoresis and electro-transfer were performed with XCell SureLock™ Mini-Cell (Thermo Fisher Scientific, USA) and Mini Trans-Blot® Electrophoretic Transfer Cell (BioRad, USA), respectively.

DPBS (-Mg^{2+}, -Ca^{2+}, phosphate-buffered saline), TBST (Tris-Buffered Saline, 0.1% TWEEN-20), NuPAGE™ 4 to 12% Bis-Tris gel, PVDF membrane, running buffer, transfer buffer, RIPA buffer, BCA kit and ECL plus kit were purchased from Thermo Fisher Scientific. Murine colorectal carcinoma MC38 and CT26 cells and human kidney endothelial HEK293T cells were obtained from the American Type Culture Collection (ATCC, Rockville, MD) and were cultured in DMEM (Dublecco's Modified Eagle Medium; GE Healthcare, USA) or RPMI-1640 (Corning, USA) supported with 10% fetal bovine serum (VWR, USA), 100 U/ml penicillin G sodium and 100 μg/ml streptomycin sulphate in a humidified atmosphere containing 5% CO_2 at 37°C. C57BL/6 and BALB/c mice (6-8 weeks) were obtained from Harlan-Envigo Laboratories, Inc (USA). The study protocol was reviewed and approved by the Institutional Animal Care and Use Committee (IACUC) at the University of Chicago. The Human Tissue Resource Center at the University of Chicago provided the histology related services for this study.

2.4.2. Synthetic and characterization procedures

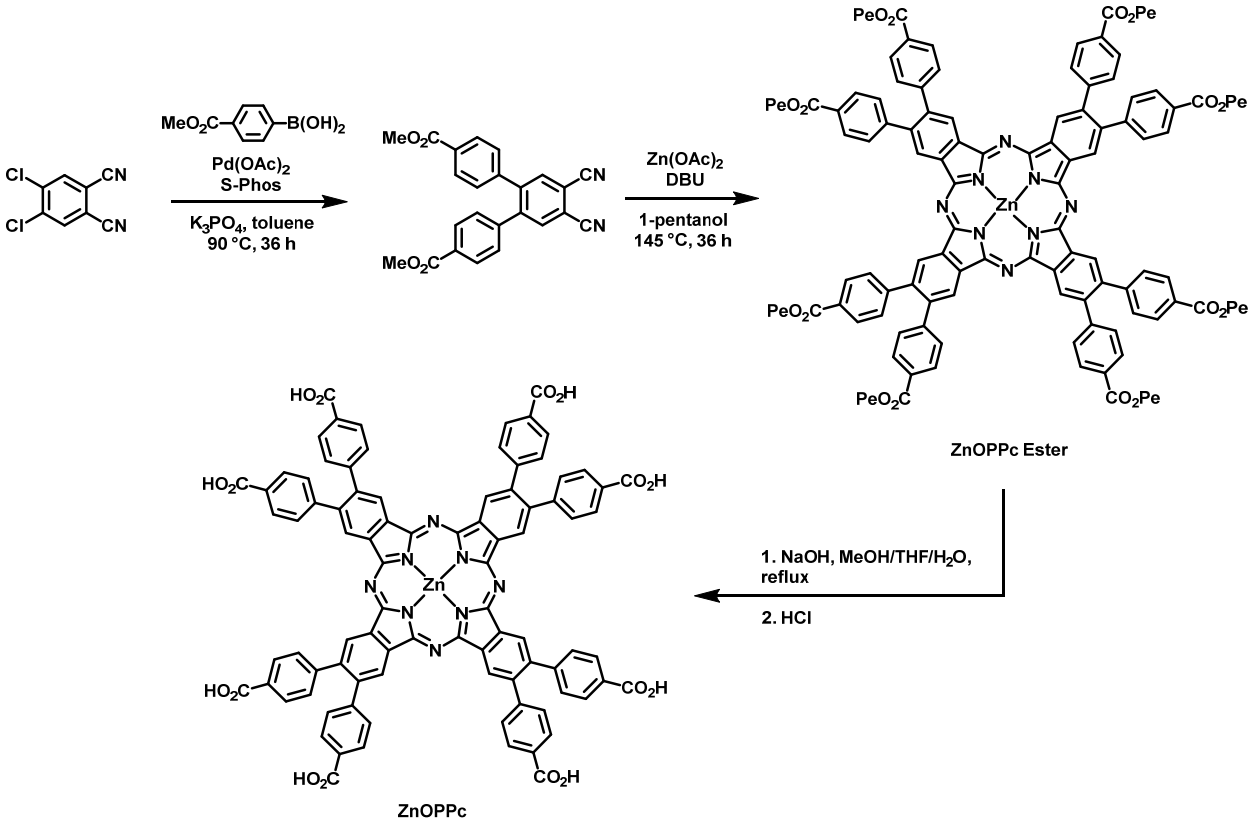

Scheme 2-1. Synthetic route to ZnOPPc.

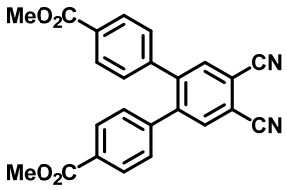

Synthesis of 4,5-Bis(4-methoxycarbonylphenyl)phthalonitrile. 4,5-bis(4-methoxycarbonylphenyl)phthalonitrile was synthesized as previously reported with minor modifications.[51] An oven-dried Schlenk tube was charged with 4,5-dichlorophthalonitrile (2.00 g, 10.2 mmol), 4-(methoxycarbonylphenyl)-boronic acid (5.4 g, 30.0 mmol), $Pd(OAc)_2$ (44 mg, 0.2 mmol), SPhos (200 mg, 0.5 mmol), anhydrous K_3PO_4 (8.48 g, 40.0 mmol), and a stir bar. The reaction vessel was sealed and backfilled with nitrogen three times. Anhydrous toluene (40 mL) was added, and the mixture was stirred at 90 °C for 36 h. After cooling to room temperature, toluene (~80 mL) was added, and the reaction mixture was filtered and washed twice with water. The combined organic

layers were dried over anhydrous Na_2SO_4 and then concentrated under vacuum. The crude product was purified by column chromatography using $CHCl_3$/hexanes/EtOAc (4:4:1) and recrystallized from EtOAc to afford the pure product as white crystals (2.11 g, 52% yield).

^{1}H NMR (400 MHz, $CDCl_3$): δ 7.97 (d, *J* = 8.6 Hz, 4H), 7.91 (s, 2H), 7.19 (d, *J* = 8.6 Hz 4H), 3.94 (s, 6H).

^{13}C NMR (101 MHz, $CDCl_3$): δ 166.21, 144.85, 141.58, 135.38, 130.46, 129.99, 129.41, 115.28, 114.99, 52.39.

TLC: R_f = 0.44 ($CHCl_3$/hexanes/EtOAc 4:4:1).

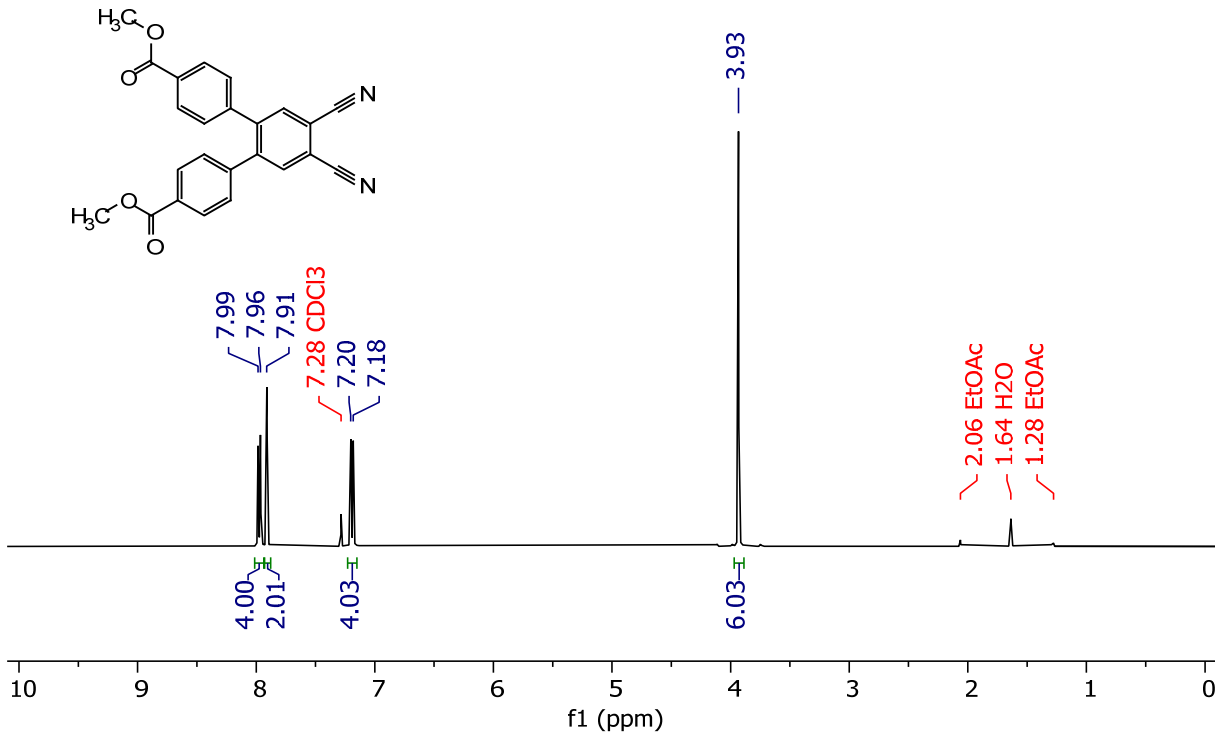

Figure 2-14. ^{1}H NMR of 4,5-bis(4-methoxycarbonylphenyl)phthalonitrile (400 MHz, $CDCl_3$).

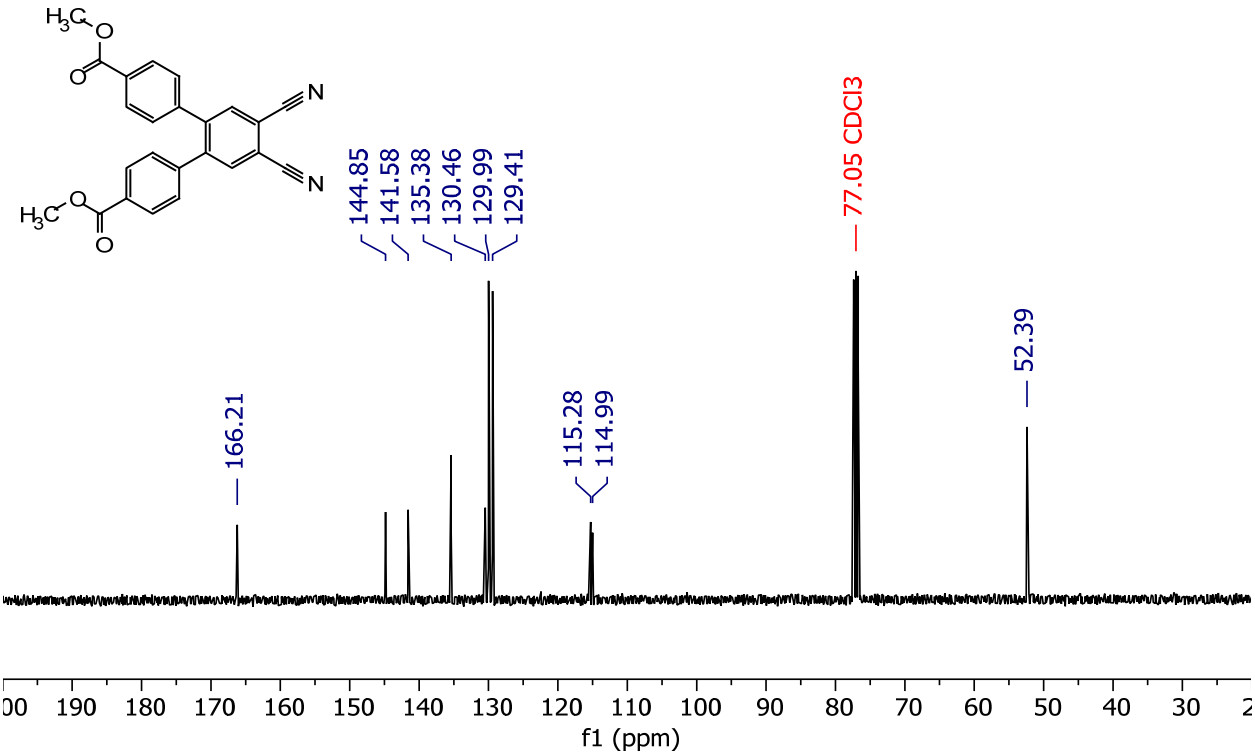

Figure 2-15. ^{13}C NMR of 4,5-bis(4-methoxycarbonylphenyl)phthalonitrile (101 MHz, $CDCl_3$).

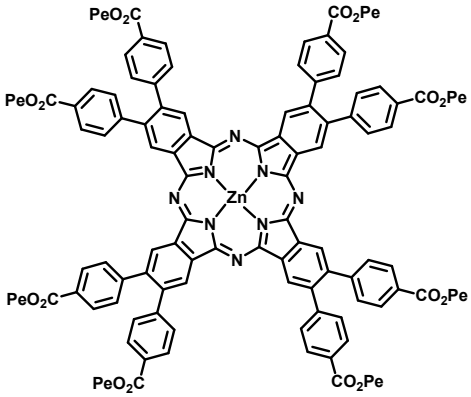

Synthesis of zinc(II) 2,3,9,10,16,17,23,24-octa[4-pentoxycarbonylphenyl] phthalocyanine (ZnOPPc ester). A mixture of 4,5-bis(4-methoxycarbonylphenyl) phthalonitrile (800 mg, 2.02 mmol), anhydrous $Zn(OAc)_2$ (93 mg, 0.507 mmol), DBU (301 µL, 2.02 mmol) and anhydrous 1-pentanol (PeOH; 30 mL) was added to a 100 mL round-bottomed flask and refluxed under nitrogen for 36 h. The reaction mixture was cooled to room temperature and MeOH (60 mL) was added to the reaction mixture and stirred for a further 30 min. The precipitated solid was collected by centrifugation, washed twice with MeOH/H_2O (4:1), once with MeOH, and thrice with acetonitrile. The crude product was purified by column

chromatography using $CHCl_3$/EtOAc (4:1). The first dark green fraction was collected and dried under vacuum to yield a dark green solid (823 mg, 19% yield).

HR-MS (MALDI-TOF): *m/z* Calcd. for $C_{128}H_{128}N_8O_{16}Zn^+$ (M^+): 2096.87, Found: 2096.765.

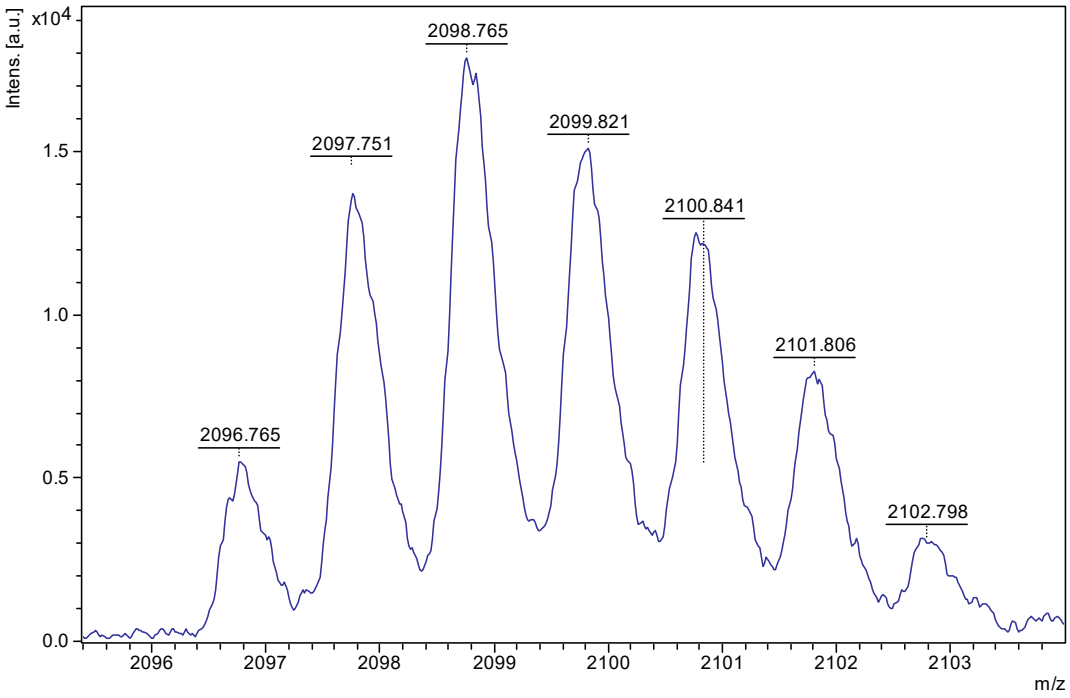

Figure 2-16. HR-MS (MALDI-TOF) spectrum of ZnOPPc ester showing the isotopic peaks of the molecular ion [M^+].

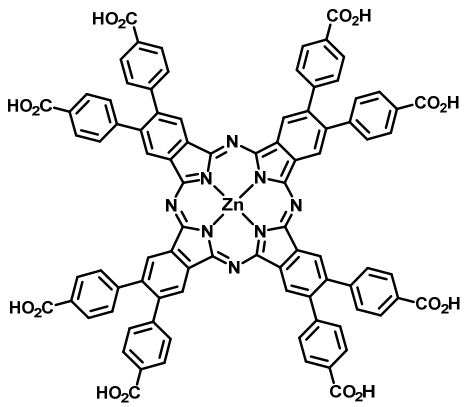

Synthesis of zinc(II) 2,3,9,10,16,17,23,24-octa[4-carboxyphenyl] phthalocyanine (ZnOPPc). A mixture of ZnOPPc ester (300 mg, 0.143 mmol) and THF/MeOH (100 mL, 1:1) was added to an aq. NaOH solution (2.90 g/40 mL H_2O) and ultrasonicated. The mixture was then refluxed for 24 h. The reaction mixture was cooled to room temperature and the volatile solvents were removed under vacuum. H_2O (80 mL) was added to the solution and acidified, using 1 M HCl, until pH = 3. The precipitated solid was collected by centrifugation,

washed with H_2O/MeOH (2:1), acetone, EtOAc, and DCM. The product was then dried under vacuum overnight to yield a dark green solid (200 mg, 91% yield).

HR-MS (MALDI-TOF): *m/z* Calcd. for $C_{88}H_{48}N_8O_{16}Zn^+$ (M^+): 1536.25, Found: 1536.202.

^{1}H NMR (500 MHz, DMSO-d_6): δ 13.06 (s, 8H), 9.03 (s, 8H), 7.97 (s, 16H), 7.63 (s, 16H).

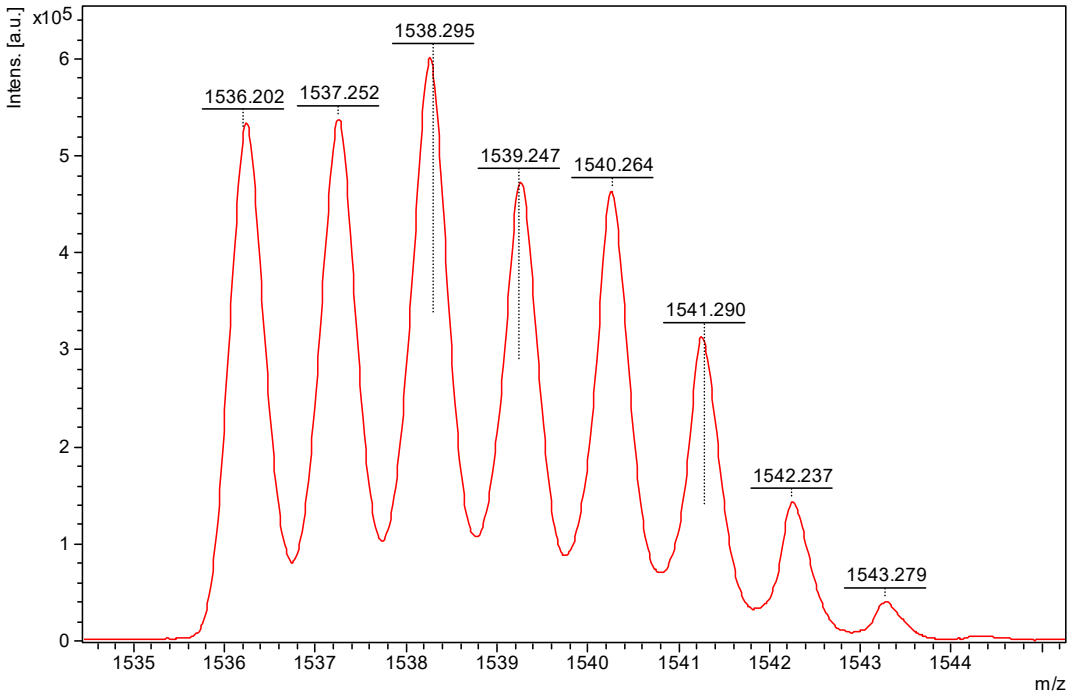

Figure 2-17. HR-MS (MALDI-TOF) spectrum of ZnOPPc showing the isotopic peaks of the molecular ion [M^+].

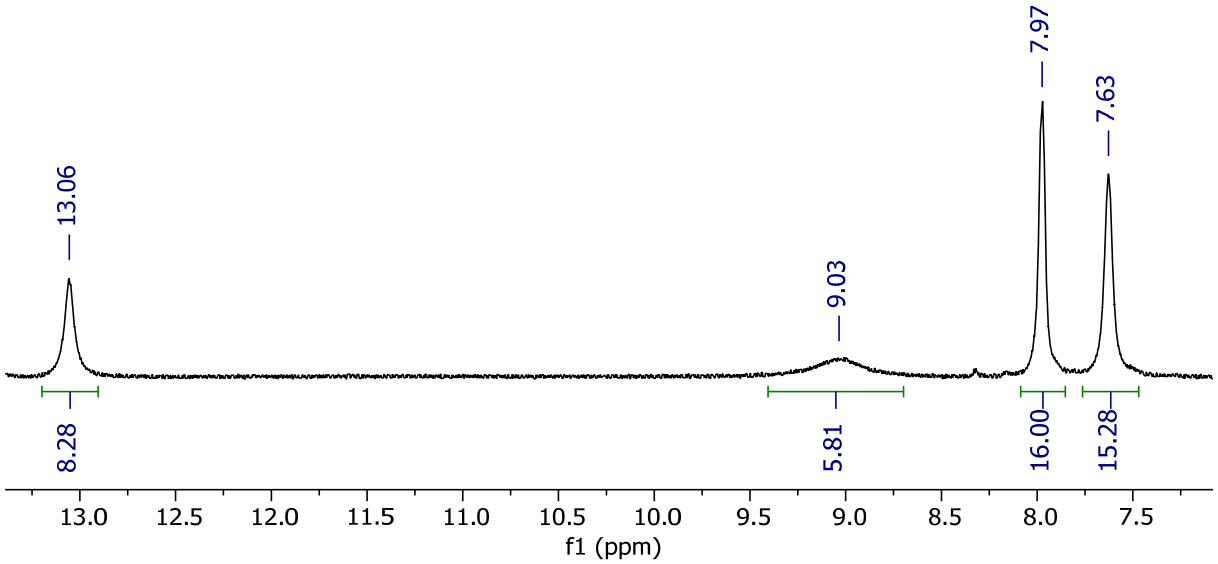

Figure 2-18. ^{1}H NMR spectrum of ZnOPPc (500 MHz, DMSO-d_6).

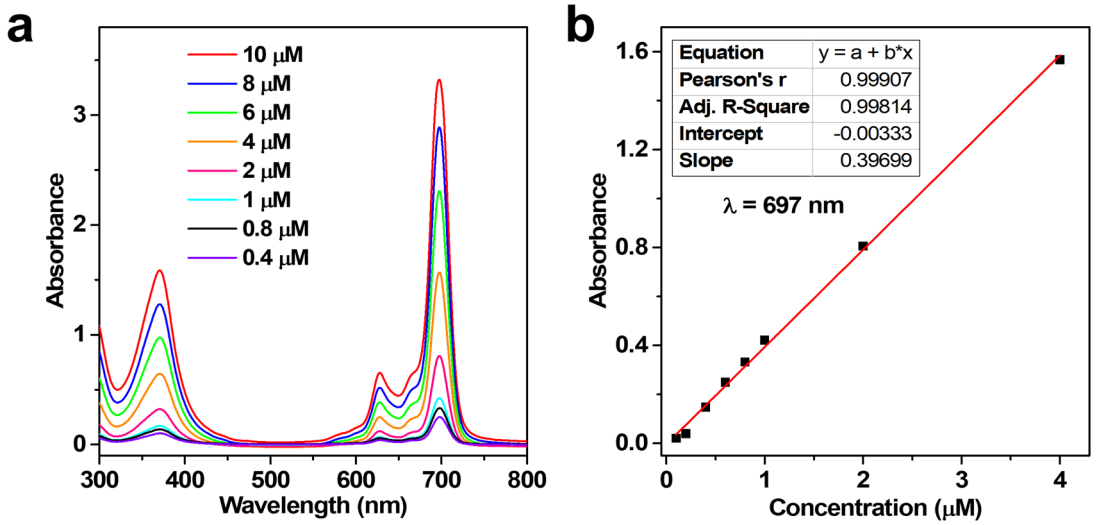

Figure 2-19. Standard curve of ZnOPPc in DMSO. (a) UV-Vis spectra of ZnOPPc in DMSO at different concentrations. The absorption of ZnOPPc at 700 nm corresponds to the $\pi \rightarrow \pi^*$ transition. (b) Plot of the absorbance of ZnOPPc at 700 nm as a function of concentration.

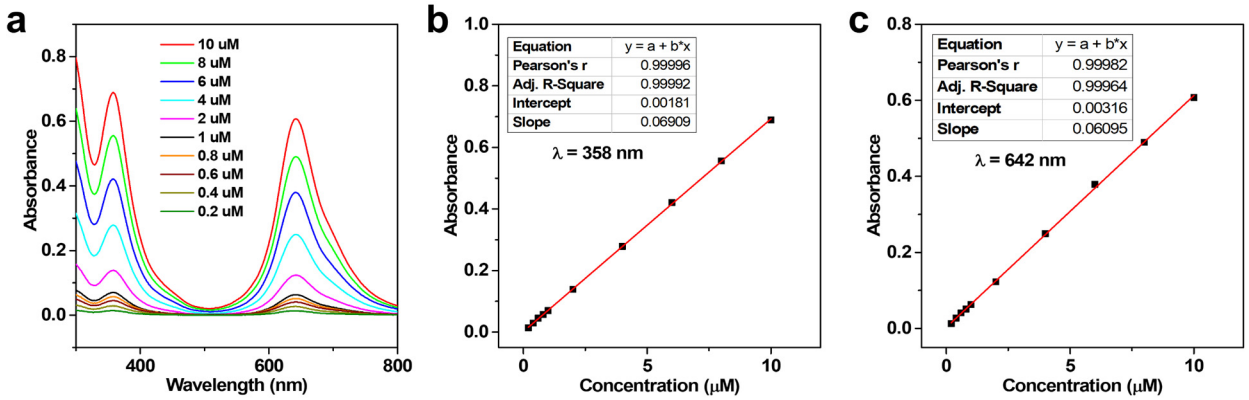

Figure 2-20. Standard curve of ZnOPPc in PBS. (a) UV-Vis spectra of ZnOPPc in PBS at different concentrations. Plots of the absorbance of ZnOPPc in PBS at (b) 358 nm and (c) 642 nm as a function of concentration.

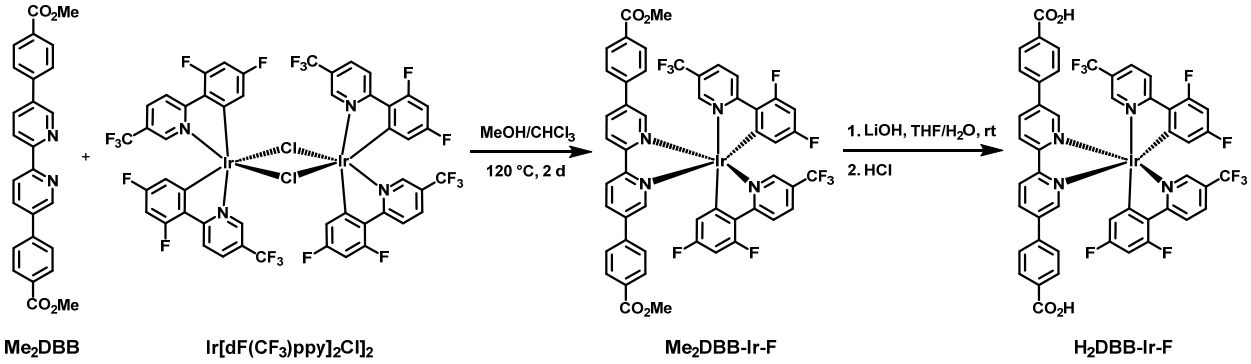

Scheme 2-2. Synthetic route to H_2DBB-Ir-F.

Synthesis of H_2DBB-Ir-F. Ir(DBB)[dF(CF3)ppy]$_2^+$ [H_2DBB-Ir-F; DBB = 4,4'-di(4-benzoato)-2,2'-bipyridine; dF(CF_3)ppy = 2-(2,4-difluorophenyl)-5-(trifluoromethyl)pyridine] was synthesized as shown in **Scheme 2-2** according to a previous literature report.[52]

^{1}H NMR (500 MHz, DMSO-d_6): δ 9.11 (d, 2H), 8.77 (dd, 2H), 8.48 (d, 2H), 8.43 (d, 2H), 8.15 (s, 2H), 8.04 (d, 4H), 7.81 (s, 2H), 7.67 (d, 4H), 7.11 (m, 2H), 5.89 (dd, 2H).

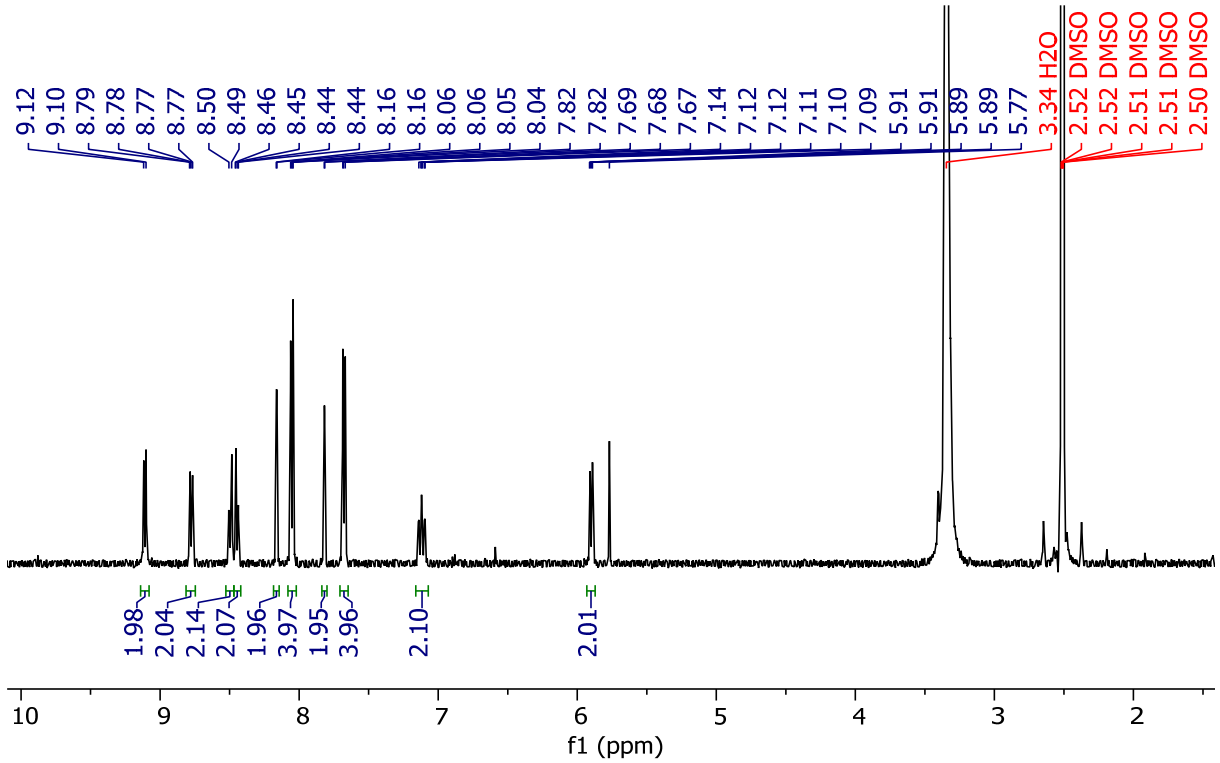

Figure 2-21. ^{1}H NMR spectrum of H_2DBB-Ir-F (500 MHz, DMSO-d_6).

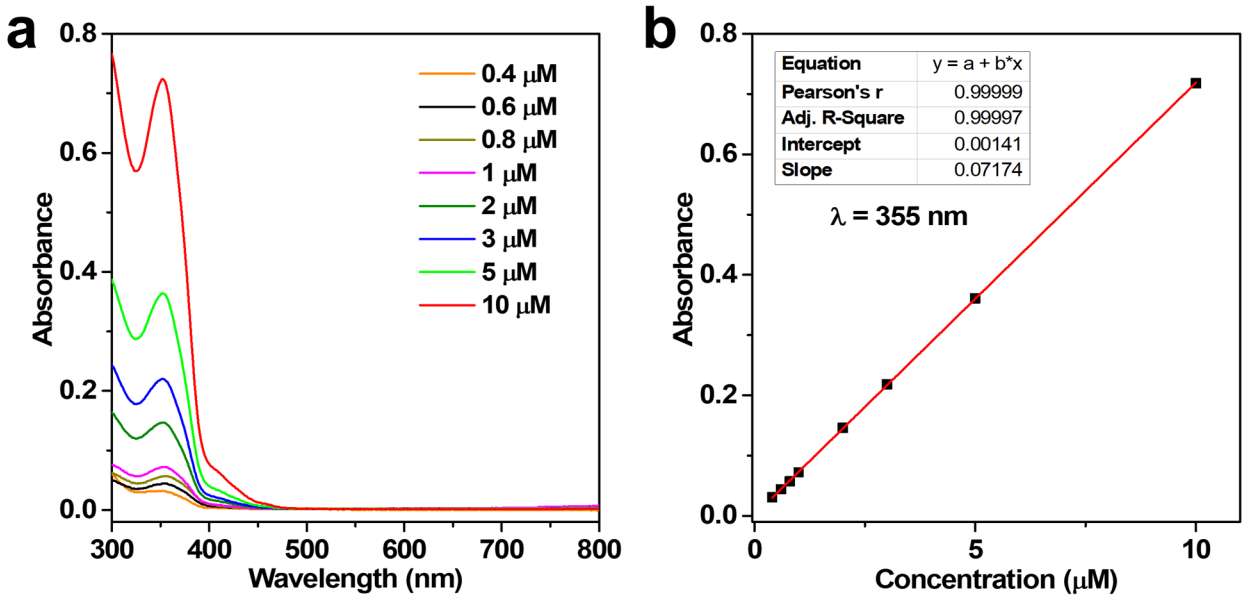

Figure 2-22. UV-Vis standard curve of H_2DBB-Ir-F in DMSO. (a) UV-Vis spectra of H_2DBB-Ir-F in DMSO at different concentrations. The characteristic absorption of H_2DBB-Ir-F corresponds to the metal-to-ligand charge-transfer (MLCT) transition. (b) Plot of the absorbance of H_2DBB-Ir-F at 350 nm as a function of concentration.

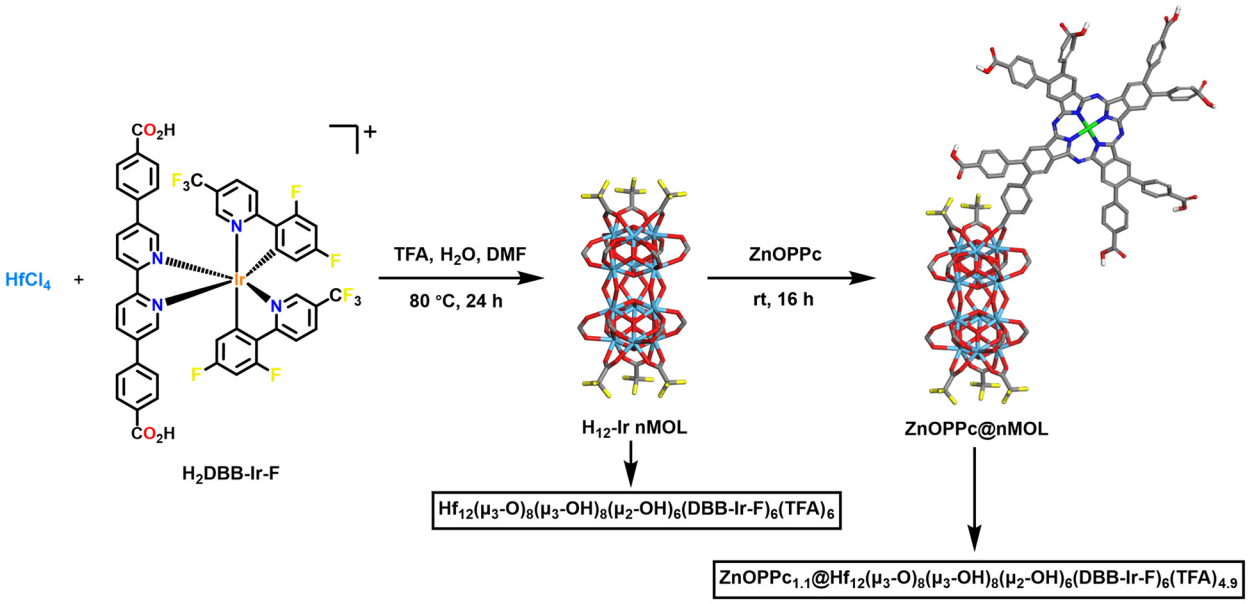

Scheme 2-3. Synthetic route to Hf_{12}-Ir nMOL and ZnOPPc@nMOL (DBB-Ir-F linkers on the Hf_{12} SBU are omitted for clarity; sky blue: Hf, yellow: F, red: O, blue: N, grey: C, white: H).

Synthesis of Hf_{12}-Ir nMOL. Hf_{12}-Ir nMOL was synthesized as shown in **Scheme 2-3** according to a previous literature report.[52] To a 4 mL glass vial was added 0.5 mL of $HfCl_4$ solb ution [2.0 mg/mL in DMF], 0.5 mL of H_2DBB-Ir-F solution (4.0 mg/mL in DMF), 2 μL of TFA, and 5 μL of water. The reaction mixture was kept in an 80 °C oven for 24 hours. The yellow precipitate was collected by centrifugation and washed with DMF and ethanol.

NMR analysis of nMOLs. 1.0 mg nMOL was dried under vacuum. To the dried solid was added a solution of 500 μL DMSO-d_6 and 50 μL D_3PO_4. The mixture was sonicated for 10 min, followed by the addition of 50 μL D_2O just before $^1H/^{19}F$ NMR analysis.

UV-Vis analysis of nMOLs. 10 μL of a dispersed solution of nMOL was added to a mixture of 940 μL DMSO and 50 μL H_3PO_4. The mixture was then sonicated for about 10 minutes and the UV-Vis absorption spectrum was recorded.

ICP-MS analysis of nMOLs. 10 μL of a dispersed solution of nMOL was added to a mixture of 980 μL HNO_3 and 10 μL HF. The mixture was vortexed and kept at room temperature for 3 days. The sample was then diluted with ultrapure water to 2% HNO_3 and analyzed by ICP-MS.

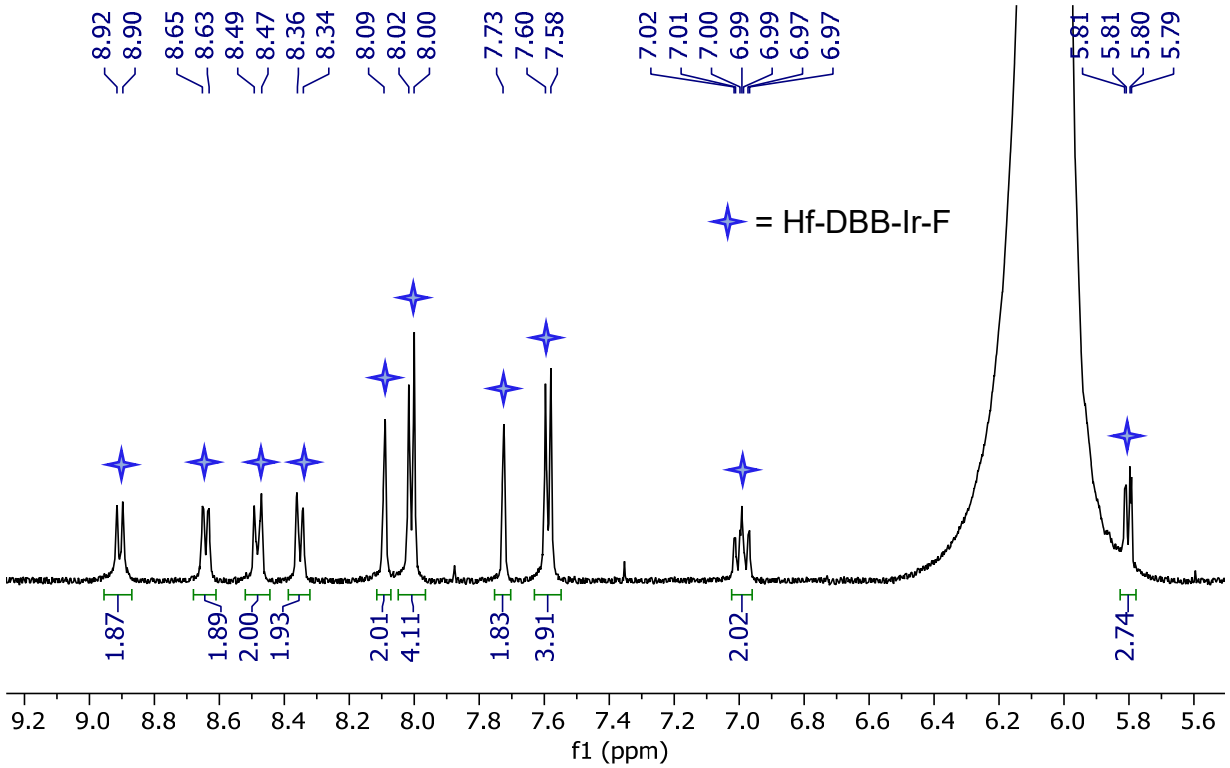

Figure 2-23. ^{1}H NMR spectrum of digested Hf$_{12}$-Ir nMOL (500 MHz, DMSO-d_6).

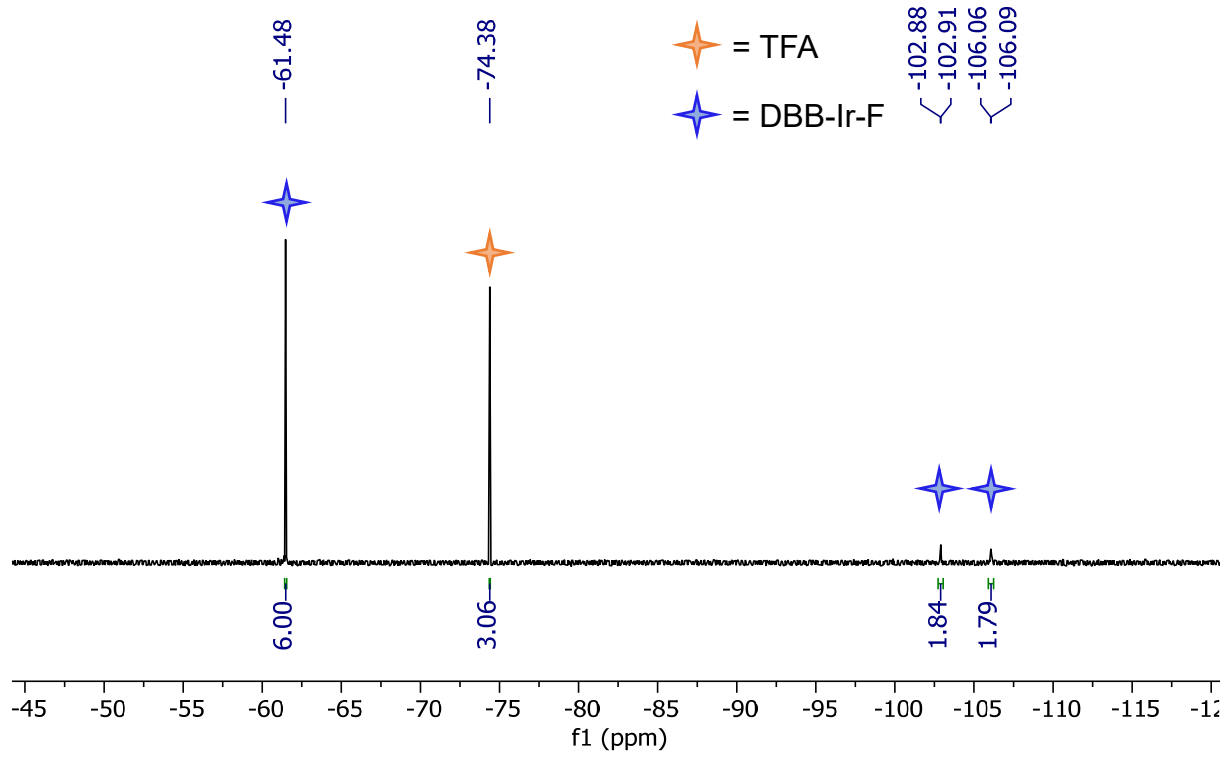

Figure 2-24. ^{19}F NMR spectrum of digested Hf$_{12}$-Ir nMOL (377 MHz, DMSO-d_6).

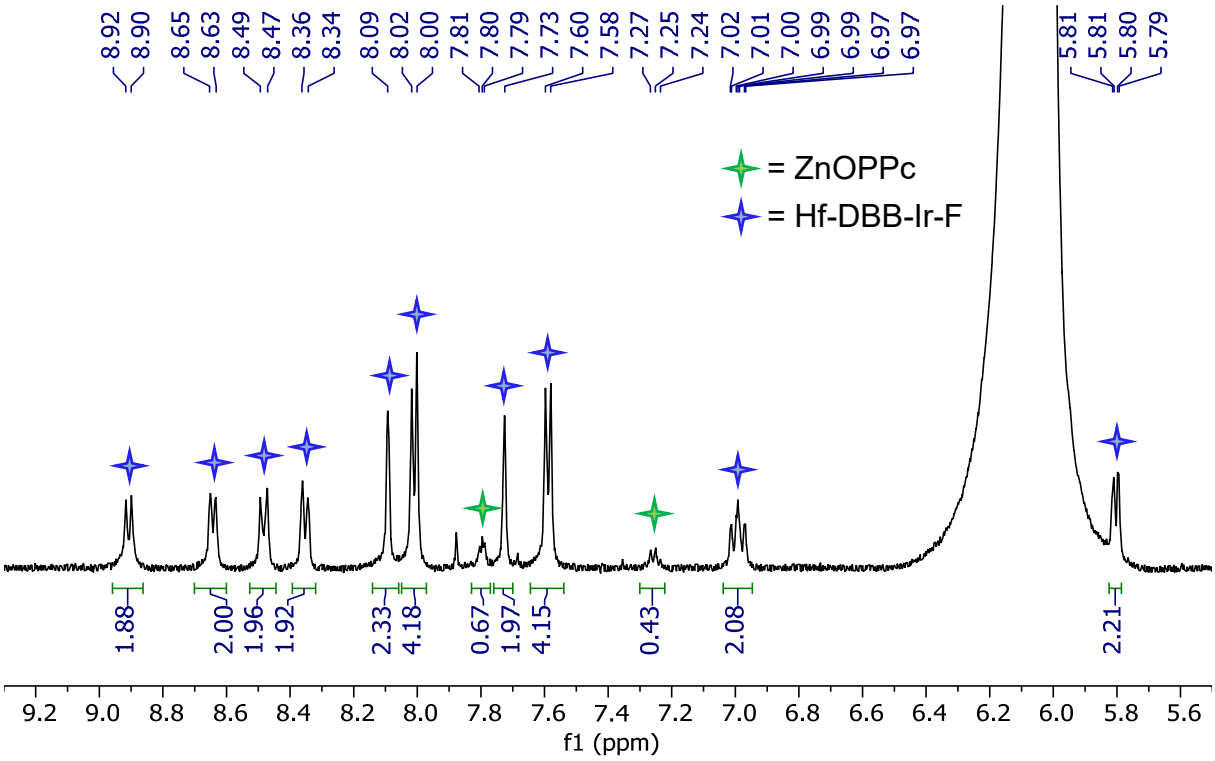

Figure 2-25. ^{1}H NMR spectrum of digested ZnOPPc@nMOL (500 MHz, DMSO-d_6).

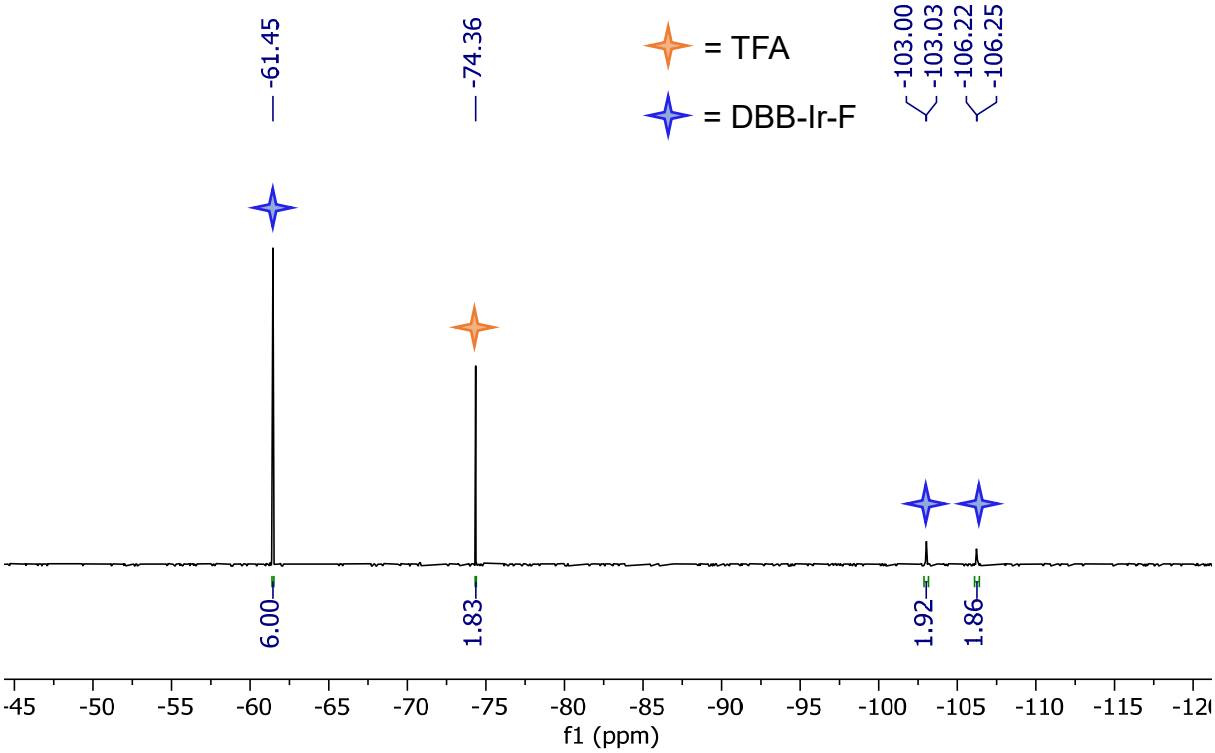

Figure 2-26. ^{19}F NMR spectrum of digested ZnOPPc@nMOL (377 MHz, DMSO-d_6).

Synthesis of ZnOPPc@nMOL. To a 4 mL glass vial was added 0.5 mL of Hf_{12}-Ir nMOL solution (3.6 mM in ethanol based on Hf), 1.0 mL of ZnOPPc solution (0.6 mg/mL in DMF) and a stir bar. The mixture was stirred at room temperature overnight, collected by centrifugation and washed twice with ethanol.

ZnOPPc@MOL loading. The weight % loading of ZnOPPc on ZnOPPc@nMOL was calculated to be 14.9% based on two methods. The first method employed UV-Vis spectroscopy to determine the ZnOPPc concentration (295.49 μM) based on the characteristic absorption peak at 700 nm and ICP-MS to determine the Hf concentration (3.265 mM) to give a weight % loading of 14.9%. The second method used UV-Vis spectroscopy to determine the ZnOPPc concentration (295.49 μM) and the DBB-Ir-F ligand concentration (1.578 mM) based on the characteristic absorption peak at 350 nm to give a weight % loading of 15.2%. To determine the DBB-Ir-F ligand concentration, the ZnOPPc concentration was first calculated based on the peak at 700 nm and then that concentration was used to determine the ZnOPPc absorption at 350 nm, which was subsequently subtracted from the absolute value to give the absorption at 350 nm arising from the DBB-Ir-F ligand.

2.4.3. *In vitro* procedures

Test tube singlet oxygen detection. The time-dependent $^1O_2$ generation of Hf_{12}-Ir nMOL, ZnOPPc, and ZnOPPc@nMOL was detected by Singlet Oxygen Sensor Green (SOSG, Life Technologies, USA) assay upon light irradiation. Hf_{12}-Ir nMOL, ZnOPPc, and ZnOPPc@nMOL suspensions were prepared with an equivalent dose of 0.3 μM ZnOPPc and 234 μM DBB-Ir-F (based on the ratio for ZnOPPc@nMOL) in 0.1X PBS. To 2 mL of each of these suspensions, an

SOSG stock solution (5 μL at 5 mM) was added (final SOSG concentration = 12.5 μM) before fluorescence measurements. The mixed solution was exposed to an LED light (700 nm, 100 mW/cm^2) for 0, 10, 20, 30, 60, 120, 180, 300, 420 and 600 seconds and the fluorescence intensity at different time points was measured by a fluorimeter.

Cellular uptake. The cellular uptake of ZnOPPc, ZnOPPc@nMOL, and Hf_{12}-Ir nMOL was evaluated on MC38 cells. The cells were seeded on 6-well plates at a density of 2.5×10^5/ml in 2 mL DMEM medium followed by overnight culture. First, ZnOPPc and ZnOPPc@nMOL were added to each well to reach an equivalent ZnOPPc concentration of 10 μM in medium (n = 3) and the plates were shaken at 150 rpm for 1 min. The cells were put back into the 37 ℃ incubator and incubated for 1, 2, 4, and 8 hours. At each time point, the medium was removed, the cells were washed with DPBS three times, trypsinized and collected by centrifugation and counted by a hemocytometer. The cell pellets were digested with DMSO and 10% H_3PO_4 in 1.5 ml Eppendorf tubes for 48 hours with strong vortex and sonication every 12 hours and the ZnOPPc concentration was determined by UV-Vis absorbance at 700 nm (ε_{700} = 343,600 M^{-1} cm^{-1}). With nMOL delivery, the cellular uptake of ZnOPPc was enhanced more than 10 times. Then the uptake of ZnOPPc@nMOL and Hf_{12}-Ir nMOL was measured in the same way at an equivalent DBB-Ir-F concentration of 53.3 μM except the digestion step where the cell pellets were treated with 99% concentrated HNO_3 (67-70% trace metal grade) and 1% HF in 1.5 ml Eppendorf tubes for 48 hours with strong vortex and sonication every 12 hours. The Hf concentration was determined by ICP-MS and two nMOLs showed similar uptake results. In addition, the relative cellular uptake was also confirmed by flow cytometry after 8-hour incubation of MC38 cells with ZnOPPc@nMOL and Hf_{12}-Ir nMOL. The fluorescence intensity of DBB-Ir-F ligands was monitored by BV711

channel. The relative mean fluorescence intensity (MFI) was qualitatively consistent with ICP-MS results above.

Cell viability assay. The light (denoted as (+)) and dark (denoted as (-)) cytotoxicity of ZnOPPc, ZnOPPc@nMOL, and Hf_{12}-Ir nMOL was evaluated on MC38 cells with 3-(4,5-dimethylthiazol-2-yl)-5-(3-carboxymethoxyphenyl)-2-(4-sulfo-phenyl)-2H-tetrazolium (MTS) assay (Promega, USA, 1/10 dilution in DMEM). The cells were first seeded on 96-well plates at a density of 15000 cells/mL with 100 μL DMEM medium per well and further cultured overnight. ZnOPPc or ZnOPPc@nMOL was added to the wells at an equivalent ZnOPPc concentration of 0, 0.005, 0.01, 0.02, 0.05, 0.1, 0.2, 0.5, 1, 2, 5 and 10 μM and incubated for 8 hours (n = 6), followed by light irradiation (700 nm, 100 mW/cm^2, 15 min, 90 J/cm^2 as total dose). Hf_{12}-Ir nMOL was added to the wells at an equivalent DBB-Ir-F concentration of 0, 0.027, 0.053, 0.11, 0.27, 0.53, 1.1, 2.7, 5.3, 10.7, 26.7, 53.3 μM, followed by the same treatment as above. During light irradiation, a water jacket was placed above the plate to avoid heating of the plate by the LED. Then the cells were further incubated for 48 hours before determining the cell viability by MTS assay. IC_{50} value of ZnOPPc@nMOL(+) was determined as 0.112 ± 0.001 μM by fitting the dose response curves in Origin Lab. As for ZnOPPc(+), no significant toxicity was found until 10 μM. No obvious toxicity was observed for ZnOPPc(-), ZnOPPc@nMOL(-), Hf_{12}-Ir nMOL(+), or Hf_{12}-Ir nMOL(-).

Cell viability and morphology. To further validate the biosafety of nMOLs, we observed cell proliferation and morphology by IncuCyte S3. HEK293T, MC38, and CT26 cells were first seeded in 6-well plate with a density of 1×10^5 cells/mL and cultured overnight. Then ZnOPPc@nMOL or Hf_{12}-Ir nMOL was added at an equivalent ZnOPPc concentration of 10 μM (or DBB-Ir-F

concentration of 53.3 μM) and further incubated for 8 hours. The cells were washed with DPBS three times, to remove excess nMOLs, and trypsinized to obtain a single cell suspension. The cells were then counted and reseeded in 24-well plate at a density of 1×10^4 cells / mL and the plate was put in IncuCyte S3 for 4 consecutive days. The phase images were acquired, and confluence was analyzed by IncuCyte 2020B software.

Apoptotic cell death. The apoptosis after PDT treatment was evaluated by flow cytometry and CLSM. For flow cytometry analysis, on two 6-well plates, MC38 cells were seeded at a density of 2.5×10^5 cells/ml with DMEM medium and cultured overnight. The cells on both plates were treated with ZnOPPc, ZnOPPc@nMOL, or Hf_{12}-Ir nMOL at an equivalent ZnOPPc concentration of 10 μM (or DBB-Ir-F concentration of 53.3 μM) and further incubated for 8 hours. Then one of the plates was irradiated with LED light (700 nm, 100 mW/cm^2) for 10 min. The cells on both plates were washed with cold DPBS, exchanged with warm fresh medium and further incubated for another 24 hours. The cells were then trypsinized and stained with Alexa Fluor 488 Annexin V/dead cell apoptosis kit (1:20 dilution in 1x binding buffer) and propidium iodide (PI, 1 μg/mL, 15 min on ice; Thermo Fisher Scientific, USA) following the vendor's protocol for flow cytometry analysis. For CLSM analysis, inside 35 mm glass bottom dishes, MC38 cells were seeded at a density of 1×10^5 cells/mL with DMEM medium and cultured overnight. Then the treatment and staining were the same with flow cytometry except adding a counterstain step of Hoechst-33342 3 μg/mL 5 min at room temperature. The dishes were then added with 1 mL 1x binding buffer and observed under Leica SP8 microscope immediately.

***In vitro* singlet oxygen generation.** The singlet oxygen generation of ZnOPPc, ZnOPPc@nMOL, or Hf_{12}-Ir nMOL after PDT treatment was evaluated on MC38 cells by CLSM. Inside 35 mm glass bottom dishes, MC38 cells were seeded at a density of 1×10^5 cells/mL with 2 mL DMEM medium and cultured overnight. Then ZnOPPc, ZnOPPc@nMOL, and Hf_{12}-Ir nMOL were added at an equivalent ZnOPPc concentration of 10 μM (or DBB-Ir-F concentration of 53.3 μM) and further incubated for 8 hours. The cells were washed with DPBS for three times to remove excess ligands or nMOLs and exchanged with fresh DMEM medium. To each well, 2 μL SOSG stock (5 mM in methanol according to the vendor's protocol) was added and the cells were further incubated and stained for 1 hour. The cells were then irradiated with LED light (700 nm, 100 mW/cm^2) for 10 min, washed with DPBS three times, added to warm fresh medium and immediately mounted for confocal imaging using a Leica SP8 microscope.

CRT expression. Immunogenic cell death was investigated, using flow cytometry and CLSM, by Calreticulin (CRT) expression level after PDT treatment. For flow cytometry analysis, MC38 cells were seeded on two 6-well plates at a density of 2.5×10^5 cells/mL with 2 mL DMEM medium and cultured overnight. The cells were treated with ZnOPPc, ZnOPPc@nMOL, or Hf_{12}-Ir nMOL at an equivalent ZnOPPc concentration of 10 μM (or DBB-Ir-F concentration of 53.3 μM) and further incubated for 8 hours. Then one of the plates was irradiated with LED light (700 nm, 100 mW/cm^2) for 10 min. The cells on both plates were washed with DPBS to remove excess ligands or nMOLs, exchanged with warm fresh medium and further incubated for another 24 hours. The medium was then discarded, and cells were washed with DPBS and trypsinized to obtain cell suspension. The cells were stained with anti-Calreticulin Alexa Fluor 488 (NOVUS; 1:150 dilution in 1% BSA DPBS solution) on ice for 30 min, washed with PBS once and resuspended in FACS buffer (1%

BSA, 2 mM EDTA and 0.05% NaN_3 in DPBS) for flow cytometry analysis. As for CLSM analysis, the PDT treatment procedure was the same with flow cytometry except MC38 cells were seeded with a coverslip in each well with a cell density diluted to 1×10^5 cells/mL. At 24 hours after treatment, the cells were fixed with -20 ℃ methanol for 5 min, blocked with 3% BSA and 1% FBS at RT for 1h, and then stained with anti-Calreticulin Alexa Fluor 488 (NOVUS) (1:150 dilution in 1% BSA DPBS solution) at RT for 1h. The cells were washed with DPBS and counterstained with Hoechst (3 μg/mL 5 min RT), and the coverslips were mounted on glass slides with 50% glycerol in DPBS and sealed for confocal imaging under Leica SP8 microscope.

Time dependent mitochondria colocalization. By CLSM, time-dependent mitochondria uptake of nMOLs was investigated on MC38 cells. The cells were seeded in 6-well plates with a coverslip in each well at a density of 1×10^5 cells/mL with 2 mL DMEM medium and cultured overnight. ZnOPPc@nMOL or Hf_{12}-Ir nMOL at an equivalent DBB-Ir-F concentration of 53.3 μM were added to each well and further incubated for 15 minutes, 30 minutes, 1 hour and 2 hours. At each time point, the cells were washed once with cold DPBS and exchanged with warm medium containing 100 nM MitoTracker Red CMXROS (Thermo Fisher Scientific, USA). The cells were incubated with MitoTracker for 15 minutes at 37 ℃, and then the medium was exchanged with fresh warm medium and further incubated for 5 minutes. The cells were washed by cold DPBS twice and fixed with 3.7% paraformaldehyde (PFA) in DPBS (pH = 7.0) for 5 min at 37 ℃. The cells were then washed by cold DPBS three times and mounted on coverslips with 50% glycerol in DPBS for CLMS imaging under Leica SP8 microscope. The red channel showed mitochondria and the cyan channel showed fluorescence signals from DBB-Ir-F. The Pearson's coefficients R and overlapping coefficients M1&M2 were calculated by JACoP plugin in ImageJ.[53] Scatter plots

were generated by Colocalization Finder plugin in ImageJ (the particles obviously out of cells were manually excluded from analysis).

Mitochondria isolation and mitochondria uptake of nMOLs. MC38 cells were seeded on 6-well plates at a density of 2.5×10^5 cells/mL with 2 mL DMEM medium and cultured overnight. The cells were treated with ZnOPPc@nMOL, Hf_{12}-Ir nMOL or Hf-DBP (negatively charged nMOF with similar morphology as a negative control) at an equivalent Hf concentration of 20 μM and further incubated for 1 hour or 4 hours. At each time point, the medium was removed, the cells were washed with DPBS three times, trypsinized and collected by centrifugation, and counted by a hemocytometer. The total cellular uptake was obtained by direct digestion of cell pellets by 99% HNO_3 and 1% HF for 48 hours and Hf contents were measured by ICP-MS. The mitochondria fraction was isolated by mitochondria isolation kit for cultured cells (Thermo Fisher Scientific, USA). The isolated mitochondria pellets were digested by 99% HNO_3 and 1% HF for 48 hours and Hf contents were measured by ICP-MS. The mitochondria uptake percentage of nMOLs were calculated by mitochondria Hf / total Hf (assuming the yield of mitochondria isolation was 100%).

Cytochrome c release. MC38 cells were seeded on two 6-well plates at a density of 2.5×10^5 cells/mL with 2 mL DMEM medium and cultured overnight. The cells were treated with ZnOPPc, ZnOPPc@nMOL, or Hf_{12}-Ir nMOL at an equivalent ZnOPPc concentration of 10 μM (or DBB-Ir-F concentration of 53.3 μM) and further incubated for 8 hours. Then one of the plates was irradiated with LED light (700 nm, 100 mW/cm^2) for 10 min. The cells on both plates were washed with DPBS to remove excess ligands or nMOLs, exchanged with warm fresh medium and further incubated for another 8 hours. The cells were then exchanged with warm medium containing 100

nM MitoTracker Red CMXROS and were incubated for 15 minutes at 37 ℃, and then the medium was exchanged with fresh warm medium and further incubated for 5 minutes. The cells were washed by cold DPBS twice and fixed with 3.7% PFA in DPBS (pH=7.0) for 15 min at 37 ℃. The cells were then washed by cold DPBS three times, blocked and permeabilized by 3% BSA + 1% BSA + 0.3% Triton-X in DPBS at RT for 1 hour. The cells were then incubated with FITC-conjugated cytochrome c antibody (Thermo Fisher Scientific, USA) 1:150 in 1% BSA + 0.3% Triton-X in DPBS at 4℃ for 8 hours. The cells were washed with cold DPBS three times, mounted on coverslips with 50% glycerol in DPBS and observed under a Leica SP8 microscope. The Pearson's coefficients R and scatter plots were generated by Colocalization Finder plugin in ImageJ.

Depolarization of mitochondria membrane potential. The depolarization of mitochondria membrane potential after PDT treatment was evaluated on MC38 cells by JC-1 assay (Abcam). Inside 35 mm glass bottom dishes, MC38 cells were seeded at a density of 1×10^5 cells/mL with 2 mL DMEM medium and cultured overnight. Then ZnOPPc, ZnOPPc@nMOL, or Hf_{12}-Ir nMOL was added at an equivalent ZnOPPc concentration of 10 μM (or DBB-Ir-F concentration of 53.3 μM) and further incubated for 8 hours. The cells were washed by DPBS twice, to remove excess ligands or nMOLs, and exchanged with fresh DMEM medium. The cells were then irradiated with LED light (700 nm, 100 mW/cm^2) for 10 min, exchanged with warm medium containing 10 μM JC-1 and further incubated for 15 min. The JC-1 containing medium was aspirated and exchanged with warm fresh medium and the cells were incubated for additional 5 min. The cells were washed twice with cold DPBS, added with warm fresh medium and immediately observed under a Leica SP8 microscope.

Caspase-3 and Bcl-2 regulation. MC38 cells were seeded on two 6-well plates at a density of 4×10^5 cells /mL with 2 mL DMEM medium and cultured overnight. The cells were treated with PBS, ZnOPPc, ZnOPPc@nMOL, or Hf_{12}-Ir nMOL at an equivalent ZnOPPc concentration of 10 μM (or DBB-Ir-F concentration of 53.3 μM) and further incubated for 4 hours. The excess particles were washed away with cold DPBS and the cells were exchanged with warm fresh medium. Both plates were irradiated with LED light (700 nm, 100 mW/cm^2) for 2.5 min except for the well with PBS(-). After 1, 2, 4, 8 hours, the cells were washed with DPBS three times and collected with a scratcher and centrifugation. Cell pellets were digested by RIPA lysis buffer (Pierce, Thermo Fisher) on ice for 15 min. The suspension was then collected by centrifugation (15000 RCF) at 4 °C and protein concentrations of the supernatants were measured and normalized by BCA assay. The supernatant was mixed with 4X SDS sample loading buffer and heated to 95 °C for 5 min. 15 μg of samples were loaded on NuPAGE™ 4 to 12%, Bis-Tris gel for electrophoresis (200 V, 50 min) and electrotransfer to PVDF membrane (200 mA, 90 min) by wet tank method. The membrane was blocked by 5% BSA at RT for 1 hour and incubated with 1:1000 mouse Bcl-2 antibody (Thermo Fisher), rabbit caspase-3 antibody (Cell Signaling Technology) and mouse α-tubulin antibody (Cell Signaling Technology) at 4 °C overnight. The membrane was then washed with TBST (TBS with 0.05% Tween-20) three times and incubated with anti-mouse HRP and anti-rabbit HRP secondary antibodies at RT for 1 hour. Followed by 3 washes of TBST, Pierce ECL plus reagent mix was added to the membrane. Approximately 5 min later, the membrane was scanned by Bio-Rad ChemiDoc XRS+ Gel Imaging System and the grey value was quantified by ImageJ.

We observed that caspase-3 was downregulated in the first 4 hours and upregulated afterward. We hypothesized that the phenomenon was caused by cleavage of caspase-3 to the active form after ROS damage from strong PDT effects.[54] The rapid loss of mitochondria potential and cytochrome c dislocation could also lead caspase-3 cleavage and downregulation, which is consistent with our experimental observations of JC-1 assay and cytochrome c staining.[55-56] The hemostasis between pro-caspase-3 and caspase-3 drove the upregulation of caspase-3 at 8h. For Bcl-2, no obvious signals or changes were observed, which is consistent with low levels of intrinsic Bcl-2 in MC38 cells in the literature.[57-58]

2.4.4. *In vivo* procedures

***In vivo* anticancer efficacy.** To evaluate the *in vivo* PDT efficacy of ZnOPPc@nMOL, MC38 tumor bearing C57Bl/6 mouse model was established by inoculating 5×10^6 cells/mice subcutaneously at day 0. After 7 days, 25 mice with tumor volumes between 100 mm^3 and 175 mm^3 were randomized for PDT treatment. ZnOPPc, Hf_{12}-Ir nMOL, or ZnOPPc@nMOL was injected intravenously with equivalent ZnOPPc dose of 0.1 μmol (or DBB-Ir-F dose of 0.53 μmol) (n = 5). Control group was treated with PBS (n = 5). After 12 hours, the mice were anaesthetized with 2.5% (V/V) isoflurane/O_2 and only the tumor area was irradiated with LED light (700 nm, 100 mW/cm^2, 15 min). Tumor sizes were measured by an electronic caliper (tumor volume = length × $width^2$ / 2) and body weight was monitored. At day 24, the mice were sacrificed, and the tumors were weighed and frozen sectioned for H&E, TUNEL and CRT staining. Major organs were sectioned for H&E staining. CT26 tumor bearing BALB/c mouse model was established by inoculating 2×10^6 cells/mouse subcutaneously at day 0. All subsequent treatments were the same as MC38 except that all groups received light irradiation. At day 22, the mice were sacrificed, and

the tumors were weighed and photographed. Tumor growth inhibition (TGI) is defined as (1-[Te/Ts]/[Ce/Cs])/(1-[Cs/Ce]) x 100%, where Te, Ts, Ce, and Cs represent average tumor volumes of treated mice at endpoint, treated mice at starting-point, control mice at endpoint and control mice at starting-point, respectively.

***In vivo* immunogenic cell death.** To evaluate the *in vivo* immunogenic cell death after PDT treatment, tumors were sectioned and stained with anti-CRT-AlexFluor488 antibody and TUNEL assay. The frozen tumor sections were hydrated and fixed with 4% PFA solution at 37 °C for 15 min. For CRT staining, the tumor slides were directly blocked with 3% BSA and 1% FBS DPBS solution for 2 hours and then stained with anti-Calreticulin Alexa Fluor 488 (1:100 in 1% BSA DPBS solution) at 4 °C overnight. The slides were then counterstained with Hoechst 33324 (1:3000 in DPBS), washed and mounted for CLSM imaging. For TUNEL assay, the tumor slides were permeabilized with 0.25% Triton-X in DPBS, treated with proteinase K and blocked with 3% BSA and 0.1% Triton X-100 for 2 hours. To each slide was added 100 μL TUNEL-Mix and then the slides were incubated at 37 °C for 1 h in a dark and humid environment. The slides were then washed and stained with Alexa Fluor 488 dye-labeled anti-BrdU antibody for 1 hour at room temperature. The slides were counterstained with PI and RNase, washed and mounted for CLSM imaging.

2.5 References

1. Agostinis, P.; Berg, K.; Cengel, K. A.; Foster, T. H.; Girotti, A. W.; Gollnick, S. O.; Hahn, S. M.; Hamblin, M. R.; Juzeniene, A.; Kessel, D.; Korbelik, M.; Moan, J.; Mroz, P.; Nowis, D.; Piette, J.; Wilson, B. C.; Golab, J., Photodynamic therapy of cancer: An update. *CA: A Cancer Journal for Clinicians* **2011,** *61* (4), 250-281.

2. Dolmans, D. E. J. G. J.; Fukumura, D.; Jain, R. K., Photodynamic therapy for cancer. *Nature Reviews Cancer* **2003,** *3* (5), 380-387.

3. Huang, Z.; Xu, H.; Meyers, A. D.; Musani, A. I.; Wang, L.; Tagg, R.; Barqawi, A. B.; Chen, Y. K., Photodynamic therapy for treatment of solid tumors—potential and technical challenges. *Technology in cancer research & treatment* **2008,** *7* (4), 309-320.

4. Lovell, J. F.; Liu, T. W. B.; Chen, J.; Zheng, G., Activatable Photosensitizers for Imaging and Therapy. *Chemical Reviews* **2010,** *110* (5), 2839-2857.

5. Luby, B. M.; Walsh, C. D.; Zheng, G., Advanced Photosensitizer Activation Strategies for Smarter Photodynamic Therapy Beacons. *Angewandte Chemie International Edition* **2019,** *58* (9), 2558-2569.

6. Lucky, S. S.; Soo, K. C.; Zhang, Y., Nanoparticles in Photodynamic Therapy. *Chemical Reviews* **2015,** *115* (4), 1990-2042.

7. Mallidi, S.; Anbil, S.; Bulin, A.-L.; Obaid, G.; Ichikawa, M.; Hasan, T., Beyond the Barriers of Light Penetration: Strategies, Perspectives and Possibilities for Photodynamic Therapy. *Theranostics* **2016,** *6* (13), 2458-2487.

8. O'Connor, A. E.; Gallagher, W. M.; Byrne, A. T., Porphyrin and Nonporphyrin Photosensitizers in Oncology: Preclinical and Clinical Advances in Photodynamic Therapy. *Photochemistry and Photobiology* **2009,** *85* (5), 1053-1074.

9. Detty, M. R.; Gibson, S. L.; Wagner, S. J., Current Clinical and Preclinical Photosensitizers for Use in Photodynamic Therapy. *Journal of Medicinal Chemistry* **2004,** *47* (16), 3897-3915.

10. Nyokong, T., Effects of substituents on the photochemical and photophysical properties of main group metal phthalocyanines. *Coordination Chemistry Reviews* **2007,** *251* (13), 1707-1722.

11. Lo, P.-C.; Rodríguez-Morgade, M. S.; Pandey, R. K.; Ng, D. K. P.; Torres, T.; Dumoulin, F., The unique features and promises of phthalocyanines as advanced photosensitisers for photodynamic therapy of cancer. *Chemical Society Reviews* **2020,** *49* (4), 1041-1056.

12. Baron, E. D.; Malbasa, C. L.; Santo-Domingo, D.; Fu, P.; Miller, J. D.; Hanneman, K. K.; Hsia, A. H.; Oleinick, N. L.; Colussi, V. C.; Cooper, K. D., Silicon phthalocyanine (pc 4) photodynamic therapy is a safe modality for cutaneous neoplasms: results of a phase 1 clinical trial. *Lasers in Surgery and Medicine* **2010,** *42* (10), 888-895.

13. Dumoulin, F.; Durmuş, M.; Ahsen, V.; Nyokong, T., Synthetic pathways to water-soluble phthalocyanines and close analogs. *Coordination Chemistry Reviews* **2010,** *254* (23), 2792-2847.

14. Lu, K.; He, C.; Guo, N.; Chan, C.; Ni, K.; Weichselbaum, R. R.; Lin, W., Chlorin-Based Nanoscale Metal–Organic Framework Systemically Rejects Colorectal Cancers via Synergistic Photodynamic Therapy and Checkpoint Blockade Immunotherapy. *Journal of the American Chemical Society* **2016,** *138* (38), 12502-12510.

15. Lu, K.; He, C.; Guo, N.; Chan, C.; Ni, K.; Lan, G.; Tang, H.; Pelizzari, C.; Fu, Y.-X.; Spiotto, M. T.; Weichselbaum, R. R.; Lin, W., Low-dose X-ray radiotherapy–radiodynamic therapy via

nanoscale metal–organic frameworks enhances checkpoint blockade immunotherapy. *Nature Biomedical Engineering* **2018,** *2* (8), 600-610.

16. Zhang, Y.; Wang, F.; Liu, C.; Wang, Z.; Kang, L.; Huang, Y.; Dong, K.; Ren, J.; Qu, X., Nanozyme Decorated Metal–Organic Frameworks for Enhanced Photodynamic Therapy. *ACS Nano* **2018,** *12* (1), 651-661.

17. McKinlay, A. C.; Morris, R. E.; Horcajada, P.; Férey, G.; Gref, R.; Couvreur, P.; Serre, C., BioMOFs: Metal–Organic Frameworks for Biological and Medical Applications. *Angewandte Chemie International Edition* **2010,** *49* (36), 6260-6266.

18. Lu, K.; He, C.; Lin, W., Nanoscale Metal–Organic Framework for Highly Effective Photodynamic Therapy of Resistant Head and Neck Cancer. *Journal of the American Chemical Society* **2014,** *136* (48), 16712-16715.

19. Furukawa, H.; Cordova, K. E.; O'Keeffe, M.; Yaghi, O. M., The Chemistry and Applications of Metal-Organic Frameworks. *Science* **2013,** *341* (6149), 1230444.

20. Long, J. R.; Yaghi, O. M., The pervasive chemistry of metal–organic frameworks. *Chemical Society Reviews* **2009,** *38* (5), 1213-1214.

21. Lan, G.; Ni, K.; Veroneau, S. S.; Feng, X.; Nash, G. T.; Luo, T.; Xu, Z.; Lin, W., Titanium-Based Nanoscale Metal–Organic Framework for Type I Photodynamic Therapy. *Journal of the American Chemical Society* **2019,** *141* (10), 4204-4208.

22. Lu, K.; Aung, T.; Guo, N.; Weichselbaum, R.; Lin, W., Nanoscale Metal–Organic Frameworks for Therapeutic, Imaging, and Sensing Applications. *Advanced Materials* **2018,** *30* (37), 1707634.

23. Lismont, M.; Dreesen, L.; Wuttke, S., Metal-Organic Framework Nanoparticles in Photodynamic Therapy: Current Status and Perspectives. *Advanced Functional Materials* **2017,** *27* (14), 1606314.

24. Lan, G.; Ni, K.; Lin, W., Nanoscale metal–organic frameworks for phototherapy of cancer. *Coordination Chemistry Reviews* **2019,** *379*, 65-81.

25. Luo, T.; Fan, Y.; Mao, J.; Yuan, E.; You, E.; Xu, Z.; Lin, W., Dimensional Reduction Enhances Photodynamic Therapy of Metal–Organic Nanophotosensitizers. *Journal of the American Chemical Society* **2022,** *144* (12), 5241-5246.

26. Lan, G.; Ni, K.; Veroneau, S. S.; Song, Y.; Lin, W., Nanoscale Metal–Organic Layers for Radiotherapy–Radiodynamic Therapy. *Journal of the American Chemical Society* **2018,** *140* (49), 16971-16975.

27. Lan, G.; Ni, K.; Veroneau, S. S.; Luo, T.; You, E.; Lin, W., Nanoscale Metal–Organic Framework Hierarchically Combines High-Z Components for Multifarious Radio-Enhancement. *Journal of the American Chemical Society* **2019,** *141* (17), 6859-6863.

28. Orrenius, S., Reactive Oxygen Species in Mitochondria-Mediated Cell Death. *Drug Metabolism Reviews* **2007,** *39* (2-3), 443-455.

29. Green, D. R.; Reed, J. C., Mitochondria and Apoptosis. *Science* **1998,** *281* (5381), 1309-1312.

30. Neupert, W.; Herrmann, J. M., Translocation of Proteins into Mitochondria. *Annual Review of Biochemistry* **2007,** *76* (1), 723-749.

31. Ni, K.; Lan, G.; Veroneau, S. S.; Duan, X.; Song, Y.; Lin, W., Nanoscale metal-organic frameworks for mitochondria-targeted radiotherapy-radiodynamic therapy. *Nature Communications* **2018,** *9* (1), 4321.

32. Cao, R.; Jia, J.; Ma, X.; Zhou, M.; Fei, H., Membrane Localized Iridium(III) Complex Induces Endoplasmic Reticulum Stress and Mitochondria-Mediated Apoptosis in Human Cancer Cells. *Journal of Medicinal Chemistry* **2013,** *56* (9), 3636-3644.

33. Poynton, F. E.; Bright, S. A.; Blasco, S.; Williams, D. C.; Kelly, J. M.; Gunnlaugsson, T., The development of ruthenium(ii) polypyridyl complexes and conjugates for in vitro cellular and in vivo applications. *Chemical Society Reviews* **2017,** *46* (24), 7706-7756.

34. Gao, Z.; Li, Y.; Zhang, Y.; Cheng, k.; An, P.; Chen, F.; Chen, J.; You, C.; Zhu, Q.; Sun, B., Biomimetic Platinum Nanozyme Immobilized on 2D Metal–Organic Frameworks for Mitochondrion-Targeting and Oxygen Self-Supply Photodynamic Therapy. *ACS Applied Materials & Interfaces* **2020,** *12* (2), 1963-1972.

35. Liu, C.; Liu, B.; Zhao, J.; Di, Z.; Chen, D.; Gu, Z.; Li, L.; Zhao, Y., Nd3+-Sensitized Upconversion Metal–Organic Frameworks for Mitochondria-Targeted Amplified Photodynamic Therapy. *Angewandte Chemie International Edition* **2020,** *59* (7), 2634-2638.

36. Wei, S.; Zhou, J.; Huang, D.; Wang, X.; Zhang, B.; Shen, J., Synthesis and Type I/Type II photosensitizing properties of a novel amphiphilic zinc phthalocyanine. *Dyes and Pigments* **2006,** *71* (1), 61-67.

37. Çamur, M.; Durmuş, M.; Bulut, M., Highly singlet oxygen generative water-soluble coumarin substituted zinc(II) phthalocyanine photosensitizers for photodynamic therapy. *Polyhedron* **2012,** *41* (1), 92-103.

38. Yousif, L. F.; Stewart, K. M.; Kelley, S. O., Targeting Mitochondria with Organelle-Specific Compounds: Strategies and Applications. *ChemBioChem* **2009,** *10* (13), 2131-2131.

39. Lan, G.; Ni, K.; You, E.; Wang, M.; Culbert, A.; Jiang, X.; Lin, W., Multifunctional Nanoscale Metal–Organic Layers for Ratiometric pH and Oxygen Sensing. *Journal of the American Chemical Society* **2019,** *141* (48), 18964-18969.

40. Murphy, M. P.; Smith, R. A. J., Drug delivery to mitochondria: the key to mitochondrial medicine. *Advanced Drug Delivery Reviews* **2000,** *41* (2), 235-250.

41. Weissig, V.; Boddapati, S. V.; Jabr, L.; D'Souza, G. G., Mitochondria-specific nanotechnology. *Nanomedicine* **2007,** *2* (3), 275-285.

42. Wongrakpanich, A.; Geary, S. M.; Joiner, M.-l. A.; Anderson, M. E.; Salem, A. K., Mitochondria-targeting particles. *Nanomedicine* **2014,** *9* (16), 2531-2543.

43. Ogunsipe, A.; Chen, J.-Y.; Nyokong, T., Photophysical and photochemical studies of zinc(ii) phthalocyanine derivatives—effects of substituents and solvents. *New Journal of Chemistry* **2004,** *28* (7), 822-827.

44. Lan, G.; Ni, K.; Xu, Z.; Veroneau, S. S.; Song, Y.; Lin, W., Nanoscale Metal–Organic Framework Overcomes Hypoxia for Photodynamic Therapy Primed Cancer Immunotherapy. *Journal of the American Chemical Society* **2018,** *140* (17), 5670-5673.

45. Goff, B. A.; Bachor, R.; Kollias, N.; Hasan, T., Effects of photodynamic therapy with topical application of 5-aminolevulinic acid on normal skin of hairless guinea pigs. *Journal of Photochemistry and Photobiology B Biology* **1992,** *15* (3), 239-251.

46. Wolf, P.; Rieger, E.; Kerl, H., Topical photodynamic therapy with endogenous porphyrins after application of 5-aminolevulinic acid: An alternative treatment modality for solar keratoses, superficial squamous cell carcinomas, and basal cell carcinomas? *Journal of the American Academy of Dermatology* **1993,** *28* (1), 17-21.

47. Menter, J. M.; Hollins, T. D.; Sayre, R. M.; Etemadi, A. A.; Willis, I.; Hughes, S. N. G., Protection against photodynamic therapy (PDT)-induced photosensitivity by fabric materials. *Photodermatology, Photoimmunology & Photomedicine* **1998,** *14* (5-6), 154-159.

48. Mack, J.; Stillman, M. J., Band deconvolution analysis of the absorption and magnetic circular dichroism spectral data of ZnPc (-2) recorded at cryogenic temperatures. *Journal of Physical Chemistry* **1995,** *99* (20), 7935-7945.

49. Ricciardi, G.; Rosa, A.; Baerends, E. J., Ground and Excited States of Zinc Phthalocyanine Studied by Density Functional Methods. *Journal of Physical Chemistry A* **2001,** *105* (21), 5242-5254.

50. Quan, Y.; Lan, G.; Fan, Y.; Shi, W.; You, E.; Lin, W., Metal–Organic Layers for Synergistic Lewis Acid and Photoredox Catalysis. *Journal of the American Chemical Society* **2020,** *142* (4), 1746-1751.

51. Eu, S.; Katoh, T.; Umeyama, T.; Matano, Y.; Imahori, H., Synthesis of sterically hindered phthalocyanines and their applications to dye-sensitized solar cells. *Dalton Transactions* **2008,** (40), 5476-5483.

52. Zhu, Y.-Y.; Lan, G.; Fan, Y.; Veroneau, S. S.; Song, Y.; Micheroni, D.; Lin, W., Merging Photoredox and Organometallic Catalysts in a Metal–Organic Framework Significantly Boosts Photocatalytic Activities. *Angewandte Chemie International Edition* **2018,** *57* (43), 14090-14094.

53. Bolte, S.; CordeliÈRes, F. P., A guided tour into subcellular colocalization analysis in light microscopy. *Journal of Microscopy* **2006,** *224* (3), 213-232.

54. Mroz, P.; Yaroslavsky, A.; Kharkwal, G. B.; Hamblin, M. R., Cell death pathways in photodynamic therapy of cancer. *Cancers* **2011,** *3* (2), 2516-39.

55. Garrido, C.; Galluzzi, L.; Brunet, M.; Puig, P. E.; Didelot, C.; Kroemer, G., Mechanisms of cytochrome c release from mitochondria. *Cell Death & Differentiation* **2006,** *13* (9), 1423-1433.

56. Slee, E. A.; Harte, M. T.; Kluck, R. M.; Wolf, B. B.; Casiano, C. A.; Newmeyer, D. D.; Wang, H.-G.; Reed, J. C.; Nicholson, D. W.; Alnemri, E. S.; Green, D. R.; Martin, S. J., Ordering the Cytochrome c–initiated Caspase Cascade: Hierarchical Activation of Caspases-2, -3, -6, -7, -8, and -10 in a Caspase-9–dependent Manner. *Journal of Cell Biology* **1999,** *144* (2), 281-292.

57. Christiansen, A. J.; West, A.; Banks, K. M.; Haynes, N. M.; Teng, M. W.; Smyth, M. J.; Johnstone, R. W., Eradication of solid tumors using histone deacetylase inhibitors combined with immune-stimulating antibodies. *Proceedings of the National Academy of Sciences of the United States of America* **2011,** *108* (10), 4141-6.

58. Feng, D.; Qin, B.; Pal, K.; Sun, L.; Dutta, S.; Dong, H.; Liu, X.; Mukhopadhyay, D.; Huang, S.; Sinicrope, F. A., BRAF(V600E)-induced, tumor intrinsic PD-L1 can regulate chemotherapy-induced apoptosis in human colon cancer cells and in tumor xenografts. *Oncogene* **2019,** *38* (41), 6752-6766.

Chapter 3: Nanoscale Metal–Organic Framework Confines Zinc-Phthalocyanine Photosensitizers for Enhanced Photodynamic Therapy

3.1 Introduction

Photodynamic therapy (PDT) is an efficient anticancer modality that destroys a malignant tumor while sparing surrounding normal tissues by localizing a photosensitizer (PS) in the tumor and irradiating the tumor with visible or near-infrared light to produce cytotoxic reactive oxygen species (ROS).[1-4] The clinical utility of PDT is limited by tissue penetration of light, localization of the PS in the tumor, and the solubility and photophysical properties of the PS.[5-6] For example, clinically tested porphyrin-based PSs often cause phototoxicity side effects, due to their strong absorption in the visible spectrum and retention in tissue.[7] Phthalocyanine PSs present a promising alternative due to their very strong absorption in the optical therapeutic window, 650−800 nm, and weaker absorption in the 400−600 nm region, allowing for effective treatment of tumors with significantly lower PS doses and reduced phototoxicity.[8] Metalation of phthalocyanines with diamagnetic ions (e.g., Zn^{2+}, Si^{4+}, Al^{3+}) increases triplet state yields and lifetimes to enhance the generation of cytotoxic singlet oxygen ($^1O_2$).[9-11]

Despite their nearly ideal photophysical properties, phthalocyanines have not been widely used for PDT due to their limited synthetic accessibility and their strong tendency to aggregate in biological media.[11] Phthalocyanines have been functionalized with ionic or hydrophilic groups in their peripheral positions to directly improve aqueous solubility or with bulky metal complexes (axial functionalization) to prevent π−π stacking.[12] However, the introduction of ionic or hydrophilic groups to phthalocyanines can adversely impact their cellular uptake, while axial

functionalization of phthalocyanines is limited to a few nontoxic high-valent metals such as Si^{4+} and can be synthetically challenging to both access and scale up.[13-14]

An alternative strategy to address the cellular uptake, tumor accumulation, and aggregation issues of phthalocyanines is through their encapsulation in or conjugation to liposomes, micelles, or other nanoparticles.[15-19] In particular, micelles have been widely investigated as a delivery vehicle for lipophilic conjugated phthalocyanines with superb photophysical properties.[20-21] Nanoscale metal-organic frameworks (nMOFs) have recently provided an excellent strategy to deliver porphyrin, chlorin, bacteriochlorin, and phthalocyanine PSs for PDT.[22-30] With structural tunability, rigidity, and porosity, nMOFs can efficiently load PSs via direct incorporation as bridging ligands, postsynthetic ligand exchange, postsynthetic surface modification, and physical loading into pores.[31-37] These strategies allow isolation or confinement of lipophilic PSs in rigid nMOF structures to reduce aggregation, improve cellular uptake, drive tumor accumulation through the enhanced permeation and retention (EPR) effect, and minimize photosensitivity.[38-42] We hypothesized that nMOFs could also be used to encapsulate phthalocyanines to enhance their PDT efficacy.

In this chapter, we report the design of a Hf-QC nMOF, based on Hf_{12} SBUs and QC bridging ligands (QC = 2″,3′-dinitro-[1,1’:4′,1”;4″,1’”-quaterphenyl]-4,4’”-dicarboxylate), for the delivery of zinc(II)-2,3,9,10,16,17,23,24-octa(4-carboxyphenyl)-phthalocyanine (ZnOPPc) PSs for highly efficient type II PDT (**Figure 3-1**).[43] Postsynthetic loading of ZnOPPc into the pores of the rigid Hf-QC framework afforded ZnOPPc@Hf-QC. The confined PSs in ZnOPPc@Hf-QC efficiently absorbed light, minimized non-radiative energy loss, and prevented aggregation-induced quenching to significantly enhance $^1O_2$ generation and effectively eradicate colorectal cancer in mouse models.

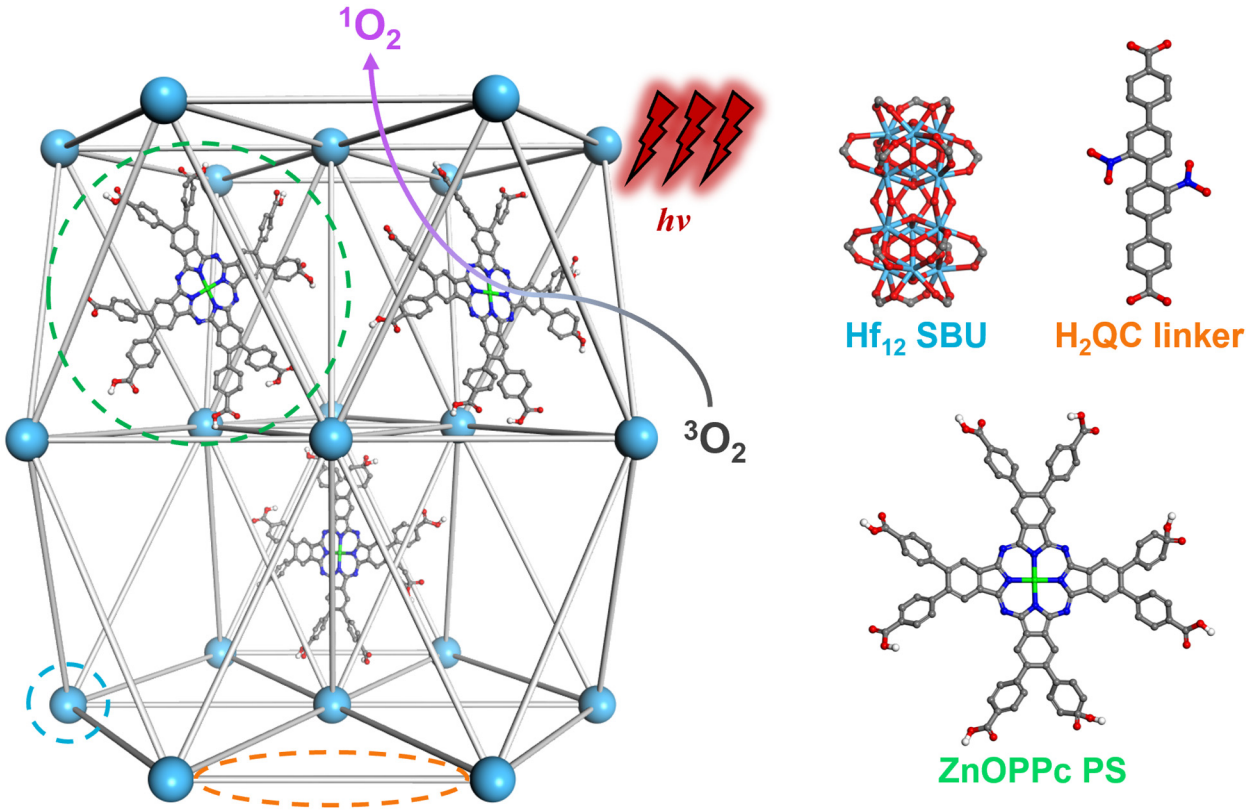

Figure 3-1. Structure of ZnOPPc@Hf-QC. Scheme showing the structure of ZnOPPc@Hf-QC consisting of a 3D framework of Hf_{12} SBUs and QC bridging ligands and ZnOPPc PSs confined in the pores. ZnOPPc@Hf-QC efficiently generates $^1O_2$ upon 700 nm light irradiation. (*hv* = 700 nm photons)

3.2 Results and discussion

3.2.1. Synthesis and characterization

Hf-QC was synthesized through a solvothermal reaction between $HfCl_4$ and H_2QC in a mixture of DMF, acetic acid, and water at 80 °C (**Figure 3-2**). Transmission electron microscopy (TEM) imaging of Hf-QC revealed a hexagonal nanoplate morphology with a diameter of ~150 nm, while atomic force microscopy (AFM) showed the particles possessed an average plate thickness of ~64 nm (**Figure 3-3**). Dynamic light scattering (DLS) particle size analysis of Hf-QC measured a number-averaged size of 167.1 ± 2.9 nm (**Figure 3-4**). Powder X-ray diffraction (PXRD) studies (**Figure 3-4**) revealed that Hf-QC adopted the same **hcp** topology as previously reported Zr_{12}-

QPDC (QPDC = para-quaterphenyldicarboxylate).[44] High-resolution transmission electron microscopy (HR-TEM) imaging of Hf-QC revealed the (010) lattice fringe with a lattice spacing of 2.3 nm and its fast Fourier transform (FFT) pattern displayed 6-fold symmetry (**Figure 3-3**), which is consistent with the structure of Zr_{12}-QPDC. ^{1}H nuclear magnetic resonance (NMR) analysis of digested Hf-QC showed an acetate (OAc) modulator to QC linker ratio of 0.11:1, corresponding to approximately 0.5 missing linkers per SBU (**Figure 3-15**, **Figure 3-16**). Thermogravimetric analysis (TGA) of Hf-QC showed a weight loss of 39.4% in the 300−800 °C region, matching the expected value of 37.9% for the Hf-QC with a 0.5 linker defect per SBU (**Figure 3-4**). Based on these results, Hf-QC was formulated as $Hf_{12}(\mu_3\text{-}O)_8(\mu_3{-}OH)_8(\mu_2{-}OH)_6(QC)_{8.5}(OAc)$.

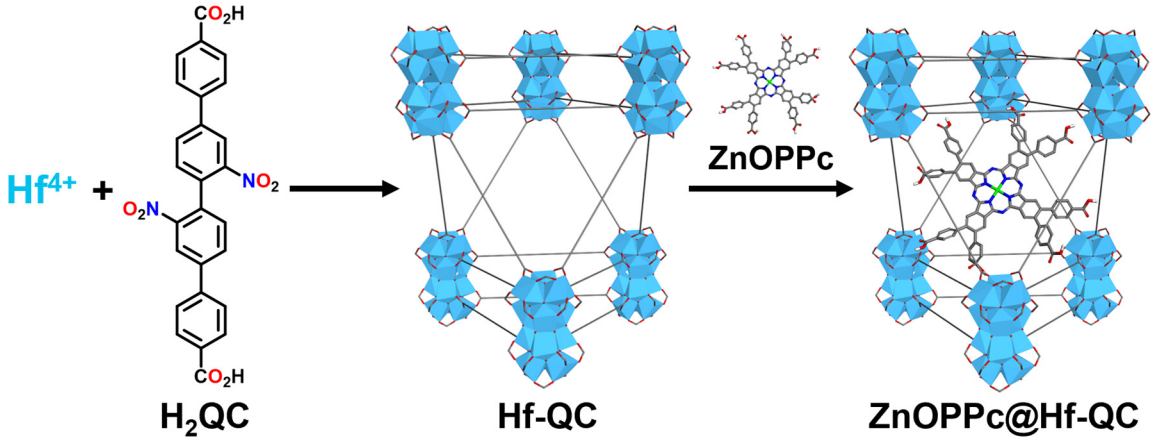

Figure 3-2. Synthesis of Hf-QC and ZnOPPc@Hf-QC.

ZnOPPc@Hf-QC was synthesized by heating a mixture of ZnOPPc and Hf-QC in DMF at 70 °C for 24 h. Successful loading of ZnOPPc was confirmed by the presence of characteristic UV-Vis and infrared (IR) peaks for ZnOPPc (**Figure 3-4**). UV−Vis spectroscopy and inductively coupled plasma-mass spectrometry (ICP-MS) analysis revealed 13.6 wt% loading of ZnOPPc in ZnOPPc@Hf-QC, corresponding to a ZnOPPc to Hf_{12} SBU ratio of 0.68:1. ^{1}H NMR analysis of digested ZnOPPc@Hf-QC showed that the OAc modulator to QC linker ratio was maintained after

ZnOPPc loading (**Figure 3-15**, **Figure 3-16**). TGA of ZnOPPc@Hf-QC showed a weight loss of 36.3% in the 300−800 °C region, which matched well with the expected value of 34.1% for the physical loading of ZnOPPc in the nMOF pores and corroborated the ZnOPPc to Hf ratio (**Figure 3-4**). Based on these results, ZnOPPc@Hf-QC was formulated as $(ZnOPPc)_{0.68}@Hf_{12}(\mu_3\text{-}O)_8(\mu_3\text{-}OH)_8(\mu_2\text{-}OH)_6(QC)_{8.5}(OAc)$.

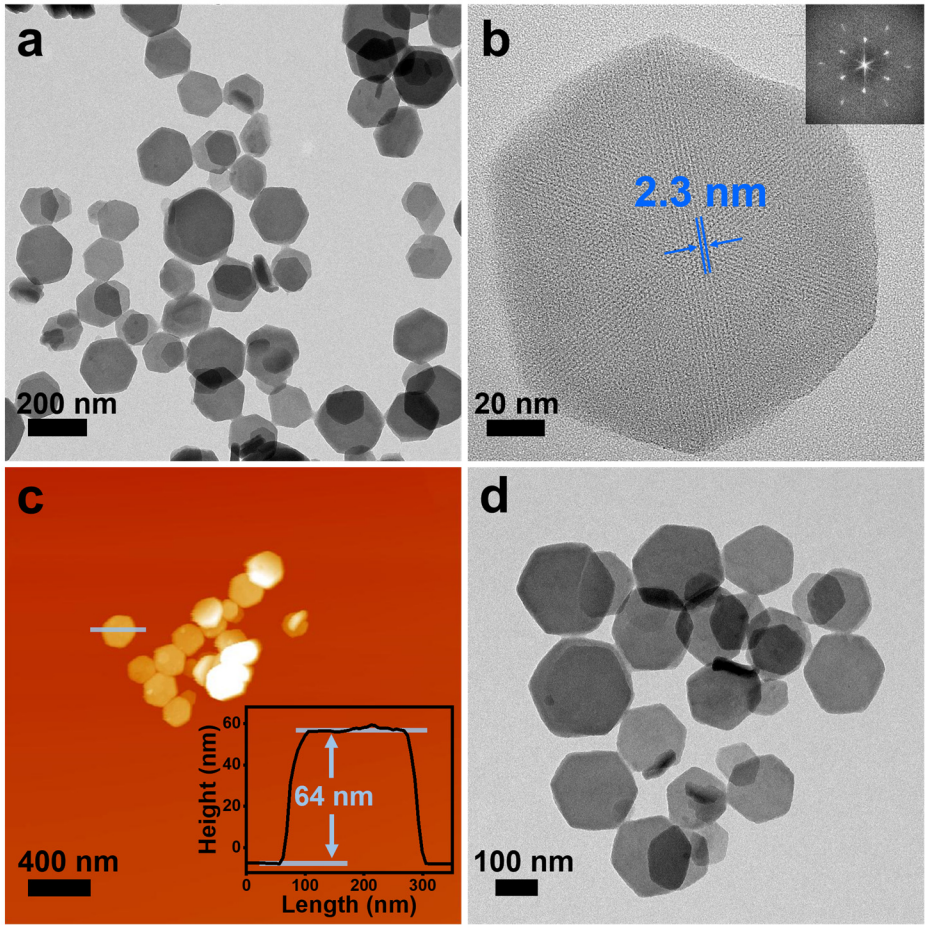

Figure 3-3. Morphological characterization of Hf-QC and ZnOPPc@Hf-QC. (a) TEM image and (b) HR-TEM image with its FFT pattern (inset) of Hf-QC. (c) AFM image and height profile (inset) of Hf-QC. (e) TEM image of ZnOPPc@Hf-QC.

TEM imaging and DLS analysis showed that ZnOPPc@Hf-QC retained the same hexagonal nanoplate morphology and size (175.8 ± 5.6 nm) as Hf-QC (**Figure 3-3**). HR-TEM imaging (**Figure 3-3**) and PXRD analysis (**Figure 3-4**) of ZnOPPc@Hf-QC supported the

retention of the core Hf-QC structure after ZnOPPc loading. ZnOPPc@Hf-QC displayed a relatively unchanged, but slightly more negative zeta (ζ) potential of −24.0 ± 1.5 mV compared to Hf-QC at −22.1 ± 0.7 mV (**Figure 3-4**), consistent with loading partially deprotonated ZnOPPc into the Hf-QC pores. The presence of QC and ZnOPPc was further confirmed by their characteristic UV−Vis absorption peaks and ^{1}H NMR signals in digested ZnOPPc@Hf-QC (**Figure 3-4**, **Figure 3-16**). The stability of ZnOPPc@Hf-QC was demonstrated by PXRD and DLS analyses after incubation in 1X PBS or Dulbecco's Modified Eagle Medium (DMEM) at 37 °C for 24 h (**Figure 3-4**).

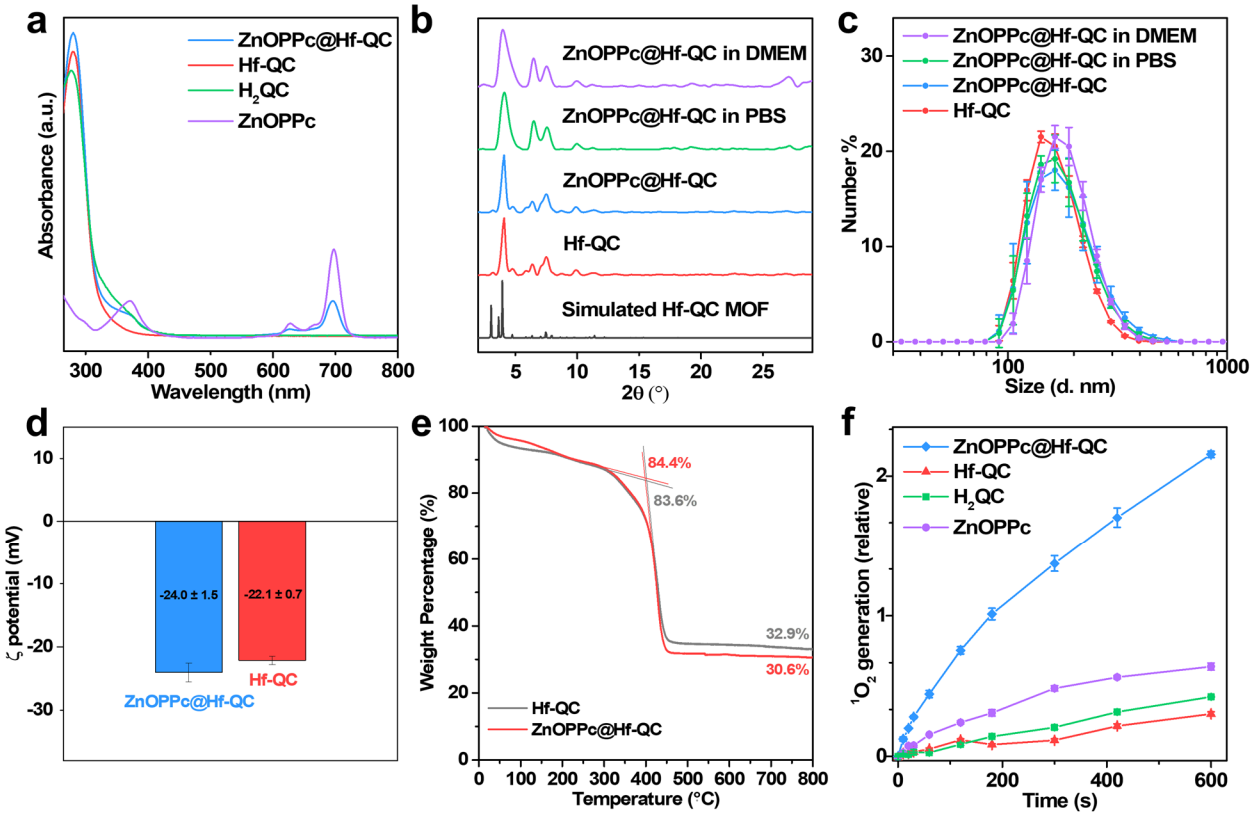

Figure 3-4. Characterization of ZnOPPc@Hf-QC. (a) Relative UV−visible absorption spectra of ZnOPPc, H_2QC, Hf-QC, and ZnOPPc@Hf-QC in DMSO. (b) PXRD patterns of Hf-QC, ZnOPPc@Hf-QC (as synthesized and after soaking in PBS or DMEM for 24 h), and the simulated pattern for the structurally analogous Zr_{12}-QPDC. (c) Number-averaged diameters of Hf-QC and ZnOPPc@Hf-QC (as synthesized and after soaking in PBS or DMEM for 24 h) in ethanol. (d) Zeta potentials of Hf-QC and ZnOPPc@Hf-QC in water. (e) TGA analysis of Hf-QC and ZnOPPc@Hf-QC. (f) $^{1}O_2$ generation of ZnOPPc, H_2QC, Hf-QC, and ZnOPPc@Hf-QC detected by SOSG assay (n = 3).

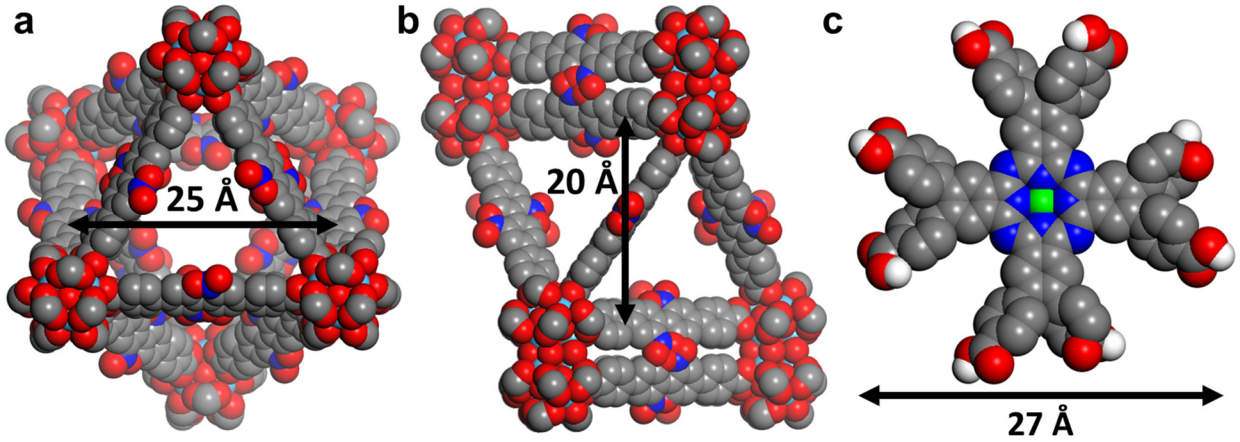

Figure 3-5. Space-filling model of Hf-QC. Model of the octahedral cavity of pristine Hf-QC viewed along the (a) c-axis and (b) a-axis. (c) Space-filling model of ZnOPPc. Because of the defect and the non-closed cage structure of MOF pores, guest molecules larger than the pore diameter can still diffuse through the MOF (particularly at elevated temperatures) and are tightly confined in the pores.

3.2.2. *In vitro* PDT anticancer efficacy

ZnOPPc@Hf-QC showed a much higher cellular uptake than free ZnOPPc and accumulated in endo/lysosomes. Confocal laser scanning microscopy (CLSM) revealed that fluorescence signals of ZnOPPc@Hf-QC began to overlap with endo/lysosomes in CT26 cells after incubation for 12 h (**Figure 3-7**).[45] However, fluorescence signals were barely observed for CT26 cells incubated with free ZnOPPc, due to aggregation-induced quenching in biological media (**Figure 3-7**). Quantification of cellular uptake by UV−Vis spectroscopy showed that ZnOPPc@Hf-QC delivered up to 15-fold more ZnOPPc than free ZnOPPc *in vitro* (**Figure 3-8**).

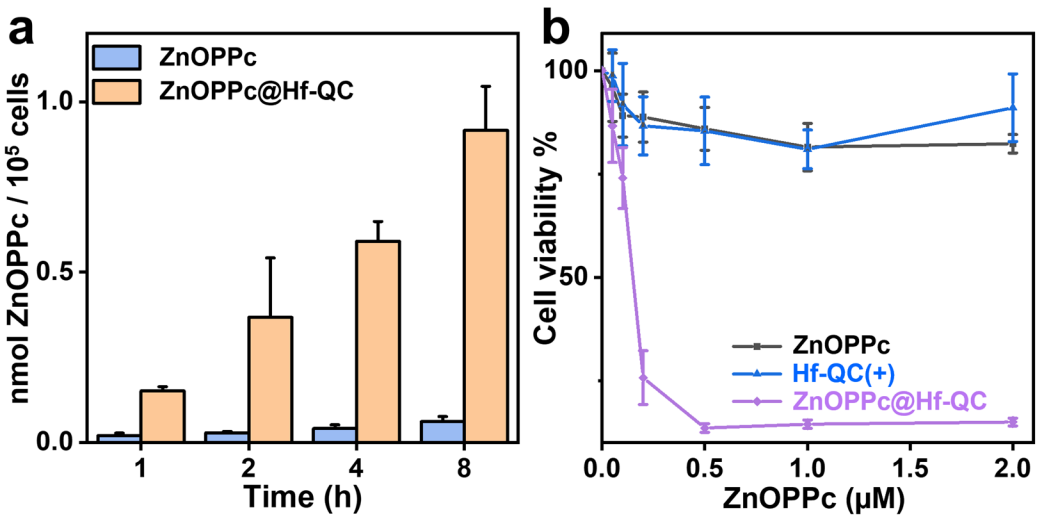

Figure 3-6. *In vitro* anticancer efficacy. (a) Cellular uptake of ZnOPPc and ZnOPPc@Hf-QC measured by UV−Vis spectroscopy (n = 3). (b) Viability of cells treated with ZnOPPc(+), Hf-QC(+), and ZnOPPc@Hf-QC(+) determined by MTS assay. CT26 cells were used for all *in vitro* experiments and a total light dose of 60 J/cm^2 was given.

$^1O_2$ generation by ZnOPPc and ZnOPPc@Hf-QC was determined by Singlet Oxygen Sensor Green (SOSG) assay. ZnOPPc@Hf-QC generated 3.4-fold as much $^1O_2$ as free ZnOPPc (**Figure 3-7**), indicating that the entrapment of ZnOPPc PSs in MOF pores prevented aggregation-induced quenching of ZnOPPc excited states and enhanced $^1O_2$ generation in a type II PDT process. CLSM imaging (**Figure 3-8**) and flow cytometry analysis showed an ROS burst in CT26 cells incubated with ZnOPPc@Hf-QC after light irradiation ("+" denotes light treatment, 100 mW/cm^2, 10 min; "-" denotes no light treatment) by 2′,7′-dichlorodihydrofluorescein diacetate (DCF-DA) assay, confirming the enhanced ROS generation by ZnOPPc@Hf-QC *in vitro*. MTS assays showed that ZnOPPc(+) exhibited minimal toxicity at concentrations up to 2 μM, while ZnOPPc@Hf-QC(+) was highly cytotoxic with an IC_{50} of 0.14 μM (**Figure 3-6**). No obvious toxicity or morphological changes were observed for CT26 cells treated with Hf-QC(-), Hf-QC(+), or ZnOPPc@Hf-QC(-). Live cell imaging confirmed significant growth inhibition of CT26 cells by ZnOPPc@HfQC(+).

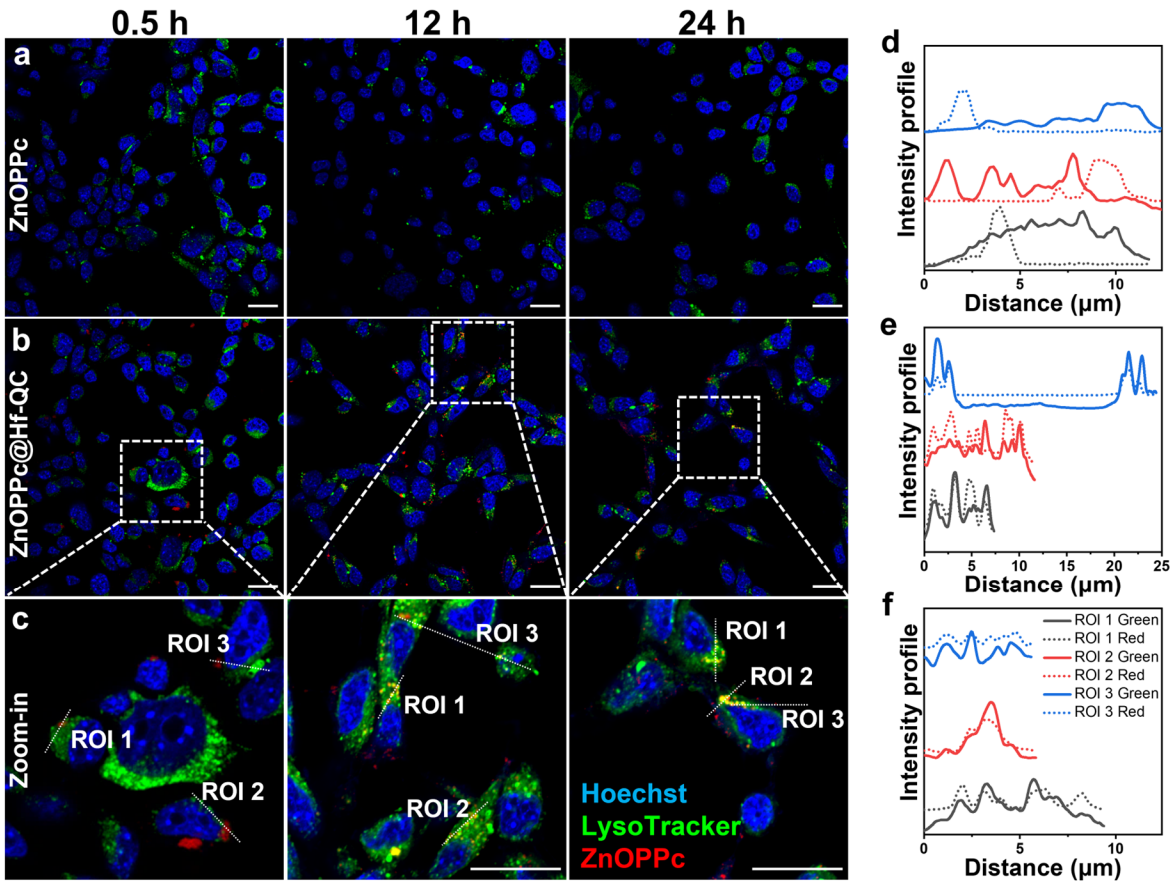

Figure 3-7. Cellular uptake and colocalization analysis. CLSM images showing colocalization of (a) ZnOPPc and (b) ZnOPPc@Hf-QC with endo/lysosomes after incubation with CT26 cells for 0.5, 12, and 24 h (yellow = green + red; scale bars = 20 μm). (c) Zoomed-in regions of ZnOPPc@Hf-QC indicated by dashed squares. (d−f) Colocalization analysis between endo/lysosomes (green) and ZnOPPc (red) in different ROIs (white dashed lines in (c)).

We then examined apoptosis and immunogenic cell death (ICD) of CT26 cells after PDT by CLSM and flow cytometry. CT26 cells treated with ZnOPPc@Hf-QC(+) showed upregulation of phosphatidylserine by Annexin V staining on cell membranes and colocalization of PI and Hoechst 33342 (**Figure 3-8**). These results indicated apoptosis and compromised membrane functions for ZnOPPc@Hf-QC(+) treated CT26 cells, which were absent in control groups. Calreticulin (CRT) staining revealed enhanced ICD and surface translocation of CRT signals in ZnOPPc@Hf-QC(+) group (**Figure 3-8**). Taken together, ZnOPPc@Hf-QC(+) not only killed

cancer cells more effectively but also induced ICD to expose tumor antigens and danger signals for immune activation.[46-47]

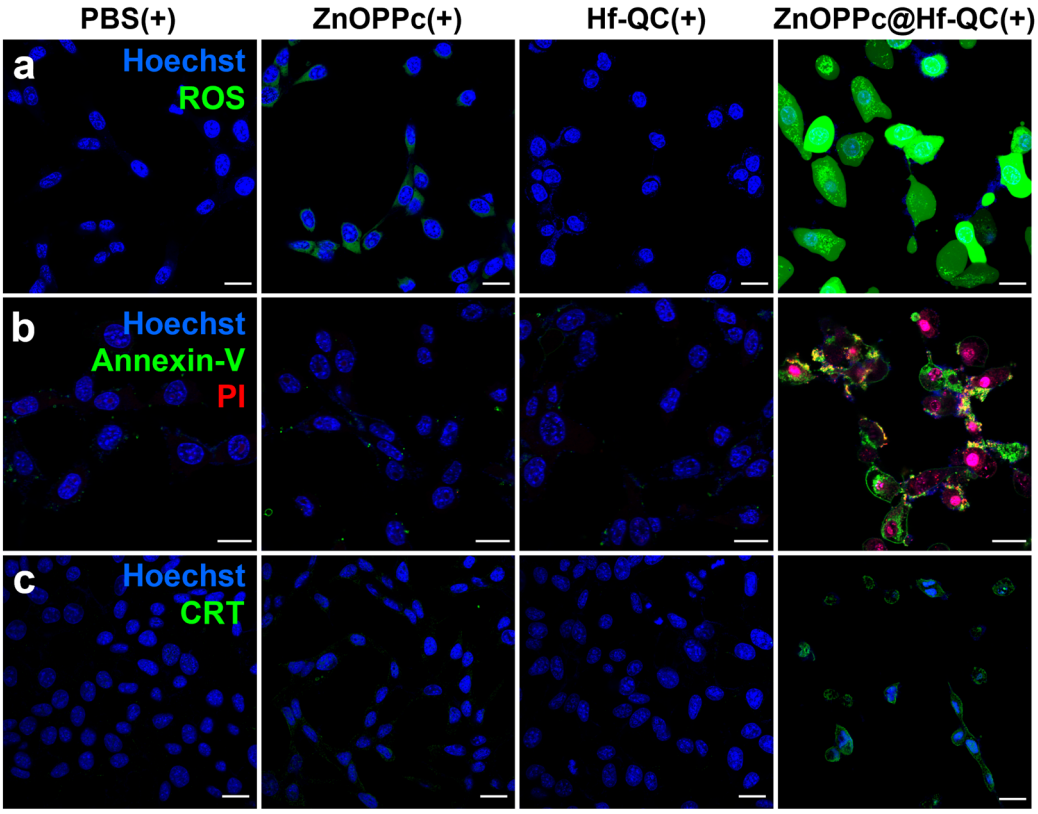

Figure 3-8. *In vitro* PDT-induced $^1O_2$ generation, apoptosis, and immunogenic cell death. (a) Total ROS generation determined by DCF-DA assay (green). (b) Cell apoptosis stained by Alexa Fluor 488 Annexin V (green) and PI (red) (pink = red + blue). (c) CRT translocation stained by Alexa Fluor 488 CRT antibody (green). Cell nuclei were stained by Hoechst 33342 (blue) in (a-c). CT26 cells were used for all *in vitro* experiments and a total light dose of 60 J/cm^2 was given. Scale bars = 20 μm.

3.2.3. *In vivo* PDT anticancer efficacy

We evaluated antitumor efficacy of ZnOPPc@Hf-QC(+) on two subcutaneous murine colon cancer models with CT26 tumors on BALB/c mice and MC38 tumors on C57BL/6 mice. Hf-QC and ZnOPPc@Hf-QC were PEGylated before intravenous administration. The mice were injected with PBS, ZnOPPc, Hf-QC, or ZnOPPc@Hf-QC via tail veins at an equivalent ZnOPPc dose of 50 nmol (equivalent Hf dose of 0.88 μmol). Twelve hours post injection, the mice were

anesthetized, and tumor areas were irradiated with 700 nm LED with a total light dose of 60 J/cm^2 (100 mW/cm^2).

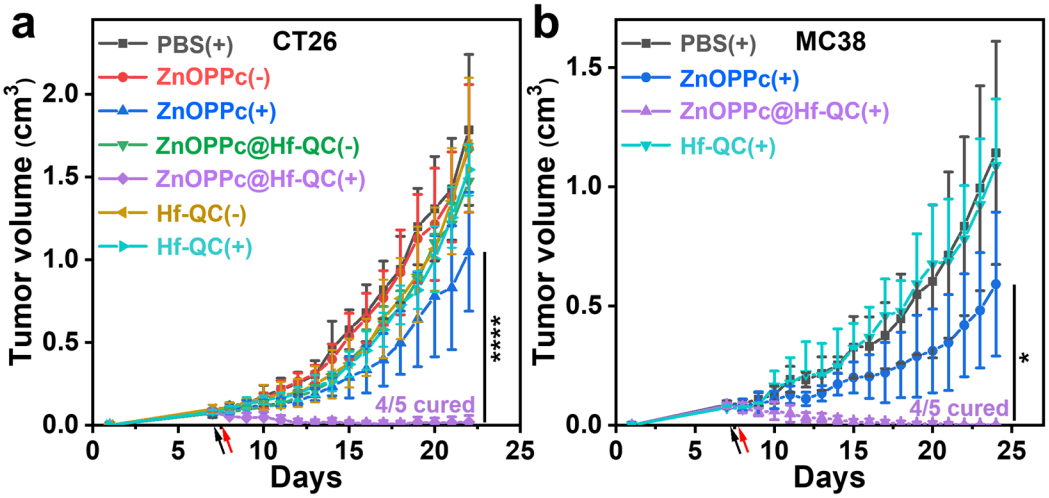

Figure 3-9. *In vivo* anticancer efficacy. Tumor growth curves of subcutaneous (a) CT26 tumor-bearing BALB/c and (b) MC38 tumor-bearing C57BL/6 mouse models (n = 5). *P < 0.05 and ****P < 0.0001 by ANOVA with Tukey's test.

Compared to PBS(+), Hf-QC(+) had little effect on tumor growth with minimal TGIs of 17.8% and 7.4% for CT26 and MC38 tumors, respectively. ZnOPPc(+) moderately slowed tumor growth with TGI values of 41.3% and 41.4% for CT26 and MC38 tumors, respectively. ZnOPPc@Hf-QC(+) treatment showed excellent antitumor efficacy with >99% TGIs and 80% cure rates for both CT26 and MC38 tumors (**Figure 3-9**). H&E and TUNEL staining revealed severe apoptosis/necrosis and infiltration of inflammatory cells in tumor regions in the ZnOPPc@Hf-QC(+) group (**Figure 3-10**).

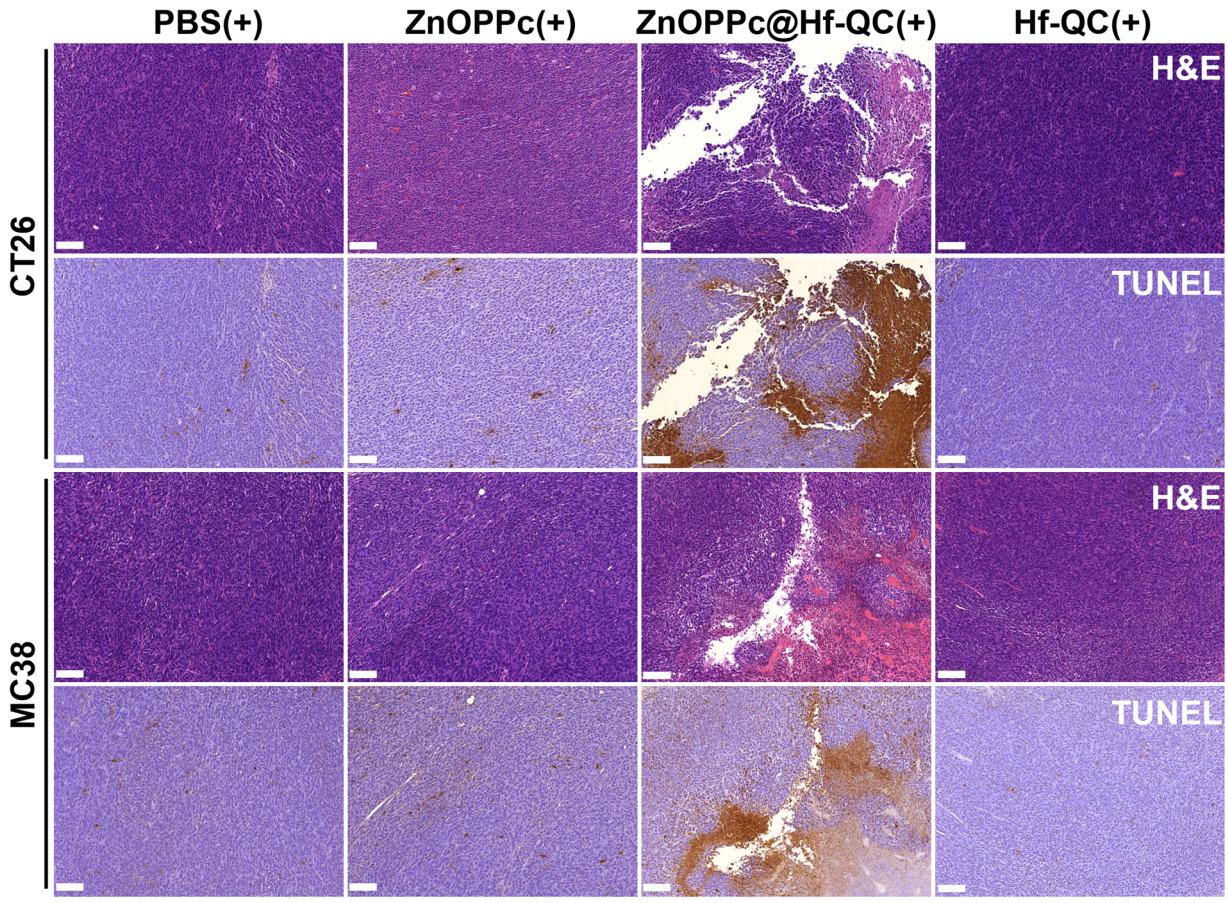

Figure 3-10. *In vivo* PDT-induced necrosis, apoptosis, and immunogenic cell death. Representative images of H&E staining and TUNEL IHC staining of excised CT26 and MC38 tumors. Scale bars = 100 μm.

Several mice in the ZnOPPc(+) and ZnOPPc(−) groups showed weight loss, pulmonary edema, and local liver inflammation (**Figure 3-12**), likely caused by aggregation of ZnOPPc into large particles *in vivo*. In comparison, although ZnOPPc@Hf-QC was observed to accumulate in spleens and livers like other nanoparticles[48-49] by tumor tissue sections (**Figure 3-11**), mice treated with ZnOPPc@Hf-QC – with or without light irradiation – showed steady body weights (**Figure 3-12**). ZnOPPc@Hf-QC and ZnOPPc aggregates were not observed in lungs and minimal abnormalities were observed in the major organs of ZnOPPc@HfQC treated mice compared to PBS control (**Figure 3-11**). The different *in vivo* behaviors between ZnOPPc and ZnOPPc@Hf-QC demonstrated that the nMOF pore loading strategy provides an effective, safe, and

biocompatible approach to deliver PSs with unfavorable solubility and pharmacokinetic properties.

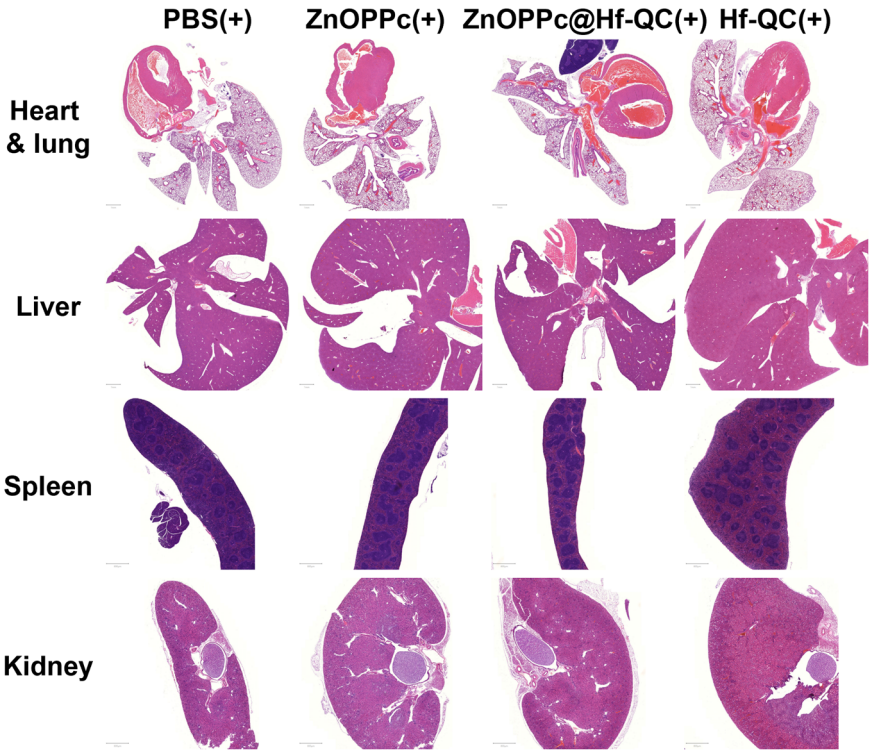

Figure 3-11. H&E staining of major organs. Stained organs are from MC38 tumor-bearing C57BL/6 mice in different treatment groups (scale bars for heart/lung and liver are 1 mm and scale bars for spleen and kidney are 800 μm).

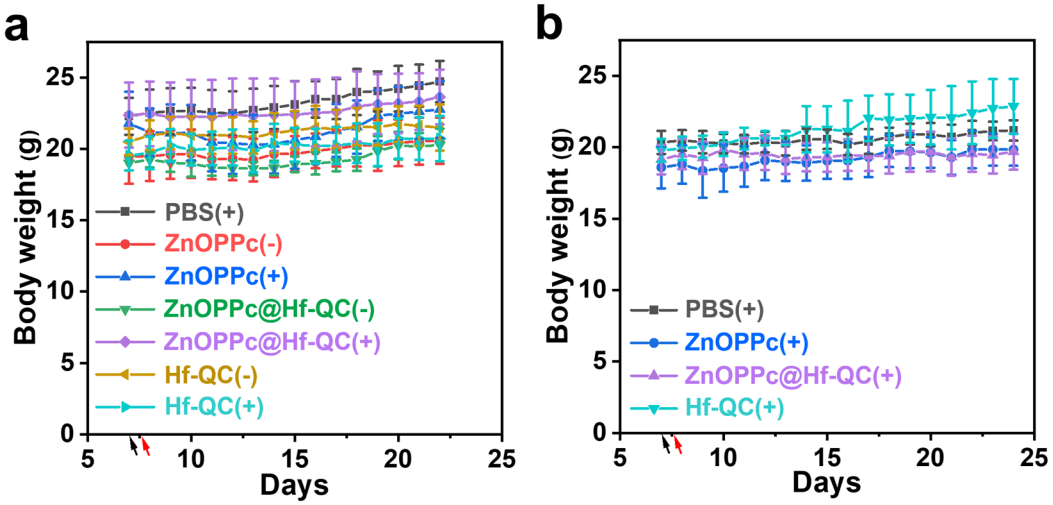

Figure 3-12. Body weight percentage curves. Mouse body weight percentages of (a) CT26 bearing BALB/c mice and (b) MC38 bearing C57BL/6 mice over the treatment period (black arrow: intravenous injection of different treatments; red arrow: PDT treatment).

3.3 Conclusion

In this chapter, we developed an nMOF confinement strategy to isolate ZnOPPc PSs and prevent their aggregation and excited state quenching. As a result, ZnOPPc@Hf-QC mediated PDT effectively eradicated/regressed colorectal cancers in two mouse models. With higher cellular uptake, enhanced ROS generation, and better biocompatibility, ZnOPPc@Hf-QC mediated PDT exhibited an IC_{50} of 0.14 μM and achieved exceptional antitumor efficacy with >99% tumor growth inhibition and 80% cure rates. The confinement of photosensitizers in nMOF pores provides a new strategy to unleash the potential of poorly soluble, highly conjugated PSs in PDT.

3.4 Experimental section

3.4.1. Materials and methods

All chemical reagents were purchased at the highest quality from commercial sources and used without further purification. TEM was performed on a TECNAI Spirit TEM (120 kV), and HR-TEM was performed on a TECNAI Spirit F30 TEM (300 kV). AFM images were taken on a Bruker Multimode 8-HR instrument. PXRD data was collected on a Bruker D8 Venture diffractometer using a Cu Kα radiation source (λ = 1.54178 Å) and processed with PowderX software. UV-Vis spectra were collected using a Shimadzu UV-2600 UV-Vis spectrophotometer. Fourier-transform infrared (FT-IR) spectroscopy data was collected between 400-4000 cm^{-1} on a Thermo Scientific Nicolet iS50 FT-IR spectrophotometer equipped with a built-in diamond attenuated total reflectance (ATR) accessory (for powder samples). Fluorescence emission spectra were obtained using a Shimadzu RF-5301PC spectrofluorophotometer. DLS particle size anaysis and ζ potential measurements were performed on a Malvern Zetasizer Nano ZS instrument. ICP-MS data was collected using an Agilent 7700x ICP-MS and analyzed using an ICP-MS Mass

Hunter version B01.03. Samples were diluted in a 2% HNO_3 matrix and analyzed with ^{159}Tb and internal standards against a 10-point standard curve between 1 ppb and 500 ppb. The correlation was given R>0.999 for all analyses of interest. Data collection was performed in Spectrum Mode with three replicates per sample and 100 sweeps per replicate. ^1H NMR spectra were recorded on a Bruker NMR 400 DRX spectrometer at 400 MHz and referenced to the proton resonance resulting from incomplete deuteration of CDCl3 (δ 7.26) or DMSO-d_6 (δ 2.50). MALDI-TOF HR-MS data was collected on a Bruker Ultraflextreme MALDI-TOF/TOF using negative ion mode. TGA was performed in air using a Shimadzu TGA-50 equipped with an alumina crucible and heated at a rate of 1 °C per min.

Flow cytometry data was collected on an LSR-Fortessa 4-15 (BD Biosciences, USA) and analyzed by FlowJo software (Tree Star, USA). Confocal laser scanning microscope images were collected on a Leica Stellaris 8 laser scanning confocal microscope. CLSM imaging was performed at the University of Chicago Integrated Light Microscopy Facility and analysis was done with LAS X (Leica) and ImageJ software (NIH, USA). Live cell imaging was recorded and analyzed by IncuCyte S3 with standard mode at Cellular Screening Center at the University of Chicago. The histological slides were scanned on a CRi Pannoramic SCAN 40x whole slide scanner by Integrated Light Microscopy Core in the University of Chicago and analyzed with the QuPath-0.2.3 software.[50]

DPBS (-Mg^{2+}, -Ca^{2+}) was purchased from Thermo Fisher Scientific. MTS assay was purchased from Promega (USA). Murine colorectal carcinoma CT26 and MC38 cells were obtained from the American Type Culture Collection (ATCC, Rockville, MD) and were cultured in RPMI-1640 (Corning, USA) (Gibco, USA) or DMEM supported with 10% heat-inactivated fetal bovine serum (56 ℃, 30 min, VWR, USA), 100 U/ml penicillin G sodium and 100 μg/ml

streptomycin sulphate in a humidified atmosphere containing 5% CO_2 at 37 °C. Mycoplasma was tested for all cells before use by MycoAlert detection kit (Lonza Nottingham, Ltd.). C57BL/6 and BALB/c mice (6-8 weeks) were obtained from Charles River Laboratories (USA). The study protocol was reviewed and approved by the Institutional Animal Care and Use Committee (IACUC) at the University of Chicago. The Human Tissue Resource Center at the University of Chicago provided the histology related services for this study.

3.4.2. Synthetic and characterization procedures

Synthesis of ZnOPPc. ZnOPPc was synthesized according to the procedure in chapter 2 and literature report.[43]

HR-MS (MALDI-TOF): *m/z* Calcd. for $C_{88}H_{48}N_8O_{16}Zn^+$ (M^+): 1536.25, Found: 1536.145.

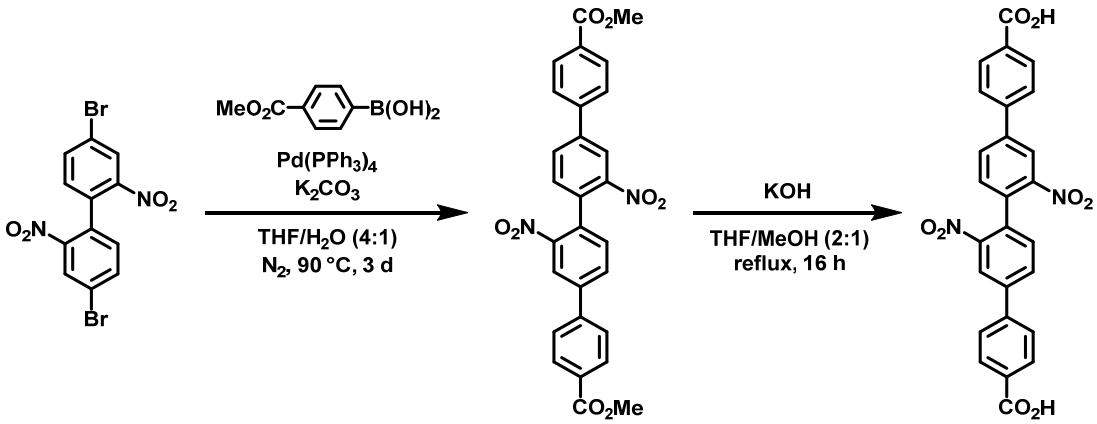

Scheme 3-1. Synthetic route to H_2QC.

Synthesis of Me_2QC. A mixture of $Pd(PPh_3)_4$ (231 mg, 0.2 mmol), K_2CO_3 (1.38 g, 10 mmol), 4,4'-dibromo-2,2'-dinitro-1,1'-biphenyl (804 mg, 2 mmol) and 4-methoxy-carbonylphenylboronic acid (1.08 g, 6 mmol) was dissolved in degassed THF/H_2O (40 mL/10 mL) in a 250 mL Schlenk tube. The resulting mixture was stirred under inert atmosphere at 90 °C for 3

days. The mixture was then cooled to room temperature, filtered, and washed with THF and ether to afford Me_2QC (568 mg, 1.11 mmol, 55% yield).

^{1}H NMR (400 MHz, DMSO-d_6): δ 8.59 (s, 2H), 8.27 (d, 2H), 8.13 (d, 4H), 8.06 (d, 4H), 7.70 (d, 2H), 3.91 (s, 6H).

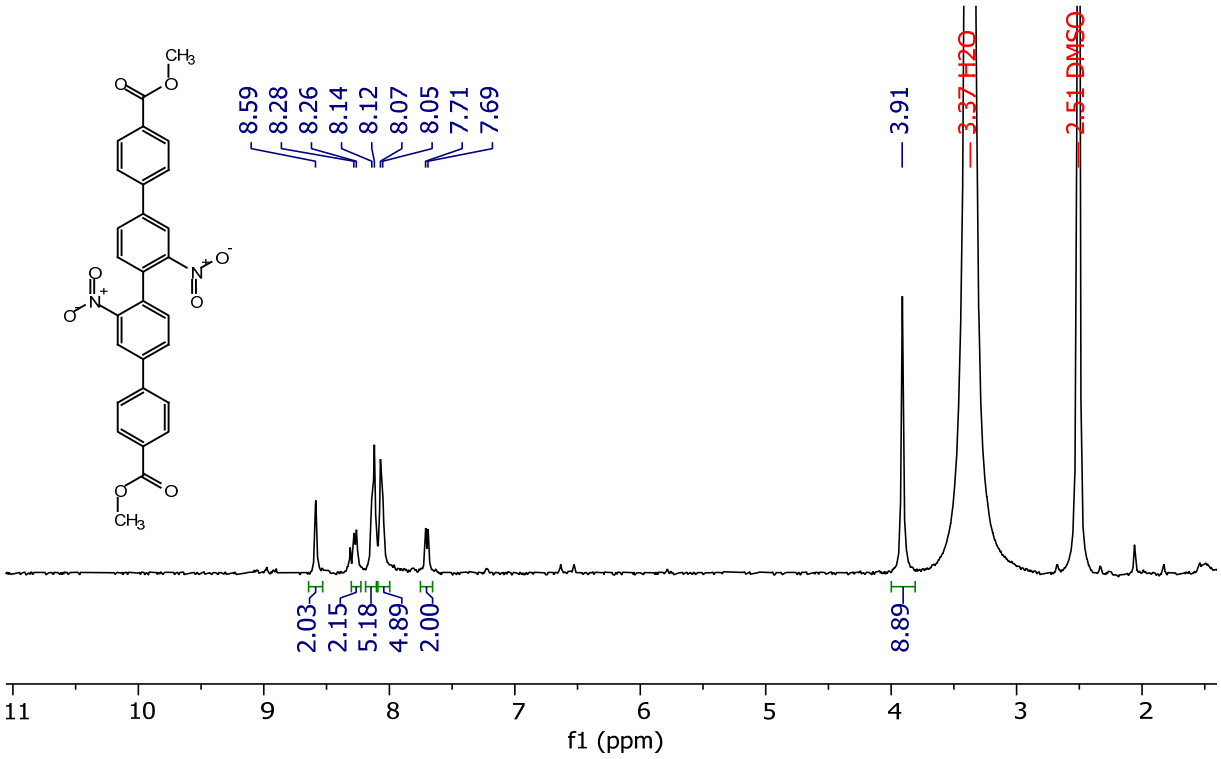

Figure 3-13. ^{1}H NMR spectrum of Me_2QC (400 MHz, DMSO-d_6).

Synthesis of H_2QC. Me_2QC (256 mg, 0.5 mmol) was suspended in 20 mL THF in a 50 mL round-bottomed flask followed by dropwise addition of a KOH/MeOH solution (2.8 g KOH in 10 mL MeOH). After the mixture was stirred at 40 °C for 16 h, 1M HCl (aq.) was slowly added until the solution reached pH = 3. The solid was collected and washed with water, THF, and ether before being dried under vacuum to give the solid (215 mg, 0.444 mmol, 89% yield).

^{1}H NMR (400 MHz, DMSO-d_6): δ 8.57 (s, 2H), 8.27 (d, 2H), 8.11 (d, 4H), 8.02 (d, 4H), 7.69 (d, 2H).

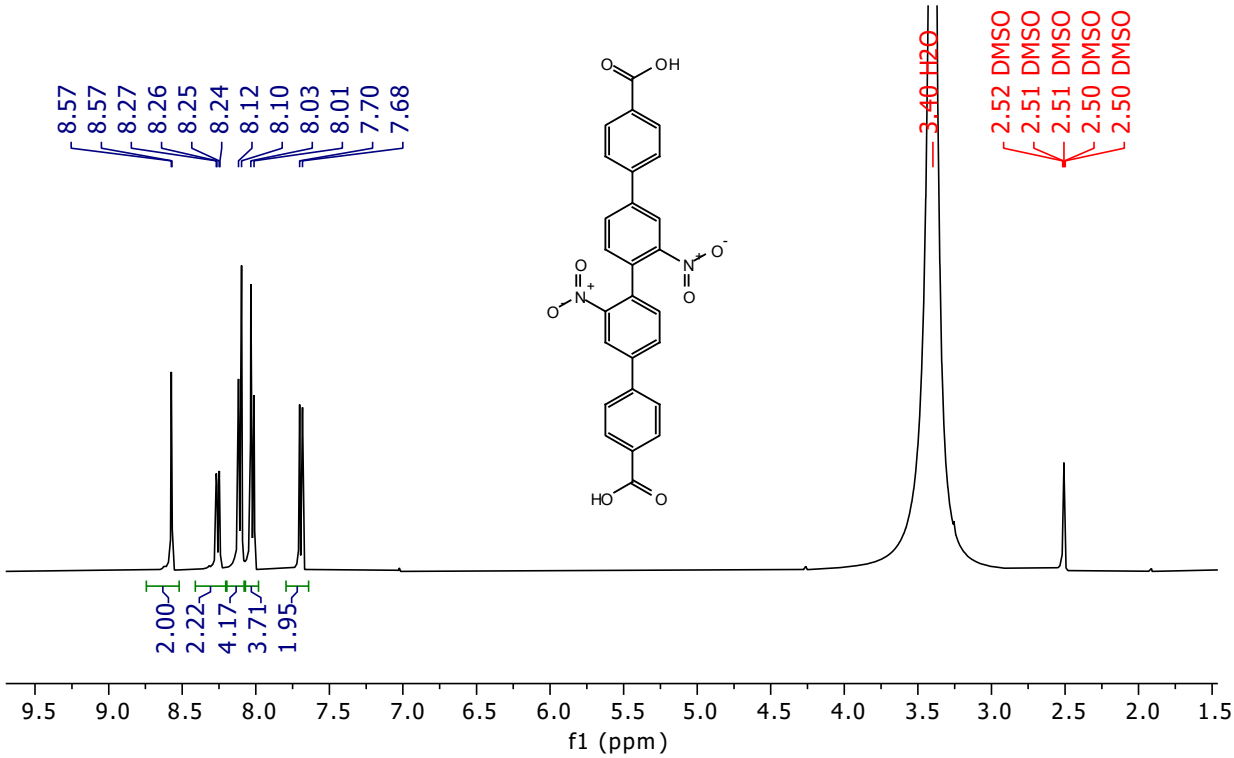

Figure 3-14. ^{1}H NMR spectrum of H_2QC (400 MHz, DMSO-d_6).

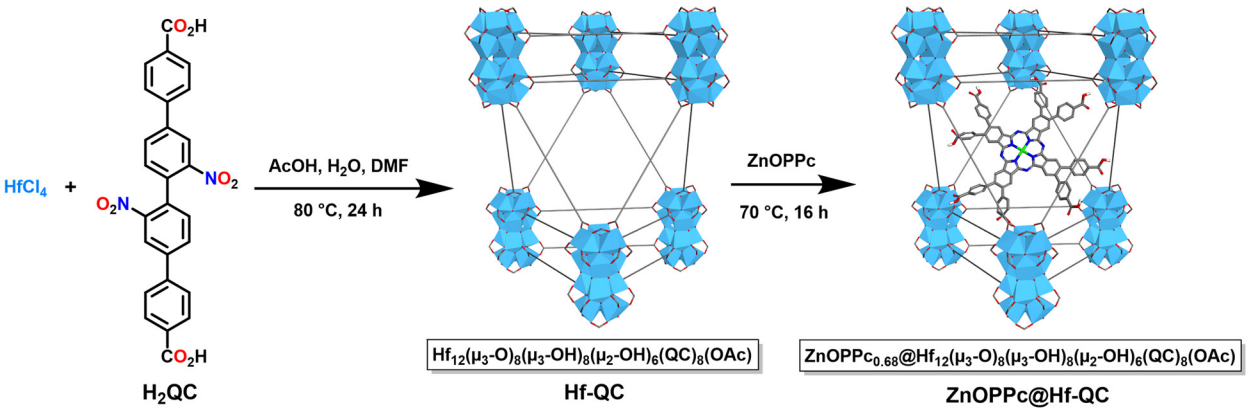

Scheme 3-2. Synthetic route to ZnOPPc@Hf-QC.

Synthesis of Hf-QC. Hf-QC was synthesized as shown in **Scheme 3-2**. To a 4 mL glass vial was added 0.5 mL of $HfCl_4$ solution (2.0 mg/mL in DMF), 0.5 mL of H_2QC solution (3.0 mg/mL in DMF), 75 μL of acetic acid (AcOH) and 5 μL of water. The reaction mixture was kept in an 80 °C

oven for 24 hours. The off-white precipitate was collected by centrifugation and washed with DMF and ethanol.

^{1}H NMR analysis of nMOFs. 1.0 mg nMOF was dried under vacuum. To the dried solid was added a solution of 500 μL DMSO-d_6 and 50 μL D_3PO_4. The mixture was sonicated for 10 min, followed by the addition of 50 μL D_2O just before ^{1}H NMR analysis.

UV-Vis analysis of nMOFs. 10 μL of a dispersed solution of nMOF was added to a mixture of 940 μL DMSO and 50 μL H_3PO_4. The mixture was then sonicated for about 10 minutes and the UV-Vis absorption spectrum was recorded.

ICP-MS analysis of nMOFs. 10 μL of a dispersed solution of nMOF was added to a mixture of 980 μL HNO_3 and 10 μL HF. The mixture was vortexed and kept at room temperature for 3 days. The sample was then diluted with ultrapure water to 2% HNO_3 and analyzed by ICP-MS.

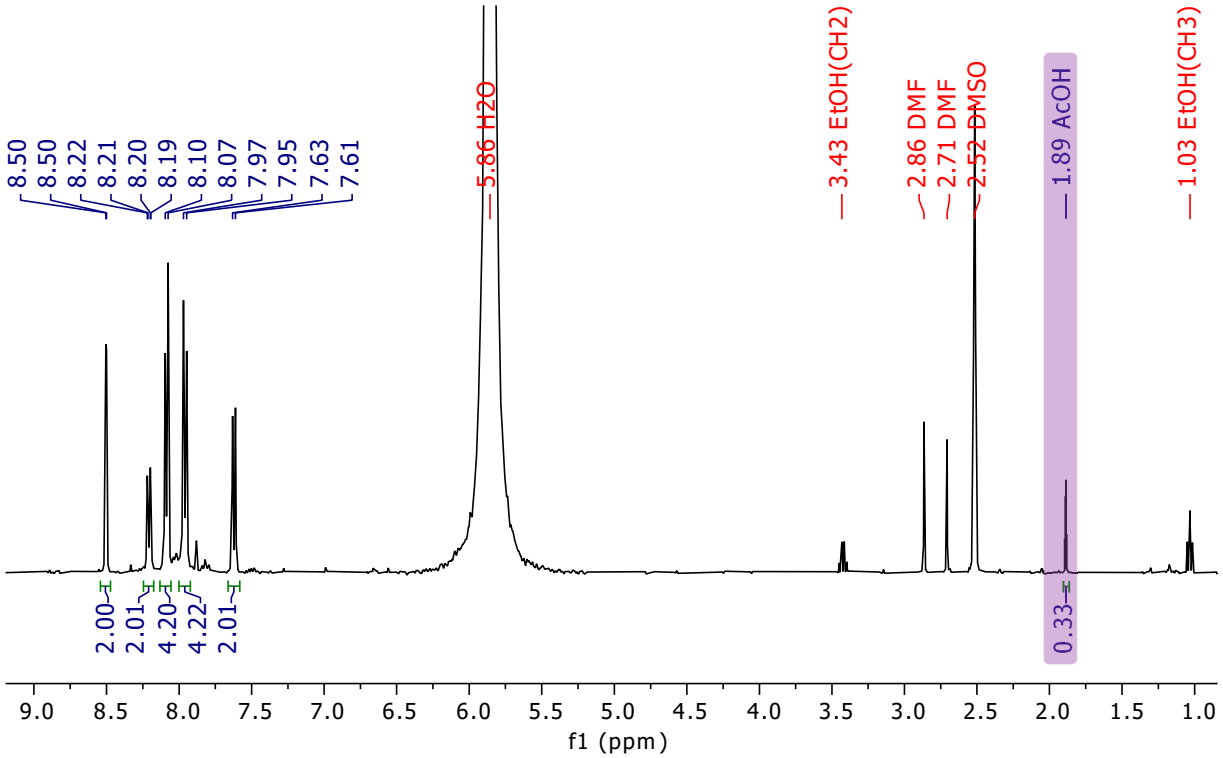

Figure 3-15. ^{1}H NMR spectrum of digested Hf-QC. Analysis of the integrals for the QC linker aromatic peaks (7.6-8.5 ppm) and the OAc modulator peak (1.9 ppm) gives an OAc modulator to QC linker ratio of 0.11:1, consistent with the formula $Hf_{12}(\mu_3\text{-}O)_8(\mu_3\text{-}OH)_8(\mu_2\text{-}OH)_6(QC)_{8.5}(OAc)$.

Synthesis of ZnOPPc@Hf-QC. To a 4 mL glass vial was added 0.5 mL of Hf-QC solution (1.53 mM in EtOH based on Hf), 0.5 mL of ZnOPPc solution (1.0 mg/mL in DMF) and a stir bar. The mixture was stirred for 16 h in a pre-heated oil bath set to 70 °C, collected by centrifugation, washed twice with DMF, and re-dispersed in EtOH.

ZnOPPc@Hf-QC loading. The wt% loading of ZnOPPc in ZnOPPc@Hf-QC was calculated to be 13.6% based on UV-Vis spectroscopy, which gave a ZnOPPc concentration of 69.5 μM from the characteristic absorption peak at 700 nm, and ICP-MS analysis, which gave a Hf concentration of 1.23 mM. The loading of ZnOPPc@Hf-QC was calculated using the formula $(ZnOPPc)_{0.68}@Hf_{12}(\mu_3\text{-}O)_8(\mu_3\text{-}OH)_8(\mu_2\text{-}OH)_6(QC)_{8.5}(OAc)$, which was determined from UV-Vis spectroscopy and ^{1}H NMR analysis of digested ZnOPPc@Hf-QC and corroborated by TGA.

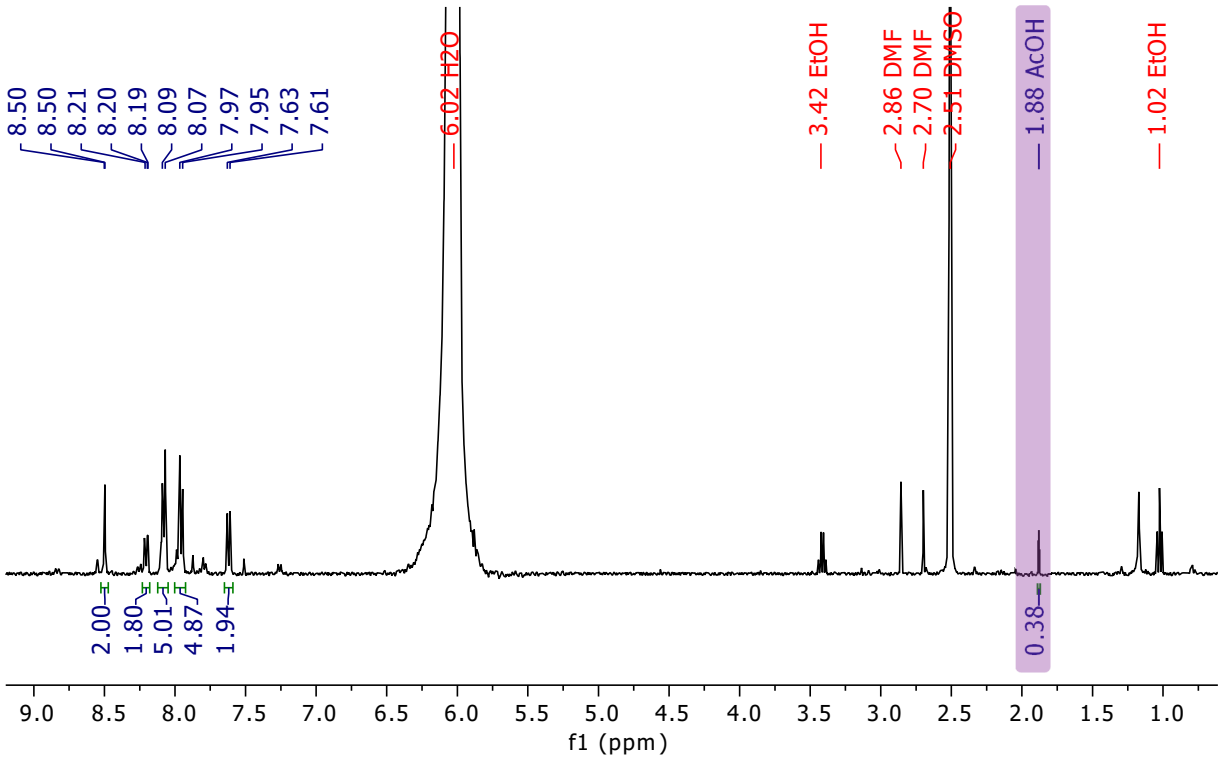

Figure 3-16. ^{1}H NMR spectrum of digested ZnOPPc@Hf-QC. Digested ZnOPPc@Hf-QC maintains the same OAc modulator to QC linker ratio (0.11:1) as Hf-QC, consistent with the formula $(ZnOPPc)_{0.68}@Hf_{12}(\mu_3\text{-}O)_8(\mu_3\text{-}OH)_8(\mu_2\text{-}OH)_6(QC)_{8.5}(OAc)$ and confirming the physical loading of ZnOPPc.

3.4.3. *In vitro* procedures

Test tube singlet oxygen detection. The time-dependent $^{1}O_2$ generation of ZnOPPc, H_2QC, Hf-QC and ZnOPPc@Hf-QC was detected by SOSG assay upon light irradiation. ZnOPPc, H_2QC, Hf-QC and ZnOPPc@Hf-QC suspensions were prepared with an equivalent dose of 0.5 μM ZnOPPc and 71.8 μM QC in PBS. To 2 mL of each of these suspensions, an SOSG stock solution (5 μL at 5 mM) was added (final SOSG concentration = 12.5 μM) before fluorescence measurements. The mixed solutions were exposed to an LED light (700 nm, 100 mW/cm^2) for 0, 10, 20, 30, 60, 120, 180, 300, 420 and 600 seconds and the fluorescence intensities at each time point was measured by a fluorimeter.

Cellular uptake. The cellular uptake of ZnOPPc, Hf-QC and ZnOPPc@Hf-QC was evaluated on CT26 cells. The cells were seeded on 6-well plates at a density of 5×10^5 cells/well followed by overnight culture. First, ZnOPPc and ZnOPPc@Hf-QC were added to each well to reach an equivalent ZnOPPc concentration of 5 μM in medium (n = 3). The cells were incubated at 37 °C for 1, 2, 4, and 8 hours. At each time point, the medium was aspirated, the cells were washed with DPBS three times, trypsinized, collected by centrifugation, and counted by a hemocytometer. The cell pellets were digested with a mixture of DMSO and 10% H_3PO_4 in 1.5 mL Eppendorf tubes for 48 hours with strong vortex and sonication every 12 hours, and the ZnOPPc concentration was determined by UV-Vis absorbance at 700 nm (ε_{700} = 422,000 M^{-1} cm^{-1}). The uptake of ZnOPPc@Hf-QC and Hf-QC was measured in the same way at an equivalent Hf concentration of 85.7 μM, except the digestion step where the cell pellets were treated with 99% of concentrated HNO_3 (67-70% trace metal grade) and 1% of hydrofluoric acid in 1.5 ml Eppendorf tubes for 48 hours with strong vortex and sonication every 12 hours. The Hf concentration was then determined by ICP-MS analysis.

In addition, the relative cellular uptake was also confirmed by flow cytometry and confocal microscopy after 8-hour incubation of CT26 cells with ZnOPPc, Hf-QC and ZnOPPc@Hf-QC. The fluorescence intensity of ZnOPPc was monitored by APCR700 channel (Ex: 640 nm, Em: 730/745 nm). The colocalization between ZnOPPc (red channel) and LysoTracker (green channel) was not only verified by ROI analysis, but was also confirmed by whole image analysis. The 2D intensity profiles and Pearson's coefficient were calculated by Coloc2 plugin in ImageJ software. From 0.5 h to 24 h, the R value increased and ZnOPPc had increasing signal overlap with LysoTracker.

Cell viability assay. The cytotoxicity of ZnOPPc, Hf-QC and ZnOPPc@Hf-QC was evaluated on CT26 cells by the MTS assay. The cells were first seeded on 96-well plates at a density of 1×10^5 cells/mL with 100 μL RPMI medium per well and further cultured overnight. ZnOPPc or ZnOPPc@Hf-QC was added to the wells at an equivalent ZnOPPc concentration of 0, 20, 50, 100, 200, 500, 1000 and 2000 nM and incubated for 8 hours (n = 6), followed by light irradiation (700 nm, 100 mW/cm^2, 10 min; 60 J/cm^2 total dose). Hf-QC was added to the wells, at an equivalent Hf concentration of 0, 0.34, 0.86, 1.7, 3.4, 8.6, 17.1, 34.3 μM, followed by the same PDT treatment. During light irradiation, a water jacket was placed above the plate to avoid heating of the plate by the LED. The cells were further incubated for 48 hours and the cell viability was determined by MTS assay. IC_{50} value of ZnOPPc@Hf-QC(+) was determined as 139 nM by fitting the dose response curves in Origin Lab. No significant toxicity of ZnOPPc(+) or Hf-QC(+) was found until 2 μM. No obvious dark toxicity was observed for ZnOPPc(-), Hf-QC(-) and ZnOPPc@Hf-QC(-).

Live cell imaging. To further verify the PDT killing effect by ZnOPPc@Hf-QC(+), we observed cell proliferation and morphology of CT26 cells after PDT treatment by IncuCyte S3. CT26 cells were first seeded in a 96-well plate with a density of 1.5×10^3 cells/well and cultured overnight. ZnOPPc@Hf-QC was then added, at an equivalent ZnOPPc concentration of 1 μM, and further incubated for 8 hours, followed by light irradiation (700 nm, 100 mW/cm^2, 10 min; 60 J/cm^2 total dose). The plate was then put in the IncuCyte S3 for 46 hours before phase contrast images and live cell proliferation videos were acquired.

Apoptotic cell death. The apoptosis after PDT treatment was evaluated on CT26 cells by flow cytometry and CLSM. For flow cytometry analysis, CT26 cells were seeded on two 6-well plates at a density of 2.5×10^5 cells/mL with RPMI medium and cultured overnight. The cells on both plates were treated with ZnOPPc, Hf-QC, or ZnOPPc@Hf-QC at an equivalent ZnOPPc concentration of 2 μM (or Hf concentration of 34.3 μM) and further incubated for 8 hours. One of the plates was irradiated with LED light (700 nm, 100 mW/cm^2) for 10 min. The cells on both plates were washed with cold DPBS, exchanged with warm fresh medium and further incubated for another 24 hours. The cells were then trypsinized and stained with Alexa Fluor 488 Annexin V/dead cell apoptosis kit (1:20 dilution in 1x binding buffer) and PI (1 μg/mL, 15 min on ice; Thermo Fisher Scientific, USA) for flow cytometry analysis. For CLSM analysis, inside 35 mm glass bottom dishes, CT26 cells were seeded at a density of 1×10^5 cells/mL with RPMI medium and cultured overnight. The treatment and staining were the same as the flow cytometry protocol except with the addition of a counterstain of Hoechst-33342 3 μg/mL 5 min at room temperature and fixation by 2% PFA (in 1x binding buffer). The dishes were then washed by DPBS and added with 1 mL 1x binding buffer and immediately observed under a Leica Stellaris 8 microscope.

***In vitro* ROS generation.** The ROS generation of ZnOPPc, Hf-QC and ZnOPPc@Hf-QC, during PDT treatment, was evaluated on CT26 cells by flow cytometry and CLSM. For flow cytometry analysis, CT26 cells were seeded on two 6-well plates at a density of 2.5×10^5 cells/mL with RPMI medium and cultured overnight. The cells on both plates were treated with ZnOPPc, Hf-QC, or ZnOPPc@Hf-QC at an equivalent ZnOPPc concentration of 2 μM (or Hf concentration of 34.3 μM) and further incubated for 7 hours. 20 μM DCF-DA (Invitrogen) was then added to each well for another 1 hour incubation. One of the plates was irradiated with LED light (700 nm, 100

mW/cm^2) for 10 min. The cells were then washed with PBS, trypsinized, and analyzed by flow cytometry. For CLSM, inside 35 mm glass bottom dishes, CT26 cells were seeded at a density of 1×10^5 cells/mL with 2 mL RPMI medium and cultured overnight. The cells were treated in the same way as the flow cytometry protocol but not detached. The cells were washed with DPBS three times, exchanged with cold DPBS and immediately mounted for confocal imaging using a Leica Stellaris 8 microscope.

CRT expression. By flow cytometry and CLSM, immunogenic cell death was investigated by CRT expression level after PDT treatment. For flow cytometry analysis, CT26 cells were seeded on two 6-well plates at a density of 2.5×10^5 cells/mL with 2 mL RPMI medium and cultured overnight. The cells were treated with ZnOPPc, Hf-QC or ZnOPPc@Hf-QC at an equivalent ZnOPPc concentration of 2 μM (or Hf concentration of 34.3 μM) and incubated for 8 hours. One of the plates was irradiated with LED light (700 nm, 100 mW/cm^2) for 10 min. The cells on both plates were washed with DPBS to remove excess ligands or Hf-QC, exchanged with warm fresh medium, and incubated for another 24 hours. The medium was then discarded, and cells were washed with DPBS and trypsinized to obtain cell suspension. The cells were stained with anti-Calreticulin Alexa Fluor 488 (NOVUS) (1:150 dilution in 0.5% BSA DPBS solution) on ice for 30 min, washed once with PBS and resuspended in FACS buffer (0.5% BSA, 2 mM EDTA and 0.05% NaN_3 in DPBS) for flow cytometry analysis. As for CLSM analysis, the PDT treatment procedure was the same with flow cytometry except MC38 cells were seeded with a coverslip in each well with a cell density diluted to 1×10^5 cells/mL. 24 hours after treatment, the cells were fixed with -20 ℃ methanol for 5 min, blocked with 3% BSA and 1% FBS at RT for 1 hour, and then stained with anti-Calreticulin Alexa Fluor 488 (NOVUS) (1:150 dilution in 0.5% BSA DPBS

solution) at 4 ℃ overnight. The cells were washed with DPBS and counterstained with Hoechst (3 μg/mL, 5 min, room temperature), and the coverslips were mounted on glass slides with ProLong™ Glass Antifade Mountant, cured for 6 hours, and sealed for confocal imaging under a Leica Stellaris 8 microscope.

3.4.4. *In vivo* procedures

***In vivo* anti-cancer efficacy.** Hf-QC and ZnOPPc@Hf-QC were PEGylated before intravenous administration. Briefly, the nMOF was first dispersed in water and the same weight amount of DSPE-PEG(2000) was added. The mixture was stirred at room temperature for 4 hours and lyophilized to afford the PEGylated solid. The solid was suspended in PBS immediately before use. To evaluate the *in vivo* PDT efficacy of ZnOPPc@Hf-QC, CT26 tumor-bearing BALB/c and MC38 tumorbearing C57Bl/6 mouse models were established by inoculating 2×10^6 cells/mouse subcutaneously at day 1. At day 7, 25 mice with tumor volume around 100 mm^3 were randomized for PDT treatment. ZnOPPc, Hf-QC or ZnOPPc@Hf-QC was injected intravenously with equivalent ZnOPPc dose of 50 nmol (or Hf dose of 0.88 μmol) (n = 5). Control group was treated with PBS (n = 5). After 12 hours, the mice were anaesthetized with 2.5% (V/V) isoflurane/O_2 and only the tumor area was irradiated with LED light (700 nm, 100 mW/cm^2, 10 min). Tumor sizes were measured by an electronic caliper (tumor volume = length × $width^2$ / 2) and body weight was monitored. At day 22 and day 24 for CT26 and MC38 model, respectively, the mice were sacrificed, and the tumors were weighed, photographed, and sectioned for H&E and TUNEL staining. Major organs were sectioned for H&E staining to evaluate biosafety. The tumor growth inhibition index (TGI) was calculated based on the equation below:

$$TGI = 1 - \frac{\left(\frac{T_e}{T_s} \Big/ \frac{C_e}{C_s}\right)}{1 - \frac{C_s}{C_e}} \times 100\%$$

where T_e, T_s, C_e, and C_s represent average tumor volumes of treated mice at endpoint, treated mice at starting-point, control mice at endpoint, and control mice at starting-point, respectively.

In vivo **immunogenic cell death.** To evaluate the *in vivo* immunogenic cell death after PDT treatment, tumors were fixed in 10% neutral buffer (Thermo Fisher Scientific) for 3 days and 70% ethanol for 1 day. Tissues were embedded in paraffin, sectioned, and stained for TUNEL assay by the Human Tissue Resource Center at the University of Chicago. Briefly, after deparaffinization and rehydration, tissue sections were treated with 20 μg/mL of proteinase K (S3004, DAKO) for 15 minutes. 3% hydrogen peroxidase was used to block the endogenous enzyme activity followed by equilibration buffer incubation. Working strength TDT enzyme was applied on tissue sections for 1 hour incubation at 37°C in a wet chamber. Following stop/wash buffer wash, TdT labeled DNA fragments were visualized through anti-Digoxigenin Conjugate and DAB+ chromogen (DAKO, K3468). Tissue sections were briefly immersed in hematoxylin for counterstaining and were covered with cover glasses. The slides were then sealed and scanned on a CRi Pannoramic SCAN 40x whole slide scanner by Integrated Light Microscopy Core in the University of Chicago. The images were analyzed by QuPath-0.2.3 software.

In vivo **biodistribution.** To evaluate the *in vivo* biodistribution of Hf-QC and ZnOPPc@Hf-QC, CT26 tumor-bearing BALB/c mouse model was established by inoculating 2×10^6 cells/mouse subcutaneously at day 1. At day 7, mice with tumor volumes around 100 mm^3 were intravenously injected with PEGylated Hf-QC or ZnOPPc@Hf-QC with an equivalent Hf dose of 0.88 μmol (*n*

= 3). After 12 hours, the mice were sacrificed, and blood, tumor, tumor draining lymph node, heart, lung, liver, spleen and kidney were weighed and digested with 99% concentrated HNO_3 and 1% HF. The Hf amount was determined by ICP-MS and Hf ID%/g was used to assess the *in vivo* biodistribution of Hf-QC and ZnOPPc@Hf-QC.

Statistical analysis. All statistical analysis for the *in vivo* efficacy study was performed on Origin Lab software by One-way Repeated Measures ANOVA method with Tukey's honest significance test to determine whether the difference between each group was significant. The p values were defined as * $p<0.05$, ** $p<0.01$, *** $p<0.001$, **** $p<0.0001$ in all the figures. The tumor volumes and tumor weights of the last day of experiment were chosen for analysis ($n = 5$).

3.5 References

1. Lovell, J. F.; Liu, T. W. B.; Chen, J.; Zheng, G., Activatable Photosensitizers for Imaging and Therapy. *Chemical Reviews* **2010,** *110* (5), 2839-2857.

2. Li, X.; Lovell, J. F.; Yoon, J.; Chen, X., Clinical development and potential of photothermal and photodynamic therapies for cancer. *Nature Reviews Clinical Oncology* **2020,** *17* (11), 657-674.

3. Zhao, X.; Liu, J.; Fan, J.; Chao, H.; Peng, X., Recent progress in photosensitizers for overcoming the challenges of photodynamic therapy: from molecular design to application. *Chemical Society Reviews* **2021,** *50* (6), 4185-4219.

4. Zhou, Z.; Ni, K.; Deng, H.; Chen, X., Dancing with reactive oxygen species generation and elimination in nanotheranostics for disease treatment. *Advanced Drug Delivery Reviews* **2020,** *158*, 73-90.

5. Lim, C.-K.; Heo, J.; Shin, S.; Jeong, K.; Seo, Y. H.; Jang, W.-D.; Park, C. R.; Park, S. Y.; Kim, S.; Kwon, I. C., Nanophotosensitizers toward advanced photodynamic therapy of Cancer. *Cancer Letters* **2013,** *334* (2), 176-187.

6. Mallidi, S.; Anbil, S.; Bulin, A.-L.; Obaid, G.; Ichikawa, M.; Hasan, T., Beyond the Barriers of Light Penetration: Strategies, Perspectives and Possibilities for Photodynamic Therapy. *Theranostics* **2016,** *6* (13), 2458-2487.

7. Hamblin, M. R., Photodynamic Therapy for Cancer: What's Past is Prologue. *Photochemistry and Photobiology* **2020,** *96* (3), 506-516.

8. Detty, M. R.; Gibson, S. L.; Wagner, S. J., Current Clinical and Preclinical Photosensitizers for Use in Photodynamic Therapy. *Journal of Medicinal Chemistry* **2004,** *47* (16), 3897-3915.

9. Machacek, M.; Cidlina, A.; Novakova, V.; Svec, J.; Rudolf, E.; Miletin, M.; Kučera, R.; Simunek, T.; Zimcik, P., Far-Red-Absorbing Cationic Phthalocyanine Photosensitizers: Synthesis and Evaluation of the Photodynamic Anticancer Activity and the Mode of Cell Death Induction. *Journal of Medicinal Chemistry* **2015,** *58* (4), 1736-1749.

10. Kobayashi, N.; Ogata, H.; Nonaka, N.; Luk'yanets, E. A., Effect of Peripheral Substitution on the Electronic Absorption and Fluorescence Spectra of Metal-Free and Zinc Phthalocyanines. *Chemistry – A European Journal* **2003,** *9* (20), 5123-5134.

11. Lo, P.-C.; Rodríguez-Morgade, M. S.; Pandey, R. K.; Ng, D. K. P.; Torres, T.; Dumoulin, F., The unique features and promises of phthalocyanines as advanced photosensitisers for photodynamic therapy of cancer. *Chemical Society Reviews* **2020,** *49* (4), 1041-1056.

12. Dumoulin, F.; Durmuş, M.; Ahsen, V.; Nyokong, T., Synthetic pathways to water-soluble phthalocyanines and close analogs. *Coordination Chemistry Reviews* **2010,** *254* (23), 2792-2847.

13. Roguin, L. P.; Chiarante, N.; García Vior, M. C.; Marino, J., Zinc(II) phthalocyanines as photosensitizers for antitumor photodynamic therapy. *The International Journal of Biochemistry & Cell Biology* **2019,** *114*, 105575.

14. Kollar, J.; Machacek, M.; Halaskova, M.; Lenco, J.; Kucera, R.; Demuth, J.; Rohlickova, M.; Hasonova, K.; Miletin, M.; Novakova, V.; Zimcik, P., Cationic Versus Anionic Phthalocyanines for Photodynamic Therapy: What a Difference the Charge Makes. *Journal of Medicinal Chemistry* **2020,** *63* (14), 7616-7632.

15. Macháček, M.; Carter, K. A.; Kostelanský, F.; Miranda, D.; Seffouh, A.; Ortega, J.; Šimůnek, T.; Zimčík, P.; Lovell, J. F., Binding of an amphiphilic phthalocyanine to pre-formed liposomes confers light-triggered cargo release. *Journal of Materials Chemistry B* **2018,** *6* (44), 7298-7305.

16. Ghosh, S.; Carter, K. A.; Lovell, J. F., Liposomal formulations of photosensitizers. *Biomaterials* **2019,** *218*, 119341.

17. van Nostrum, C. F., Polymeric micelles to deliver photosensitizers for photodynamic therapy. *Advanced Drug Delivery Reviews* **2004,** *56* (1), 9-16.

18. Setaro, F.; Wennink, J. W. H.; Mäkinen, P. I.; Holappa, L.; Trohopoulos, P. N.; Ylä-Herttuala, S.; van Nostrum, C. F.; de la Escosura, A.; Torres, T., Amphiphilic phthalocyanines in polymeric micelles: a supramolecular approach toward efficient third-generation photosensitizers. *Journal of Materials Chemistry B* **2020,** *8* (2), 282-289.

19. Lucky, S. S.; Soo, K. C.; Zhang, Y., Nanoparticles in Photodynamic Therapy. *Chemical Reviews* **2015,** *115* (4), 1990-2042.

20. Gao, D.; Lo, P.-C., Polymeric micelles encapsulating pH-responsive doxorubicin prodrug and glutathione-activated zinc(II) phthalocyanine for combined chemotherapy and photodynamic therapy. *Journal of Controlled Release* **2018,** *282*, 46-61.

21. Yu, W.; Ye, M.; Zhu, J.; Wang, Y.; Liang, C.; Tang, J.; Tao, H.; Shen, Y., Zinc phthalocyanine encapsulated in polymer micelles as a potent photosensitizer for the photodynamic therapy of osteosarcoma. *Nanomedicine: Nanotechnology, Biology and Medicine* **2018,** *14* (4), 1099-1110.

22. Lismont, M.; Dreesen, L.; Wuttke, S., Metal-Organic Framework Nanoparticles in Photodynamic Therapy: Current Status and Perspectives. *Advanced Functional Materials* **2017,** *27* (14), 1606314.

23. Lu, K.; He, C.; Guo, N.; Chan, C.; Ni, K.; Weichselbaum, R. R.; Lin, W., Chlorin-Based Nanoscale Metal–Organic Framework Systemically Rejects Colorectal Cancers via Synergistic Photodynamic Therapy and Checkpoint Blockade Immunotherapy. *Journal of the American Chemical Society* **2016,** *138* (38), 12502-12510.

24. Lu, K.; He, C.; Lin, W., Nanoscale Metal–Organic Framework for Highly Effective Photodynamic Therapy of Resistant Head and Neck Cancer. *Journal of the American Chemical Society* **2014,** *136* (48), 16712-16715.

25. Luo, T.; Ni, K.; Culbert, A.; Lan, G.; Li, Z.; Jiang, X.; Kaufmann, M.; Lin, W., Nanoscale Metal–Organic Frameworks Stabilize Bacteriochlorins for Type I and Type II Photodynamic Therapy. *Journal of the American Chemical Society* **2020,** *142* (16), 7334-7339.

26. Zeng, J.-Y.; Zou, M.-Z.; Zhang, M.; Wang, X.-S.; Zeng, X.; Cong, H.; Zhang, X.-Z., π-Extended Benzoporphyrin-Based Metal–Organic Framework for Inhibition of Tumor Metastasis. *ACS Nano* **2018,** *12* (5), 4630-4640.

27. Zheng, X.; Wang, L.; Pei, Q.; He, S.; Liu, S.; Xie, Z., Metal–Organic Framework@Porous Organic Polymer Nanocomposite for Photodynamic Therapy. *Chemistry of Materials* **2017,** *29* (5), 2374-2381.

28. Park, J.; Jiang, Q.; Feng, D.; Zhou, H.-C., Controlled Generation of Singlet Oxygen in Living Cells with Tunable Ratios of the Photochromic Switch in Metal–Organic Frameworks. *Angewandte Chemie International Edition* **2016,** *55* (25), 7188-7193.

29. Song, Y.; Wang, L.; Xie, Z., Metal–Organic Frameworks for Photodynamic Therapy: Emerging Synergistic Cancer Therapy. *Biotechnology Journal* **2021,** *16* (2), 1900382.

30. Gao, P.; Chen, Y.; Pan, W.; Li, N.; Liu, Z.; Tang, B., Antitumor Agents Based on Metal–Organic Frameworks. *Angewandte Chemie International Edition* **2021,** *60* (31), 16763-16776.

31. Xu, W.; Tu, B.; Liu, Q.; Shu, Y.; Liang, C.-C.; Diercks, C. S.; Yaghi, O. M.; Zhang, Y.-B.; Deng, H.; Li, Q., Anisotropic reticular chemistry. *Nature Reviews Materials* **2020,** *5* (10), 764-779.

32. Helal, A.; Yamani, Z. H.; Cordova, K. E.; Yaghi, O. M., Multivariate metal-organic frameworks. *National Science Review* **2017,** *4* (3), 296-298.

33. Della Rocca, J.; Liu, D.; Lin, W., Nanoscale Metal–Organic Frameworks for Biomedical Imaging and Drug Delivery. *Accounts of Chemical Research* **2011,** *44* (10), 957-968.

34. Lan, G.; Ni, K.; Lin, W., Nanoscale metal–organic frameworks for phototherapy of cancer. *Coordination Chemistry Reviews* **2019,** *379*, 65-81.

35. Hu, F.; Mao, D.; Kenry; Wang, Y.; Wu, W.; Zhao, D.; Kong, D.; Liu, B., Metal–Organic Framework as a Simple and General Inert Nanocarrier for Photosensitizers to Implement Activatable Photodynamic Therapy. *Advanced Functional Materials* **2018,** *28* (19), 1707519.

36. Cai, X.; Xie, Z.; Ding, B.; Shao, S.; Liang, S.; Pang, M.; Lin, J., Monodispersed Copper(I)-Based Nano Metal–Organic Framework as a Biodegradable Drug Carrier with Enhanced Photodynamic Therapy Efficacy. *Advanced Science* **2019,** *6* (15), 1900848.

37. Jiang, X.; He, C.; Lin, W., Supramolecular metal-based nanoparticles for drug delivery and cancer therapy. *Current Opinion in Chemical Biology* **2021,** *61*, 143-153.

38. Yu, W.; Zhen, W.; Zhang, Q.; Li, Y.; Luo, H.; He, J.; Liu, Y., Porphyrin-Based Metal−Organic Framework Compounds as Promising Nanomedicines in Photodynamic Therapy. *ChemMedChem* **2020,** *15* (19), 1766-1775.

39. Bao, Z.; Li, K.; Hou, P.; Xiao, R.; Yuan, Y.; Sun, Z., Nanoscale metal–organic framework composites for phototherapy and synergistic therapy of cancer. *Materials Chemistry Frontiers* **2021,** *5* (4), 1632-1654.

40. Liu, J.; Huang, J.; Zhang, L.; Lei, J., Multifunctional metal–organic framework heterostructures for enhanced cancer therapy. *Chemical Society Reviews* **2021,** *50* (2), 1188-1218.

41. Zeng, J.-Y.; Wang, X.-S.; Song, W.-F.; Cheng, H.; Zhang, X.-Z., Metal-Organic Framework Mediated Multifunctional Nanoplatforms for Cancer Therapy. *Advanced Therapeutics* **2019,** *2* (2), 1800100.

42. Wang, Y.; Wu, W.; Liu, J.; Manghnani, P. N.; Hu, F.; Ma, D.; Teh, C.; Wang, B.; Liu, B., Cancer-Cell-Activated Photodynamic Therapy Assisted by Cu(II)-Based Metal–Organic Framework. *ACS Nano* **2019,** *13* (6), 6879-6890.

43. Nash, G. T.; Luo, T.; Lan, G.; Ni, K.; Kaufmann, M.; Lin, W., Nanoscale Metal–Organic Layer Isolates Phthalocyanines for Efficient Mitochondria-Targeted Photodynamic Therapy. *Journal of the American Chemical Society* **2021,** *143* (5), 2194-2199.

44. Dai, R.; Peng, F.; Ji, P.; Lu, K.; Wang, C.; Sun, J.; Lin, W., Electron Crystallography Reveals Atomic Structures of Metal–Organic Nanoplates with M12(μ3-O)8(μ3-OH)8(μ2-OH)6 (M = Zr, Hf) Secondary Building Units. *Inorganic Chemistry* **2017,** *56* (14), 8128-8134.

45. Brilkina, A. A.; Dubasova, L. V.; Sergeeva, E. A.; Pospelov, A. J.; Shilyagina, N. Y.; Shakhova, N. M.; Balalaeva, I. V., Photobiological properties of phthalocyanine photosensitizers Photosens, Holosens and Phthalosens: A comparative in vitro analysis. *Journal of Photochemistry and Photobiology B: Biology* **2019,** *191*, 128-134.

46. Krysko, D. V.; Garg, A. D.; Kaczmarek, A.; Krysko, O.; Agostinis, P.; Vandenabeele, P., Immunogenic cell death and DAMPs in cancer therapy. *Nature Reviews Cancer* **2012,** *12* (12), 860-875.

47. Castano, A. P.; Mroz, P.; Hamblin, M. R., Photodynamic therapy and anti-tumour immunity. *Nature Reviews Cancer* **2006,** *6* (7), 535-545.

48. Zhang, Y.-N.; Poon, W.; Tavares, A. J.; McGilvray, I. D.; Chan, W. C. W., Nanoparticle–liver interactions: Cellular uptake and hepatobiliary elimination. *Journal of Controlled Release* **2016,** *240*, 332-348.

49. Balasubramanian, S. K.; Jittiwat, J.; Manikandan, J.; Ong, C.-N.; Yu, L. E.; Ong, W.-Y., Biodistribution of gold nanoparticles and gene expression changes in the liver and spleen after intravenous administration in rats. *Biomaterials* **2010,** *31* (8), 2034-2042.

50. Bankhead, P.; Loughrey, M. B.; Fernández, J. A.; Dombrowski, Y.; McArt, D. G.; Dunne, P. D.; McQuaid, S.; Gray, R. T.; Murray, L. J.; Coleman, H. G.; James, J. A.; Salto-Tellez, M.; Hamilton, P. W., QuPath: Open source software for digital pathology image analysis. *Scientific reports* **2017,** *7* (1), 16878.

Chapter 4: Synthesis and Characterization of Three-dimensional Phthalocyanine-based Zirconium and Hafnium Nanoscale Metal-Organic Frameworks

4.1 Introduction

Phthalocyanines are a synthetic analogue to porphyrins, but their structural differences yield vastly different electronic properties. The addition of fused benzene rings and replacement of the *meso* carbons with *aza* linkages break the degeneracy of the molecular orbitals, causing a large shift in the Q-bands and a dramatic increase in its absorption coefficient compared to porphyrins.[1] Additionally, these structural changes confer excellent photo- and chemo-stability, which makes phthalocyanines interesting for applications beyond pigmentation, such as photodynamic therapy (PDT) or catalysis.[2-8] The two main issues preventing the clinical implementation of phthalocyanines are their strong tendency to aggregate in aqueous solution (due to π-π stacking of the conjugated planar rings) and their synthetic inflexibility.[9-11]

Metal-organic frameworks (MOFs) have been shown to alleviate these issues, via postsynthetic incorporation of hydrophobic macrocycles into the framework pores or postsynthetic exchange with modulator ligands on the metal cluster secondary building units (SBUs).[12-13] However, to date there is only one reported crystalline 3D MOF composed entirely of phthalocyanine bridging ligands,[14] with all other examples being amorphous or π-stacked (J-aggregate) 2D layers.[15-18] The 3D MOF, termed MOF-1992, is built from uniquely shaped Fe_3 clusters and a cobalt phthalocyanine complex with catechol functionalization on the fused benzene rings, resulting in a rather unusual topology.[14] However, this MOF is incompatible with nanomedicine applications due to the presence of iron clusters and cobalt-metalated

phthalocyanine catecholate linkers, which can undergo redox-cycling reactions leading to oxidative stress and unwanted toxicity.[19-21] Furthermore, the unique framework topology and cluster coordination geometry prevent any further peripheral functionalization of the phthalocyanine ligand and limiting its ability to grow other MOFs. In the case of nanomedicine, many metal SBUs cannot be used due to their potential redox-cycling toxicity and poor aqueous stability, with only Zr and Hf-based SBUs showing good biocompatibility and adequate aqueous stability. To unlock the potential applications of phthalocyanine-based MOFs, further ligand design is necessary to develop a functionally versatile MOF platform.

The immense difficulty of designing, synthesizing, and purifying a suitable phthalocyanine ligand for MOF growth becomes apparent upon closer look of the ligand requirements and available synthetic routes. For the ligand design, we used principles from two porphyrin ligands that can form a large variety of MOFs – including with Zr and Hf – which are the linear coordinating 5,15-di(*p*-benzoato)porphyrin (DBP) and the square planar coordinating 5,10,15,20-tetra(*p*-benzoato)porphyrin (TBP).[22-27] First and foremost, the ligand must have low enough solubility to confer good aqueous stability, but high enough solubility to not aggregate severely in *N*,*N*-dimethylformamide (DMF) during MOF growth. Secondly, if the ligand is a rigid macrocycle, there should be fewer coordination groups (2 or 4) and each pair of coordinating groups should be aligned linearly on the same axis (**Figure 4-1**). Since phthalocyanines have an extended conjugated structure and must be built from the cyclic tetramerization of phthalonitriles, they inherently make for poor MOF linkers. Without additional peripheral or axial substitution to bestow solubility, phthalocyanines will aggregate heavily even in a coordinating solvent like DMF, resulting in aggregated particles or an amorphous phase.[28] The eight substitution points around the phthalocyanine, on the 4 and 5 positions of the fused benzene ring, preventing the linear alignment

of the coordinating groups (**Figure 4-1**). Consequently, this also results in the formation of amorphous phases, as observed in the case of the previously synthesized zinc(II) 2,3,9,10,16,17,23,24-octa(4-carboxyphenyl)phthalocyanine (ZnOPPc).

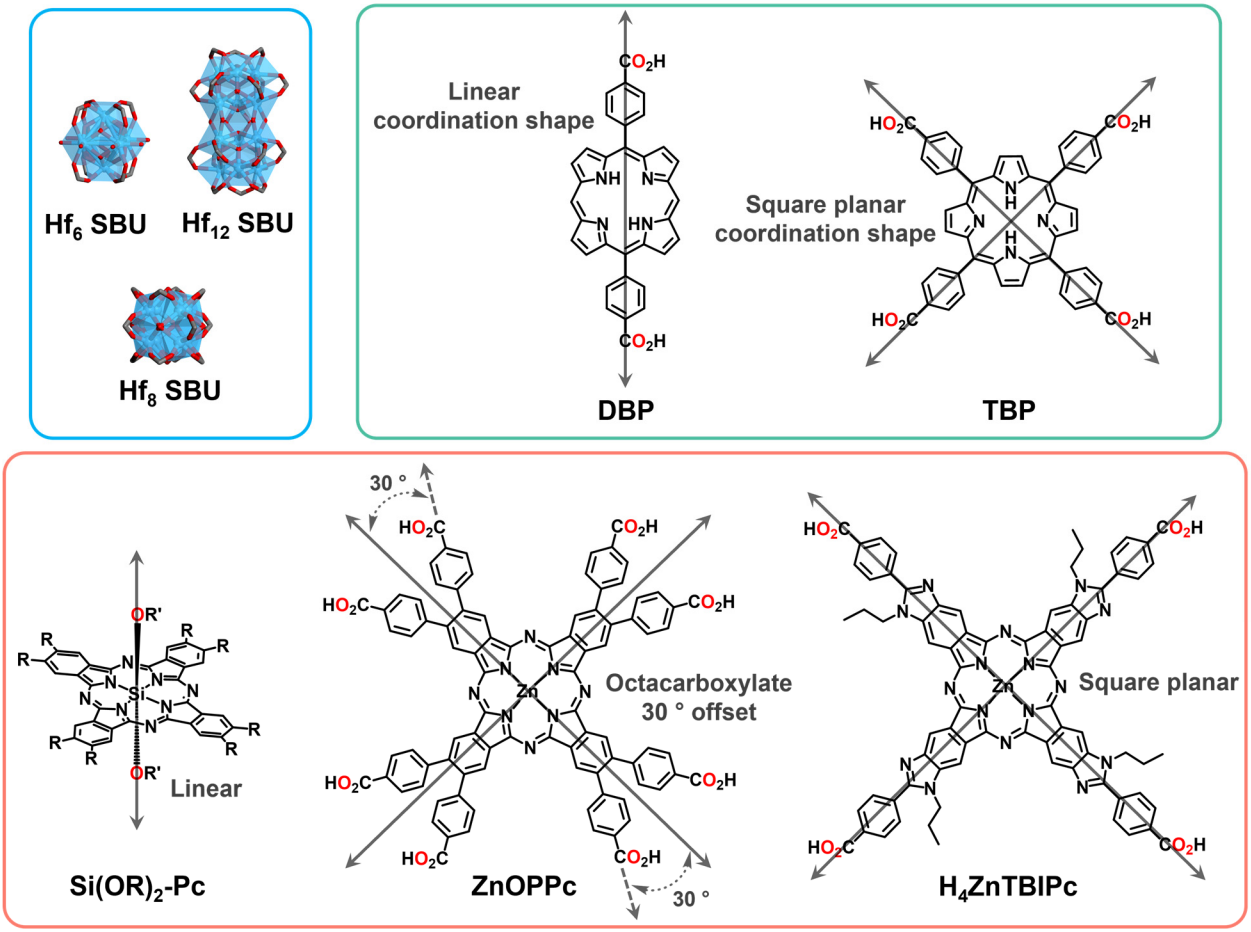

Figure 4-1. Illustration of typical hafnium coordination geometries (top left), porphyrin ligand shapes (top right), and phthalocyanine ligand designs with their coordination shapes (bottom).

Attempts to use peripheral substitution, such as with ZnOPPc, or axial substitution[29] to get the right denticity and ligand coordination shape have demonstrated poor results or do not yield 3D MOF crystals. While it may be possible to optimize the growth conditions of silicon phthalocyanines with axially substituted carboxylic acids to obtain a 3D MOF (**Figure 4-1**),[29-30] the Si-OR linkages are labile and will not be appropriate as a MOF linker in nanomedicine applications.[31-33] To overcome the increasing number of synthetic limitations, we decided to

investigate a rarely studied phthalocyanine analogue, tetraimidazophthalocyanines, which feature fused imidazole rings on the phthalocyanine that allow linear alignment of coordinating carboxylic acid groups (**Figure 4-1**).[34-37] We surmised that mimicking the square planar coordination geometry of TBP would enable its use as a versatile linker for 3D MOF synthesis. Here, we report the design of an *N*-alkylated zinc-tetraimidazophthalocyanine (H_4ZnTBIPc) with square planar coordination shape and its successful implementation in nanoscale MOF (nMOF) synthesis with Zr and Hf. The resulting MOFs, Zr-ZnTBIPc and Hf-ZnTBIPc, revealed a 3D cubic structure matching that of PCN-221.[22] To our knowledge, this is the first report of a 3D phthalocyanine MOF with metal-carboxylate linkages.

4.2 Results and discussion

4.2.1. Ligand synthesis and characterization

The synthetic route to the benzimidazophthalonitrile precursor, **2**, of the tetraimidazophthalocyanine target, **4**, was initially based on a previous literature report,[34] but inadequate yields led us to use different conditions. The annulation of phthalonitrile **1** with methyl 4-formylbenzoate in the presence of 10 mol% $Zn(OTf)_2$ (OTf = R-OSO_2CF_3) yielded the benzimidazophthalonitrile precursor **2** in 59% yield, after purification by recrystallization from DMF (**Scheme 4-1**).[38] The $Zn(OTf)_2$-catalyzed cyclization is a significantly milder and scalable alternative to oxidative cyclization using $FeCl_3/O_2$ or condensation of phenylenediamines with substituted benzoic acids that use concentrated and viscous acids (e.g. polyphosphoric acid).[34, 39-40] The zinc-templated synthesis of the tetraimidazophthalocyanine ester **3** proceeded using standard phthalocyanine reaction conditions, with $ZnCl_2$ as the metal source, 1,8-diazabicyclo(5.4.0)undec-7-ene (DBU) as a base, and 1-pentanol as high-boiling point solvent

(**Scheme 4-1**). However, the hydrolysis of **3** proved difficult, as typical aqueous hydrolysis conditions (e.g. aq. LiOH or NaOH) appeared to decompose the phthalocyanine structure.

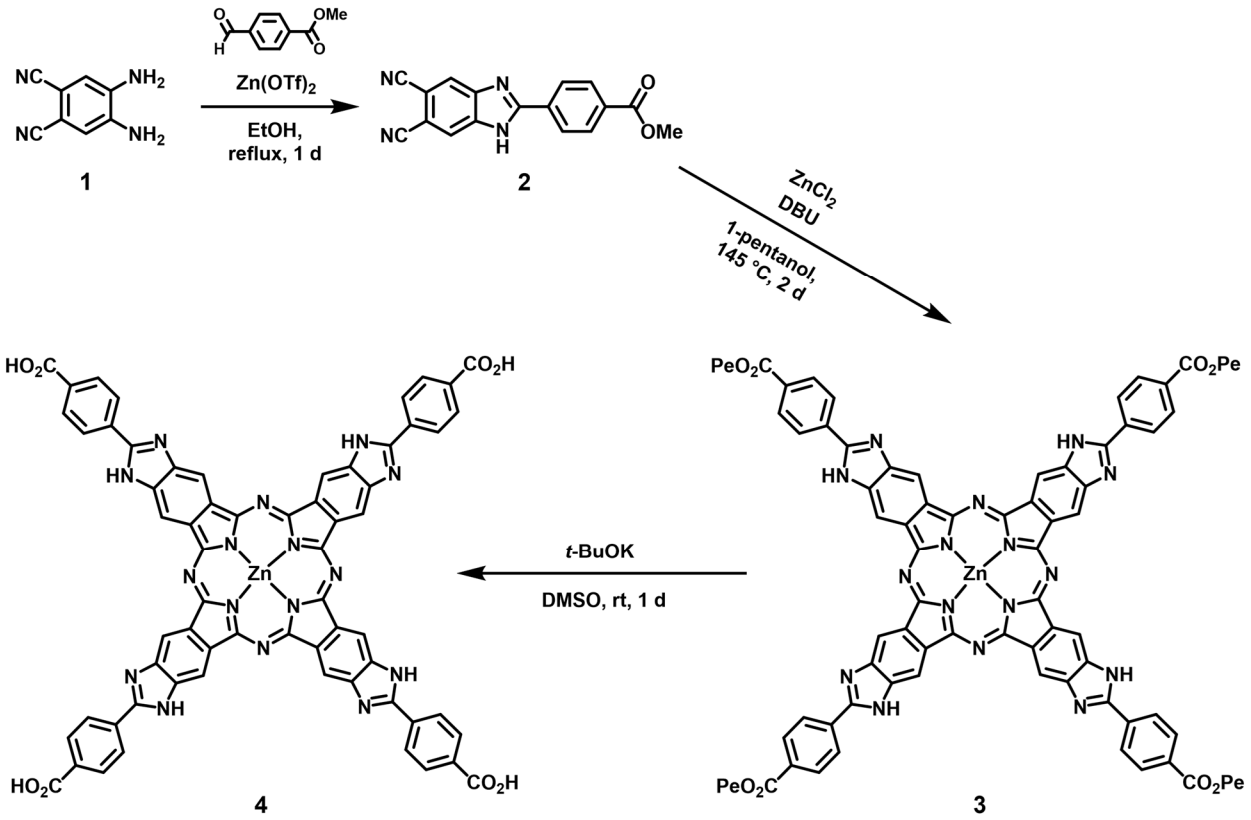

Scheme 4-1. Synthetic route to the first iteration of the ZnTBIPc ligand **4**.

We found that the hydrolysis to the desired tetracarboxylic acid phthalocyanine **4** proceeded well using potassium *tert*-butoxide (*t*-BuOK) in dimethylsulfoxide (DMSO) at room temperature overnight (**Scheme 4-1**). The structures of **3** and **4** were confirmed using matrix-assisted laser desorption/ionization-time of flight high-resolution mass spectrometry (MALDI-TOF HR-MS), as their solubility in typical organic solvents was too low for nuclear magnetic resonance (NMR) analysis. However, the exceptionally poor solubility of **4** in coordinating solvents like DMF and DMSO meant that attempts to grow MOFs with this compound resulted in aggregated or amorphous particles settling at the bottom of the reaction vial.

As a result of the poor solubility of **4**, due to the extended conjugation and planarity compared to typical phthalocyanines, we sought to iterate and functionalize the phthalonitrile precursor **2** to improve the solubility of the phthalocyanine. Alkylation of the pyrrole-like nitrogen in the benzimidazole ring has been shown to improve the solubility of the resulting tetraimidazophthalocyanine as the additional steric bulk can prevent their cofacial aggregation in solution.[34] Although initial attempts to deprotonate **2** with DBU or sodium hydride and *N*-alkylate proved unsuccessful, further optimization showed that the benzimidazole moiety can be deprotonated and *N*-alkylated to **5** in 73% yield using several successive additions of 1-iodopropane and K_2CO_3 (**Scheme 4-2**). The tetraimidazophthalocyanine ester, Pe_4ZnTBIPc (Pe = pentyl), was synthesized using similar conditions to **3**, but with $ZnBr_2$ as the metal source (**Scheme 4-2**). The ester was then hydrolyzed using standard aqueous hydrolysis conditions by refluxing with 1M aq. NaOH to yield the desired tetraimidazophthalocyanine acid, H_4ZnTBIPc, in 80% yield (23% overall yield; **Scheme 4-2**). The structure was confirmed by MALDI-TOF HR-MS, with the isotopic molecular ion peaks matching the predicted mass peaks. H_4ZnTBIPc shows significantly better solubility in both DMF and DMSO and was deemed suitable for MOF growth. It is important to note that H_4ZnTBIPc exists as a mixture of four regioisomers due to the asymmetry of the *N*-propylated benzimidazole units. However, this does not interfere with MOF growth as the coordinating carboxylate groups remain tetragonally aligned in all regioisomers.

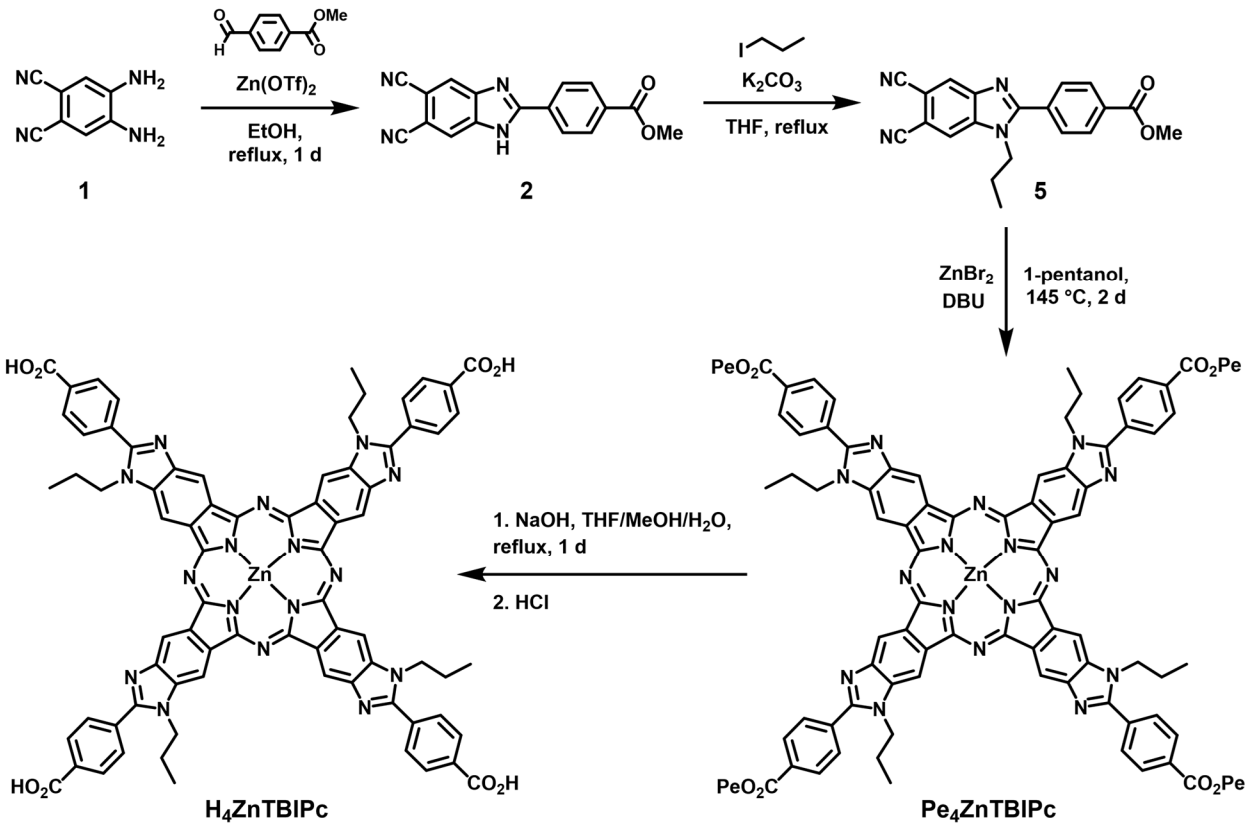

Scheme 4-2. Synthetic route to *N*-alkylated benzimidazole **5** and H_4ZnTBIPc.

4.2.2. nMOF synthesis and characterization

The square planar shape and tetragonally aligned carboxylate groups in the new H_4ZnTBIPc ligand successfully allowed the growth of two isostructural nMOFs: Zr-ZnTBIPc and Hf-ZnTBIPc. The two nMOFs were synthesized in a solvothermal reaction between $ZrCl_4$/$HfCl_4$ and H_4ZnTBIPc in DMF at 90 °C using acetic acid (AcOH) as modulator. The resulting dark green dispersion was collected by centrifugation and then washed with excess DMF, 1% (v/v) triethylamine in ethanol, and ethanol. The washed powder was redispersed in ethanol and stored in the dark before further analysis.

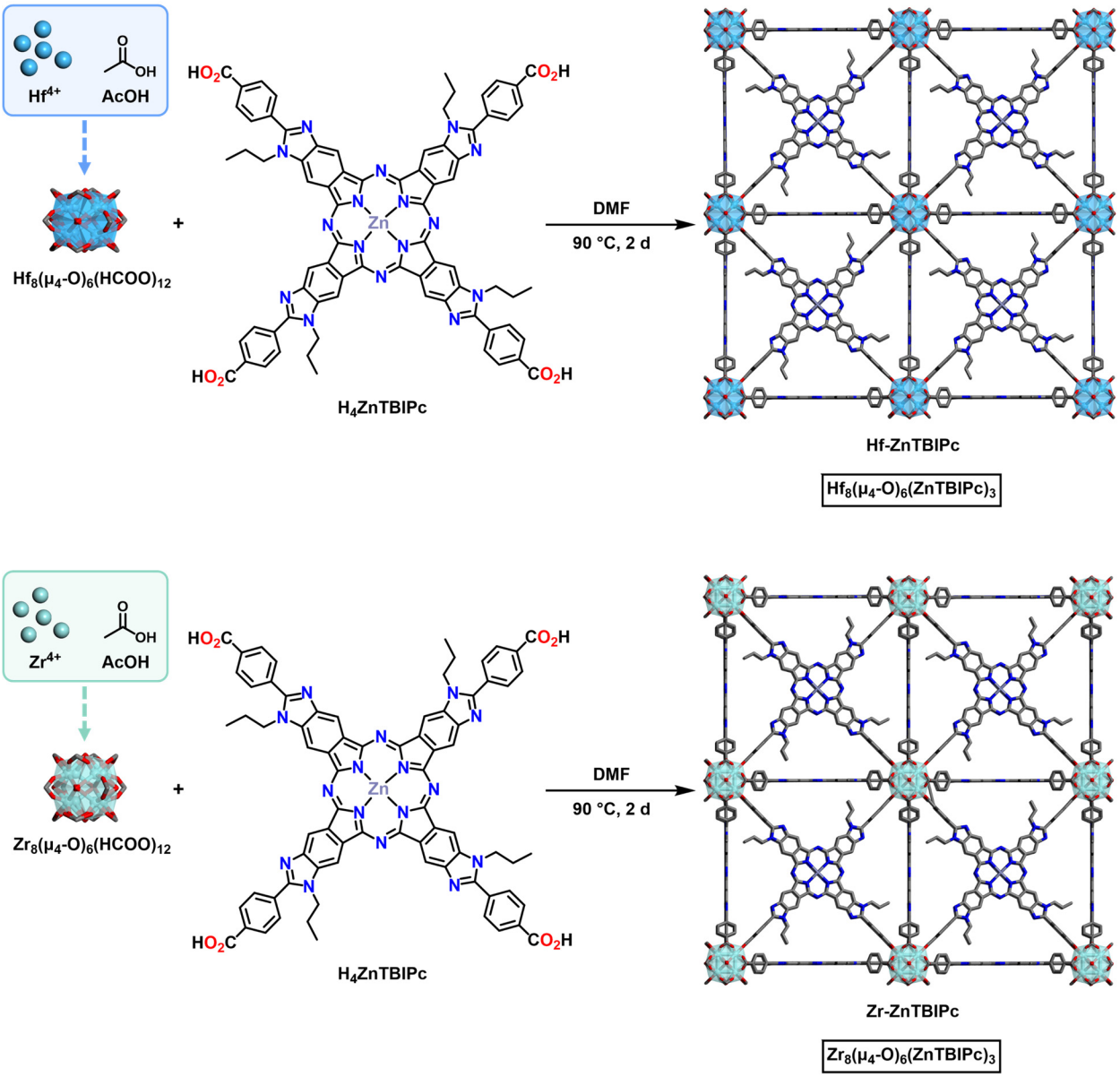

Scheme 4-3. Synthetic scheme of Hf-ZnTBIPc and Zr-ZnTBIPc MOFs.

Several attempts failed to grow Zr-ZnTBIPc or Hf-ZnTBIPc single crystals suitable for single-crystal X-ray diffraction analysis to elucidate their structure. Since H_4ZnTBIPc shares the same ligand shape as TBP but with a larger simulated length of ~3.1 nm along the carboxylic acid axis (compared to ~2.0 nm for TBP), we hypothesized that the phthalocyanine nMOF structures should have the same topology as those reported for TBP. Fortunately, the experimental powder X-ray diffraction (PXRD) patterns of Zr-ZnTBIPc and Hf-ZnTBIPc matched very well with the

simulated PXRD pattern of PCN-221 (with expanded lattice parameters $a = b = c = 25.2998$ Å, determined from powder indexing; **Table 4-1**), with a few absent peaks likely due to preferential orientation of the nanoparticles (**Figure 4-2**).[22, 41] Simulated powder indexing of the Hf-ZnTBIPc experimental PXRD pattern, using TREOR90 in Materials Studio, produced a cubic system with the lattice parameters given above and a de Wolff figure of merit of 73 (**Figure 4-2**, **Table 4-1**, **Table 4-2**).[42]

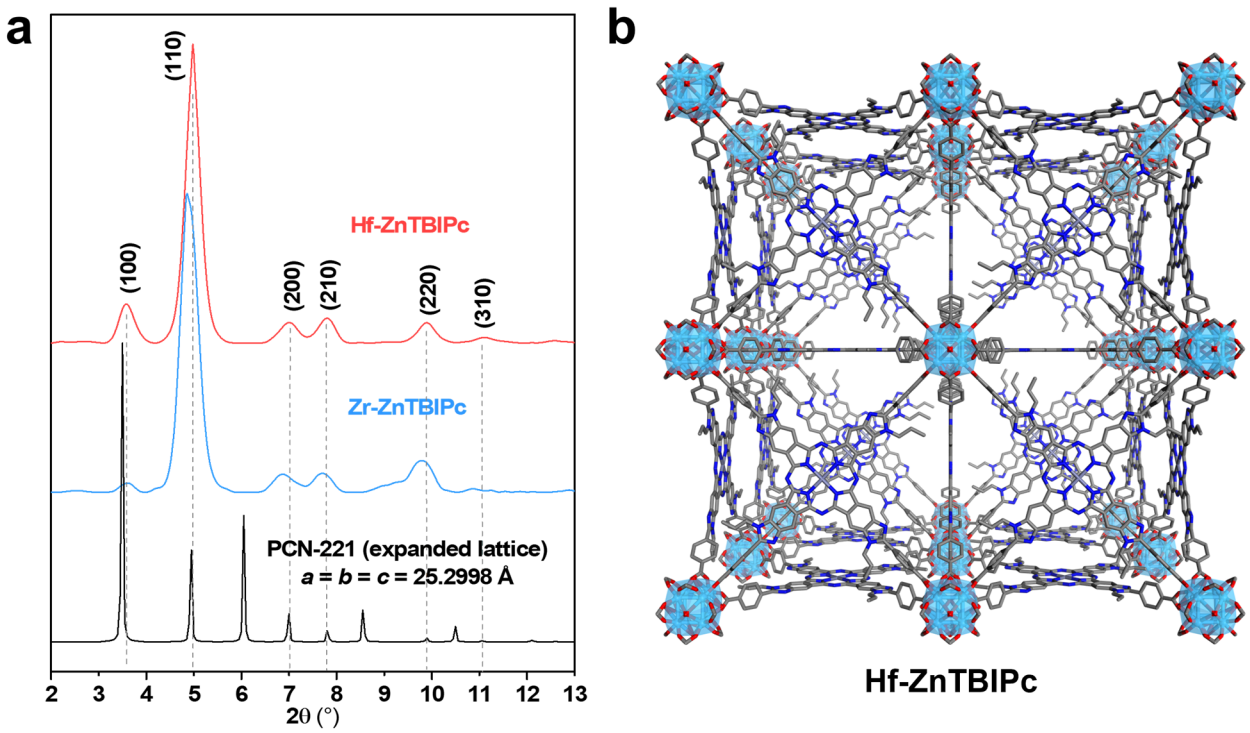

Figure 4-2. Structure model of Zr-ZnTBIPc Hf-ZnTBIPc from PXRD. (a) Experimental PXRD patterns of Hf-ZnTBIPc and Zr-ZnTBIPc with simulated PXRD pattern of PCN-221 with expanded lattice parameters to mimic the increased unit cell size from ZnTBIPc. (b) Perspective view of the Hf-ZnTBIPc structure model built from the **ftw** topology.

Table 4-1. Powder indexing output for the experimental PXRD pattern of Hf-ZnTBIPc using TREOR90 in Materials Studio (FOM = de Wolff figure of merit).

FOM	Peaks Found	Crystal System	a (Å)	b (Å)	c (Å)	α (°)	β (°)	γ (°)	Volume (Å^3)
73.0	3 of 5	Cubic	25.2998	25.2998	25.2998	90	90	90	16193.9

Table 4-2. Powder indexing calculation peak list and Miller indices for the experimental PXRD pattern of Hf-ZnTBIPc using TREOR90 in Materials Studio.

h	k	l	2θ observed (°)	2θ calculated (°)
1	0	0	3.498	3.492
1	1	0	4.940	4.939
2	0	0	7.000	6.988
2	1	0	7.800	7.814
2	2	0	9.890	9.888

Table 4-3. Experimental PXRD peak positions, d-spacings and Miller indices for Hf-ZnTBIPc.

2θ (°)	θ (°)	d (Å)	d (nm)	hkl
3.58	1.79	24.68	2.47	(1 0 0)
4.98	2.49	17.74	1.77	(1 1 0)
7.00	3.5	12.63	1.26	(2 0 0)
7.80	3.9	11.33	1.13	(2 1 0)
9.90	4.95	8.93	0.89	(2 2 0)

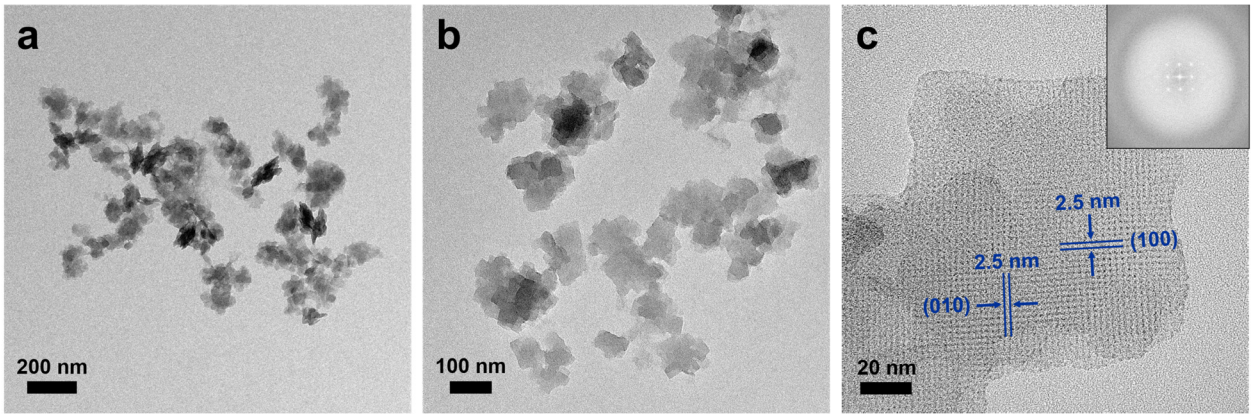

Figure 4-3. Morphological characterization of Zr-ZnTBIPc and Hf-ZnTBIPc. TEM images of (a) Zr-ZnTBIPc and (b) Hf-ZnTBIPc showing their cubic morphology. (c) HR-TEM image of Hf-ZnTBIPc showing the 2.5 nm distance between (100) or (010) planes in the lattice fringe. The FFT (inset) displays four-fold symmetry and further confirms the cubic structure of the nMOF.

The cubic PCN-221 structure was also supported by TEM and HR-TEM images of Hf-ZnTBIPc, which shows twinned nanoparticles ~100 nm in length with cubic morphology and 4-

fold symmetry in their fast Fourier transform (FFT) patterns (**Figure 4-3**). Additionally, the measured distances between the (010) or (100) planes (~2.5 nm) in the HR-TEM lattice fringe of Hf-ZnTBIPc matched the expected diagonal length of the bridging ZnTBIPc ligands (~2.5 nm) and the calculated d-spacings (**Figure 4-3**, **Table 4-3**).

Ultraviolet-visible (UV-Vis) absorption spectroscopy and inductively coupled plasma mass spectrometry (ICP-MS) of the digested nMOFs revealed metal-to-ligand ratios of 2.93 and 2.89 for Zr-ZnTBIPc and Hf-ZnTBIPc, respectively, which match well with the expected metal-to-ligand ratio of 2.66 for pristine PCN-221 (**Table 4-4**). The slight increase in the metal-to-ligand ratio in our nMOFs is likely due to the presence of defect sites within the nMOF crystals. Based on these results, we assign Zr-ZnTBIPc and Hf-ZnTBIPc with the ideal formula $M_8(\mu_4\text{-}O_6)(ZnTBIPc)_3$ (M = Hf or Zr), where the M_8 clusters are 12-connected and result in a 3D network with **ftw** topology (**Figure 4-2**).

Table 4-4. Concentrations and metal-to-ligand ratios (M:L) of ZnTBIPc and Hf/Zr in Zr-ZnTBIPc and Hf-ZnTBIPc. Metal-to-ligand ratios of the ideal structures in PCN-221,[22] PCN-222,[26] and PCN-224.[27]

Sample	UV-Vis ZnTBIPc	ICP-MS Hf	ICP-MS Zr	M : L ratio
Zr-ZnTBIPc	478 μM	-	1403 μM	2.93
Hf-ZnTBIPc	556 μM	1607 μM	-	2.89
PCN-221	-	-	-	2.66
PCN-222	-	-	-	3.00
PCN-224	-	-	-	4.00

The UV-Vis absorption spectrum of H_4ZnTBIPc in DMF showed its characteristic phthalocyanine Soret band around 360 nm and Q-band maximum at 720 nm along with its shoulder peaks (**Figure 4-4**). The molar absorption coefficient at 720 nm in DMF is 198,200 M^{-1} cm^{-1}, while

in DMSO the Q-band peak maximum is at 725 nm with a coefficient of 354,166 M^{-1} cm^{-1}. The absorption spectra of Zr-ZnTBIPc and Hf-ZnTBIPc show significant broadening potentially due to inequivalent ligand environments and framework distortions (**Figure 4-4**). Although the Q-band maximum appears to lose its intense absorption after MOF loading, digestion of the framework recovers the characteristic absorption profile of the H_4ZnTBIPc ligand. Dynamic light scattering (DLS) measurements gave number-averaged diameters of 110.9 ± 4.4 nm and 87.8 ± 6.7 nm for Zr-ZnTBIPc and Hf-ZnTBIPc, respectively (**Figure 4-4**). Additionally, Zr-ZnTBIPc and Hf-ZnTBIPc displayed negative zeta potential values of -28.2 ± 3.8 mV and -15.2 ± 1.6 mV, respectively (**Figure 4-4**).

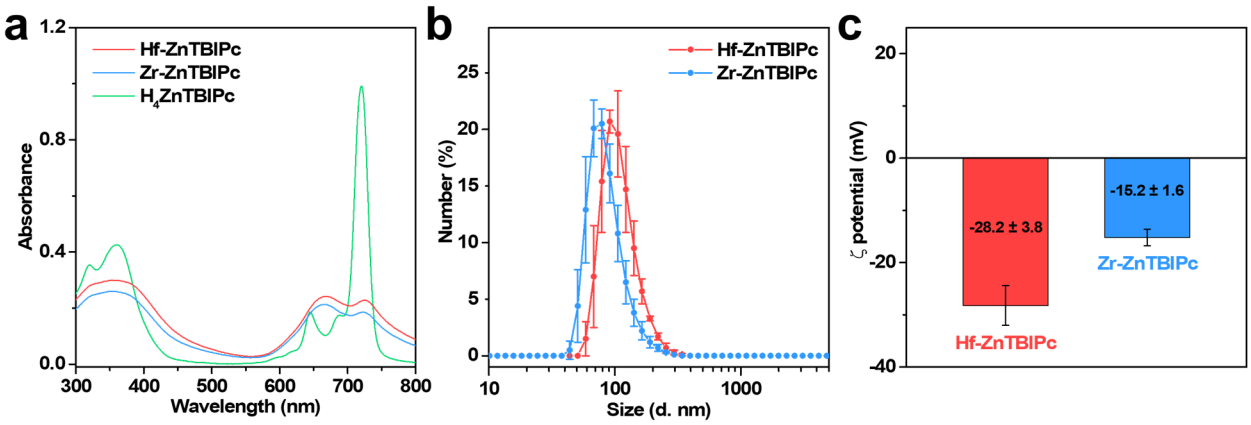

Figure 4-4. Characterization of Hf-ZnTBIPc and Zr-ZnTBIPc. (a) Characteristic UV-Vis spectra of Hf-ZnTBIPc, Zr-ZnTBIPc and H_4ZnTBIPc at 5 µM ZnTBIPc concentrations in DMF. (b) Number-averaged sizes of ethanol dispersions of Hf-ZnTBIPc and Zr-ZnTBIPc. (c) Zeta potential measurements of Hf-ZnTBIPc and Zr-ZnTBIPc in water.

A second Hf nMOF phase was synthesized at 120 °C using formic acid (HCOOH) as modulator, but the structure of this phase is currently unknown. It does not have the same PXRD peak positions or cubic morphology as the acetic acid modulated nMOFs and does not seem to match well with other known structures of TBP-based MOFs (**Figure 4-5**, **Figure 4-6**). Simulated structural analysis using powder indexing did not produce any crystal systems with a reliable figure

of merit as in the case of Hf-ZnTBIPc. Further studies, such as electron diffraction,[43] are likely required to elucidate the structure of this nMOF phase.

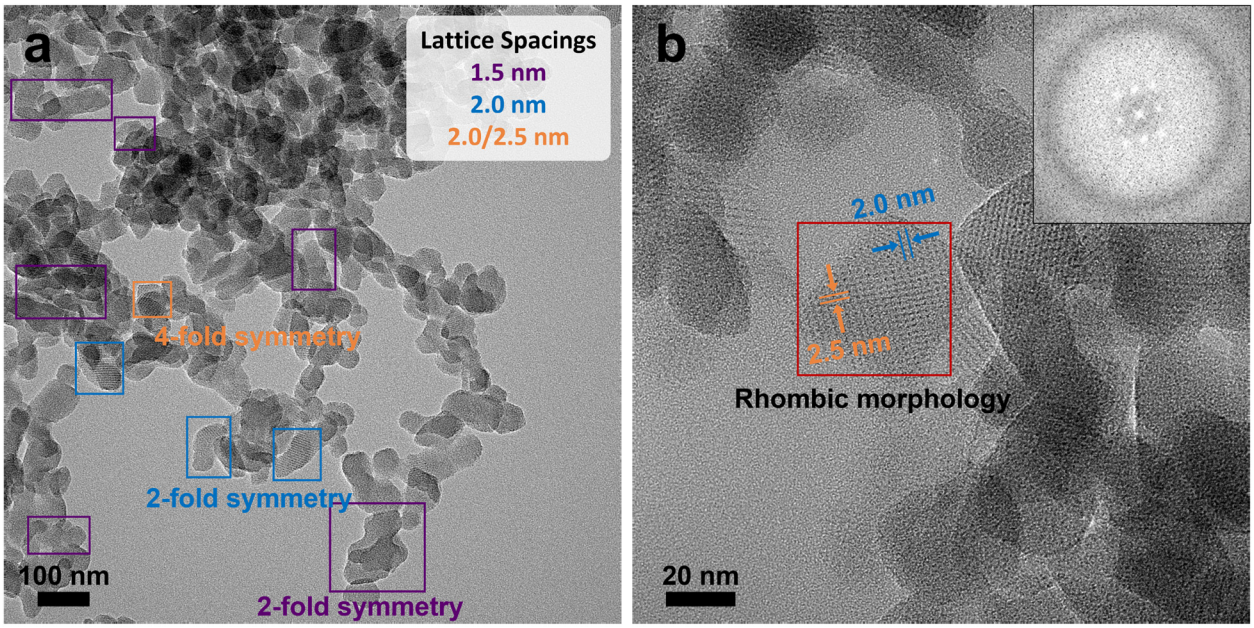

Figure 4-5. Morphological characterization of Hf-ZnTBIPc (unknown phase). (a) TEM image and (b) HR-TEM image of Hf-ZnTBIPc (unknown phase), showing the rounded and rhombic morphology of the particles as well as their 2- or 4-fold symmetry in their FFT depending on the preferred orientation of the nanocrystals on the TEM grid.

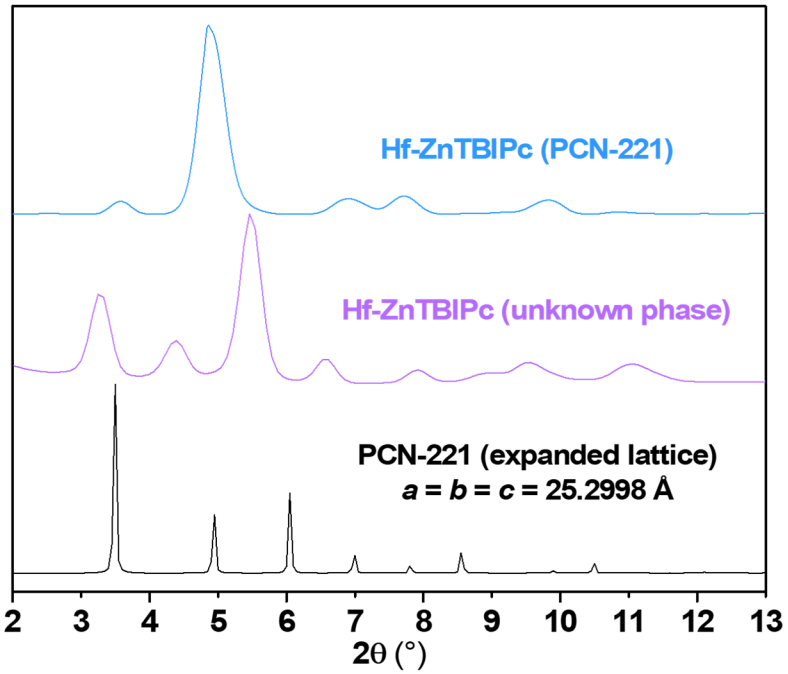

Figure 4-6. Experimental PXRD patterns of Hf-ZnTBIPc (PCN-221), Hf-ZnTBIPc (unknown phase), and simulated PCN-221 with expanded lattice parameters.

4.3 Conclusion

In this chapter, we have designed and synthesized a tetraimidazophthalonitrile ligand with square planar shape and linearly aligned carboxylate groups that can grow nMOFs with Hf and Zr SBUs. The resulting nMOF is the first reported 3D phthalocyanine framework built from metal-carboxylate coordination. More importantly, the ligand is versatile as it leaves room for axial or peripheral functionalization, while maintaining a predictable ligand coordination shape. Therefore, this system may unlock the potential applications of phthalocyanine nMOFs that were previously hindered by their synthetic/geometric inflexibility. We believe the Hf-based nMOF can have strong efficacy in radiotherapy-radiodynamic therapy (RT-RDT) and may also give us mechanistic insight into ligand design for this complex therapeutic modality.

4.4 Experimental section

4.4.1. Materials and methods

All chemical reagents were purchased at the highest quality from commercial sources and used without further purification. Transmission electron microscopy (TEM) was performed on a TECNAI Spirit TEM (120 kV), and high-resolution TEM (HR-TEM) was performed on a TECNAI Spirit F30 TEM (300 kV). Powder X-ray diffraction (PXRD) patterns were obtained on a Bruker D8 Venture diffractometer using a Cu Kα radiation source (λ = 1.54178 Å) and processed with PowderX software. UV-Vis spectra were collected using a Shimadzu UV-2600 UV-Vis spectrophotometer. Dynamic light scattering (DLS) and zeta-potential measurements were collected on a Malvern Zetasizer Nano ZS instrument. ^{1}H and ^{13}C NMR spectra were collected on a Bruker NMR 400 DRX spectrometer at 400 MHz and 101 MHz, respectively, and referenced to the proton resonance resulting from incomplete deuteration of CDCl3 (^{1}H NMR: δ 7.26; ^{13}C NMR:

δ 77.16) or DMSO-d_6 (^{1}H NMR: δ 2.50; ^{13}C NMR: δ 39.52). Matrix-assisted laser desorption/ionization-time of flight high-resolution mass spectrometry (MALDI-TOF HR-MS) was performed on a Bruker autoflex maX MALDI-TOF/TOF using positive-ion reflectron mode. Inductively coupled plasma-mass spectrometry (ICP-MS) data were collected using an Agilent 7700x ICP-MS and analyzed using an ICP-MS Mass Hunter version B01.03. Samples were diluted in a 2% HNO_3 matrix and analyzed with ^{159}Tb and internal standards against a 10-point standard curve between 1 ppb and 500 ppb. The correlation was given R>0.999 for all analyses of interest. Data collection was performed in Spectrum Mode with three replicates per sample and 100 sweeps per replicate.

4.4.2. Synthetic and characterization procedures

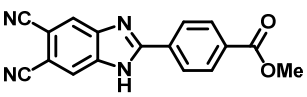

Synthesis of methyl 4-(5,6-dicyano-1H-benzo[d]imidazol-2-yl)benzoate (2). A mixture of 4,5-diaminophthalonitrile (**1**; 4.50 g, 28.45 mmol, 1 equiv.), methyl 4-formylbenzoate (4.67 g, 28.45 mmol, 1 equiv.), and ethanol (465 mL) was added to a round-bottom flask, equipped with a stir bar and a reflux condenser, and heated to reflux. Zinc triflate (1.03 g, 2.85 mmol, 0.1 equiv.) was then added to the mixture and the resulting slurry was refluxed for 24 h. The reaction mixture was cooled to room temperature, filtered, and washed with copious amounts of water and ethanol. The crude solid was collected, recrystallized twice from *N*,*N*-dimethylformamide (DMF), washed with ethanol, and dried under vacuum to afford the benzimidazole product as a white powder (5.09 g, 59% yield).

^{1}H NMR (400 MHz, DMSO-d_6): δ 14.26 (s, 1H), 8.47 (s, 2H), 8.37 (d, J = 8.5 Hz, 2H), 8.16 (d, J = 8.5 Hz, 2H), 3.91 (s, 3H).

^{13}C NMR (101 MHz, DMSO-d_6): δ 166.07, 156.31, 132.97, 132.18, 130.41, 128.07, 117.44, 107.78, 52.92.

MS (ESI): *m/z* calculated for $C_{17}H_{11}N_4O_2^+$ [$(M+H)^+$]: 303.08, found: 303.1.

TLC: R_f = 0.38 (hexanes/THF 3:2)

Note: Reaction times longer than 24 h will result in transesterification of the methyl ester with the ethanol solvent, resulting in the analogous ethyl ester of the benzimidazole. However, this does not affect the final phthalocyanine product in our synthetic route as the ester will be hydrolyzed in the final step.

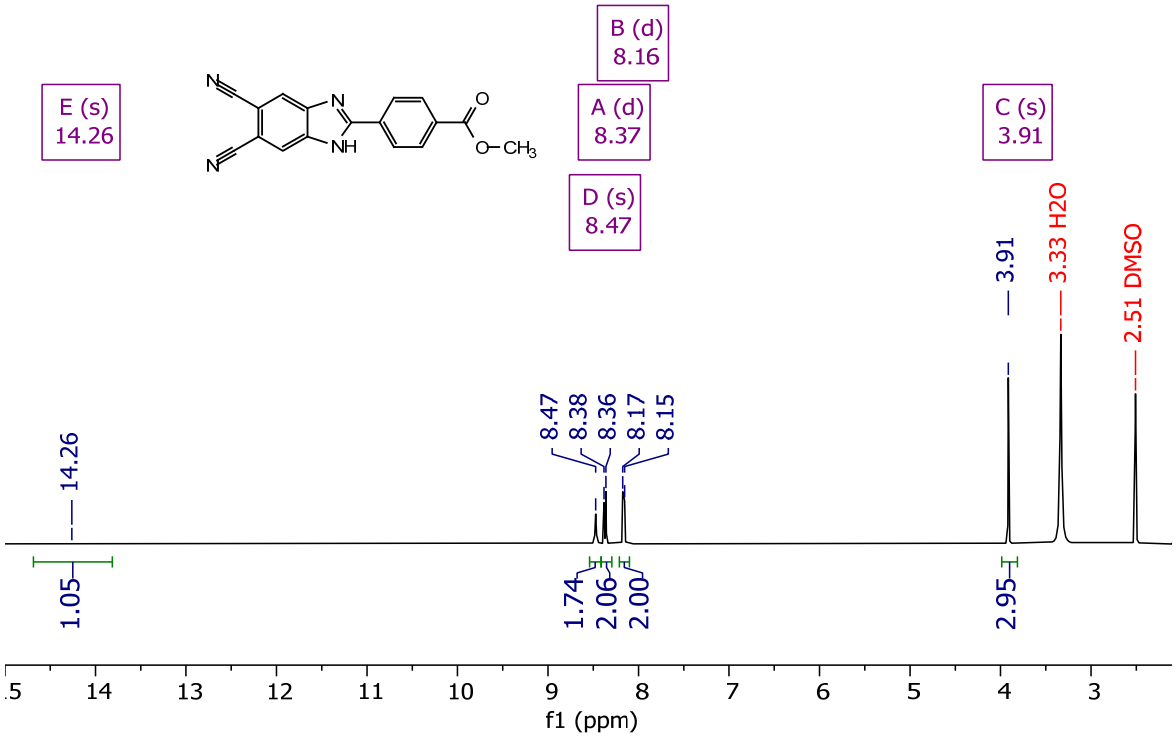

Figure 4-7. ^{1}H NMR spectrum of methyl 4-(5,6-dicyano-1H-benzo[d]imidazol-2-yl)benzoate **2** (400 MHz, DMSO-d_6).

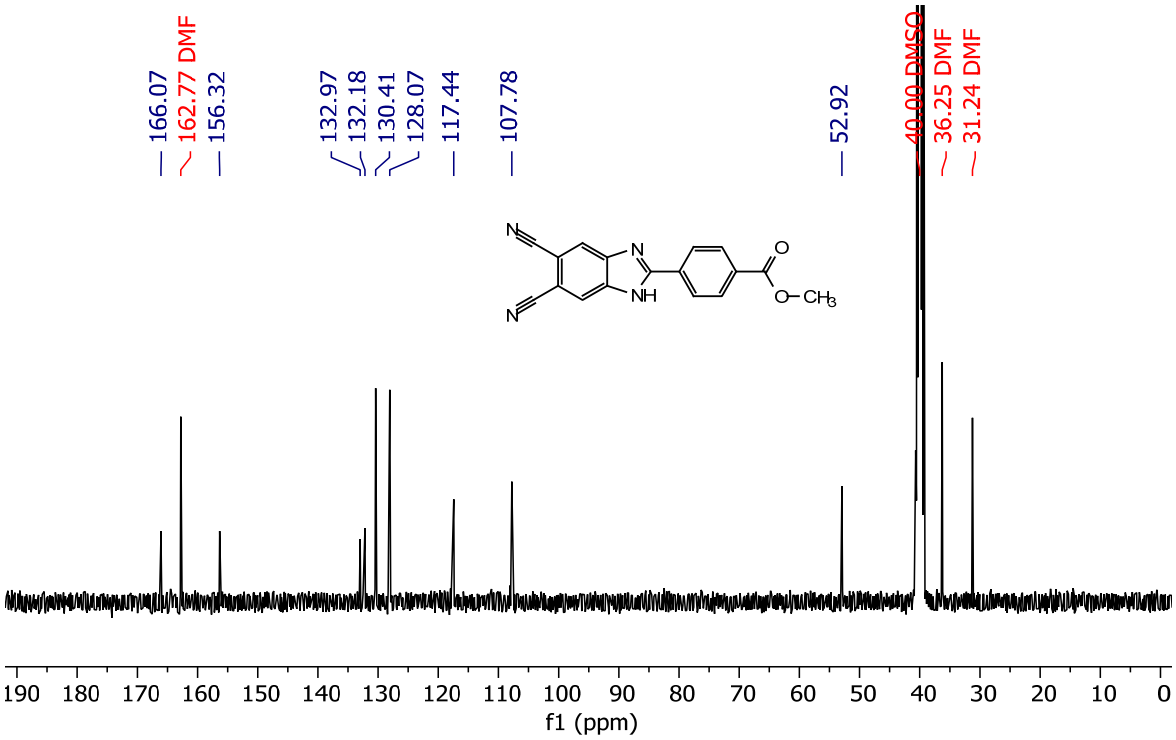

Figure 4-8. ^{13}C NMR spectrum of methyl 4-(5,6-dicyano-1H-benzo[d]imidazol-2-yl)benzoate **2** (101 MHz, DMSO-*d*$_6$).

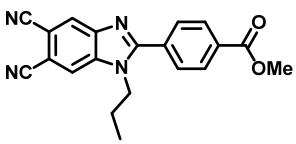

Synthesis of methyl 4-(5,6-dicyano-1-propyl-1H-benzo[d]imidazol-2-yl)benzoate (5). A mixture of methyl 4-(5,6-dicyano-1H-benzo[d]imidazol-2-yl)benzoate (2.50 g, 8.27 mmol, 1 equiv.), K_2CO_3 (5.72 g, 41.35 mmol, 5 equiv.), 1-iodopropane (8.07 mL, 82.70 mmol, 10 equiv.), and THF (300 mL) was added to a 1000 mL round-bottom flask, equipped with a stir bar and a reflux condenser, and heated to reflux. The reaction was monitored by TLC (hexanes:THF 3:2) and further additions of K_2CO_3 and 1-iodopropane were added to the flask every 6-10 hours until completion (~4-5 total additions). The reaction mixture was cooled to room temperature, filtered, and washed with copious amounts of water and ethanol. The crude solid was collected, recrystallized from *N*,*N*-dimethylformamide (DMF), washed with ethanol, and dried under vacuum to afford the *N*-alkylated benzimidazole product **5** as a white powder (2.08g, 73% yield).

^{1}H NMR (400 MHz, DMSO-d_6): δ 8.79 (s, 1H), 8.61 (s, 1H), 8.18 (d, J = 8.6 Hz, 2H), 8.01 (d, J = 8.7 Hz, 2H), 4.42 (t, J = 7.6 Hz, 2H), 3.93 (s, 3H), 1.69 (h, J = 7.6 Hz, 2H), 0.74 (t, J = 7.4 Hz, 3H).

^{13}C NMR (101 MHz, DMSO-d_6): δ 166.10, 157.75, 144.74, 138.46, 133.64, 131.91, 130.27, 126.84, 119.50, 117.44, 107.79, 52.99, 46.93, 23.10, 11.17.

MS (ESI): *m/z* calculated for $C_{20}H_{17}N_4O_2^+$ [$(M+H)^+$]: 345.13, found: 345.2.

TLC: R_f = 0.58 (hexanes/THF 3:2)

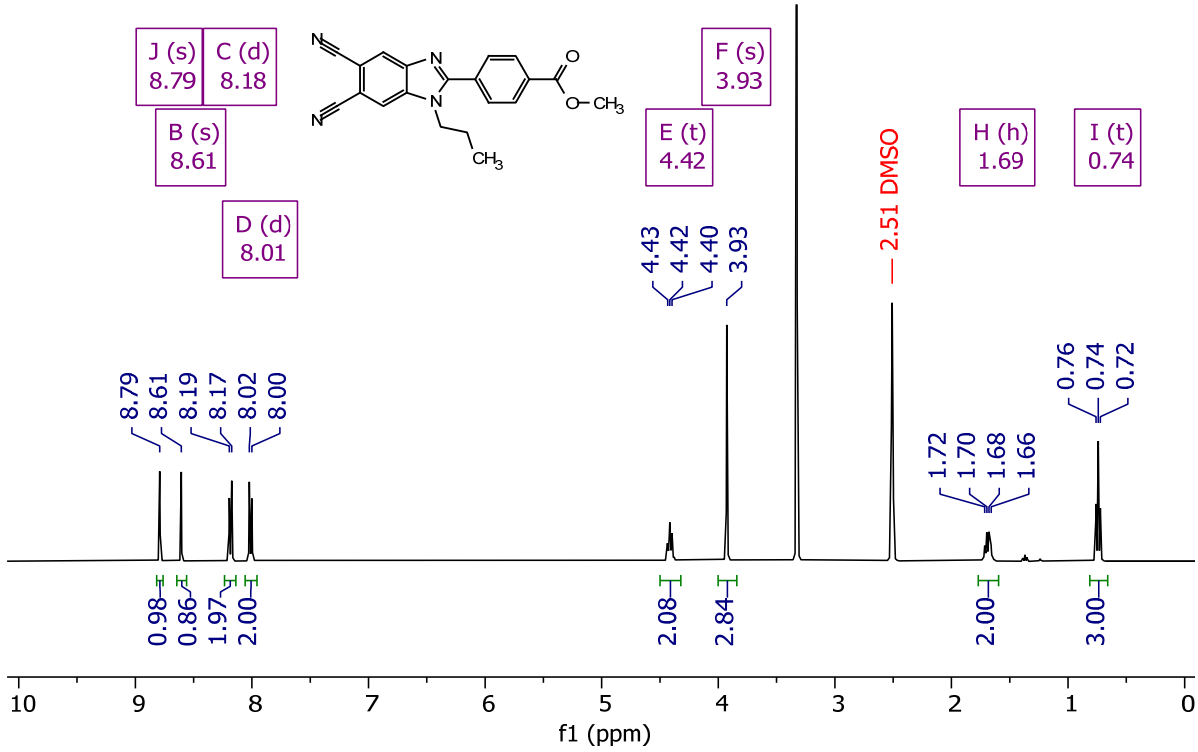

Figure 4-9. ^{1}H NMR spectrum of methyl 4-(5,6-dicyano-1-propyl-1H-benzo[d]imidazol-2-yl)benzoate **5** (400 MHz, DMSO-d_6).

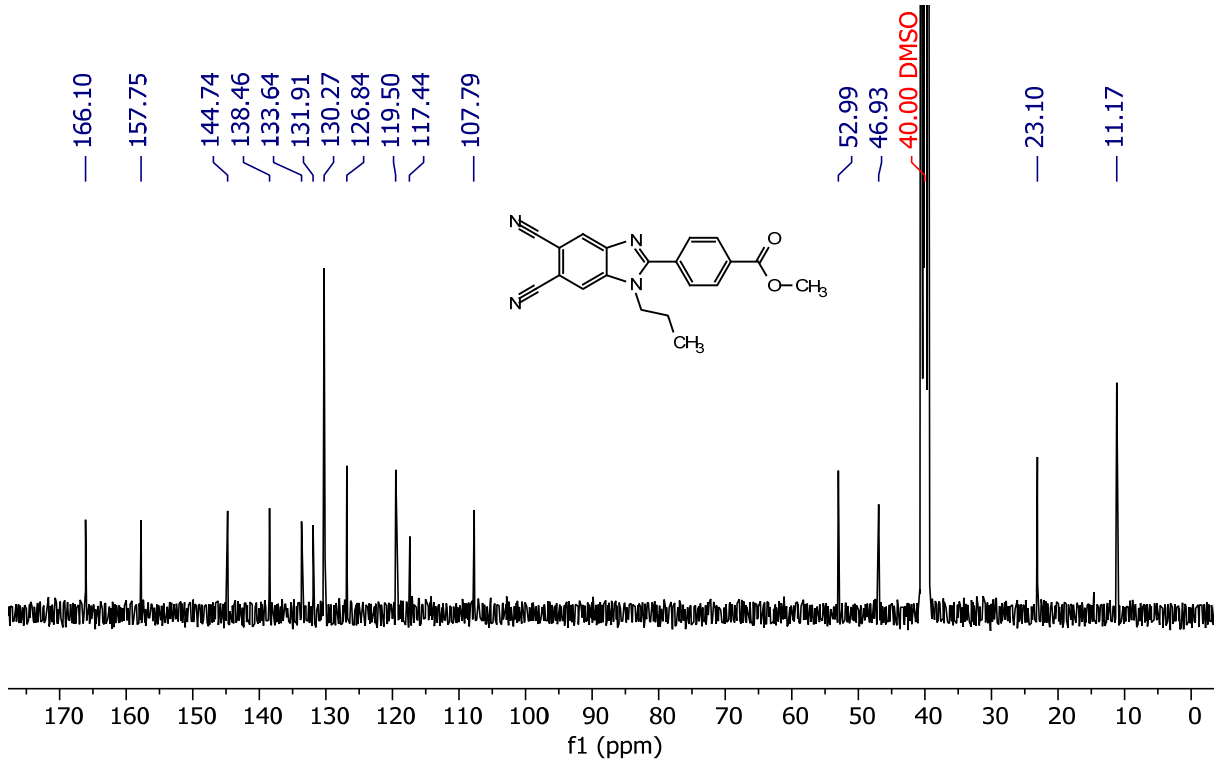

Figure 4-10. ^{13}C NMR spectrum of methyl 4-(5,6-dicyano-1-propyl-1H-benzo[d]imidazol-2-yl)benzoate **5** (101 MHz, DMSO-d_6).

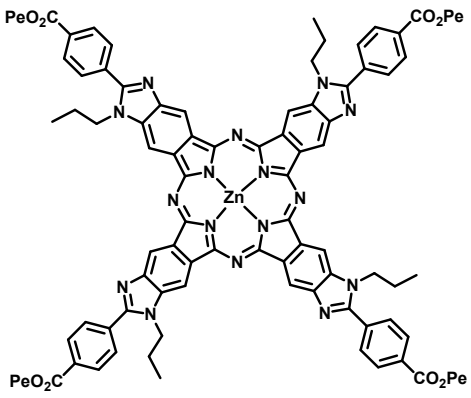

Synthesis of Pe$_4$ZnTBIPc. A mixture of methyl 4-(5,6 dicyano-1-propyl-1H-benzo[d]imidazol-2-yl)benzoate (2.02 g, 5.87 mmol, 1 equiv.), anhydrous $ZnBr_2$ (396 mg, 1.76 mmol, 0.3 equiv.), 1,8-diazabicyclo[5.4.0]undec-7-ene (DBU; 875 µL, 5.87 mmol, 1 equiv.), and anhydrous 1-pentanol (60 mL) was added to an oven-dried 250 mL pressure vessel and stirred in a pre-heated oil bath set to 145 °C for 48 h. The reaction mixture was cooled to room temperature and an acetonitrile/water (4:1) solution was added to the reaction mixture to precipitate the product. The precipitated solid was collected by centrifugation, washed three times with acetonitrile/water (5:1), and dried under vacuum to yield the tetra-pentyl ester phthalocyanine product as a dark green solid (1.65 g, 67% yield).

HR-MS (MALDI-TOF): *m/z* calculated for $C_{96}H_{96}N_{16}O_8Zn^+$ [M^+]: 1664.69, found: 1664.840.

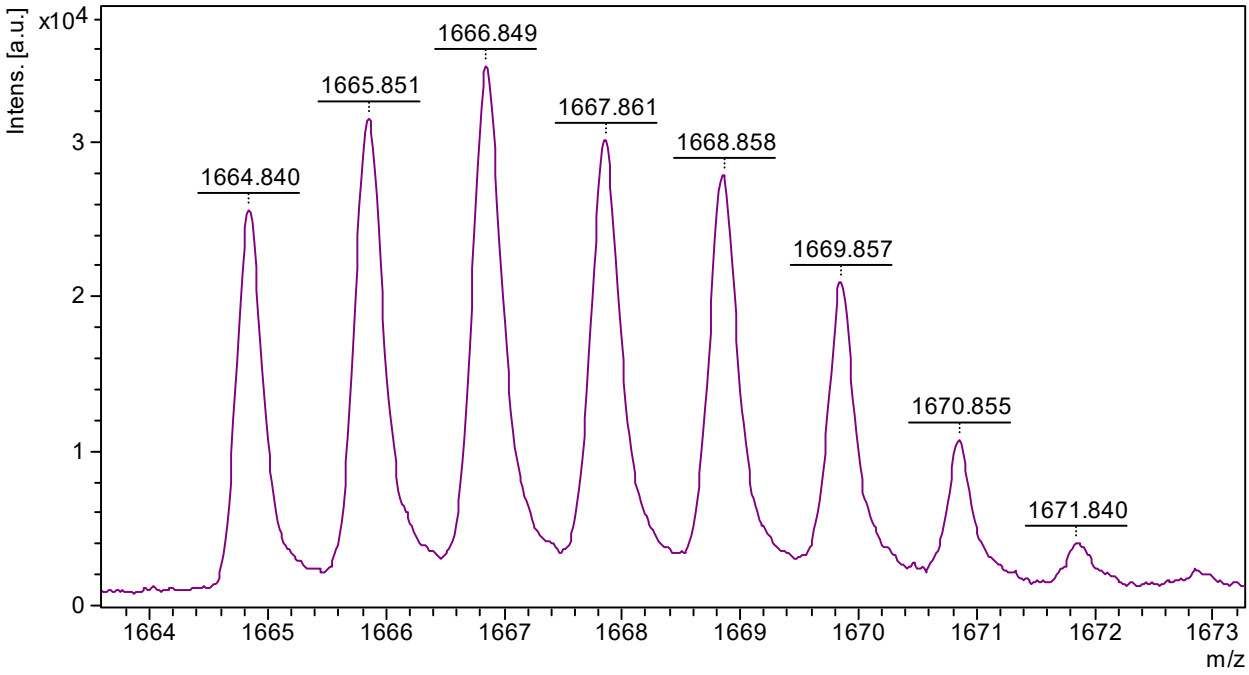

Figure 4-11. HR-MS (MALDI-TOF) spectrum of $Pe_4ZnTBIPc$ showing the isotopic peaks of the molecular ion [M^+].

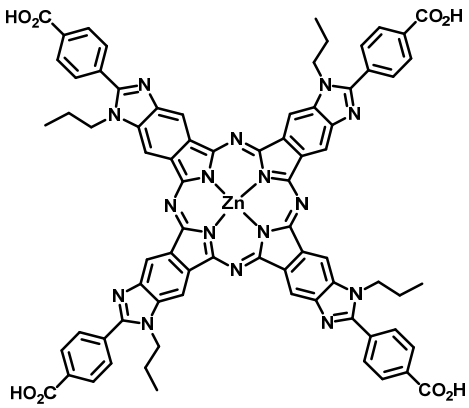

Synthesis of $H_4ZnTBIPc$. A mixture of $Pe_4ZnTBIPc$ (800 mg, 0.48 mmol) dissolved in THF/MeOH (300 mL, 1:1) was added to a 1M aqueous NaOH solution (115 mL) in a 1000 mL round-bottomed flask and refluxed for 24 h. The reaction mixture was cooled to room temperature and the volatile solvents were removed under vacuum. Water was added and the reaction mixture was acidified using 1M HCl until pH = 3. The precipitated solid was collected by centrifugation, washed three times with acetonitrile/water (4:1), and dried under vacuum to yield the tetra-carboxylic acid phthalocyanine product as a dark green solid (534 mg, 80% yield).

HR-MS (MALDI-TOF): *m/z* calculated for $C_{76}H_{56}N_{16}O_8Zn^+$ [M^+]: 1384.38, found: 1384.262.

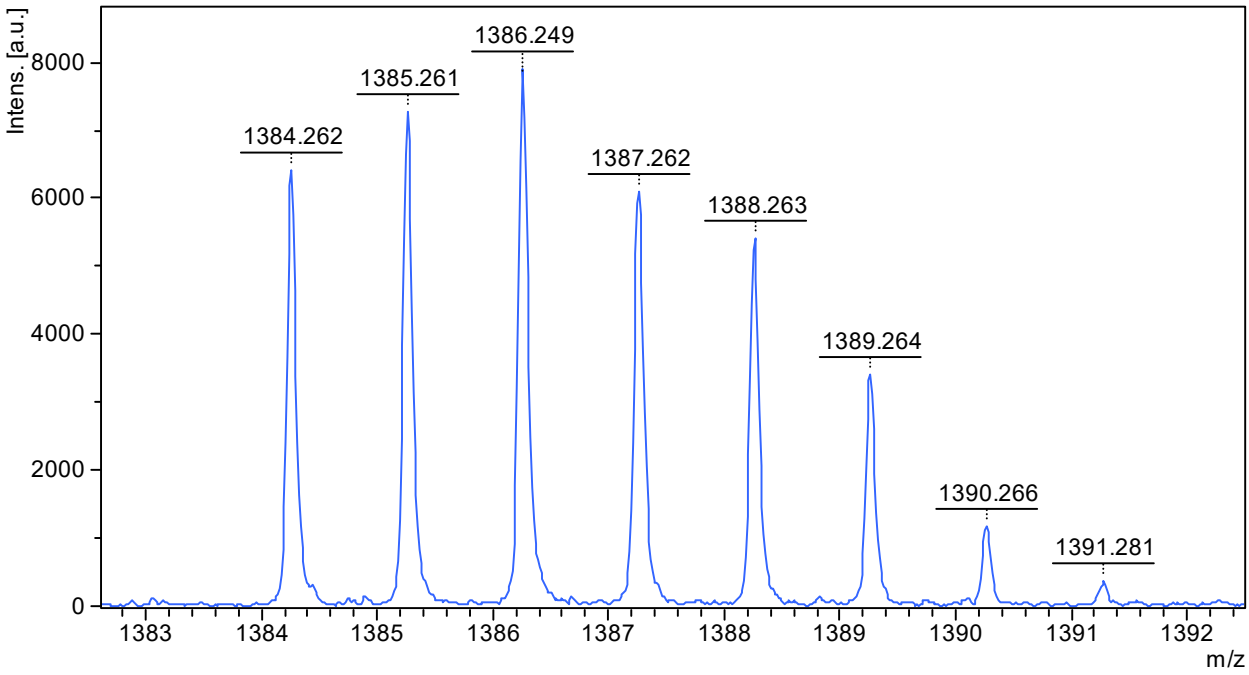

Figure 4-12. HR-MS (MALDI-TOF) spectrum of H_4ZnTBIPc showing the isotopic peaks of the molecular ion [M^+].

Synthesis of Hf-ZnTBIPc. To a 4 mL (1 dram) glass vial was added 0.25 mL of $HfCl_4$ solution (2.0 mg/mL in DMF), 0.25 mL of H_4ZnTBIPc solution (2.9 mg/mL in DMF), and 65 µL of acetic acid (AcOH). The reaction mixture was kept in a 90 °C oven for 48 hr. The green precipitate was collected by centrifugation and washed with DMF, 1% triethylamine (TEA) in ethanol, and ethanol. The precipitate was redispersed in ethanol and stored in the dark (45.2% yield based on ICP-MS analysis).

Synthesis of Zr-ZnTBIPc. To a 4 mL (1 dram) glass vial was added 0.25 mL of $ZrCl_4$ solution (1.44 mg/mL in DMF), 0.25 mL of H_4ZnTBIPc solution (2.9 mg/mL in DMF), and 65 µL of acetic acid (AcOH). The reaction mixture was kept in a 90 °C oven for 48 hr. The green precipitate was

collected by centrifugation and washed with DMF, 1% triethylamine (TEA) in ethanol, and ethanol. The precipitate was redispersed in ethanol and stored in the dark (45.4% yield based on ICP-MS analysis).

Synthesis of Hf-ZnTBIPc (unknown phase). To a 4 mL (1 dram) glass vial was added 0.25 mL of $HfCl_4$ solution (2.0 mg/mL in DMF), 0.25 mL of H_4ZnTBIPc solution (2.9 mg/mL in DMF), and 50 μL of 98% formic acid. The reaction mixture was kept in a 120 °C oven for 48 hr. The green precipitate was collected by centrifugation and washed with DMF, 1% triethylamine (TEA) in ethanol, and ethanol. The precipitate was redispersed in ethanol and stored in the dark (44.9% yield based on ICP-MS analysis).

UV-Vis analysis of nMOFs. 10 μL of a dispersed solution of nMOF was added to a mixture of 940 μL DMSO and 50 μL H_3PO_4. The mixture was then sonicated for about 10 minutes and the UV-Vis absorption spectrum was recorded.

ICP-MS analysis of nMOFs. 10 μL of a dispersed solution of nMOF was added to a mixture of 980 μL HNO_3 and 10 μL HF. The mixture was vortexed and kept at room temperature for 3 days. The sample was then diluted with ultrapure water to 2% HNO_3 and analyzed by ICP-MS.

4.5 References

1. Rio, Y.; Salomé Rodríguez-Morgade, M.; Torres, T., Modulating the electronic properties of porphyrinoids: a voyage from the violet to the infrared regions of the electromagnetic spectrum. *Organic & Biomolecular Chemistry* **2008,** *6* (11), 1877-1894.

2. Lo, P.-C.; Rodríguez-Morgade, M. S.; Pandey, R. K.; Ng, D. K. P.; Torres, T.; Dumoulin, F., The unique features and promises of phthalocyanines as advanced photosensitisers for photodynamic therapy of cancer. *Chemical Society Reviews* **2020,** *49* (4), 1041-1056.

3. Lukyanets, E. A., Phthalocyanines as Photosensitizers in the Photodynamic Therapy of Cancer. *Journal of Porphyrins and Phthalocyanines* **1999,** *03* (06), 424-432.

4. Jakub, R. A. K.; Pavla, P.; Jiri, B.; David, V., Drug Delivery Systems for Phthalocyanines for Photodynamic Therapy. *Anticancer Research* **2019,** *39* (7), 3323.

5. Nyokong, T., Desired properties of new phthalocyanines for photodynamic therapy. *Pure and Applied Chemistry* **2011,** *83* (9), 1763-1779.

6. Sorokin, A. B., Phthalocyanine Metal Complexes in Catalysis. *Chemical Reviews* **2013,** *113* (10), 8152-8191.

7. Lee, B.-H.; Shin, H.; Rasouli, A. S.; Choubisa, H.; Ou, P.; Dorakhan, R.; Grigioni, I.; Lee, G.; Shirzadi, E.; Miao, R. K.; Wicks, J.; Park, S.; Lee, H. S.; Zhang, J.; Chen, Y.; Chen, Z.; Sinton, D.; Hyeon, T.; Sung, Y.-E.; Sargent, E. H., Supramolecular tuning of supported metal phthalocyanine catalysts for hydrogen peroxide electrosynthesis. *Nature Catalysis* **2023,** *6* (3), 234-243.

8. Yang, S.; Yu, Y.; Gao, X.; Zhang, Z.; Wang, F., Recent advances in electrocatalysis with phthalocyanines. *Chemical Society Reviews* **2021,** *50* (23), 12985-13011.

9. Ogunsipe, A.; Maree, D.; Nyokong, T., Solvent effects on the photochemical and fluorescence properties of zinc phthalocyanine derivatives. *Journal of Molecular Structure* **2003,** *650* (1), 131-140.

10. Ghani, F.; Kristen, J.; Riegler, H., Solubility Properties of Unsubstituted Metal Phthalocyanines in Different Types of Solvents. *Journal of Chemical & Engineering Data* **2012,** *57* (2), 439-449.

11. Kadish, K.; Guilard, R.; Smith, K. M., *The Porphyrin Handbook: Phthalocyanines: Synthesis*. Elsevier: 2012.

12. Luo, T.; Nash, G. T.; Xu, Z.; Jiang, X.; Liu, J.; Lin, W., Nanoscale Metal–Organic Framework Confines Zinc-Phthalocyanine Photosensitizers for Enhanced Photodynamic Therapy. *Journal of the American Chemical Society* **2021,** *143* (34), 13519-13524.

13. Nash, G. T.; Luo, T.; Lan, G.; Ni, K.; Kaufmann, M.; Lin, W., Nanoscale Metal–Organic Layer Isolates Phthalocyanines for Efficient Mitochondria-Targeted Photodynamic Therapy. *Journal of the American Chemical Society* **2021,** *143* (5), 2194-2199.

14. Matheu, R.; Gutierrez-Puebla, E.; Monge, M. Á.; Diercks, C. S.; Kang, J.; Prévot, M. S.; Pei, X.; Hanikel, N.; Zhang, B.; Yang, P.; Yaghi, O. M., Three-Dimensional Phthalocyanine Metal-Catecholates for High Electrochemical Carbon Dioxide Reduction. *Journal of the American Chemical Society* **2019,** *141* (43), 17081-17085.

15. Nagatomi, H.; Yanai, N.; Yamada, T.; Shiraishi, K.; Kimizuka, N., Synthesis and Electric Properties of a Two-Dimensional Metal-Organic Framework Based on Phthalocyanine. *Chemistry – A European Journal* **2018,** *24* (8), 1806-1810.

16. Jia, H.; Yao, Y.; Zhao, J.; Gao, Y.; Luo, Z.; Du, P., A novel two-dimensional nickel phthalocyanine-based metal–organic framework for highly efficient water oxidation catalysis. *Journal of Materials Chemistry A* **2018,** *6* (3), 1188-1195.

17. Zhong, H.; Ly, K. H.; Wang, M.; Krupskaya, Y.; Han, X.; Zhang, J.; Zhang, J.; Kataev, V.; Büchner, B.; Weidinger, I. M.; Kaskel, S.; Liu, P.; Chen, M.; Dong, R.; Feng, X., A Phthalocyanine-Based Layered Two-Dimensional Conjugated Metal–Organic Framework as a Highly Efficient Electrocatalyst for the Oxygen Reduction Reaction. *Angewandte Chemie International Edition* **2019,** *58* (31), 10677-10682.

18. Yi, J. D.; Si, D. H.; Xie, R.; Yin, Q.; Zhang, M. D.; Wu, Q.; Chai, G. L.; Huang, Y. B.; Cao, R., Conductive Two-Dimensional Phthalocyanine-based Metal–Organic Framework Nanosheets for Efficient Electroreduction of CO2. *Angewandte Chemie* **2021,** *133* (31), 17245-17251.

19. Kappus, H.; Sies, H., Toxic drug effects associated with oxygen metabolism: Redox cycling and lipid peroxidation. *Experientia* **1981,** *37* (12), 1233-1241.

20. Cohen, G. M.; d'Arcy Doherty, M., Free radical mediated cell toxicity by redox cycling chemicals. *The British journal of cancer. Supplement* **1987,** *8*, 46-52.

21. Valko, M.; Morris, H.; Cronin, M. T., Metals, toxicity and oxidative stress. *Current medicinal chemistry* **2005,** *12* (10), 1161-208.

22. Feng, D.; Jiang, H.-L.; Chen, Y.-P.; Gu, Z.-Y.; Wei, Z.; Zhou, H.-C., Metal–Organic Frameworks Based on Previously Unknown Zr8/Hf8 Cubic Clusters. *Inorganic Chemistry* **2013,** *52* (21), 12661-12667.

23. Lu, K.; He, C.; Lin, W., Nanoscale Metal–Organic Framework for Highly Effective Photodynamic Therapy of Resistant Head and Neck Cancer. *Journal of the American Chemical Society* **2014,** *136* (48), 16712-16715.

24. Lu, K.; He, C.; Lin, W., A Chlorin-Based Nanoscale Metal–Organic Framework for Photodynamic Therapy of Colon Cancers. *Journal of the American Chemical Society* **2015,** *137* (24), 7600-7603.

25. Lu, K.; He, C.; Guo, N.; Chan, C.; Ni, K.; Lan, G.; Tang, H.; Pelizzari, C.; Fu, Y.-X.; Spiotto, M. T.; Weichselbaum, R. R.; Lin, W., Low-dose X-ray radiotherapy–radiodynamic therapy via nanoscale metal–organic frameworks enhances checkpoint blockade immunotherapy. *Nature Biomedical Engineering* **2018,** *2* (8), 600-610.

26. Feng, D.; Gu, Z. Y.; Li, J. R.; Jiang, H. L.; Wei, Z.; Zhou, H. C., Zirconium-metalloporphyrin PCN-222: mesoporous metal–organic frameworks with ultrahigh stability as biomimetic catalysts. *Angewandte Chemie* **2012,** *124* (41), 10453-10456.

27. Feng, D.; Chung, W.-C.; Wei, Z.; Gu, Z.-Y.; Jiang, H.-L.; Chen, Y.-P.; Darensbourg, D. J.; Zhou, H.-C., Construction of Ultrastable Porphyrin Zr Metal–Organic Frameworks through Linker Elimination. *Journal of the American Chemical Society* **2013,** *135* (45), 17105-17110.

28. Dumoulin, F.; Durmuş, M.; Ahsen, V.; Nyokong, T., Synthetic pathways to water-soluble phthalocyanines and close analogs. *Coordination Chemistry Reviews* **2010,** *254* (23), 2792-2847.

29. Haldar, R.; Fu, Z.; Joseph, R.; Herrero, D.; Martín-Gomis, L.; Richards, B. S.; Howard, I. A.; Sastre-Santos, A.; Wöll, C., Guest-responsive polaritons in a porous framework: chromophoric sponges in optical QED cavities. *Chemical Science* **2020,** *11* (30), 7972-7978.

30. Sobrino-Bastán, V.; Martín-Gomis, L.; Sastre-Santos, Á., Synthesis of 4-methylthiophenyl silicon phthalocyanines axially substituted with carboxylic acids for MOF materials. *Journal of Porphyrins and Phthalocyanines* **2023,** *27* (01n04), 331-339.

31. Li, Z.; Lieberman, M., Axial Reactivity of Soluble Silicon(IV) Phthalocyanines. *Inorganic Chemistry* **2001,** *40* (5), 932-939.

32. Mitra, K.; Hartman, M. C. T., Silicon phthalocyanines: synthesis and resurgent applications. *Organic & Biomolecular Chemistry* **2021,** *19* (6), 1168-1190.

33. Takakura, H.; Matsuhiro, S.; Kobayashi, M.; Goto, Y.; Harada, M.; Taketsugu, T.; Ogawa, M., Axial-ligand-cleavable silicon phthalocyanines triggered by near-infrared light toward design of photosensitizers for photoimmunotherapy. *Journal of Photochemistry and Photobiology A: Chemistry* **2022,** *426*, 113749.

34. Youngblood, W. J., Synthesis of a New trans-A2B2 Phthalocyanine Motif as a Building Block for Rodlike Phthalocyanine Polymers. *The Journal of Organic Chemistry* **2006,** *71* (9), 3345-3356.

35. Topal, S. Z.; Önal, E.; Gürek, A. G.; Hirel, C., pH-induced "off–on–off" type molecular switch behaviors of zinc and free tetraimidazophthalocyanines. *Dalton Transactions* **2013,** *42* (32), 11528-11536.

36. Kudrik, E. V.; Shaposhnikov, G. P., Symmetrical tetrasubstituted phtalocyanines containing condensed 2-alkylimidazole units. *Mendeleev communications* **1999,** *9* (2), 85-86.

37. Önal, E.; Dumoulin, F.; Hirel, C., Tetraimidazophthalocyanines: influence of protonation and aggregation on spectroscopic observations. *Journal of Porphyrins and Phthalocyanines* **2009,** *13* (06), 702-711.

38. Srinivasulu, R.; Kumar, K. R.; Satyanarayana, P. V. V., Facile and Efficient Method for Synthesis of Benzimidazole Derivatives Catalyzed by Zinc Triflate. *Green and Sustainable Chemistry* **2014,** *Vol.04No.01*, 5.

39. Singh, M. P.; Sasmal, S.; Lu, W.; Chatterjee, M. N., Synthetic utility of catalytic Fe (III)/Fe (II) redox cycling towards fused heterocycles: a facile access to substituted benzimidazole, bisbenzimidazole and imidazopyridine derivatives. *Synthesis* **2000,** *2000* (10), 1380-1390.

40. Grimmett, M. R., *Imidazole and benzimidazole synthesis*. Academic press: 1997.

41. Holder, C. F.; Schaak, R. E., Tutorial on Powder X-ray Diffraction for Characterizing Nanoscale Materials. *ACS Nano* **2019,** *13* (7), 7359-7365.

42. De Wolff, P. M., A simplified criterion for the reliability of a powder pattern indexing. *Journal of Applied Crystallography* **1968,** *1* (2), 108-113.

43. Dai, R.; Peng, F.; Ji, P.; Lu, K.; Wang, C.; Sun, J.; Lin, W., Electron Crystallography Reveals Atomic Structures of Metal–Organic Nanoplates with M12(μ3-O)8(μ3-OH)8(μ2-OH)6 (M = Zr, Hf) Secondary Building Units. *Inorganic Chemistry* **2017,** *56* (14), 8128-8134.

Chapter 5: Two-Dimensional Nanosonosensitizers Facilitate Energy Transfer to Enhance Sonodynamic Therapy

5.1 Introduction

Sonodynamic therapy (SDT) utilizes ultrasonic cavitation to produce broad-spectrum sonoluminescence that can excite sonosensitizers (SSs) for the generation of cytotoxic reactive oxygen species (ROS).[1-4] With significantly increased tissue penetration depth, SDT has emerged as a promising alternative modality to photodynamic therapy (PDT).[5-12] Although organic sensitizers such as porphyrins are efficacious for PDT, they have proven inadequate for SDT, likely due to their nonideal tumor uptake, low solubility in physiological environments, and, more importantly, the very low emission intensity of sonoluminescence compared to direct light irradiation in PDT.[13-17] Low aqueous solubility of SSs leads to aggregation-induced quenching (AIQ) of their excited states, which impairs ROS generation.[18-19] Nanotechnology has been used to isolate and deliver SSs to reduce AIQ and increase bioavailability.[20-25]

Nanoscale metal–organic frameworks (MOFs) have provided an exceptionally versatile platform for designing nano-photosensitizers for PDT owing to their structural tunability, porosity, and ability to isolate organic photosensitizers in high loadings in a rigid framework.[26-32] However, MOFs have not been extensively explored as nano-sonosensitizers for SDT and have shown only modest SDT efficacy to date.[33-37] Unlike MOF-based nano-photosensitizers, no established methods exist to improve and optimize ROS generation from SS-loaded MOFs under ultrasound (US) irradiation.

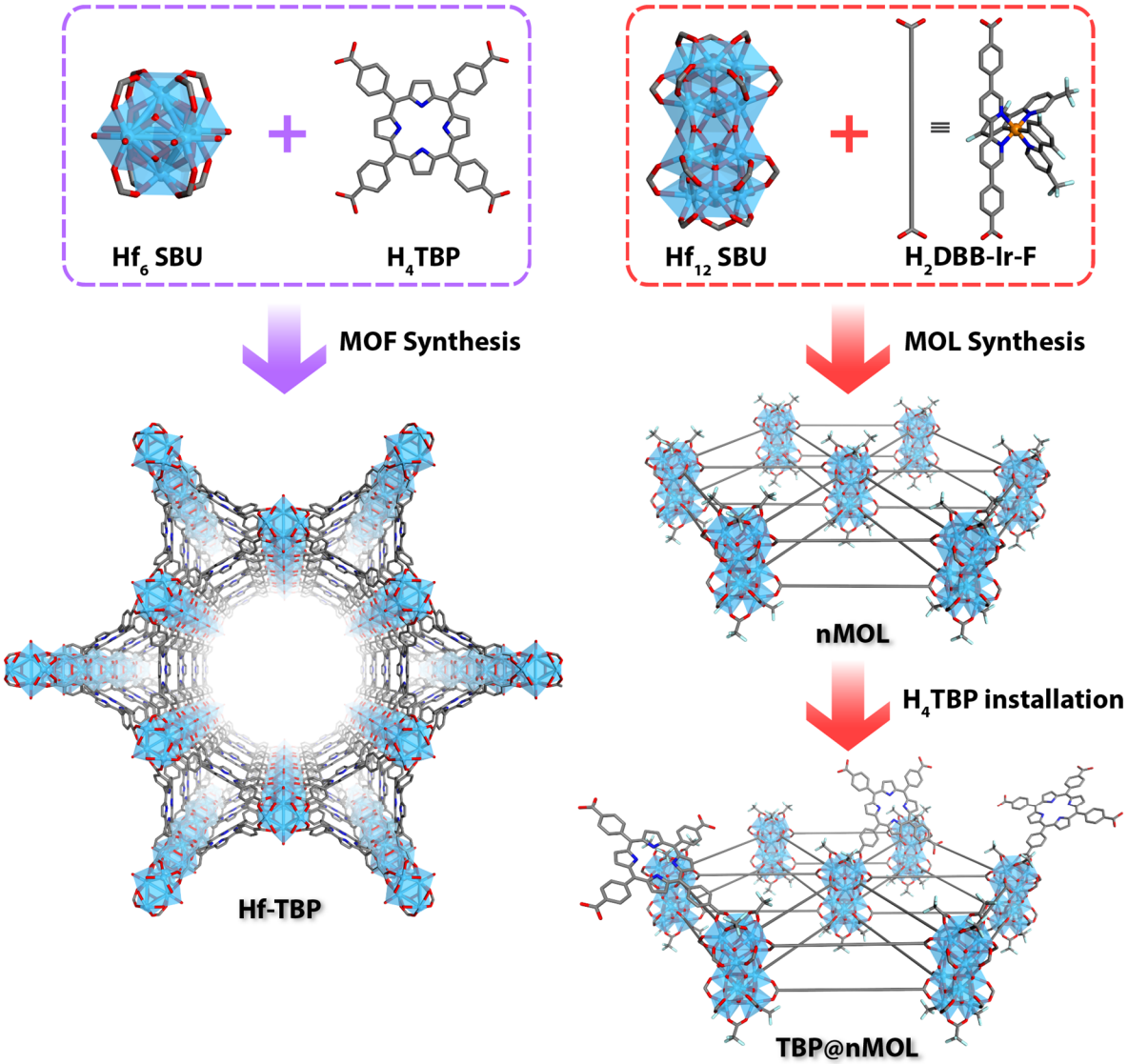

Figure 5-1. Synthesis of Hf-TBP and TBP@MOL. TBP SSs are rigidly confined in the 3D framework of Hf-TBP but flexibly anchored to the SBUs of the 2D MOL in TBP@MOL (orange: Ir, sky blue: Hf, pale light blue: F, red: O, blue: N, grey: C; H atoms are omitted for clarity).

In this chapter, the design of a new 2D nanoscale metal–organic layer (MOL), TBP@MOL, for enhanced singlet oxygen ($^1O_2$) generation. TBP@MOL was prepared by anchoring 5,10,15,20-tetra(*p*-benzoato)porphyrin (TBP) sensitizers to the Hf_{12} SBUs of the MOL comprising Hf_{12} SBUs and $Ir(DBB)[dF(CF_3)ppy]_2^+$ (denoted as DBB-Ir) bridging ligands. Under US irradiation, TBP@MOL shows 14.1- and 7.4-fold higher $^1O_2$ generation than TBP and Hf-TBP, a 3D TBP-based MOF, respectively. With proximity of TBP sensitizers to the DBB-Ir donor ligands (~10 Å)

via flexible TBP attachment to the SBUs, TBP@MOL enables effective SDT via triplet–triplet Dexter energy transfer from excited DBB-Ir to SBU-anchored TBP sensitizers and enhances energy transfer between excited triplet-state TBP and ground-state triplet oxygen ($^3O_2$). Consequently, TBP@MOL displays significantly higher SDT efficacy than its Hf-TBP and free TBP counterparts on mouse models of colon and breast cancer.

5.2 Results and discussion

5.2.1. Synthesis and characterization

TBP@MOL was synthesized in two steps (**Figure 5-1**). Free-standing Hf_{12}-DBB-Ir MOL was synthesized as previously reported through a solvothermal reaction between $HfCl_4$ and DBB-Ir in DMF at 80 °C with trifluoroacetic acid (TFA) and water as modulators.[38] The MOL is built from an infinite 2D network of Hf_{12} SBUs laterally bridged by DBB-Ir and vertically terminated by TFA capping agents to afford a monolayer structure with **kgd** topology and the ideal formula $Hf_{12}(\mu_3\text{-}O)_8(\mu_3\text{-}OH)_8(\mu_2\text{-}OH)_6(DBB\text{-}Ir)_6(TFA)_6$ (**Figure 5-2**). ^{19}F NMR analysis of the digested MOL confirmed the DBB-Ir to TFA ratio of 1:1 (**Figure 5-34**). Transmission electron microscopy (TEM) and atomic force microscopy (AFM) imaging of the MOL confirmed the monolayer morphology with a diameter of ~250 nm and a thickness of ~1.8 nm (**Figure 5-2**).

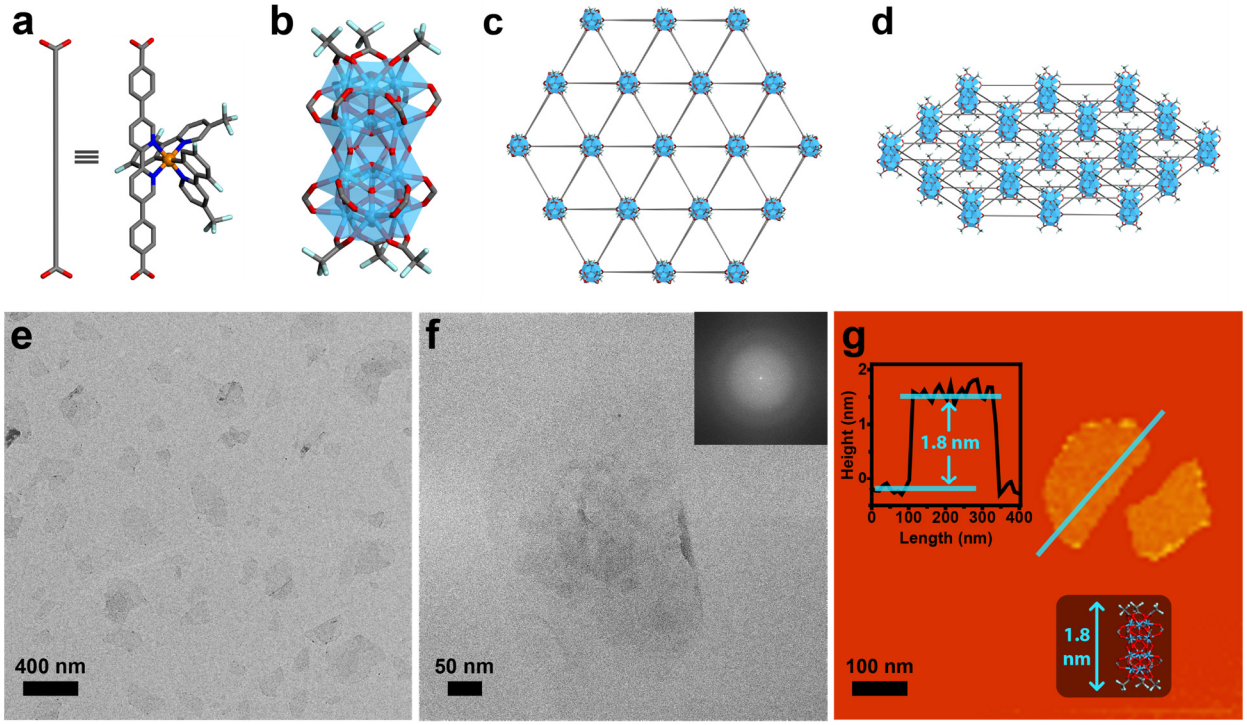

Figure 5-2. Structure model and morphological characterization of MOL. (a) Simplified (left) and full (right) structure model of bridging ligand DBB-Ir. (b) The structure of SBU $Hf_{12}(\mu_3\text{-}O)_8(\mu_3\text{-}OH)_8(\mu_2\text{-}OH)_6(RCO_2)_{12}(TFA)_6$ [RCO_2 represents the carboxylate group on DBB-Ir]. (c) A view along the *c* axis of the MOL showing its monolayer morphology. (d) Side view of the MOL showing the positions of the bridging DBB-Ir ligands within the monolayered framework. (e) TEM image of the MOL. (f) HR-TEM image of the MOL with its FFT (inset). (g) AFM topographic image, measured height profile (inset, left) and modeled height (inset, bottom) of the MOL.

TBP SSs were covalently anchored to the MOL by partially replacing TFA capping agents on Hf_{12} SBUs via carboxylate exchange to afford TBP@MOL with the calculated formula $(TBP)_{1.7}@Hf_{12}(\mu_3\text{-}O)_8(\mu_3\text{-}OH)_8(\mu_2\text{-}OH)_6(DBB\text{-}Ir\text{-}F)_6(TFA)_{4.3}$ (**Figure 5-3**). ^{19}F NMR analysis of digested TBP@MOL displayed a decreased TFA to DBB-Ir ratio compared to the MOL, supporting the partial replacement of TFA with TBP on the MOL (**Figure 5-4**). The remaining TFA signal in the ^{19}F NMR spectrum indicates that the large size of TBP prevented complete replacement of all TFA groups (**Figure 5-4**). Upon TBP conjugation to the cationic MOL, the zeta (ζ) potential reversed from $+38.5 \pm 1.0$ mV to -25.3 ± 0.4 mV, consistent with the surface loading of partially deprotonated (anionic) TBP (**Figure 5-5**). The presence of both TBP and DBB-Ir in

TBP@MOL was supported by the presence of their characteristic UV–Vis absorption peaks and ^{1}H NMR signals in the digested TBP@MOL (**Figure 5-5**, **Figure 5-36**). Dynamic light scattering (DLS) measurements gave number-averaged sizes of 221.0 ± 5.7 nm and 203.7 ± 21.0 nm for the MOL and TBP@MOL, respectively (**Figure 5-5**).

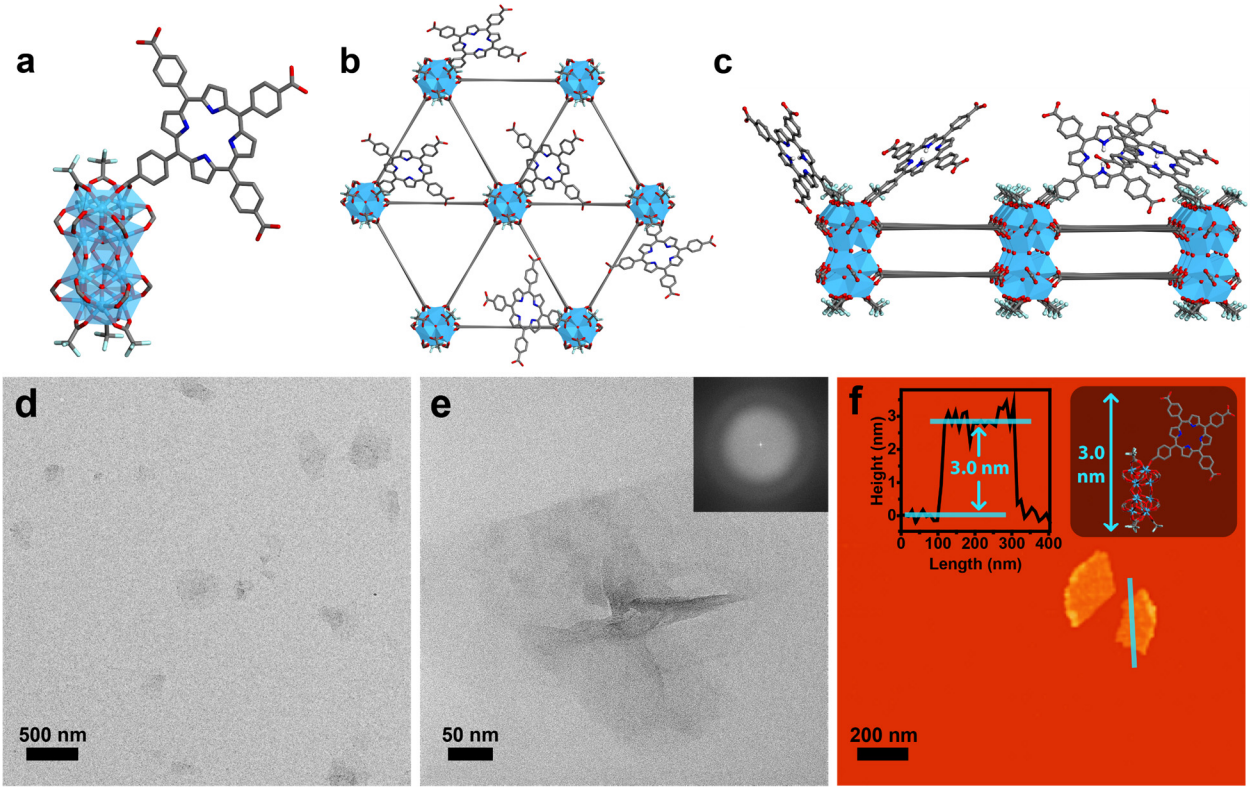

Figure 5-3. Structure model and morphological characterization of TBP@MOL. (a) The structure of monosubstituted SBU $Hf_{12}(\mu_3\text{-}O)_8(\mu_3\text{-}OH)_8(\mu_2\text{-}OH)_6(\mu_2\text{-}RCO_2)_{12}(\mu_2\text{-}TFA)_5(TBP)$ [RCO_2 represents the carboxylate group on DBB-Ir]. (b) A view along the *c* axis of TBP@MOL showing its monolayer morphology. (c) Side view of TBP@MOL showing SBU-anchored TBP sensitizers. Although not shown here, TBP can replace TFA on the top or bottom of the SBU. (e) TEM image of the TBP@MOL. (f) HR-TEM image of TBP@MOL with its FFT (inset). (g) AFM topographic image, measured height profile (inset, left) and modeled height (inset, bottom) of the TBP@MOL.

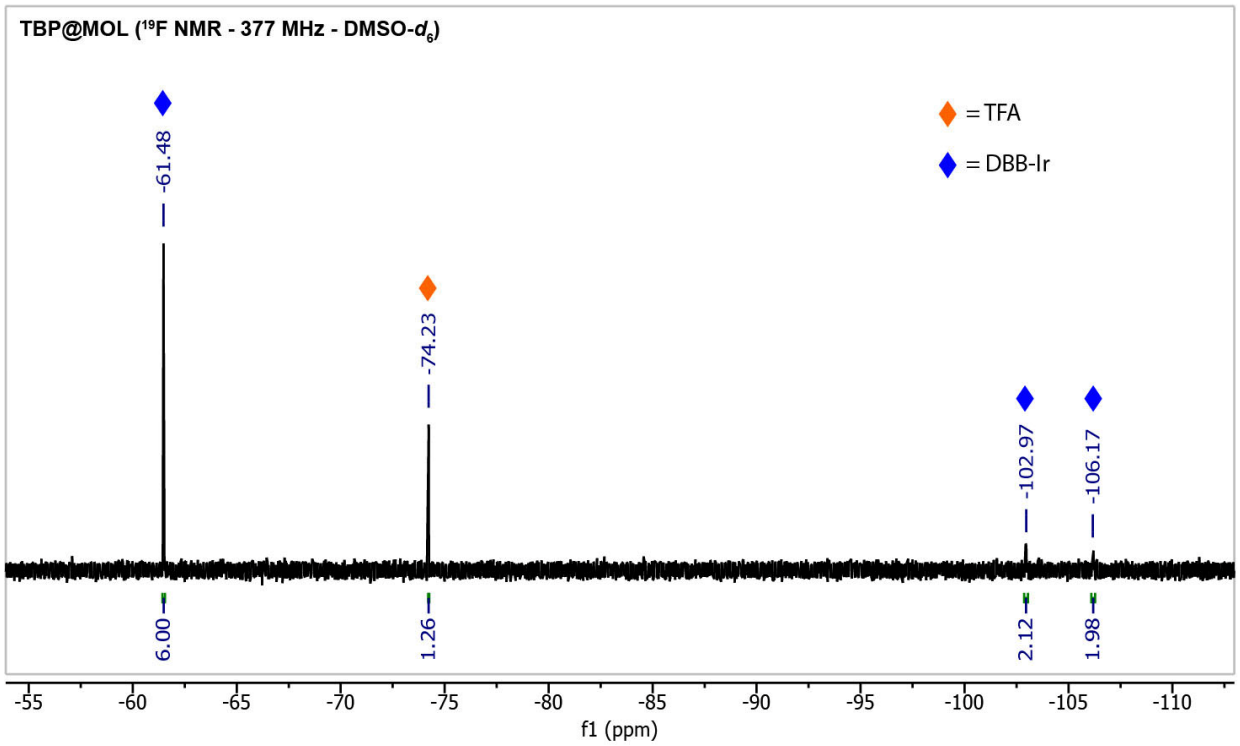

Figure 5-4. ^{19}F NMR spectrum of digested TBP@MOL. Digested TBP@MOL in DMSO-d_6 shows a reduction in the DBB-Ir to TFA integrated signal ratio compared to the MOL, suggesting partial carboxylate exchange of TFA with TBP on the Hf_{12} SBUs.

The powder X-ray diffraction (PXRD) pattern of TBP@MOL matched well with that of the MOL and the simulated pattern for the Hf_{12} MOL structure model (**Figure 5-5**). TEM imaging indicated that TBP@MOL retained the monolayer morphology of the MOL, with a diameter of ~250 nm (**Figure 5-3**). AFM imaging of TBP@MOL displayed a thickness of ~3.0 nm, which is consistent with the modeled height of a Hf_{12} SBU capped with a TBP ligand (**Figure 5-3**). TBP@MOL was stable in aqueous solutions and retained both its crystallinity and morphology after US irradiation in water (3.4 MHz, 1.0 or 2.0 W/cm^2 , 50% duty cycle, and 10 min; **Figure 5-6**, **Figure 5-7**). The TBP loading was calculated to be 12.3 wt% based on UV−Vis absorption spectroscopy and inductively coupled plasma-mass spectrometry (ICP-MS), corresponding to a TBP: Hf_{12} SBU ratio of 1.7:1.

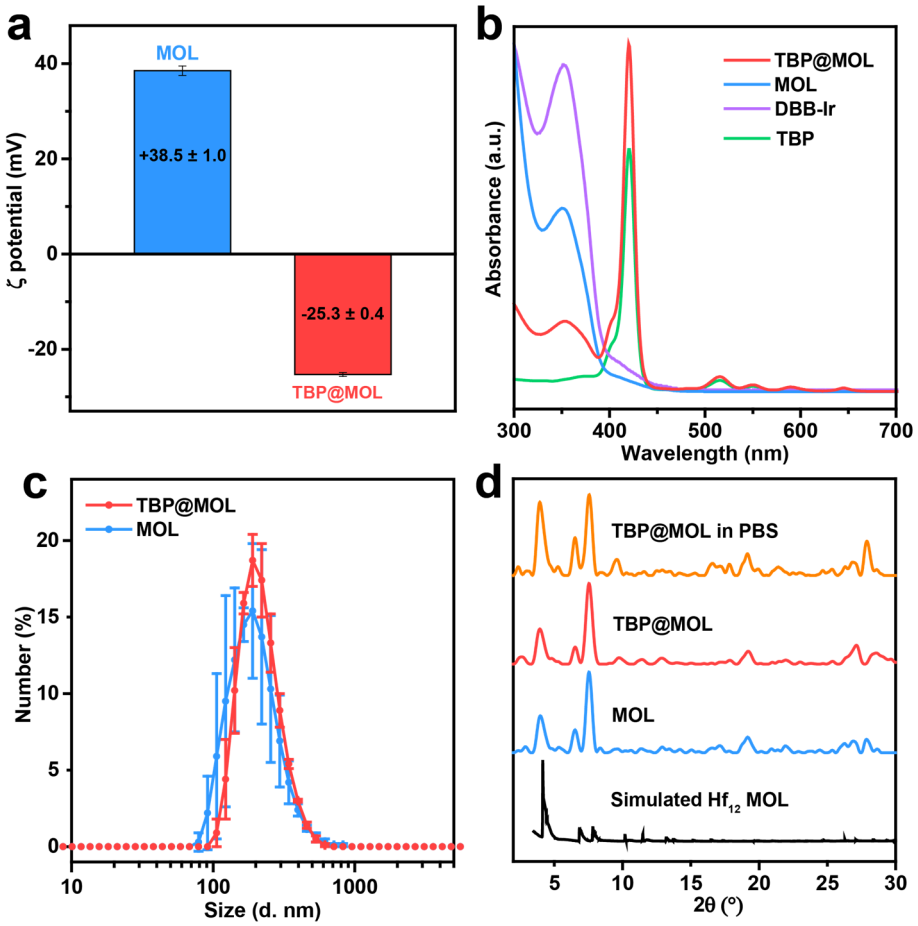

Figure 5-5. Characterization of TBP@MOL. (a) Zeta (ζ) potentials of MOL and TBP@MOL in water. (b) Normalized UV−Vis absorption spectra of TBP, DBB-Ir, MOL, and TBP@MOL in DMSO. (c) Number-averaged diameters of MOL and TBP@MOL in ethanol. (d) PXRD patterns of TBP@MOL (as-synthesized and after soaking in PBS for 24 h), MOL, and the simulated pattern of Hf_{12}-MOL.

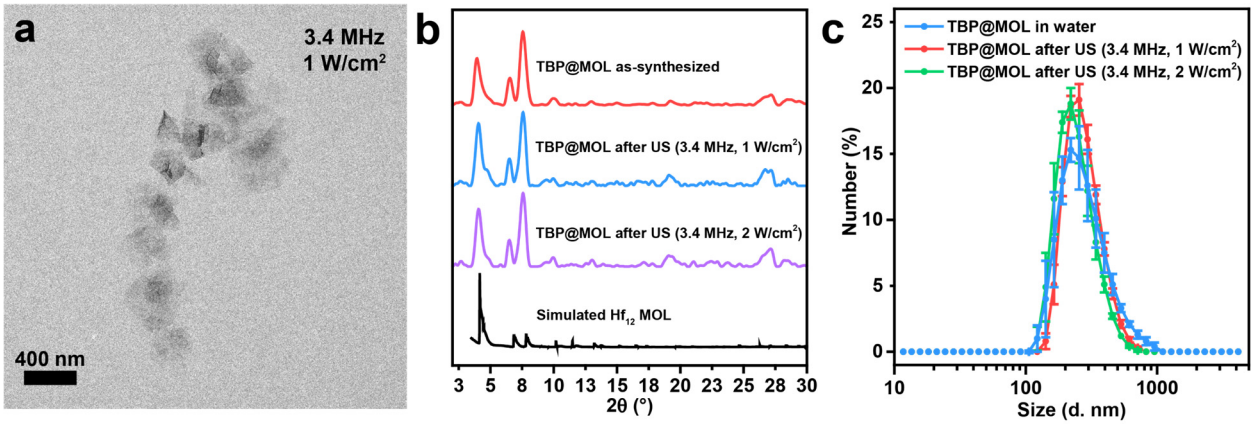

Figure 5-6. Stability of TBP@MOL after US irradiation. (a) TEM image, (b) PXRD patterns, and (c) Number-averaged diameters of TBP@MOL before and after US irradiation. All US irradiation was 1 or 2 W/cm^2, 3.4 MHz, and 50% duty cycle for 10 minutes in water. Although the crystallinity of TBP@MOL is retained, US-induced shock waves can lead to interparticle collisions. However, due to their nanoscale size, they do not have sufficient collisional energy to fuse or agglomerate.[39]

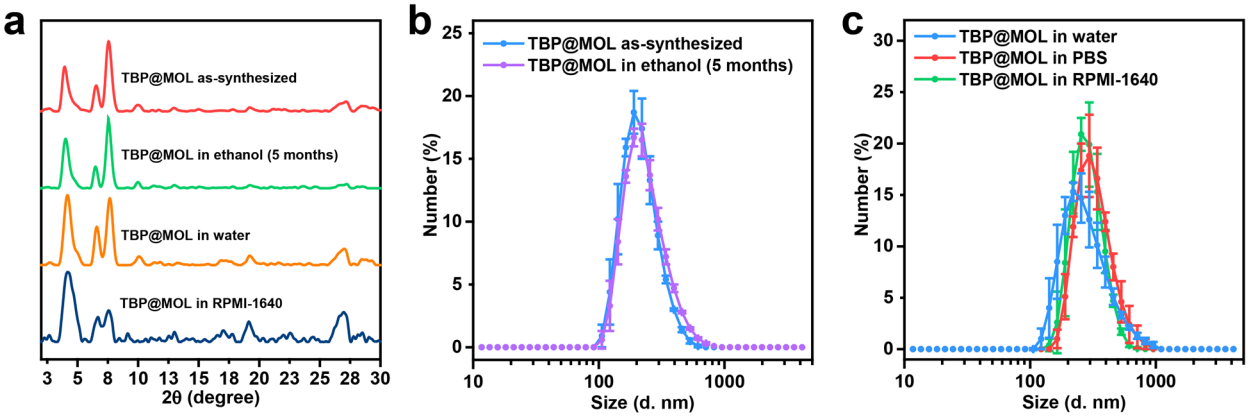

Figure 5-7. Aqueous stability of TBP@MOL. (a) PXRD patterns of TBP@MOL freshly prepared (as-synthesized), stored in ethanol for 5 months at room temperature, incubated in water for 24 hours at room temperature, and incubated in RPMI-1640 medium for 6 hours at 37 °C. (b) Number-averaged diameters of ethanol dispersions of TBP@MOL freshly prepared and stored in ethanol for 5 months at room temperature. (c) Number-averaged diameters of water dispersions of TBP@MOL incubated in water for 24 hours at room temperature, in PBS for 24 hours at room temperature, and in RPMI-1640 medium for 6 hours at 37 °C.

A TBP-based MOF, Hf-TBP, with TBP SSs rigidly confined between SBUs within the 3D framework, was synthesized as previously reported.[40] Hf-TBP has **csq** topology and the ideal formula $Hf_6(\mu_3\text{-}O)_4(\mu_3\text{-}OH)_4(OH)_4(H_2O)_4(\mu_2\text{-}TBP)_2$ (**Figure 5-8**). Hf-TBP exhibits a rod-like

morphology in TEM imaging and displays a number-averaged size of 108.7 ± 7.4 nm in DLS analysis (**Figure 5-8**).

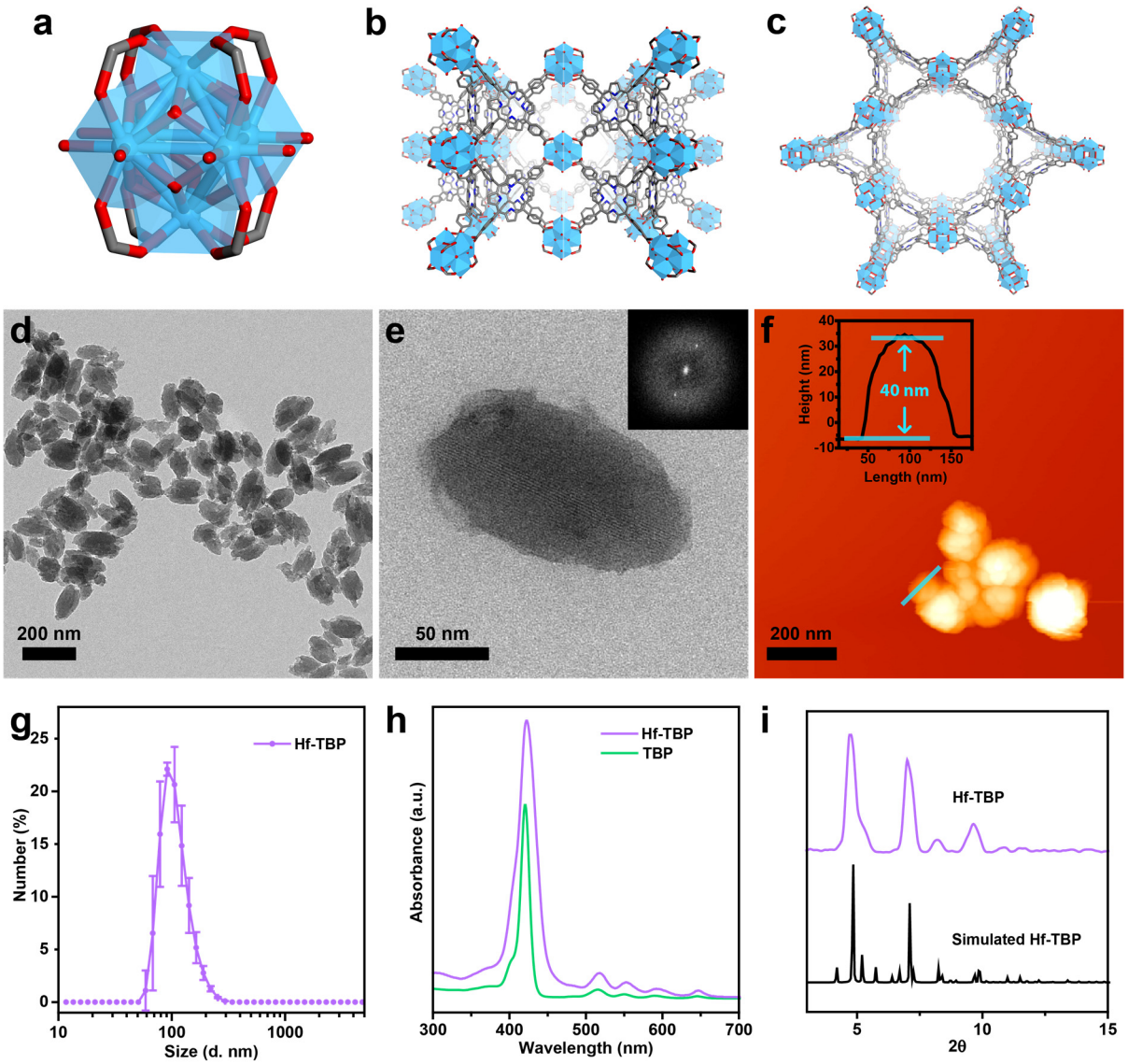

Figure 5-8. Structure and characterization of Hf-TBP. (a) The structure of SBU $Hf_6(\mu_3\text{-}O)_4(\mu_3\text{-}OH)_4(OH)_4(H_2O)_4(RCO_2)_8$ [RCO_2 represents the carboxylate group on TBP]. Models of Hf-TBP as viewed along the (b) *b* axis, and (c) *c* axis. (d) TEM image of Hf-TBP. (e) HR-TEM image of Hf-TBP with its FFT (inset). (f) AFM topographic image of Hf-TBP with its measured height profile (inset). (g) Number-averaged diameters of an ethanol dispersion of Hf-TBP measured by DLS. (h) Normalized UV-Vis absorption spectra of Hf-TBP and TBP. (i) PXRD pattern of Hf-TBP and the simulated pattern of Hf-TBP.

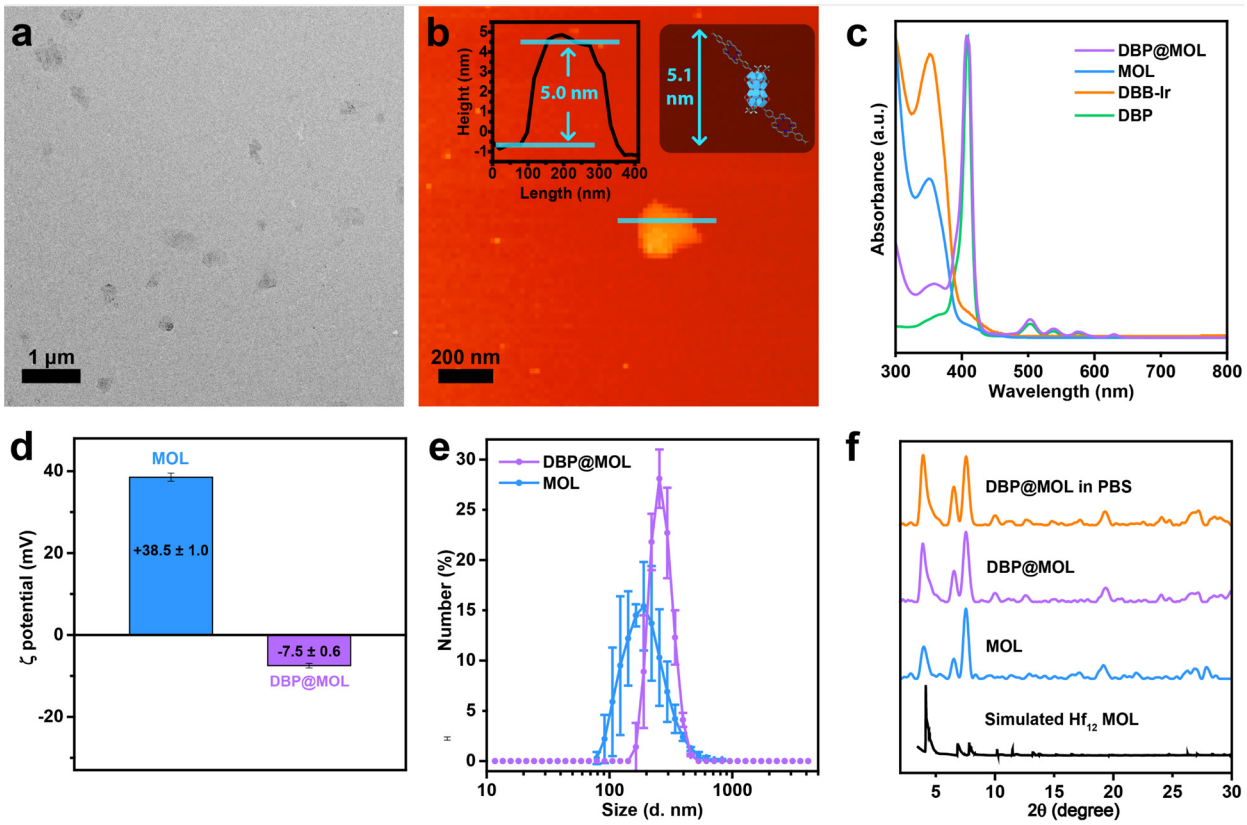

Figure 5-9. Characterization of DBP@MOL. (a) TEM image of DBP@MOL. (b) AFM topographic image, measured height profile (inset, left) and modeled height (inset, right) of DBP@MOL. (c) Normalized UV-Vis spectra of DBP@MOL and MOL showing the characteristic absorption peaks corresponding to DBP and DBB-Ir. (d) Zeta (ζ) potentials of MOL and DBP@MOL in water. Reversal of zeta potential is indicative of surface loading of anionic DBP groups to the cationic MOL. (e) Number-averaged diameters for ethanol dispersions of MOL and DBP@MOL, measured by DLS. (f) PXRD patterns of MOL, DBP@MOL as synthesized, DBP@MOL soaked in PBS for 24 hours, and simulated Hf_{12} MOL.

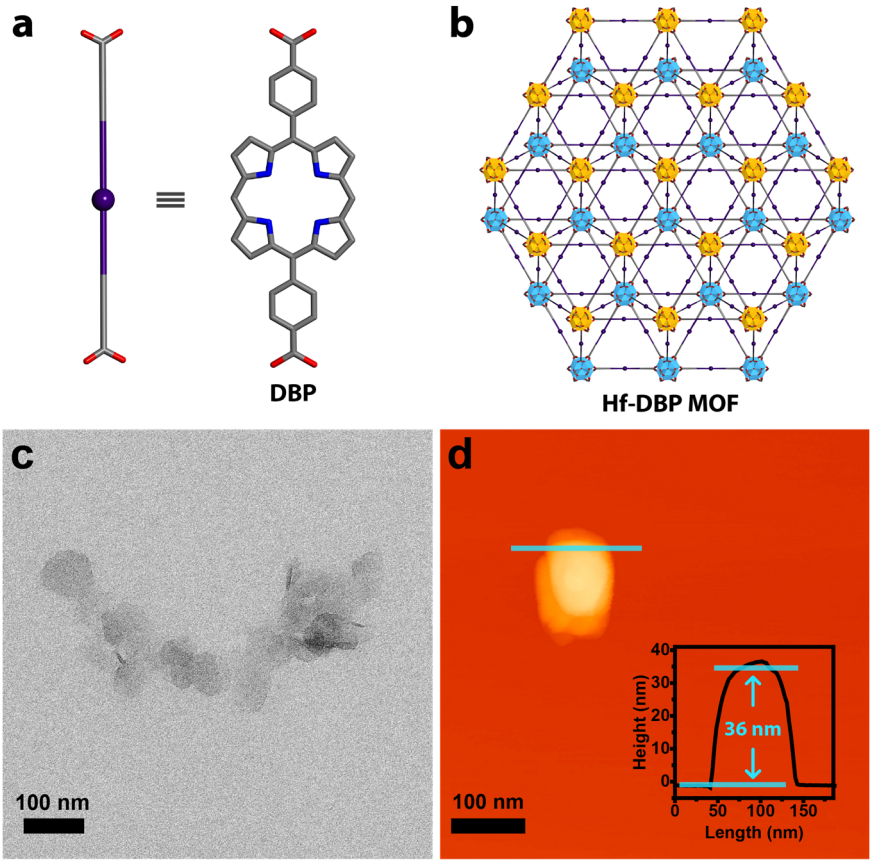

Figure 5-10. Structure model and morphological characterization of Hf-DBP MOF. (a) Simplified (left) and full (right) structure model of bridging ligand DBP. (b) View along the *c* axis of Hf-DBP MOF showing the 3D framework: top layer (blue) and bottom layer (orange). (c) TEM image of Hf-DBP MOF. (d) AFM topographic image and measured height profile (inset) of Hf-DBP MOF.

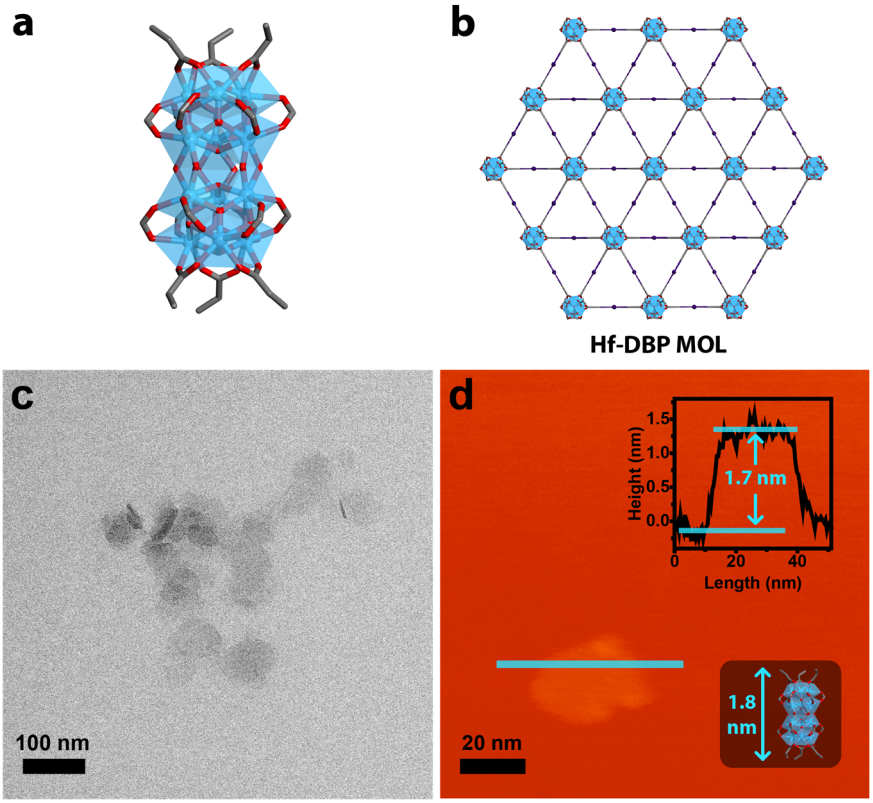

Figure 5-11. Structure model and morphological characterization of Hf-DBP MOL. (a) The structure of monosubstituted SBU $Hf_{12}(\mu_3\text{-}O)_8(\mu_3\text{-}OH)_8(\mu_2\text{-}OH)_6(\mu_2\text{-}RCO_2)_{12}(\mu_2\text{-}PA)_6$ [RCO_2 represents the carboxylate group on DBB-Ir; PA = propionic acid]. (b) View along the *c* axis of Hf-DBP MOL showing the monolayer framework. (c) TEM image of Hf-DBP MOL. (d) AFM topographic image, measured height profile (inset, top) and modeled height (inset, bottom) of Hf-DBP MOL.

5.2.2. $^1O_2$ generation efficacy

The $^1O_2$ generation efficiency of the different TBP systems was determined by singlet oxygen sensor green (SOSG) assay. Under US irradiation (3.4 MHz, 1.0 W/cm^2, 50% duty cycle, 10 min) in water, TBP@MOL generated 14.1- and 7.4-fold higher $^1O_2$ than TBP and Hf-TBP, respectively (**Figure 5-12**). Because sonoluminescence is a broad-spectrum emission (~200-700 nm), the MOL itself showed some $^1O_2$ generation due to direct excitation of DBB-Ir linkers. However, a physical mixture of TBP and the MOL generated 3.1-fold lower $^1O_2$ than TBP@MOL. Under US irradiation, TBP@MOL also showed 8-fold higher SOSG signal than a commonly

studied water-soluble SS, rose bengal, demonstrating its superior $^1O_2$ generation over traditional organic SSs.

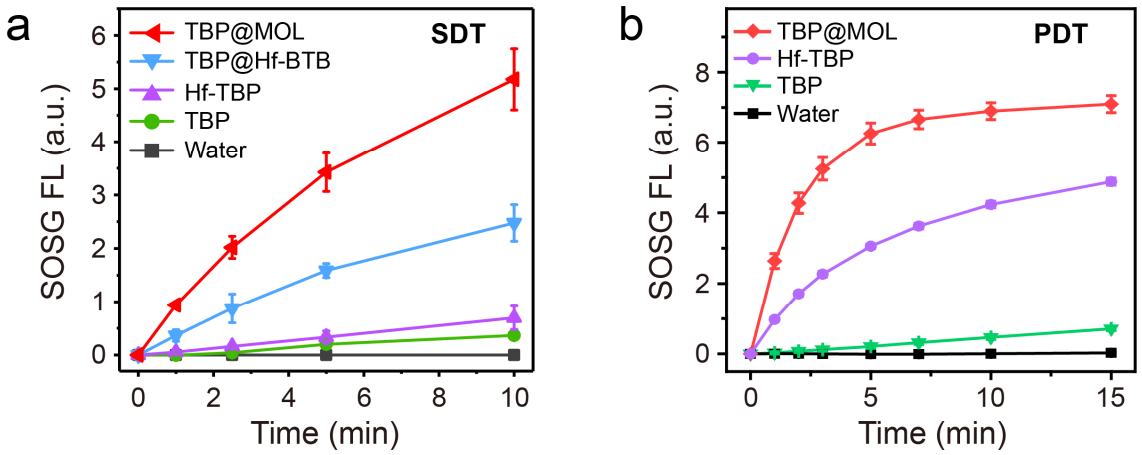

Figure 5-12. $^1O_2$ generation efficacy of TBP@MOL. SOSG assay fluorescence measurements detecting $^1O_2$ generation of various TBP systems upon (a) US or (b) visible light irradiation.

A similar trend was observed for the MOL modified with a related porphyrin sensitizer, 5,15-di(p-benzoato)porphyrin (DBP) (**Figure 5-9**, **Figure 5-13**). DBP@MOL showed 15.0- and 4.8-fold higher $^1O_2$ generation than DBP and 3D Hf-DBP MOF,[40] respectively, under US irradiation (**Figure 5-13**). DBP@MOL also showed much greater $^1O_2$ generation than the MOL itself, a physical mixture of DBP + MOL, and a 2D monolayer of Hf-DBP (denoted as Hf-DBP MOL), suggesting that this platform provides a synergistic effect beyond the two sensitizers alone and that the effect is not primarily due to the reduction in dimensionality of the MOF (**Figure 5-13**).

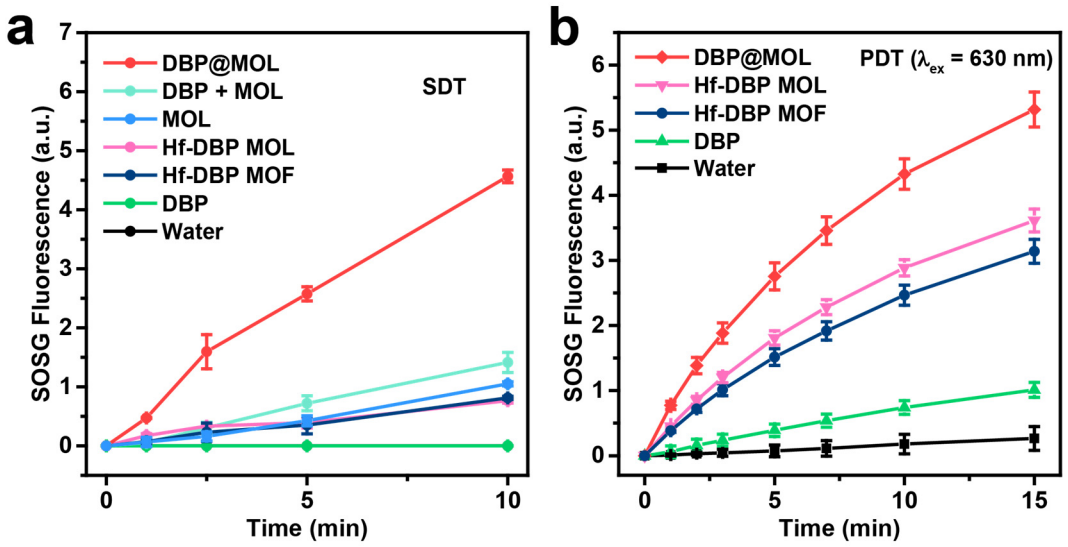

Figure 5-13. $^1O_2$ generation efficacy of DBP@MOL. SOSG assay fluorescence measurements detecting $^1O_2$ generation of various DBP systems upon (a) US or (b) visible light irradiation. Hf-DBP MOL is a 2D monolayer version of the 3D Hf-DBP MOF.

5.2.3. *In vitro* SDT anticancer efficacy

The enhanced $^1O_2$ generation of TBP@MOL was confirmed by *in vitro* SDT studies (**Figure 5-12**). US irradiation alone caused negligible cytotoxicity to CT26 colorectal and 4T1 triple-negative breast cancer cells (3.4 MHz, 1 W/cm^2, 50% duty cycle, and 5 min; "+" and "–" denote with and without US irradiation, respectively). TBP@MOL with US irradiation (denoted TBP@MOL(+)) induced significant cytotoxicity with half maximal inhibitory concentration (IC_{50}) values of 6.0 and 6.1 μm for CT26 and 4T1 cells, respectively (**Figure 5-14**). These IC_{50} values were 5.6- and 5.5-fold lower than those of TBP(+), respectively, and 12.3- and 5.6-fold lower than those of Hf-TBP(+), respectively. Without US irradiation, TBP, MOL, and TBP@MOL showed minimal toxicity at concentrations of up to 40 μM (**Figure 5-14**), indicating low intrinsic toxicity of TBP@MOL. The MOL itself displayed low cytotoxicity with and without US irradiation (**Figure 5-14**), supporting that the enhanced toxicity of TBP@MOL largely stems from efficient $^1O_2$ generation of SBU-anchored TBP.[41]

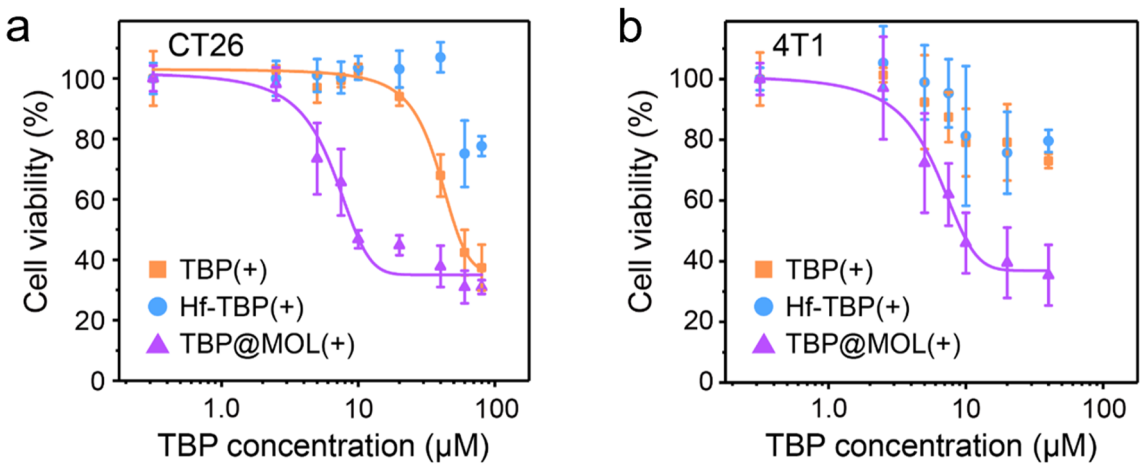

Figure 5-14. *In vitro* SDT cell viability. Cell viability assays of TBP(+), Hf-TBP(+), and TBP@MOL(+) in (a) CT26 and (b) 4T1 cells upon US irradiation (n = 4).

The enhanced SDT efficacy of TBP@MOL was supported by calcein–acetoxymethyl (AM)/propidium iodide (PI) staining under confocal laser scanning microscope (CLSM) imaging. TBP@MOL(+)-treated CT26 cells showed much stronger signals of PI, but weaker fluorescence of calcein-AM than other groups (**Figure 5-15**), indicating significantly enhanced cancer cell killing by TBP@MOL(+). US-stimulated generation of ROS was evaluated by dichlorofluorescein diacetate (DCF-DA) in CT26 cells. After US irradiation, obvious green fluorescence of DCF was observed in TBP@MOL(+)-treated CT26 cells while other treatment groups showed little DCF fluorescence (**Figure 5-15**). Flow cytometry analysis showed that TBP@MOL(+) generated more than an order of magnitude higher ROS than the other systems (**Figure 5-15**), likely due to increased cellular uptake of and enhanced $^1O_2$ generation by TBP@MOL. The slightly higher intracellular uptake of TBP@MOL compared to Hf-TBP was likely due to the smaller dimension of TBP@MOL.[42]

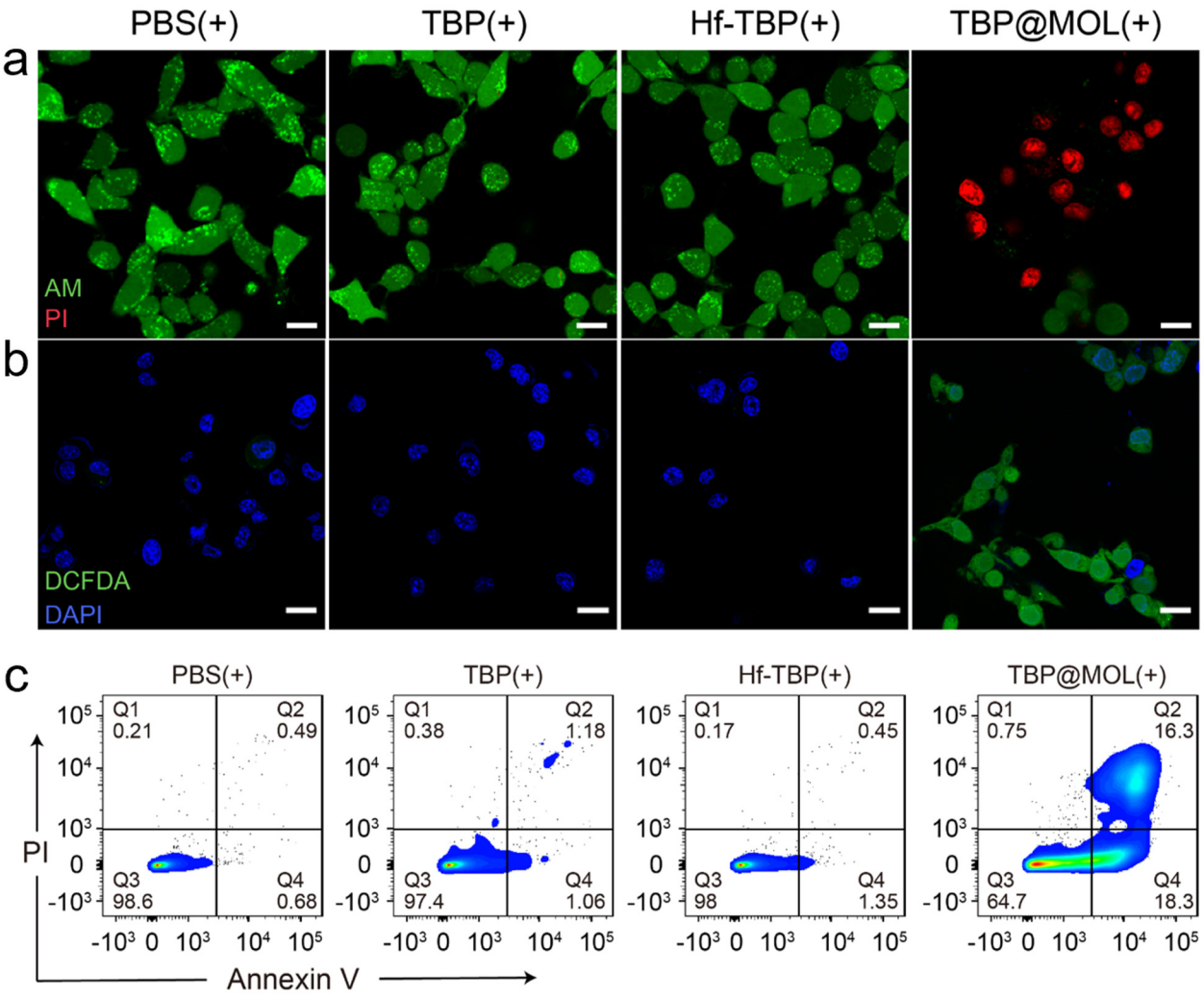

Figure 5-15. *In vitro* SDT anticancer efficacy. CLSM images showing (a) calcein-AM/PI staining and (b) DCF-DA staining after SDT treatment. (c) Flow cytometric analyses showing Annexin V/PI staining in CT26 cells after SDT treatment. Scale bar = 20 μm.

SDT-induced apoptosis was evaluated with the Annexin V/PI kit by flow cytometry. At an equivalent TBP concentration of 10 μm, TBP@MOL(+)-treated cells showed more severe apoptotic cell death with only 64.7% healthy cells remaining compared to 98.0% and 97.4% in cells treated with Hf-TBP(+) and TBP(+), respectively (**Figure 5-15**). More than 98% of healthy cells were present in the treatment groups without US irradiation. US irradiation alone did not cause cell death. Taken together, TBP@MOL is a significantly more efficient SS than free TBP and Hf-TBP.

5.2.4. Sonosensitization and $^1O_2$ generation mechanism

Since US excitation of the SSs proceeds mainly via sonoluminescence, we compared the photoexcitation dynamics of the various SS systems to understand how the SBU-anchored TBP in TBP@MOL enhances $^1O_2$ generation over the other TBP systems. Steady-state emission spectra (λ_{ex} = 420 nm) showed a significant reduction of TBP emission intensity in Hf-TBP and TBP@MOL (**Figure 5-16**). This result is supported by the time-correlated single photon counting (TCSPC) decay profiles, which yielded shorter average fluorescence lifetimes (τ_{avg}) of 3.12 and 3.33 ns for TBP@MOL and Hf-TBP, respectively, compared to a τ_{avg} of 9.52 ns for TBP (**Figure 5-16**, **Table 5-1**). This trend is similarly found in the case of DBP@MOL and Hf-DBP MOF (**Figure 5-17**, **Table 5-2**).

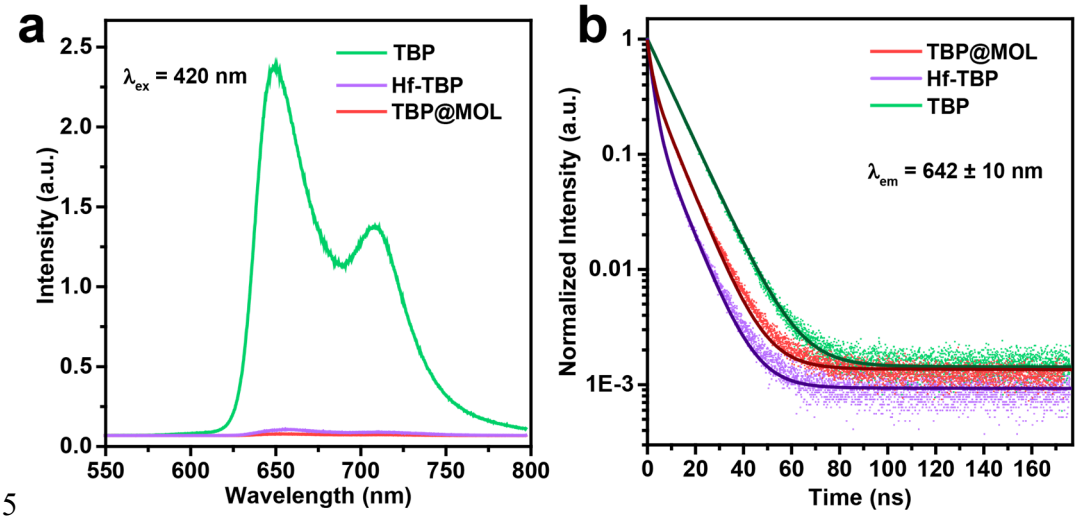

Figure 5-16. Steady state and time-resolved emission of TBP chromophores. (a) Normalized steady-state emission spectra of the TBP systems in water at equivalent TBP concentrations of 0.2 μM (λ_{ex} = 420 nm, 3 nm excitation/emission slit widths, 0.1 s integration). (b) Time-resolved emission decay spectra of the TBP systems in water measured by TCSPC experiments (λ_{ex} = 420 nm, λ_{em} = 642 ± 10 nm). Solid lines represent the fits of the correspondingly colored data points.

Table 5-1. Fluorescence decay fitting values for TBP chromophores. The table shows values for the fitted fluorescence decay times (τ_i), pre-exponential weighting coefficients (α_i), and chi-squared distribution (χ^2). τ_3 is approximate as it exceeds our 200 ns time window and is not included in calculating τ_{avg}.

Sample	τ_{avg} (ns)	τ_1 (ns)	τ_2 (ns)	τ_3 (µs)	α_1	α_2	α_3	χ^2
TBP@MOL	3.12	1.63	8.13	~50.0	0.77	0.23	0.0016	0.33
Hf-TBP	3.33	2.06	8.19	~42.0	0.78	0.21	0.0009	0.21
TBP	9.52	-	9.52	~35.0	-	1.00	-	0.22

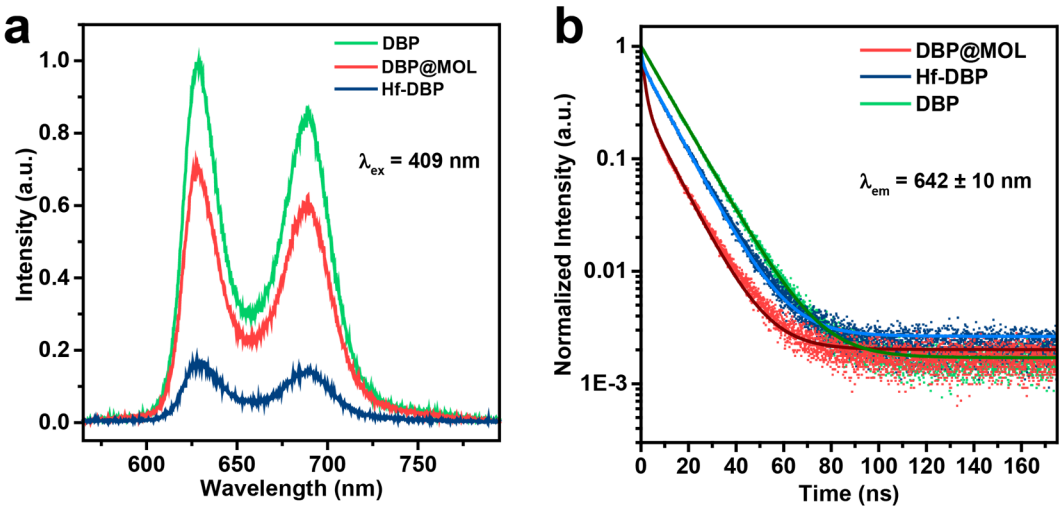

Figure 5-17. Steady state and time-resolved emission of DBP chromophores. (a) Normalized steady-state emission spectra of the DBP systems in water at equivalent DBP concentrations of 0.2 µM (λ_{ex} = 409 nm, 3 nm excitation/emission slit widths, 0.1 s integration). (b) Time-resolved emission decay spectra of the DBP systems in water measured by TCSPC experiments (λ_{ex} = 403 nm, λ_{em} = 642 ± 10 nm). Solid lines represent the fits of the correspondingly colored data points.

Table 5-2. Fluorescence decay fitting values for DBP chromophores. The table shows values for the fitted fluorescence decay times (τ_i), pre-exponential weighting coefficients (α_i), and chi-squared distribution (χ^2). τ_3 is approximate as it exceeds our 200 ns time window and is not included in calculating τ_{avg}.

Sample	τ_{avg} (ns)	τ_1 (ns)	τ_2 (ns)	τ_3 (µs)	α_1	α_2	α_3	χ^2
DBP@MOL	4.34	1.49	10.44	~15.4	0.67	0.32	0.002	0.47
Hf-DBP MOF	8.43	0.69	11.01	~13.3	0.25	0.75	0.002	0.47
DBP	11.81	-	11.81	~12.0	-	1.00	0.002	0.21

To investigate the origins of the 1–2 ns time constants for TBP@MOL and Hf-TBP, we conducted broadband transient absorption (TA) experiments. We observed a strong and broad excited state absorption feature, which we attribute to the S_1 state.[31-32] The ~2 ns time constant extracted from the TA experiments originates from the decay of the excited state absorption feature for both Hf-TBP and TBP@MOL (**Figure 5-18**, **Table 5-3**). We associate this short time constant with nonradiative decay via coupling between TBP and Hf, which facilitates intersystem crossing (ISC)[43-44] from the excited singlet state (S_1) to the triplet state (T_1). This time constant is absent in the free TBP and could therefore be attributed to orientational quenching of the excited singlet state via the phonon modes in the crystalline frameworks.[45] While the inefficient $^1O_2$ generation of TBP can be explained by AIQ in aqueous environments, similarly facile ISC between TBP@MOL and Hf-TBP fails to explain their vastly different $^1O_2$ generation efficiency.

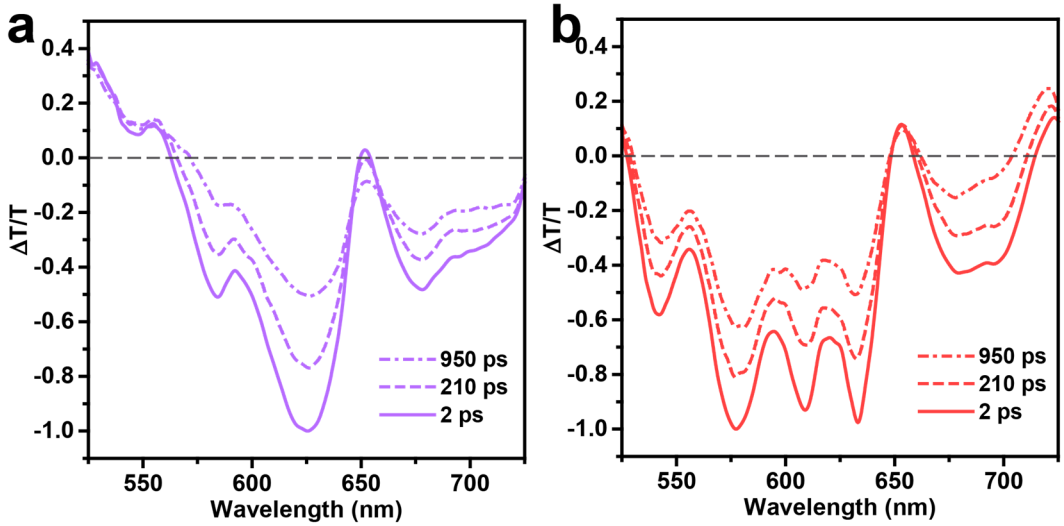

Figure 5-18. Ultrafast transient absorption measurements of Hf-TBP and TBP@MOL. Transient absorption spectra of (a) Hf-TBP and (b) TBP@MOL at various time slices, showing the decays of the excited state absorption features.

Table 5-3. Absorption (negative) feature time constants and their spread. Each time trace in the probe wavelength range were fit with mono-exponentials and the average and standard deviation of the time constants is reported. The lowest and highest values of χ^2 is reported for a given region resulting from fitting all the time traces.

Sample	λ range (nm)	τ_{avg} (ns)	σ_τ (ns)	χ^2 range
Hf-TBP	600-630	1.06	0.02	0.03-0.06
	680-710	1.15	0.09	0.03-0.07
TBP@MOL	540-630	2.10	0.45	0.01-0.04
	680-700	0.63	0.09	0.02-0.04

To eliminate the contribution of DBB-Ir linkers in SDT of TBP@MOL, we determined the $^1O_2$ generation efficiency of different TBP systems under 630 nm light irradiation. Although only TBP was excited under these conditions, TBP@MOL generated 1.5-fold more $^1O_2$ than Hf-TBP (**Figure 5-12**). The same trend is found with DBP@MOL and the other DBP systems, further supporting this (**Figure 5-13**).We observed a negligible difference in ISC between TBP@MOL and Hf-TBP (**Figure 5-16**, **Table 5-1**, **Figure 5-18**, **Table 5-3**); therefore, the enhanced $^3O_2$ sensitization by TBP@MOL likely results from a higher energy transfer efficiency in the encounter complex of T_1 excited sensitizer and oxygen, $^1(T_1–^3O_2)$, owing to the rotational freedom and accessibility of the SBU-anchored TBP. This energy transfer proceeds via internal conversion, which plays a more important role than ISC,[46] and eventually dissociates the $^1(T_1–^3O_2)$ encounter complex to afford $^1O_2$.[46-50] We propose that the less efficient $^1O_2$ generation by Hf-TBP is because the TBP chromophores are rigidly bound within the 3D framework. $^3O_2$ must diffuse through the framework to access excited TBP sensitizers and then $^1O_2$ must diffuse back out. Accordingly, we postulate that the 2D MOL morphology and surface-anchored TBP allows $^3O_2$ to have barrierless access to both faces of the sensitizer which, in combination with the relative flexibility of the TBP, facilitates better encounter complex energy transfer and sensitization efficiency (**Figure 5-19**).

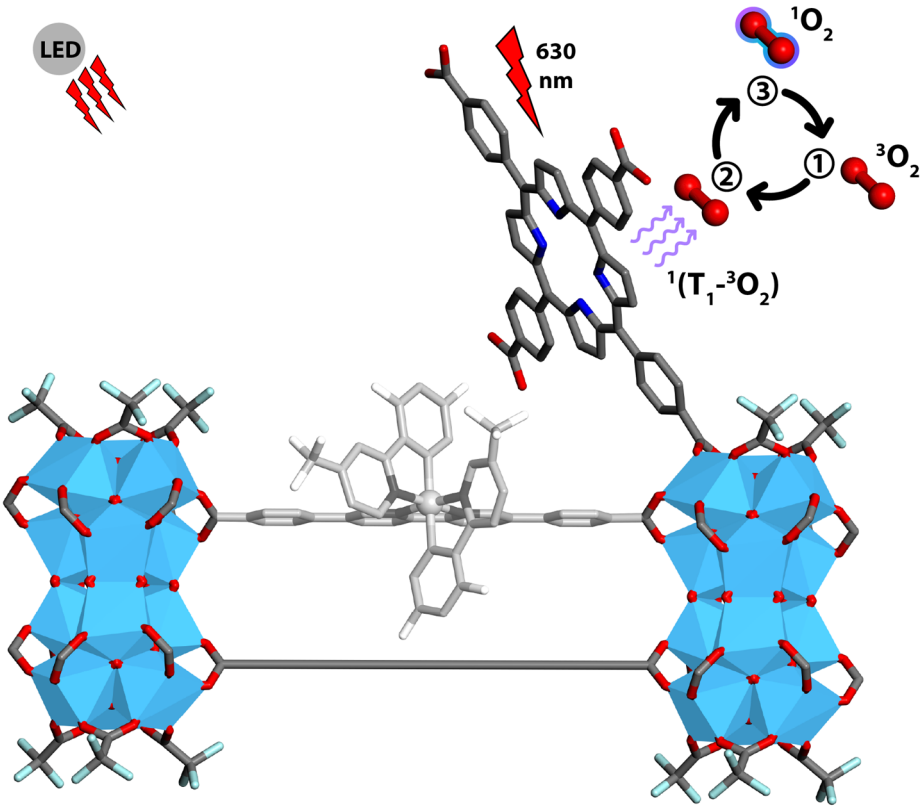

Figure 5-19. Proposed mechanism of general $^3O_2$ sensitization enhancement by surface-anchoring. Proposed mechanistic model of the efficient $^1O_2$ generation by TBP@MOL. The light irradiation at 630 nm only excites the TBP chromophores, so the DBB-Ir chromophore is inactive under PDT conditions (greyed out).

We synthesized an analogous TBP-capped 2D MOL built from 1,3,5-tris(4-carboxyphenyl)benzene (BTB) linkers, TBP@Hf-BTB, to investigate the DBB-Ir contribution in SDT (**Figure 5-20**, **Figure 5-22**, **Figure 5-23**, **Figure 5-24**). Under similar US irradiation conditions, TBP@Hf-BTB generated 3.5-fold more $^1O_2$ than Hf-TBP but 2.1-fold less $^1O_2$ than TBP@MOL (**Figure 5-12**). These results support the sonosensitization enhancement from SBU-anchored SSs as well as significant contribution from DBB-Ir linkers.

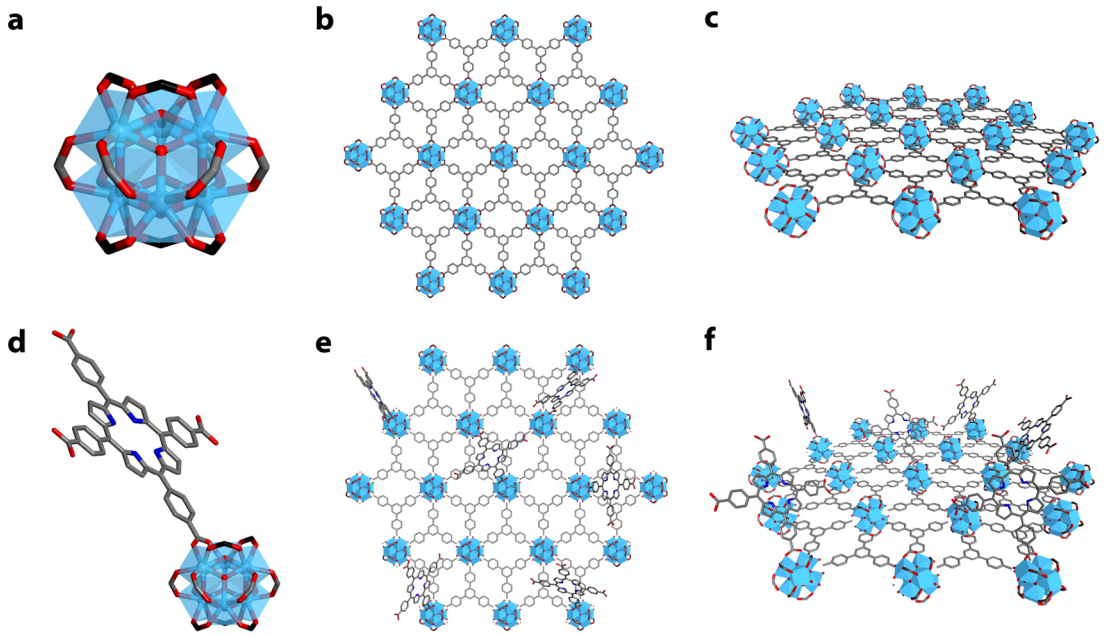

Figure 5-20. Structure models of Hf-BTB and TBP@Hf-BTB. (a) The structure of SBU $Hf_6(\mu_3\text{-}O)_4(\mu_3\text{-}OH)_4(\mu_2\text{-}FA)_6(\mu_2\text{-}RCO_2)_6$ in Hf-BTB [black atoms represent the carbon on FA; RCO_2 represents the carboxylate group on BTB]. (b) View along the *c* axis of Hf-BTB. (c) Side view of Hf-BTB showing its monolayer morphology. (d) The structure of a monosubstituted SBU $Hf_6(\mu_3\text{-}O)_4(\mu_3\text{-}OH)_4(\mu_2\text{-}FA)_6(\mu_2\text{-}RCO_2)_6(TBP)_1$ in TBP@Hf-BTB. (e) View along the *c* axis of TBP@Hf-BTB. (f) Side view of TBP@Hf-BTB showing its monolayer morphology and surface-anchored TBP.

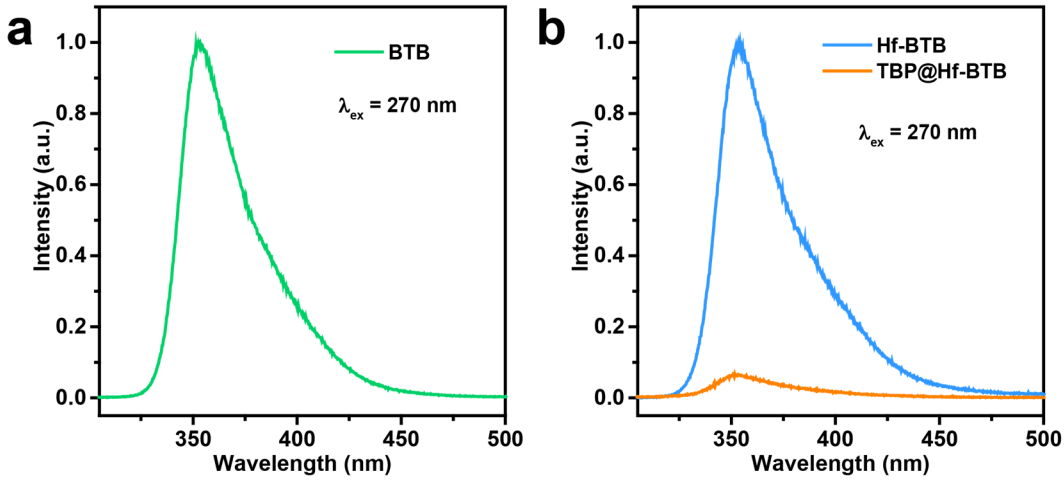

Figure 5-21. Fluorescence emission spectra of BTB in the BTB systems. (a) Normalized fluorescence spectra of BTB at 1 μM (λ_{ex} = 270 nm, 3 nm excitation/emission slit widths, 0.2 s integration) in water. (b) Relative fluorescence spectra of Hf-BTB and TBP@Hf-BTB in water at equivalent BTB concentrations of 1 μM (λ_{ex} = 270 nm, 3 nm excitation/emission slit widths, 3.0 s integration).

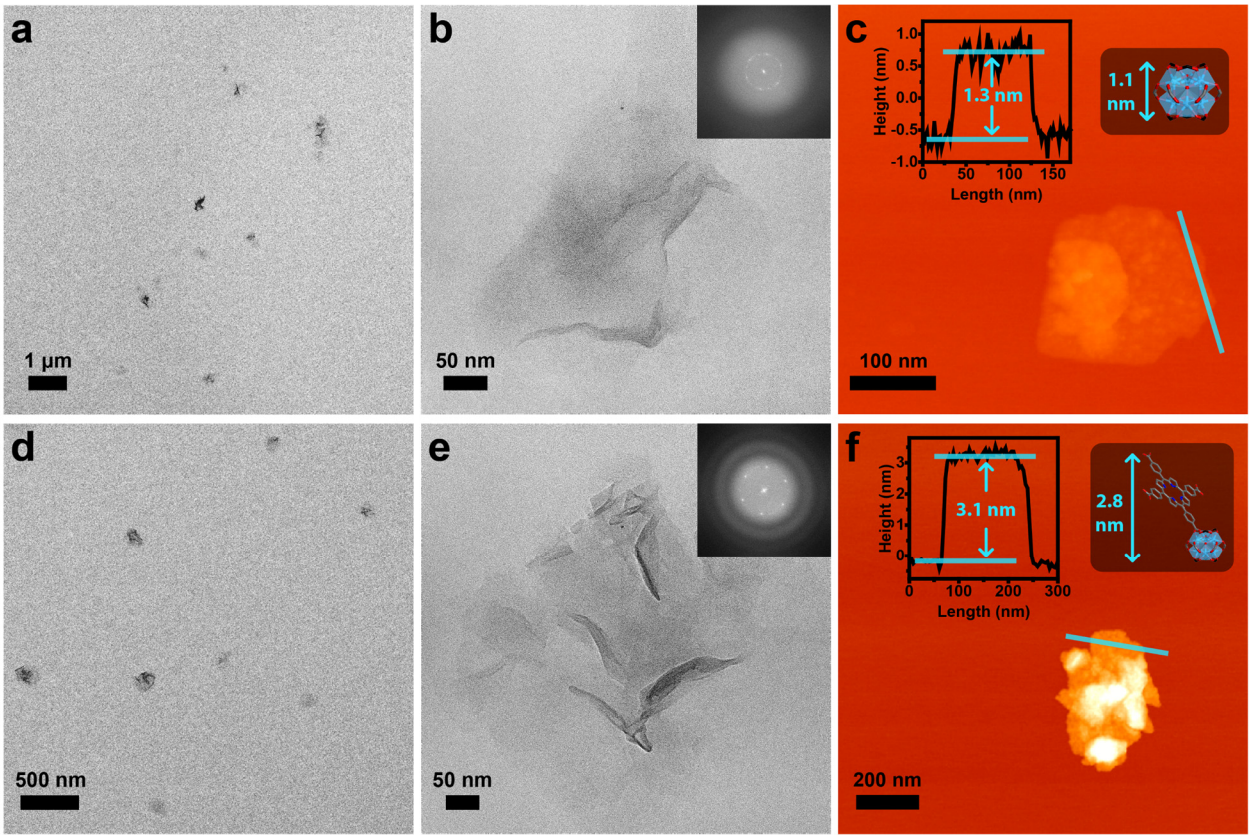

Figure 5-22. Morphological characterization of Hf-BTB and TBP@Hf-BTB. (a) TEM image of Hf-BTB. (b) HR-TEM image of Hf-TBP with its FFT (inset). (c) AFM topographic image, measured height profile (inset, left) and modeled height (inset, right) of FA-capped Hf-BTB. (d) TEM image of TBP@Hf-BTB. (e) HR-TEM image of TBP@Hf-BTB with its FFT (inset). (f) AFM topographic image, measured height profile (inset, left) and modeled height (inset, right) of TBP@Hf-BTB.

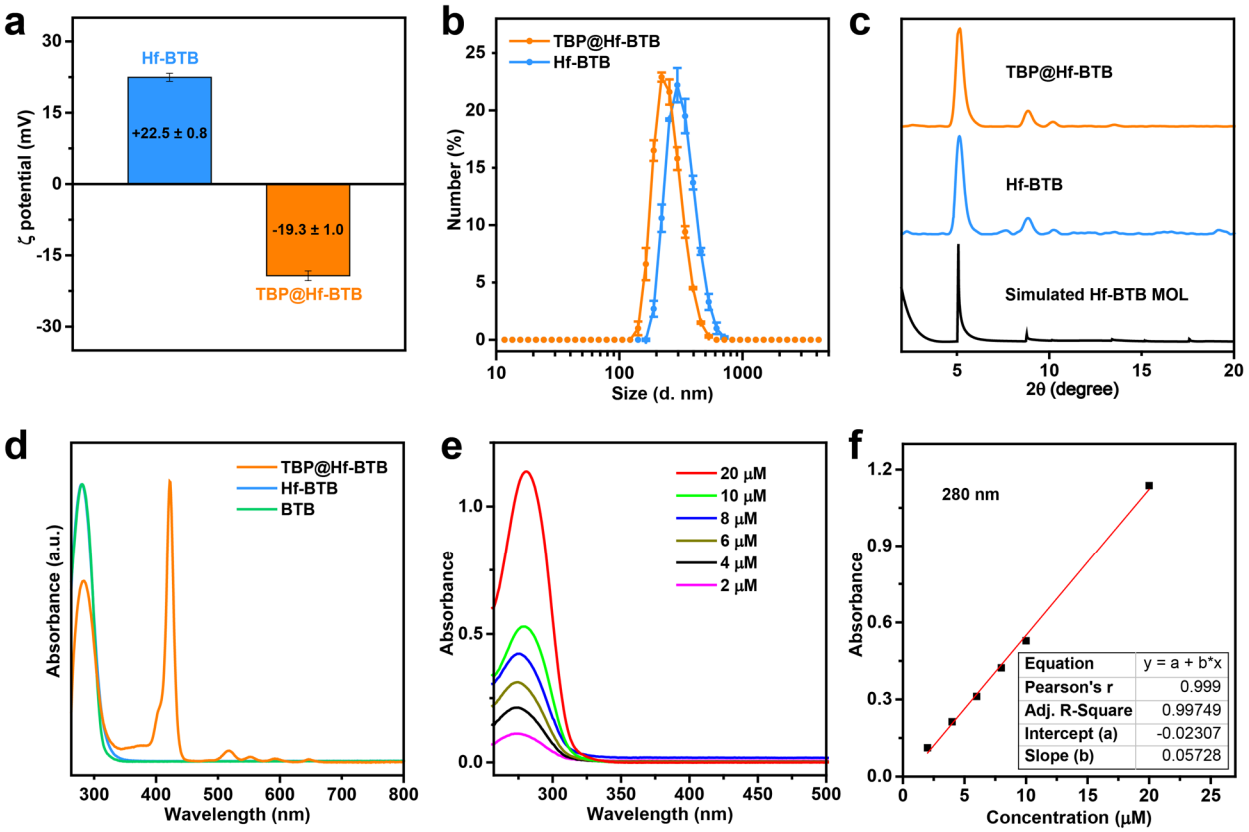

Figure 5-23. Characterization of Hf-BTB and TBP@Hf-BTB. (a) Zeta (ζ) potentials of Hf-BTB and TBP@Hf-BTB in water. Reversal of zeta potential is indicative of surface loading of anionic TBP groups to Hf-BTB. (b) Number-averaged diameters for ethanol dispersions of TBP@Hf-BTB and Hf-BTB, measured by DLS. (c) PXRD patterns of TBP@Hf-BTB, Hf-BTB, and simulated Hf-BTB MOL. (d) Normalized UV-Vis spectra of TBP@Hf-BTB and Hf-BTB showing the characteristic absorption peaks corresponding to BTB. (e) UV-Vis absorption spectra of BTB in DMSO at different concentrations. (f) Linear fit of the BTB absorbance at 280 nm as a function of concentration.

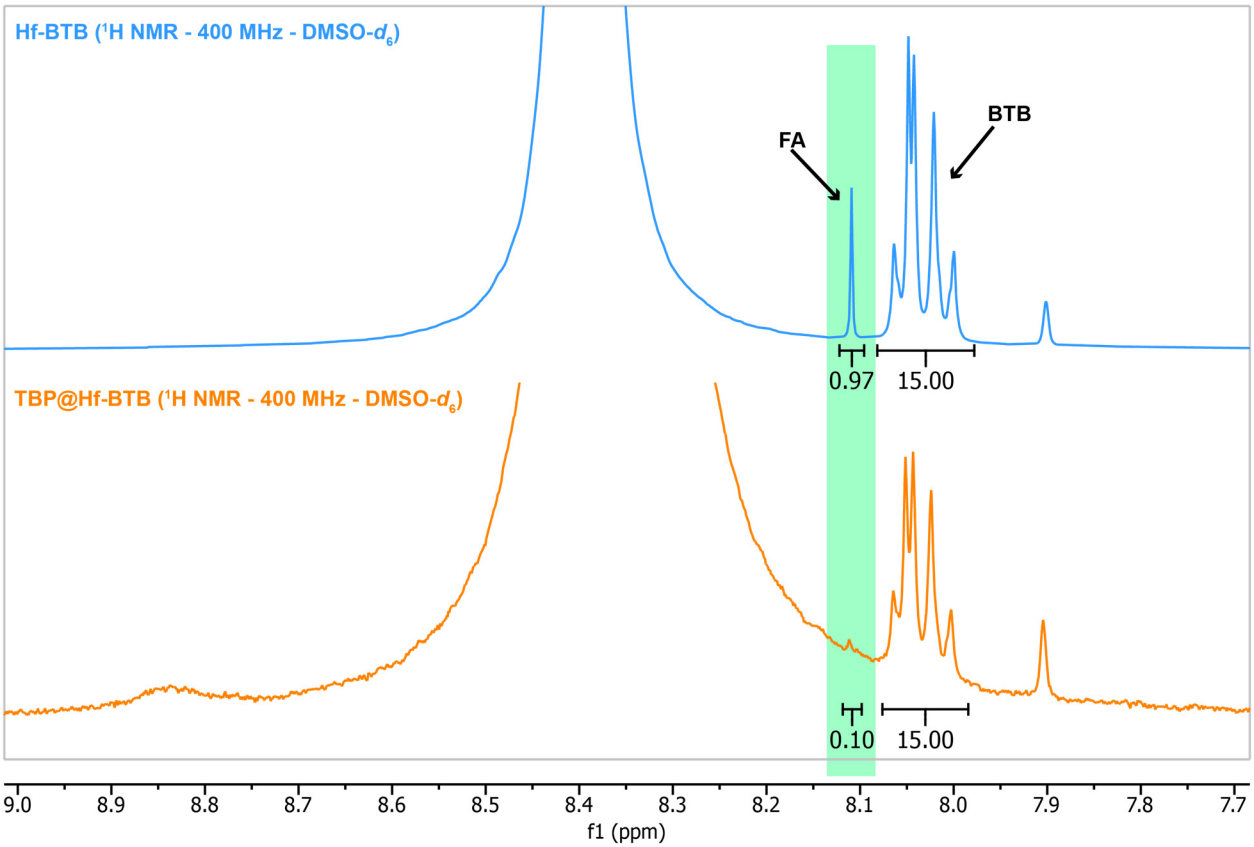

Figure 5-24. ^{1}H NMR spectra of digested Hf-BTB and TBP@Hf-BTB. The reduction of the FA (δ = 8.12 ppm) to BTB (δ = 8.07-8.00 ppm) integrated signal ratio from Hf-BTB (top) to TBP@Hf-BTB (bottom) is indicative of the carboxylate exchange of FA with TBP on the Hf_6 SBUs.

Due to the proximity of TBP to DBB-Ir linkers in TBP@MOL (estimated via simulation to be between 5-15 Å), we investigated the possibility of fluorescence resonance energy transfer (FRET). Spectral overlap integral [$J(\lambda)$] calculations showed that the 560 nm emission of the DBB-Ir linkers in the MOL (donor) overlaps well with the Q bands of TBP (acceptor) (**Figure 5-25**). The steady-state emission spectra indicated quenching of the DBB-Ir emission by SBU-anchored TBP in TBP@MOL (**Figure 5-27**). The spectral overlap integral equation is given below, where λ is the spectrum wavelength, ε_A is the acceptor absorption coefficient, F_D is the donor fluorescence emission normalized to 1.

$$J(\lambda) = \int_0^\infty \epsilon_A(\lambda)\lambda^4 F_D(\lambda)\, d\lambda$$

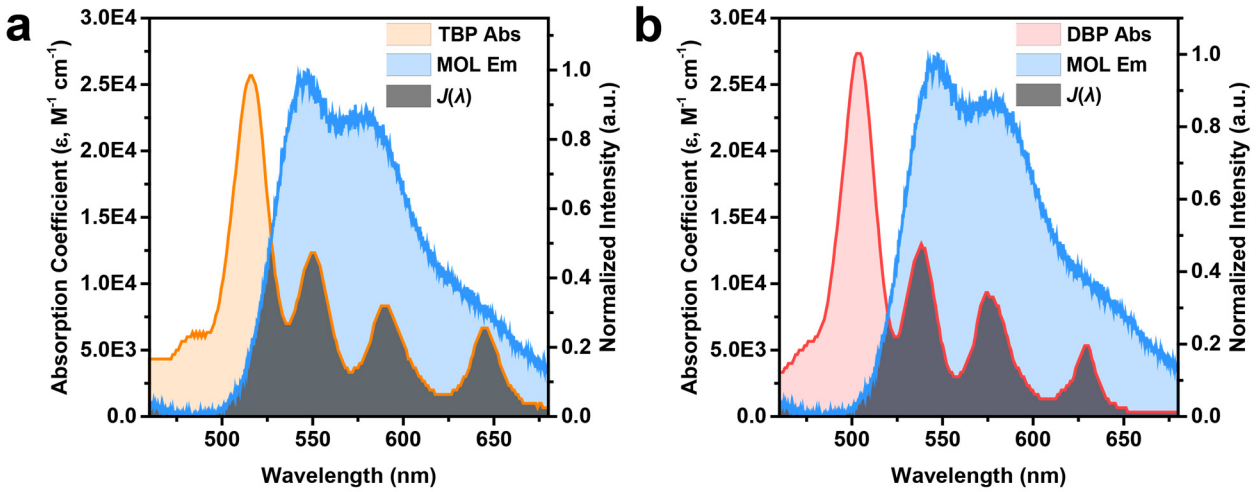

Figure 5-25. Donor-acceptor absorption and emission spectra of the TBP and DBP MOL systems. Absorption spectrum of (a) TBP (acceptor) or (b) DBP (acceptor), normalized emission spectrum of MOL (DBB-Ir linker; donor), and spectral overlap integral $J(\lambda)$.

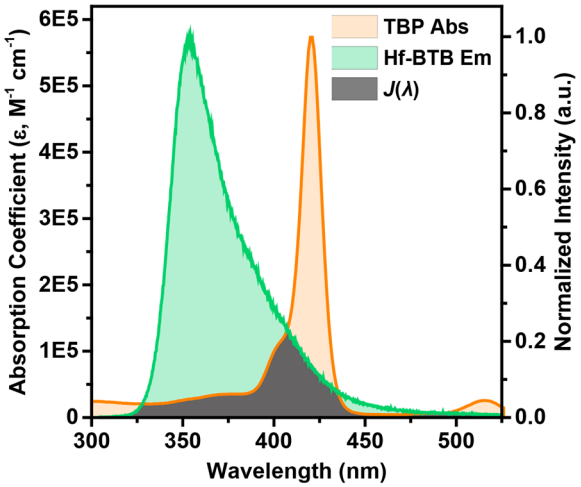

Figure 5-26. Donor-acceptor absorption and emission spectra of the Hf-BTB system. Absorption spectrum of (a) TBP (acceptor), normalized emission spectrum of Hf-BTB (BTB linker; donor), and spectral overlap integral $J(\lambda)$.

Table 5-4. Spectral overlap integrals. $J(\lambda)$ values for TBP and DBP acceptors (A) with MOL (DBB-Ir) donors (D), calculated using a|e – UV-Vis-IR Spectral Software 1.2 (FluorTools, DK).

Donor-acceptor pair	$J(\lambda)$ [nm^4 M^{-1} cm^{-1}]
TBP (*A*) + MOL (*D*)	7.10×10^{14}
DBP (*A*) + MOL (*D*)	5.42×10^{14}
TBP (*A*) + Hf-BTB (*D*)	1.43×10^{15}

Furthermore, the TCSPC decay profile of the DBB-Ir emission in TBP@MOL displayed an additional nonradiative decay around 0.91 ns that was absent in MOL (**Figure 5-27**). However, singlet FRET is not likely to be the major contributor to sonosensitization because, although the calculated $J(\lambda)$ of the BTB donor with the TBP acceptor in TBP@Hf-BTB doubles that of TBP@MOL (**Figure 5-25**, **Figure 5-26**, **Table 5-4**), its $^1O_2$ generation is 2.1-fold lower (**Figure 5-12**).

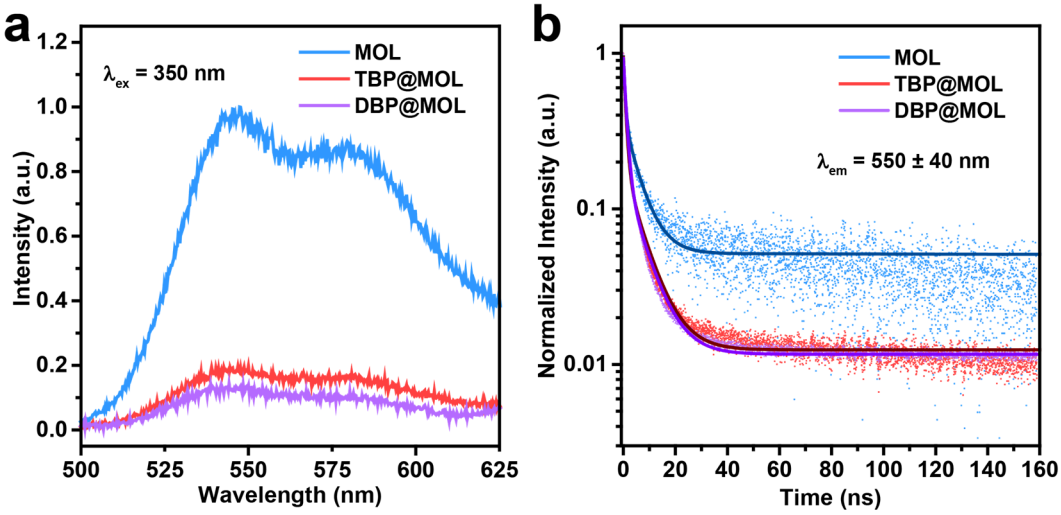

Figure 5-27. Steady state and time-resolved emission of DBB-Ir linker chromophores. (a) Normalized steady-state emission spectra of the DBP systems in water at equivalent DBP concentrations of 0.2 μM (λ_{ex} = 409 nm, 3 nm excitation/emission slit widths, 0.1 s integration). (b) Time-resolved emission decay spectra of the DBP systems in water measured by TCSPC experiments (λ_{ex} = 403 nm, λ_{em} = 642 ± 10 nm). Solid lines represent the fits of the correspondingly colored data points.

Table 5-5. Fluorescence decay fitting values for DBB-Ir chromophores. The table shows values for the fitted fluorescence decay times (τ_i), pre-exponential weighting coefficients (α_i), and chi-squared distribution (χ^2). τ_3 is approximate as it exceeds our 200 ns time window and is not included in calculating τ_{avg}.

Sample	τ_{avg} (ns)	τ_1 (ns)	τ_2 (ns)	τ_3 (μs)	α_1	α_2	α_3	χ^2
TBP@MOL	1.98	0.91	7.06	~20.0	0.78	0.18	0.001	1.04
DBP@MOL	2.11	1.13	6.98	~20.0	0.82	0.17	0.0	0.54
MOL	2.26	0.67	5.7	~12.4	0.57	0.33	0.096	2.36

Since DBB-Ir has much more efficient ISC than BTB, we postulate that the enhanced $^1O_2$ generation mainly arises from triplet–triplet Dexter energy transfer (TTET) (**Figure 5-27**, **Figure 5-21**). Therefore, TBP@MOL synergistically enhances $^1O_2$ generation by direct $^3O_2$ sensitization, singlet FRET and more importantly, TTET from DBB-Ir linkers (**Figure 5-28**).

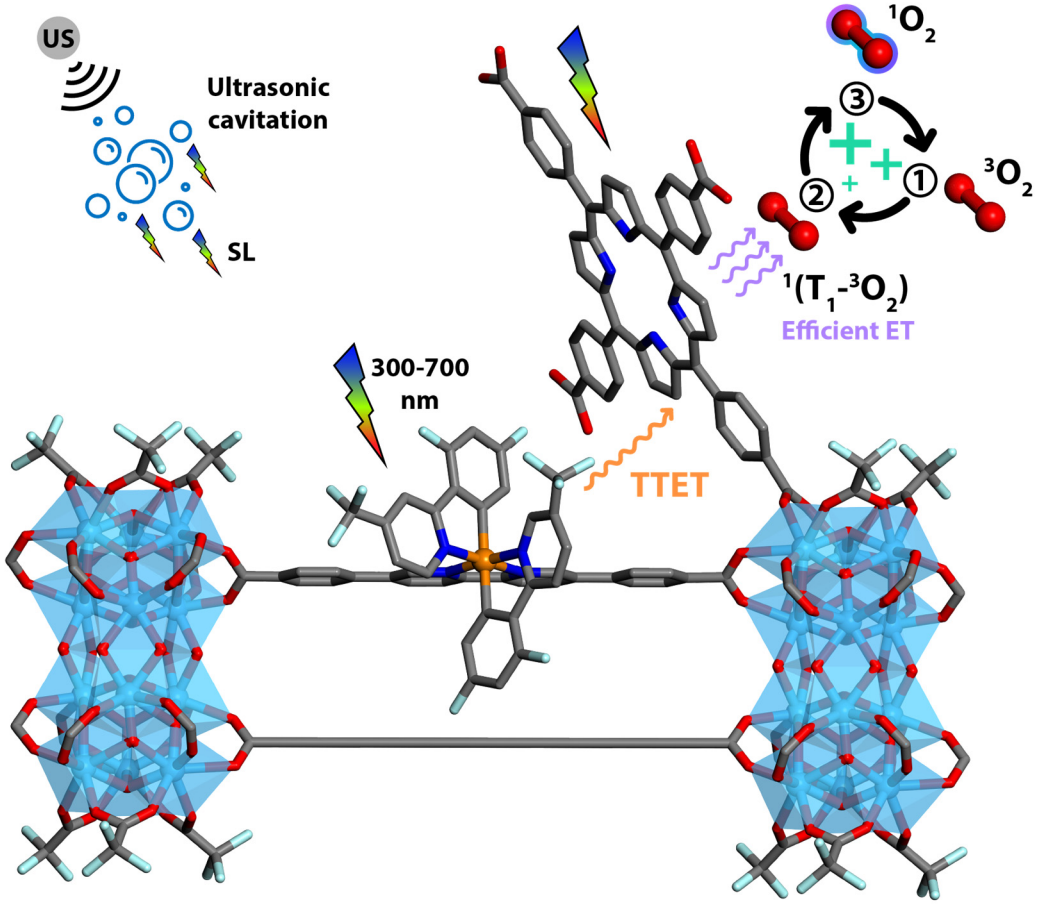

Figure 5-28. Proposed SDT mechanism of TBP@MOL. DBB-Ir and TBP absorb high- and low-energy regions of the broad sonoluminescence (SL) spectrum, respectively, and the excited DBB-Ir undergoes TTET with TBP. The excited surface-anchored TBP efficiently transfers energy to $^3O_2$ for enhanced $^1O_2$ generation.

5.2.5. *In vivo* SDT anticancer efficacy

We confirmed the *in vivo* SDT anticancer efficacy in a CT26 colorectal adenocarcinoma mouse model and a 4T1 murine triple negative breast cancer model (**Figure 5-29**). TBP@MOL(+)

exhibited outstanding SDT efficacy with tumor growth inhibition (TGI) values of 87.0% and 82.7% in CT26 and 4T1 tumor models, respectively (**Figure 5-29**).

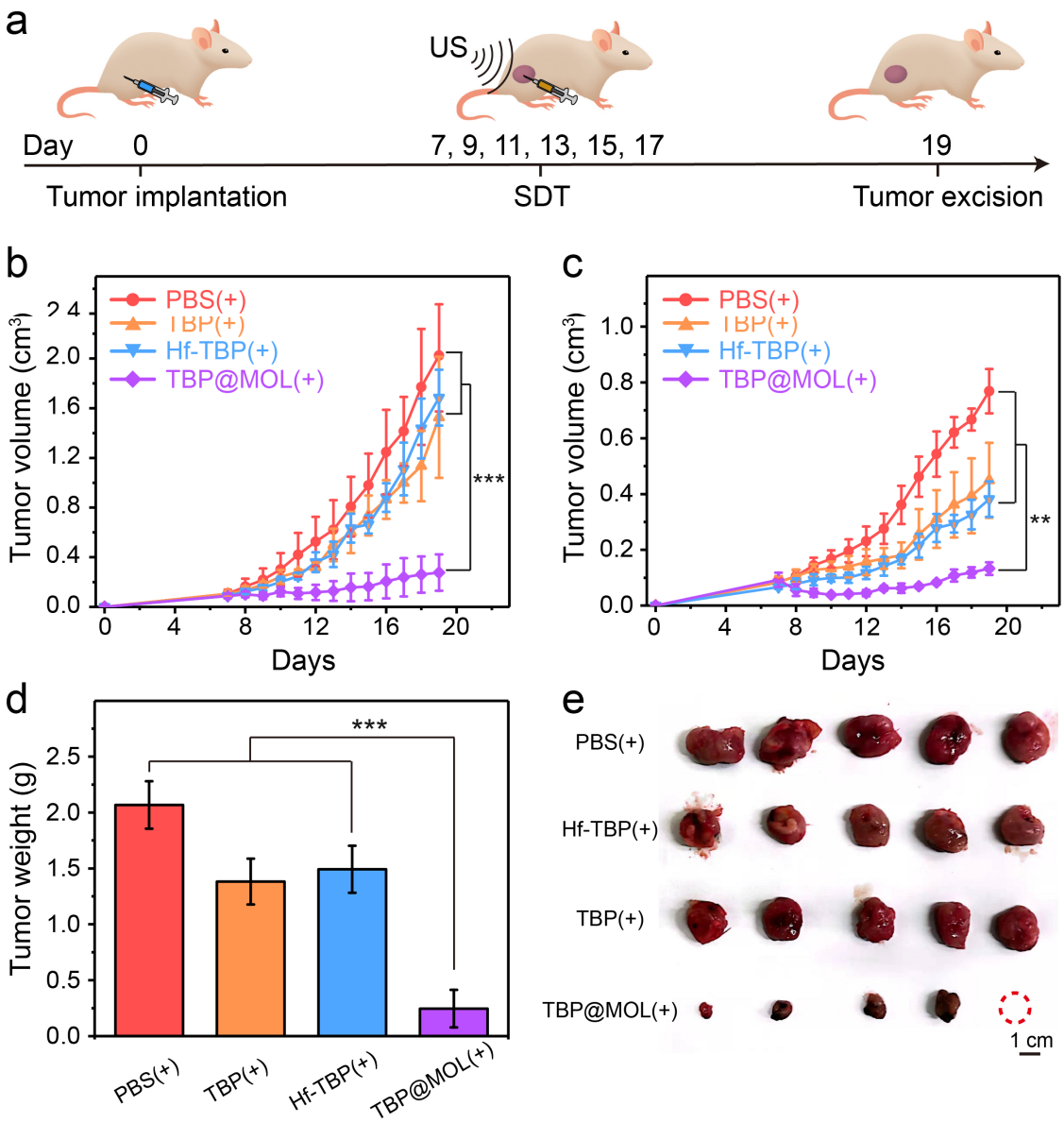

Figure 5-29. *In vivo* anticancer efficacy. (a) Schematic illustration of tumor inoculation and treatment schedule. SDT anticancer efficacy in subcutaneous (b) CT26 and (c) 4T1 tumor-bearing BALB/c mice (n = 5). (d) Measured weights and (e) photographs of excised CT26 tumors from BALB/c mice after PBS(+), TBP(+), Hf-TBP(+), or TBP@MOL(+) treatment. Scale bar = 1 cm. **, p<0.01; ***, p<0.001.

In contrast, TBP(+) displayed moderate TGI values of 25.0% and 41.5%, while Hf-TBP(+) displayed TGI values of 16.7% and 50.0% in CT26 and 4T1 models, respectively. All US-free

treatment groups showed minimal efficacy. The significantly enhanced SDT therapeutic efficacy of TBP@MOL(+) over other groups was confirmed by the smallest tumor weight among all groups at the end point (**Figure 5-29**). Hematoxylin and eosin (H&E) staining and terminal deoxynucleotidyl transferase dUTP nick end labeling (TUNEL) assays showed that TBP@MOL(+) significantly reduced the density of cancerous cells and increased apoptosis in tumor slices (**Figure 5-30**), demonstrating enhanced cancer cell killing by SDT *in vivo*.

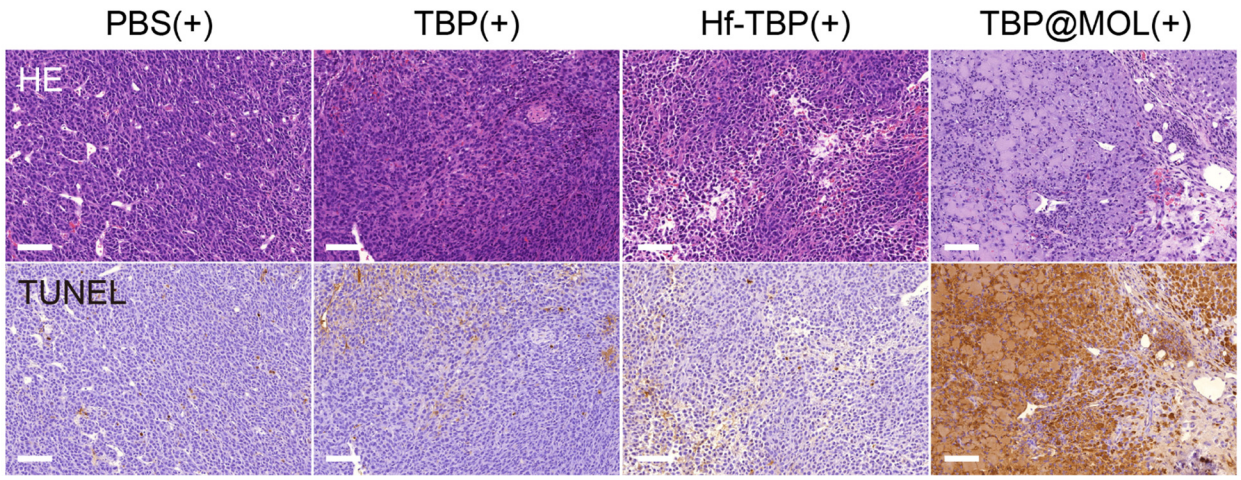

Figure 5-30. *In vivo* SDT-induced necrosis and apoptosis. Representative images of H&E staining and TUNEL staining of excised CT26 tumors after SDT treatment. Scale bars = 100 μm.

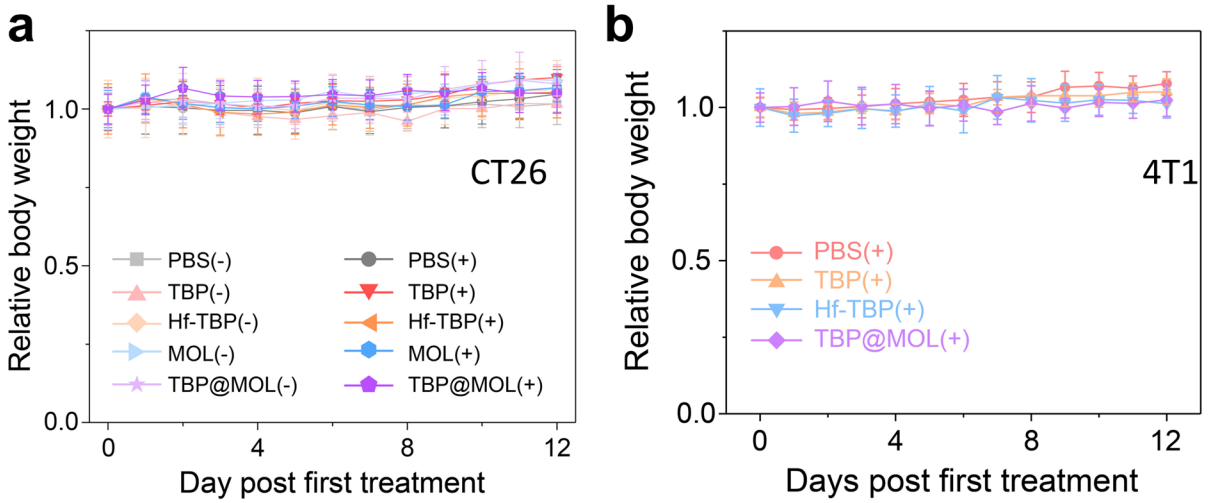

Figure 5-31. Body weight percentage curves. Mouse body weight percentages of (a) CT26 bearing BALB/c mice and (b) 4T1 bearing BALB/c mice over the treatment period.

All treatment groups showed normal body weight trends and minimal damage in major organ sections (**Figure 5-31**, **Figure 5-32**), indicating an absence of general toxicity. Thus, TBP@MOL provides a safe and efficient platform for enhanced SDT on CT26 and 4T1 tumors.

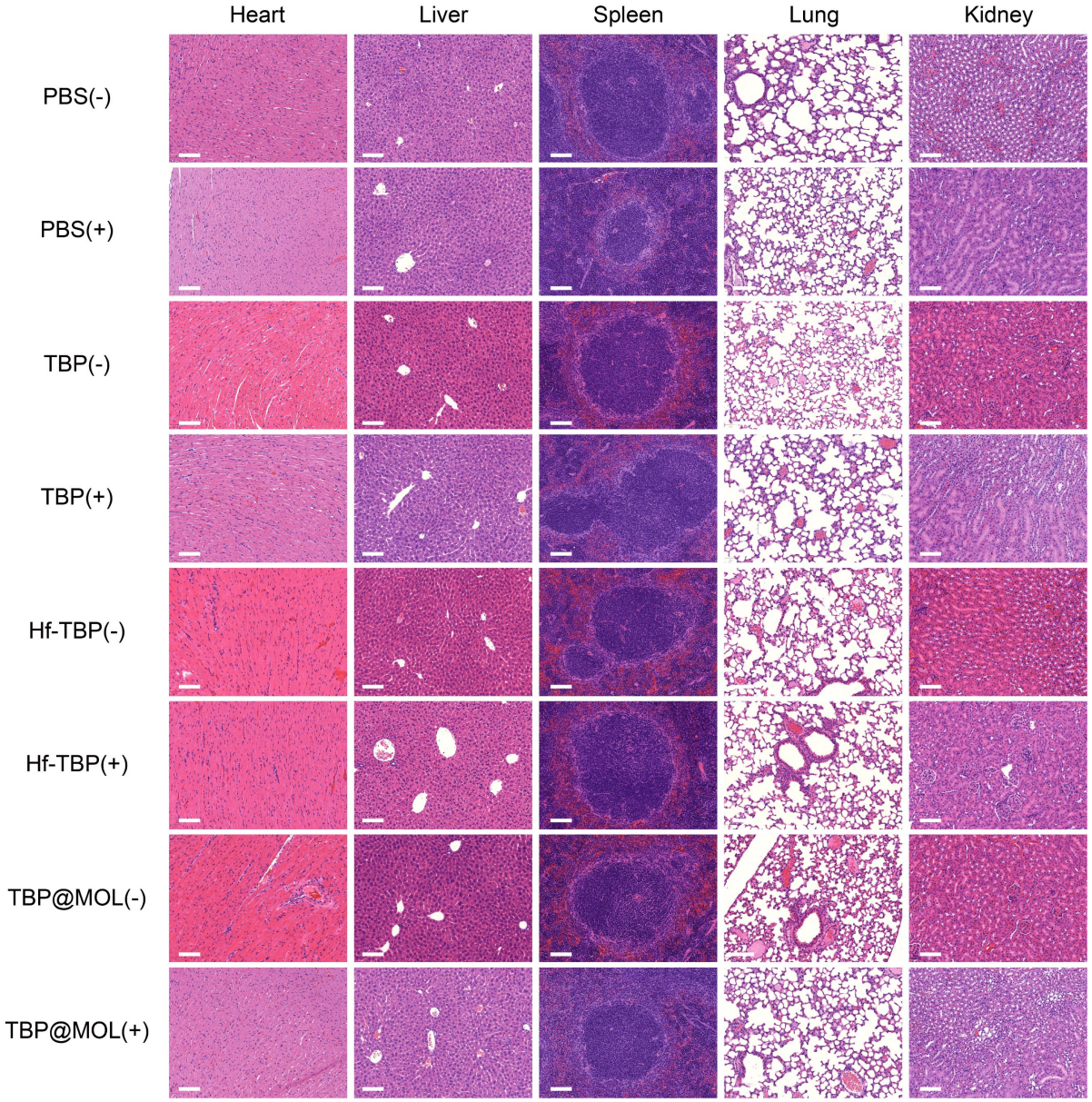

Figure 5-32. H&E staining of major organs from CT26 tumor-bearing mice in treatment and control groups. (Scale bar = 100 μm).

5.3 Conclusion

In this chapter, we report a new strategy to design efficient nanosonosensitizers based on 2D MOLs with photosensitizing iridium-based linkers and SBU-anchored TBP sonosensitizers. The TBP@MOL nano-sonosensitizer showed 14.1- and 7.4-fold higher $^1O_2$ generation efficacy than free TBP ligand and TBP-based MOF, respectively. As a result, TBP@MOL displayed about one order of magnitude higher cytotoxicity than free TBP ligand and TBP-based MOF under US irradiation. Mechanistic studies indicated that TBP@MOL enhances $^1O_2$ generation by preventing aggregation-induced quenching of the excited TBP sensitizers, efficiently capturing broad-spectrum sonoluminescence from ultrasonic cavitation via triplet–triplet Dexter energy transfer between DBB-Ir bridging linker donors and SBU-anchored TBP acceptors, and enhancing energy transfer from excited TBP sensitizers to $^3O_2$. TBP@MOL demonstrated significantly higher SDT efficacy than Hf-TBP and TBP in mouse models of colorectal and breast cancer.

5.4 Experimental section

5.4.1. Materials and methods

All chemical reagents were purchased at the highest quality from commercial sources and used without further purification. Transmission electron microscopy (TEM) was performed on a TECNAI Spirit TEM (120 kV), and high-resolution TEM (HR-TEM) was performed on a TECNAI Spirit F30 TEM (300 kV). Atomic force microscopy (AFM) was performed on a Bruker Multimode 8-HR AFM, and images were processed using NanoScope Analysis 1.40 software. Powder X-ray diffraction (PXRD) patterns were obtained on a Bruker D8 Venture diffractometer using a Cu Kα radiation source (λ = 1.54178 Å) and processed with PowderX software. Dynamic light scattering (DLS) and zeta potential measurements were obtained on a Malvern Zetasizer

Nano ZS instrument. Inductively coupled plasma-mass spectrometry (ICP-MS) was performed on an Agilent 7700x ICP-MS and analyzed using ICP-MS Mass Hunter version 4.6 C.01.06. Samples were diluted in a 2% HNO_3 matrix and analyzed with ^{159}Tb and internal standards against a 10-point standard curve between 1 ppb and 500 ppb. The correlation coefficient was R>0.999 for all analyses of interest. Data collection was performed in spectrum mode with three replicates per sample and 100 sweeps per replicate. ^{1}H and ^{19}F NMR spectra were collected on a Bruker NMR 400 DRX spectrometer (^{1}H NMR: 400 MHz, ^{19}F NMR: 377 MHz) and referenced to the proton resonance resulting from incomplete deuteration of $CDCl_3$ (^{1}H NMR: δ 7.26) or DMSO-d_6 (^{1}H NMR: δ 2.50). Matrix-assisted laser desorption/ionization-time of flight high-resolution mass spectrometry (MALDI-TOF HR-MS) was performed on a Bruker autoflex maX MALDI-TOF/TOF using negative ion reflectron mode. UV-Vis spectroscopy data was collected on a Shimadzu UV-2600 spectrophotometer. Steady-state fluorescence emission spectra were obtained on a HORIBA Fluorolog-3 spectrofluorometer equipped with a Synapse OE-CCD detector. Spectral overlap integrals were calculated using a|e – UV-Vis-IR Spectral Software 1.2 (FluorTools, DK).

US irradiation was given using a Chattanooga Intelect TranSport Ultrasound (Model 2782). The fluorescence intensity of SOSG was measured using a Synergy HTX plate reader (Agilent Technologies, USA). DPBS (-$Mg^{2+}$and -Ca^{2+}) was purchased from Thermo Fisher Scientific. Trypsin-EDTA solution was purchased from ATCC. 3-(4,5- dimethylthiazol-2-yl)-5-(3-carboxy-methoxyphenyl)-2-(4-sulfo-phenyl)2H-tetrazolium (MTS) assay was purchased from Promega (USA). Murine colorectal carcinoma CT26 cells and murine triple negative breast cancer cell line 4T1 were purchased from the American Type Culture Collection (ATCC, Rockville, MD). CT26 and 4T1 cells were cultured in RPMI-1640 (Corning, USA) and supplemented with 10% filtered

fetal bovine serum (VWR, USA) and 1% HyClone Penicillin-Streptomycin 100X solution (Cytiva, USA). The cells were kept in a water-jacketed incubator with 100% humidity and 5% CO_2 at 37°C. Flow cytometry data was collected on an LSR-Fortessa 4-15 (BD Biosciences, USA) and analyzed with FlowJo software (Tree Star, USA). Confocal laser scanning microscope (CLSM) images were collected on a Leica Stellaris 8 laser scanning confocal microscope. CLSM imaging was performed at the University of Chicago Integrated Light Microscopy Facility and analysis was done with ImageJ software (NIH, USA). The histological slides were scanned on a CRi Pannoramic SCAN 40x whole slide scanner by Integrated Light Microscopy Core in the University of Chicago and analyzed with the QuPath-0.2.3 software.[51] The absorbance and fluorescence from well plates were read by a BioTek Synergy HTX microplate reader. BALB/c breeders were obtained from Charles River Laboratories (USA) and bred in house at the animal facility at the University of Chicago. BALB/c mice with an age of 6-8 weeks were used for *in vivo* experiments. The study protocol was reviewed and approved by the Institutional Animal Care and Use Committee (IACUC) at the University of Chicago. The Human Tissue Resource Center at the University of Chicago provided the histology related services for this study.

5.4.2. Synthetic and characterization procedures

Synthesis of DBB-Ir. $Ir(DBB)[dF)CF_3)ppy]_2^+$ [DBB-Ir, DBB = 4,4'-di(4-benzoato)-2,2'-bipyridine; $dF(CF_3)ppy$ = 2-(2,4-difluorophenyl)-5-(trifluoromethyl)pyridine] was synthesized according to a previous literature report.[52] ^1H NMR (400 MHz, DMSO-d_6): δ 9.10 (d, 2H), 8.77 (dd, 2H), 8.49 (d, 2H), 8.44 (d, 2H), 8.16 (s, 2H), 8.04 (d, 4H), 7.82 (s, 2H), 7.65 (d, 4H), 7.11 (m, 2H), 5.91 (dd, 2H).

Synthesis of Hf_{12}-DBB-Ir (MOL). The MOL was synthesized according to a previous literature report with minor modifications.[38] To a 1-dram glass vial was added 0.5 mL of $HfCl_4$ solution [2.0 mg/mL in *N,N*-dimethylformamide (DMF)], 0.5 mL of DBB-Ir solution (4.0 mg/mL in DMF), 2 μL of trifluoroacetic acid (TFA), and 7 μL of water. The mixture was briefly sonicated and then kept in an 80 °C oven for 1 day. The yellow solid was collected by centrifugation and washed sequentially with DMF and ethanol and then stored as an ethanol dispersion in the dark.

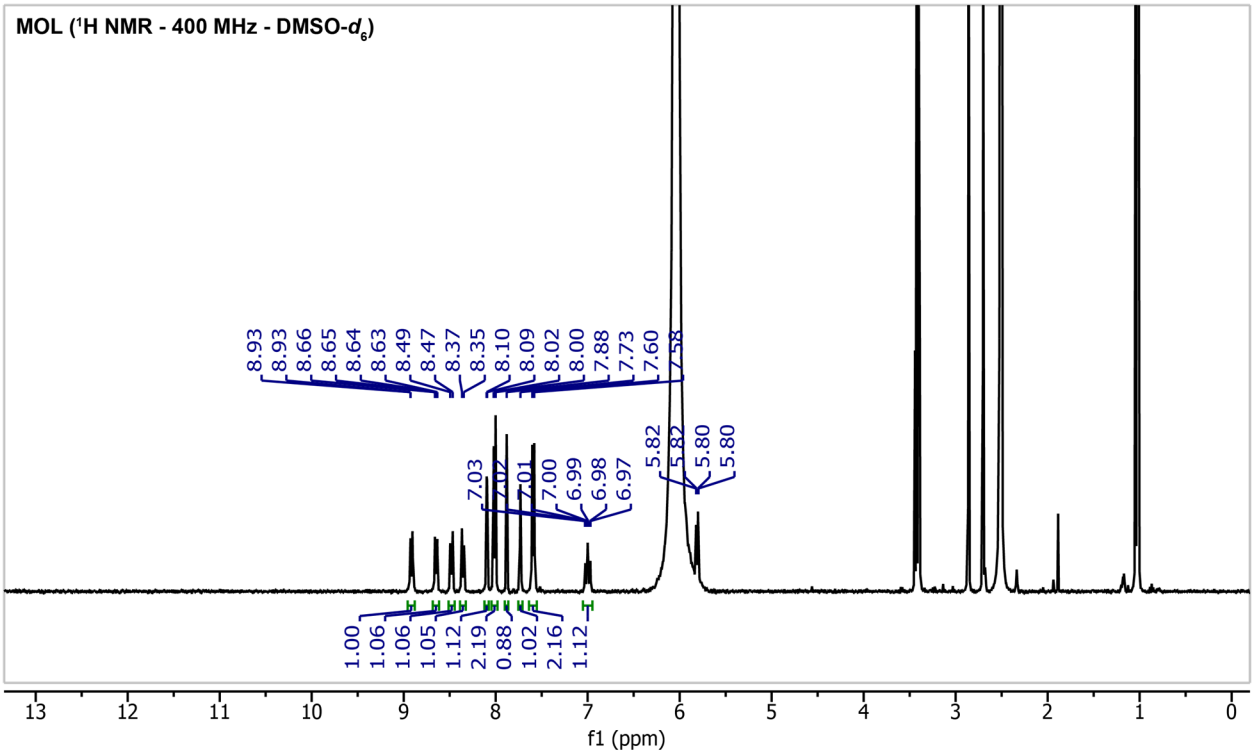

Figure 5-33. ^1H NMR spectrum of digested MOL.

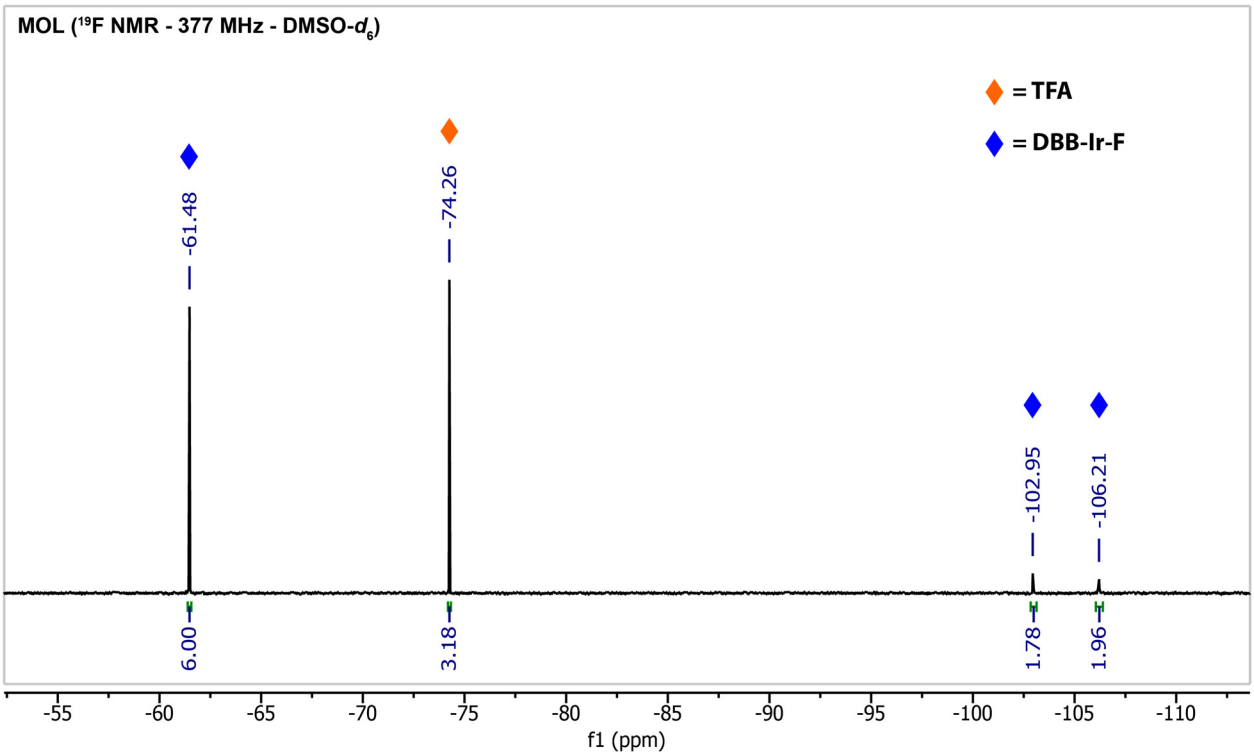

Figure 5-34. ^{19}F NMR spectrum of the digested MOL.

Synthesis of TBP@MOL. To a 1-dram glass vial was added 1.0 mL of MOL solution (4.29 mM in ethanol based on Hf), 1.0 mL of 5,10,15,20-tetra(*p*-benzoato)porphyrin (TBP) solution (0.8 mg/mL in DMF), and a stir bar. The mixture was stirred at room temperature overnight. The resulting red solid was collected by centrifugation and washed sequentially with DMF and ethanol and then stored as an ethanol dispersion in the dark.

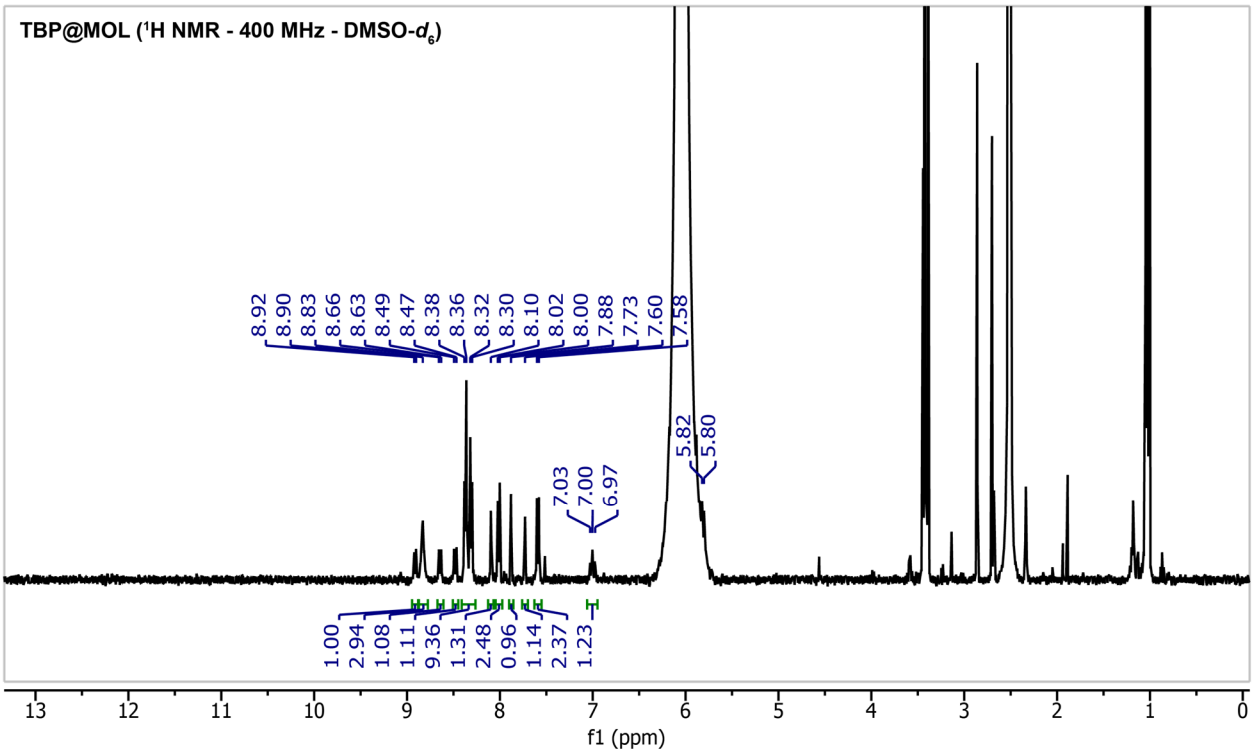

Figure 5-35. ^{1}H NMR spectrum of TBP@MOL.

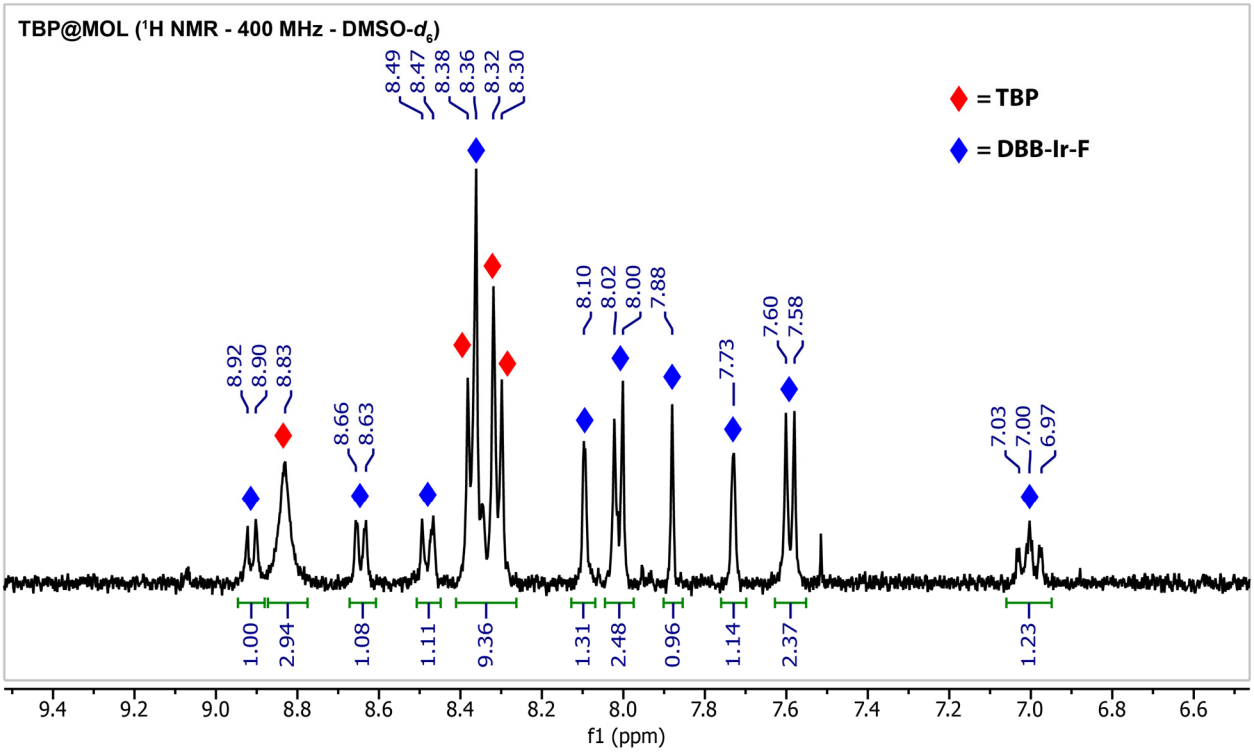

Figure 5-36. Aromatic region of the ^{1}H NMR spectrum of digested TBP@MOL. Digested TBP@MOL in DMSO-d_6 shows the characteristic peaks of both TBP and DBB-Ir.

NMR analysis of MOFs/MOLs. 1.0 mg of MOF/MOL was dried under vacuum. A solution of 500 μL DMSO-d_6 and 50 μL D_3PO_4 was added to the dried solid. The mixture was then sonicated for about 10 min, until no solid residue remained. Prior to $^{1}H/^{19}F$ NMR analysis, 50 μL D_2O was added to the mixture to shift the solvent peak away from the aromatic region.

UV-Vis analysis of MOFs/MOLs. 10 μL of a dispersed solution of MOF/MOL was added to a mixture of 940 μL DMSO and 50 μL H_3PO_4. The mixture was then sonicated for about 10 minutes and the UV-Vis absorption spectrum was recorded.

ICP-MS analysis of MOFs/MOLs. 10 μL of a dispersed solution of MOF/MOL was added to a mixture of 980 μL HNO_3 and 10 μL HF. The mixture was vortexed and kept at room temperature for 3 days. The sample was then diluted with ultrapure water to 2% HNO_3 and analyzed by ICP-MS.

Determination of TBP loading in TBP@MOL. The weight % loading of TBP in TBP@MOL was calculated to be 12.3% using UV-Vis spectroscopy to determine the TBP concentration (378.8 μM), from the Soret band at 420 nm, and ICP-MS to determine the Hf concentration (2.69 mM). The TBP:Hf_{12} SBU ratio was about 1.7:1, which yielded the formula $(TBP)_{1.7}@Hf_{12}(O)_8(OH)_8(DBB\text{-}Ir)_6(TFA)_{4.3}$. This formula was also supported by the partially reduced integration of the TFA fluorine signal at δ = -74.23 ppm in the ^{19}F NMR spectrum of TBP@MOL compared to the MOL.

Synthesis of DBP@MOL. To a 1-dram glass vial was added 1.0 mL of MOL solution (4.29 mM in DMF based on Hf), 1.0 mL of 5,15-di(*p*-benzoato)porphyrin (DBP) solution (1.0 mg/mL in DMF), and a stir bar. The mixture was stirred at room temperature overnight. The resulting red solid was collected by centrifugation and washed sequentially with DMSO, DMF and ethanol and then stored as an ethanol dispersion in the dark.

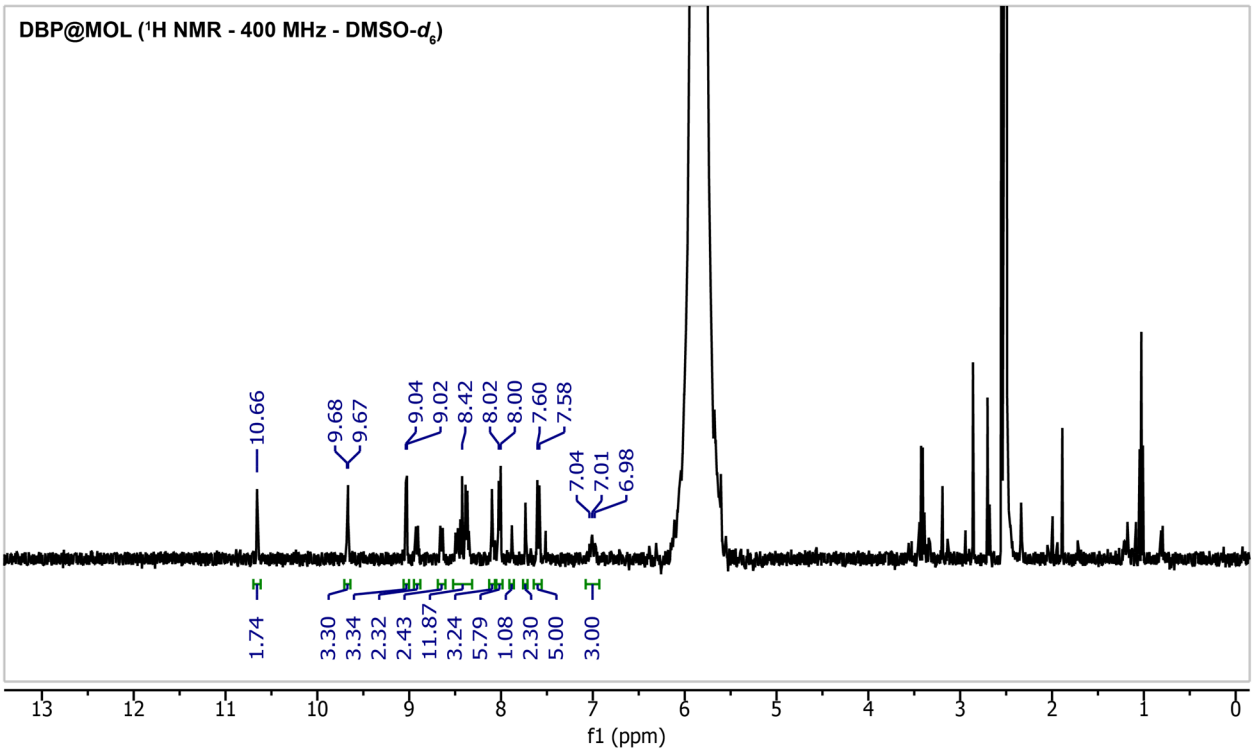

Figure 5-37. ^{1}H NMR spectrum of DBP@MOL.

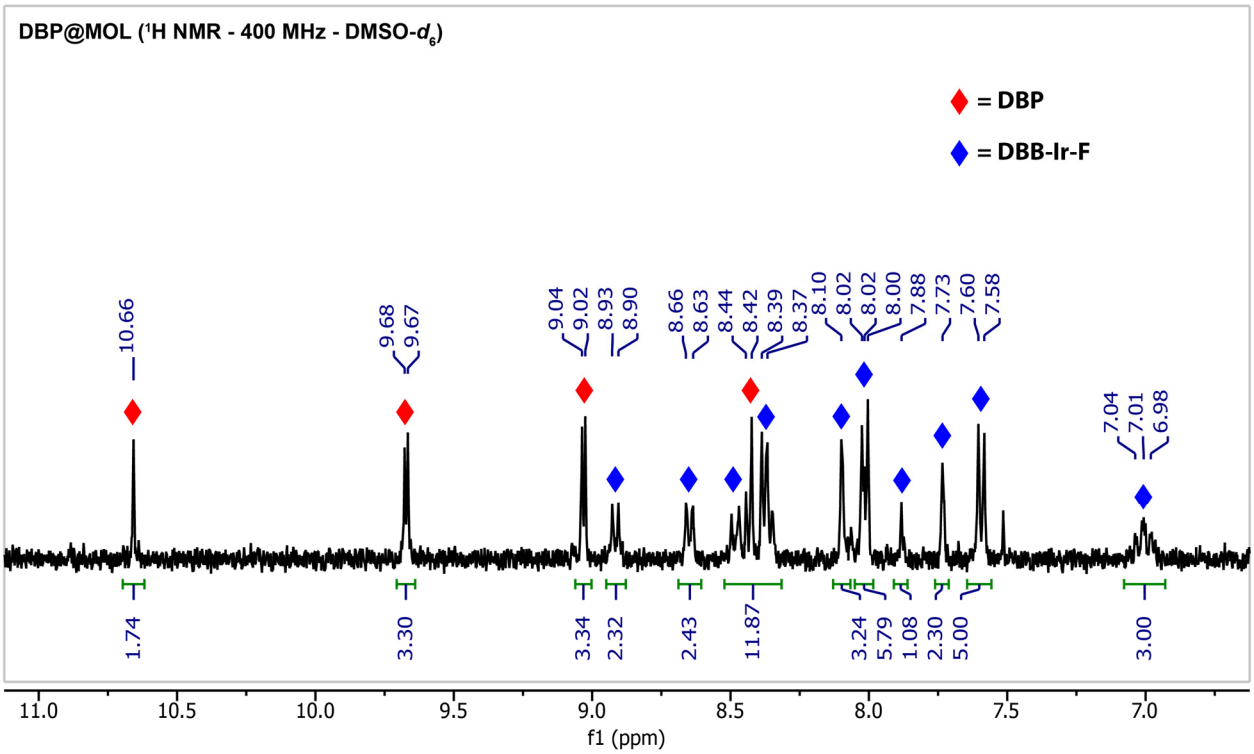

Figure 5-38. Aromatic region of the ^{1}H NMR spectrum of DBP@MOL. Digested DBP@MOL in DMSO-d_6 shows the characteristic peaks of both DBP and DBB-Ir.

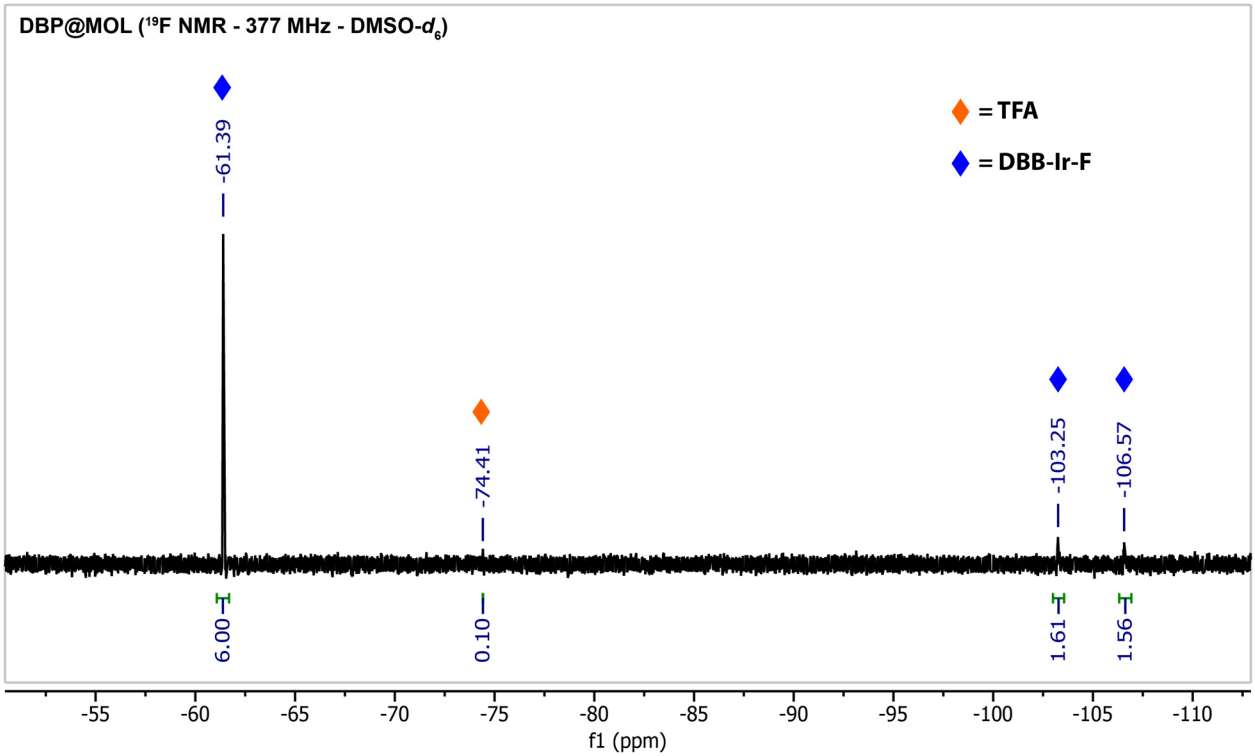

Figure 5-39. ^{19}F NMR spectrum of DBP@MOL.

Determination of DBP loading for DBP@MOL. The weight % loading of DBP in DBP@MOL was calculated to be 19.4% using UV-Vis spectroscopy to determine the DBP concentration (491.3 μM), from the Soret band at 409 nm, and ICP-MS to determine the Hf concentration (1.46 mM). The DBP:Hf_{12} SBU ratio was about 4.0:1, which yielded the ideal formula $(DBP)_{4.0}@Hf_{12}(O)_8(OH)_8(DBB\text{-}Ir)_6(TFA)_{2.0}$. This formula was also supported by the significantly reduced integration of the TFA fluorine signal at δ = -74.23 ppm in the ^{19}F NMR spectrum of DBP@MOL compared to MOL.

Synthesis of Hf-TBP and Hf-DBP MOFs. 5,10,15,20-tetra(*p*-benzoato)porphyrin (TBP) and 5,15-di(*p*-benzoato)porphyrin (DBP) were synthesized following previously reported methods.[40, 53] Hf-TBP and Hf-DBP MOFs were synthesized according to previous literature reports.[42, 53-54] Hf-TBP was synthesized by adding 2 mg $HfCl_4$, 1.9 mg TBP, 60 μL of 88% formic acid (FA), and 2 mL DMF to a 1-dram glass vial. The vial was placed in an 80 °C oven for 2 days. The purple suspension was collected by centrifugation, washed with DMF, 1% triethylamine in ethanol, and ethanol sequentially. The resulting Hf-TBP solid was redispersed in ethanol and stored in the dark. Hf-DBP MOF was synthesized by adding 2 mg $HfCl_4$, 1 mg H_2DBP, 75 μL acetic acid, and 1 mL DMF to a 1-dram glass vial. The vial was placed at 90 °C oven for 3 days. The resulting purple solid was collected by centrifugation, washed with DMF and ethanol, and stored as ethanol dispersions in the dark.

Synthesis of Hf-BTB. To a 1-dram glass vial was added 1.0 mL of $HfCl_4$ solution (2.0 mg/mL in DMF), 0.21 mL of 1,3,5-tris(4-carboxyphenyl)benzene (BTB) solution (2.0 mg/mL in DMF), 85

μL of formic acid (FA), and 15 μL of water. The mixture was briefly sonicated and then kept in an 80 °C oven for 1 day. The translucent white solid was collected by centrifugation and washed sequentially with DMF and ethanol and then stored as an ethanol dispersion in the dark. The formula for Hf-BTB is $Hf_6(\mu\text{-}O)_4(\mu\text{-}OH)_4(BTB)_2(HCO_2)_6$.

Synthesis of TBP@Hf-BTB. To a 1-dram glass vial was added 0.8 mL of Hf-BTB solution (1.16 mM in ethanol based on BTB), 0.8 mL of H_4TBP solution (0.5 mg/mL in DMF), and a stir bar. The mixture was stirred at room temperature overnight. The resulting red solid was collected by centrifugation and washed sequentially with DMF and ethanol and then stored as an ethanol dispersion in the dark.

Determination of TBP loading for TBP@Hf-BTB. The weight % loading of TBP in TBP@Hf-BTB was calculated to be 13.8% using UV-Vis spectroscopy to determine the TBP concentration (116.3 μM), from the Soret band at 420 nm, and ICP-MS to determine the Hf concentration (1.50 mM). The TBP:Hf_6 SBU ratio was about 0.47:1, which yielded the formula $(TBP)_{0.47}@Hf_6(\mu\text{-}O)_4(\mu\text{-}OH)_4(BTB)_2(HCO_2)_{5.53}$. This formula was also supported by the partially reduced integration of the FA proton signal at δ = 8.12 ppm in the ^1H NMR spectrum of TBP@Hf-BTB compared to Hf-BTB.

5.4.3. Photophysical characterization

Time-correlated single photon counting. Time-domain lifetimes were measured on a ChronosBH lifetime fluorometer (ISS, Inc.) using time-correlated single photon counting (TCSPC) methods. The fluorometer contained Becker-Hickl SPC-130 detection electronics and an

HPM-100-40 Hybrid PMT detector. Excitation was provided by a 403 nm picosecond pulsed laser source (Hamamatsu PLP-10) operating at a 5 MHz repetition rate. Emission wavelengths were selected with an interference filter at 550 nm with 40 nm bandpass (for DBB-Ir emission) or an interference filter at 642 nm with 10 nm bandpass (for TBP/DBP emission). The instrument response function (IRF) was measured to be approximately 120.0 ps FWHM with a 1 weight % suspension of Ludox LS colloidal silica in water. Multi-component exponential decay lifetimes were fit using the MATLAB *fit* function with the default 'Trust Region' algorithm. Goodness of fit is reported using reduced chi-squared values.

Ultrafast transient absorption spectroscopy. Ultrafast transient absorption spectroscopy was performed using sub-20 fs white light pump and probe pulses. A mode-locked oscillator (Coherent, Inc.) with a Ti:sapphire crystal that operates at 80 MHz seeds a Ti:sapphire regenerative amplifier (Coherent, Inc.), which in turn generates a ~40 fs pulse centered at 800 nm with a 5 kHz repetition rate. This pulse undergoes self-phase modulation in a pressurized 2 m long argon gas tube to create chirped white broadband pulses with a bandwidth ranging from 480 nm to 800 nm. Dichroic filters, bandpass filters (Thorlabs, Inc.) and chirped mirrors (Laser Quantum) are used to shape the bandwidth and temporal profile of the pulse. This results in a sub-15 fs white light pulse with a bandwidth from 500 to 730 nm. This pulse is split into pump and probe pulses, and the pump pulse is delayed temporally with respect to the probe pulse with a retroreflector on a stage up until 1 ns (Aerotech Inc.). Data is averaged over 80 runs for each sample to obtain reliable dynamics over scatter contributions due to the large sized domains of Hf-TBP and TBP@MOL in solution.

5.4.4. Reactive oxygen species generation

Singlet oxygen generation. Singlet oxygen sensor green (SOSG, Invitrogen, USA) assay was used to measure the $^1O_2$ production and sonodynamic therapy (SDT) efficacy of the sonosensitizers at various times after US irradiation. 100 μL of aqueous dispersions with equivalent doses of 2.5 μM sonosensitizer (e.g., TBP in TBP@MOL) and 15 μM SOSG solution were exposed to US irradiation (3.4 MHz, 1.0 W/cm^2, 50% duty cycle) for 0, 1, 2.5, 5, and 10 minutes, and the SOSG fluorescence intensity was measured at each time point using a fluorescence plate reader (λ_{ex} = 485 nm, λ_{em} = 520 nm). The controls for MOL and Hf-BTB were prepared using equivalent doses of either DBB-Ir (6.32 μM) or BTB (29.4 μM) as the TBP@MOL and TBP@Hf-BTB groups, respectively. The physical mixture of TBP and MOL control group was prepared using equivalent TBP (2.5 μM) and DBB-Ir (6.32 μM) doses as in TBP@MOL.

SOSG assay was also used to measure the $^1O_2$ production and photodynamic therapy (PDT) efficacy of the sensitizers at various times after visible light irradiation. Aqueous dispersions (1 mL total volume) of the sensitizers, with equivalent doses of 1.5 μM for TBP or 2.5 μM for DBP, in the presence of 15 μM SOSG were prepared. 100 μL aliquots (n = 5) of the resulting dispersions were added to a 96-well plate and were exposed to visible light irradiation (630 nm, 100 mW/cm^2) for 0, 1, 2, 3, 5, 7, 10, and 15 minutes, and the SOSG fluorescence intensity was measured at each time point using a fluorescence plate reader (λ_{ex} = 485 nm, λ_{em} = 520 nm).

Total ROS and hydroxyl radical generation. Dichlorofluorescein (DCF, Invitrogen, USA) and 3′-(p-hydroxyphenyl) fluorescein (HPF, Invitrogen, USA) assays were used to detect total reactive oxygen species (ROS) and hydroxyl (•OH) radicals in different TBP systems after US irradiation.

100 μL of aqueous dispersions with equivalent doses of 2.5 μM sonosensitizer (e.g., TBP in TBP@MOL) and 10 μM DCF (or HPF) solution were exposed to US irradiation (3.4 MHz, 1.0 W/cm^2, 50% duty cycle) for 0, 1, 2.5, 5, and 10 minutes, and the DCF (or HPF) fluorescence intensity was measured at each time point using a fluorescence plate reader (λ_{ex} = 485 nm, λ_{em} = 520 nm).

5.4.5. *In vitro* procedures

Cell viability assay. The US irradiated [denoted as (+)] and US free [denoted as (-)] cytotoxicities of TBP, Hf-TBP, TBP@MOL, and MOL were assessed on CT26 and 4T1 cells using 3-(4,5-dimethylthiazol-2-yl)-5-(3-carboxymethoxyphenyl)-2-(4-sulfo-phenyl)-2H-tetrazolium (MTS) assay (Promega, USA). Cells were seeded on 96-well plates at a density of 2000 cells/well and further cultured overnight. TBP, Hf-TBP or TBP@MOL was added to the wells at equivalent TBP concentrations of 0, 2.5, 5.0, 7.5, 10, 20, 40, 60, 80 μM and incubated for 6 hours (n = 4), followed by US irradiation (3.4 MHz, 1 W/cm^2, 50% duty cycle) for 10 minutes. MOL was added to the wells at an equivalent DBB-Ir concentration of 0, 8.75, 17.5, 26.3, 35, 70, 140, 210, 280 μM, followed by the same US treatment as above. Cells were further incubated for 24 hours and subject to cell viability measurement using MTS assay. The IC_{50} value was determined by fitting the dose response curves in Origin Lab.

Cellular uptake. Cellular uptakes of TBP, Hf-TBP and TBP@MOL were evaluated on CT26 cells. Cells were seeded on 6-well plates at a density of 5×10^5 and cultured in DMEM medium (10%) overnight. TBP, Hf-TBP or TBP@MOL was added to each well with final equivalent TBP concentrations of 10 μM (n = 3). Cells were cultured in the 37 ℃ incubator. At different time

points (1, 2, 4, 8 h), the medium was removed, and the cells were washed three times with PBS, trypsinized and collected by centrifugation. After counting by a hemocytometer, cells were digested with 1 mL of DMSO (containing 10% H_3PO_4) in 1.5 mL Eppendorf tubes for 48 hours, with strong sonication every 12 hours. The TBP concentration was determined by UV-Vis absorbance at 420 nm according to the established standard curve.

***In vitro* ROS generation.** The ROS generation from SDT treatment was evaluated on CT26 cells by flow cytometry and CLSM. For flow cytometry experiments, CT26 cells were seeded at a density of 5×10^5 cells/mL in 6-well plates and the cells were treated with TBP, Hf-TBP and TBP@MOL at equivalent TBP concentrations of 5 μM and further incubated for 6 hours. 20 μM DCF-DA (Invitrogen) was then added to each well for another 1 hour incubation. The plates were then treated with US irradiation (3.4 MHz, 1 W/cm^2, 50% duty cycle) for 10 minutes. The cells were then washed with PBS and trypsinized for flow cytometry. For CLSM, inside 35 mm glass bottom dishes, CT26 cells were seeded at a density of 1×10^5 cells/mL and treated in the same way as flow cytometry but not detached. The cells were washed with PBS, exchanged with warm phenol-red-free RPMI-1640 medium, and mounted for CLSM immediately using a Leica Stellaris 8 microscope.

AM/PI staining. The general cell death after SDT treatment was evaluated on CT26 by Calcein-AM/Propidium Iodide (PI) staining with CLSM. CT26 cells were seeded at a density of 1×10^5 cells/mL inside 35 mm glass bottom dishes. After overnight culturing, the cells were treated with TBP, Hf-TBP and TBP@MOL at equivalent TBP concentrations of 5 μM and further incubated for 6 hours. Cells were irradiated by US (3.4 MHz, 1 W/cm^2, 50% duty cycle) for 10 minutes. The

cells were further cultured for 24 hours and then stained with Calcein-AM (5 μM) and PI (1 μg/mL) in serum-free RPMI-1640 medium for 30 minutes. The cells were then washed with PBS, exchanged with warm phenol-red-free RPMI-1640 medium, and mounted for CLSM immediately using a Leica Stellaris 8 microscope.

Apoptosis analysis. The apoptosis after SDT treatment was evaluated on CT26 cells by flow cytometry. CT26 cells were seeded at a density of 2×10^5 cells/mL in 6-well plates and the cells were treated with TBP, Hf-TBP and TBP@MOL at equivalent TBP concentrations of 5 μM and further incubated for 4 hours. Then the plates were treated by US irradiation (3.4 MHz, 1 W/cm^2, 50% duty cycle) for 10 minutes. The cells were further incubated for 24 hours, washed with PBS, and trypsinized for the staining of Alexa Fluor 488 Annexin V/dead cell apoptosis kit (Thermo Fisher Scientific, USA) following the vendor's protocol.

5.4.6. *In vivo* procedures

***In vivo* SDT efficacy.** The *In vivo* SDT efficacy was tested on subcutaneous CT26 and 4T1 tumor models. BALB/c mice were inoculated with 2×10^6 CT26 or 4T1 cells per mouse subcutaneously onto the right flank. After one week, the mice with tumor volume around 80 mm^3 were randomized for SDT treatment. PBS, TBP, Hf-TBP, MOL, or TBP@MOL was injected intratumorally with an equivalent TBP dose of 0.2 μmol (n = 5) every 2 days. 6 hours later, the mice were anaesthetized with 2% (V/V) isoflurane/O_2 and the tumor was treated by the sonication (3.4 MHz, 2 W/cm^2, 50% duty cycle) for 10 minutes. Tumor sizes were measured with an electronic caliper (tumor volume = length × width^2 / 2) and body weight was monitored with an electronic scale daily. At day 19, the mice were euthanized, and the tumors were weighed, photographed and sectioned for

H&E and TUNEL staining. Major organs were sectioned for hematoxylin-eosin (H&E) staining to evaluate general toxicity.

Statistical analysis. Statistical analysis for in vivo efficacy was performed on Origin Lab software using One-way Repeated Measures ANOVA method with Tukey's honest significance test. The tumor volume and weight at the last day of experiment were chosen for analysis (n = 5).

5.5 References

1. Brotchie, A., Drug delivery: Ultrasound soothes the pain. *Nature Reviews Materials* **2017,** *2* (9), 17058.

2. Choi, V.; Rajora, M. A.; Zheng, G., Activating Drugs with Sound: Mechanisms Behind Sonodynamic Therapy and the Role of Nanomedicine. *Bioconjugate Chemistry* **2020,** *31* (4), 967-989.

3. Son, S.; Kim, J. H.; Wang, X.; Zhang, C.; Yoon, S. A.; Shin, J.; Sharma, A.; Lee, M. H.; Cheng, L.; Wu, J.; Kim, J. S., Multifunctional sonosensitizers in sonodynamic cancer therapy. *Chemical Society Reviews* **2020,** *49* (11), 3244-3261.

4. Stride, E.; Coussios, C., Nucleation, mapping and control of cavitation for drug delivery. *Nature Reviews Physics* **2019,** *1* (8), 495-509.

5. Qian, X.; Zheng, Y.; Chen, Y., Micro/Nanoparticle-Augmented Sonodynamic Therapy (SDT): Breaking the Depth Shallow of Photoactivation. *Advanced Materials* **2016,** *28* (37), 8097-8129.

6. Lin, X.; Song, J.; Chen, X.; Yang, H., Ultrasound-Activated Sensitizers and Applications. *Angewandte Chemie International Edition* **2020,** *59* (34), 14212-14233.

7. Ghosh, S.; Carter, K. A.; Lovell, J. F., Liposomal formulations of photosensitizers. *Biomaterials* **2019,** *218*, 119341.

8. Song, L.; Lu, L.; Pu, Y.; Yin, H.; Zhang, K., Nanomaterials-Based Tumor Microenvironment Modulation for Magnifying Sonodynamic Therapy. *Accounts of Materials Research* **2022,** *3* (9), 971-985.

9. Kwon, S.; Ko, H.; You, D. G.; Kataoka, K.; Park, J. H., Nanomedicines for Reactive Oxygen Species Mediated Approach: An Emerging Paradigm for Cancer Treatment. *Accounts of Chemical Research* **2019,** *52* (7), 1771-1782.

10. Bai, S.; Yang, N.; Wang, X.; Gong, F.; Dong, Z.; Gong, Y.; Liu, Z.; Cheng, L., Ultrasmall Iron-Doped Titanium Oxide Nanodots for Enhanced Sonodynamic and Chemodynamic Cancer Therapy. *ACS Nano* **2020,** *14* (11), 15119-15130.

11. Lin, X.; Liu, S.; Zhang, X.; Zhu, R.; Chen, S.; Chen, X.; Song, J.; Yang, H., An Ultrasound Activated Vesicle of Janus Au-MnO Nanoparticles for Promoted Tumor Penetration and Sono-Chemodynamic Therapy of Orthotopic Liver Cancer. *Angewandte Chemie International Edition* **2020,** *59* (4), 1682-1688.

12. Zhu, L.; Luo, M.; Zhang, Y.; Fang, F.; Li, M.; An, F.; Zhao, D.; Zhang, J., Free radical as a double-edged sword in disease: Deriving strategic opportunities for nanotherapeutics. *Coordination Chemistry Reviews* **2023,** *475*, 214875.

13. Li, D.; Yang, Y.; Li, D.; Pan, J.; Chu, C.; Liu, G., Organic Sonosensitizers for Sonodynamic Therapy: From Small Molecules and Nanoparticles toward Clinical Development. *Small* **2021,** *17* (42), 2101976.

14. Liang, X.; Chen, M.; Bhattarai, P.; Hameed, S.; Dai, Z., Perfluorocarbon@Porphyrin Nanoparticles for Tumor Hypoxia Relief to Enhance Photodynamic Therapy against Liver Metastasis of Colon Cancer. *ACS Nano* **2020,** *14* (10), 13569-13583.

15. Overchuk, M.; Zheng, M.; Rajora, M. A.; Charron, D. M.; Chen, J.; Zheng, G., Tailoring Porphyrin Conjugation for Nanoassembly-Driven Phototheranostic Properties. *ACS Nano* **2019,** *13* (4), 4560-4571.

16. Li, X.; Lovell, J. F.; Yoon, J.; Chen, X., Clinical development and potential of photothermal and photodynamic therapies for cancer. *Nature Reviews Clinical Oncology* **2020,** *17* (11), 657-674.

17. Luo, D.; Carter, K. A.; Molins, E. A. G.; Straubinger, N. L.; Geng, J.; Shao, S.; Jusko, W. J.; Straubinger, R. M.; Lovell, J. F., Pharmacokinetics and pharmacodynamics of liposomal chemophototherapy with short drug-light intervals. *Journal of Controlled Release* **2019,** *297*, 39-47.

18. Zhang, Y.; Zhang, X.; Yang, H.; Yu, L.; Xu, Y.; Sharma, A.; Yin, P.; Li, X.; Kim, J. S.; Sun, Y., Advanced biotechnology-assisted precise sonodynamic therapy. *Chemical Society Reviews* **2021,** *50* (20), 11227-11248.

19. Rwei, A. Y.; Paris, J. L.; Wang, B.; Wang, W.; Axon, C. D.; Vallet-Regí, M.; Langer, R.; Kohane, D. S., Ultrasound-triggered local anaesthesia. *Nature Biomedical Engineering* **2017,** *1* (8), 644-653.

20. Rajora, M. A.; Lou, J. W. H.; Zheng, G., Advancing porphyrin's biomedical utility via supramolecular chemistry. *Chemical Society Reviews* **2017,** *46* (21), 6433-6469.

21. Huang, P.; Qian, X.; Chen, Y.; Yu, L.; Lin, H.; Wang, L.; Zhu, Y.; Shi, J., Metalloporphyrin-Encapsulated Biodegradable Nanosystems for Highly Efficient Magnetic Resonance Imaging-

Guided Sonodynamic Cancer Therapy. *Journal of the American Chemical Society* **2017,** *139* (3), 1275-1284.

22. Gong, Z.; Dai, Z., Design and Challenges of Sonodynamic Therapy System for Cancer Theranostics: From Equipment to Sensitizers. *Advanced Science* **2021,** *8* (10), 2002178.

23. Dong, Z.; Feng, L.; Hao, Y.; Li, Q.; Chen, M.; Yang, Z.; Zhao, H.; Liu, Z., Synthesis of CaCO3-Based Nanomedicine for Enhanced Sonodynamic Therapy via Amplification of Tumor Oxidative Stress. *Chem* **2020,** *6* (6), 1391-1407.

24. Liang, S.; Deng, X.; Ma, P. a.; Cheng, Z.; Lin, J., Recent Advances in Nanomaterial-Assisted Combinational Sonodynamic Cancer Therapy. *Advanced Materials* **2020,** *32* (47), 2003214.

25. Wang, H.; Guo, J.; Lin, W.; Fu, Z.; Ji, X.; Yu, B.; Lu, M.; Cui, W.; Deng, L.; Engle, J. W.; Wu, Z.; Cai, W.; Ni, D., Open-Shell Nanosensitizers for Glutathione Responsive Cancer Sonodynamic Therapy. *Advanced Materials* **2022,** *34* (15), 2110283.

26. Luo, T.; Ni, K.; Culbert, A.; Lan, G.; Li, Z.; Jiang, X.; Kaufmann, M.; Lin, W., Nanoscale Metal–Organic Frameworks Stabilize Bacteriochlorins for Type I and Type II Photodynamic Therapy. *Journal of the American Chemical Society* **2020,** *142* (16), 7334-7339.

27. Park, J.; Jiang, Q.; Feng, D.; Mao, L.; Zhou, H.-C., Size-Controlled Synthesis of Porphyrinic Metal–Organic Framework and Functionalization for Targeted Photodynamic Therapy. *Journal of the American Chemical Society* **2016,** *138* (10), 3518-3525.

28. Zheng, X.; Wang, L.; Guan, Y.; Pei, Q.; Jiang, J.; Xie, Z., Integration of metal-organic framework with a photoactive porous-organic polymer for interface enhanced phototherapy. *Biomaterials* **2020,** *235*, 119792.

29. Cai, X.; Xie, Z.; Ding, B.; Shao, S.; Liang, S.; Pang, M.; Lin, J., Monodispersed Copper(I)-Based Nano Metal–Organic Framework as a Biodegradable Drug Carrier with Enhanced Photodynamic Therapy Efficacy. *Advanced Science* **2019,** *6* (15), 1900848.

30. Lismont, M.; Dreesen, L.; Wuttke, S., Metal-Organic Framework Nanoparticles in Photodynamic Therapy: Current Status and Perspectives. *Advanced Functional Materials* **2017,** *27* (14), 1606314.

31. Horcajada, P.; Gref, R.; Baati, T.; Allan, P. K.; Maurin, G.; Couvreur, P.; Férey, G.; Morris, R. E.; Serre, C., Metal–Organic Frameworks in Biomedicine. *Chemical Reviews* **2012,** *112* (2), 1232-1268.

32. Simon-Yarza, T.; Mielcarek, A.; Couvreur, P.; Serre, C., Nanoparticles of Metal-Organic Frameworks: On the Road to In Vivo Efficacy in Biomedicine. *Advanced Materials* **2018,** *30* (37), 1707365.

33. Xu, Q.; Zhan, G.; Zhang, Z.; Yong, T.; Yang, X.; Gan, L., Manganese porphyrin-based metal-organic framework for synergistic sonodynamic therapy and ferroptosis in hypoxic tumors. *Theranostics* **2021,** *11* (4), 1937-1952.

34. Xiao, Z.; Chen, Q.; Yang, Y.; Tu, S.; Wang, B.; Qiu, Y.; Jiang, Y.; Huang, Q.; Ai, K., State of the art advancements in sonodynamic therapy (SDT): Metal-Organic frameworks for SDT. *Chemical Engineering Journal* **2022,** *449*, 137889.

35. Zhuang, F.; Ma, Q.; Dong, C.; Xiang, H.; Shen, Y.; Sun, P.; Li, C.; Chen, Y.; Lu, B.; Chen, Y.; Huang, B., Sequential Ultrasound-Triggered and Hypoxia-Sensitive Nanoprodrug for Cascade Amplification of Sonochemotherapy. *ACS Nano* **2022,** *16* (4), 5439-5453.

36. Wang, W.; Pan, X.; Yang, H.; Wang, H.; Wu, Q.; Zheng, L.; Xu, B.; Wang, J.; Shi, X.; Bai, F.; Liu, H., Bioactive Metal–Organic Frameworks with Specific Metal–Nitrogen (M–N) Active Sites for Efficient Sonodynamic Tumor Therapy. *ACS Nano* **2021,** *15* (12), 20003-20012.

37. Zhu, Z.-H.; Liu, Y.; Song, C.; Hu, Y.; Feng, G.; Tang, B. Z., Porphyrin-Based Two-Dimensional Layered Metal–Organic Framework with Sono-/Photocatalytic Activity for Water Decontamination. *ACS Nano* **2022,** *16* (1), 1346-1357.

38. Nash, G. T.; Luo, T.; Lan, G.; Ni, K.; Kaufmann, M.; Lin, W., Nanoscale Metal–Organic Layer Isolates Phthalocyanines for Efficient Mitochondria-Targeted Photodynamic Therapy. *Journal of the American Chemical Society* **2021,** *143* (5), 2194-2199.

39. Prozorov, T.; Prozorov, R.; Suslick, K. S., High Velocity Interparticle Collisions Driven by Ultrasound. *Journal of the American Chemical Society* **2004,** *126* (43), 13890-13891.

40. Lu, K.; He, C.; Lin, W., Nanoscale Metal–Organic Framework for Highly Effective Photodynamic Therapy of Resistant Head and Neck Cancer. *Journal of the American Chemical Society* **2014,** *136* (48), 16712-16715.

41. Ettlinger, R.; Lächelt, U.; Gref, R.; Horcajada, P.; Lammers, T.; Serre, C.; Couvreur, P.; Morris, R. E.; Wuttke, S., Toxicity of metal–organic framework nanoparticles: from essential analyses to potential applications. *Chemical Society Reviews* **2022,** *51* (2), 464-484.

42. Luo, T.; Fan, Y.; Mao, J.; Yuan, E.; You, E.; Xu, Z.; Lin, W., Dimensional Reduction Enhances Photodynamic Therapy of Metal–Organic Nanophotosensitizers. *Journal of the American Chemical Society* **2022,** *144* (12), 5241-5246.

43. Kent, C. A.; Mehl, B. P.; Ma, L.; Papanikolas, J. M.; Meyer, T. J.; Lin, W., Energy Transfer Dynamics in Metal−Organic Frameworks. *Journal of the American Chemical Society* **2010,** *132* (37), 12767-12769.

44. Marydasan, B.; Nair, A. K.; Ramaiah, D., Optimization of Triplet Excited State and Singlet Oxygen Quantum Yields of Picolylamine–Porphyrin Conjugates through Zinc Insertion. *The Journal of Physical Chemistry B* **2013,** *117* (43), 13515-13522.

45. Larsen, R. W.; Omdal, D. H.; Jasuja, R.; Niu, S. L.; Jameson, D. M., Conformational Modulation of Electron Transfer within Electrostatic Porphyrin: Cytochrome c Complexes. *The Journal of Physical Chemistry B* **1997,** *101* (40), 8012-8020.

46. Kawaoka, K.; Khan, A. U.; Kearns, D. R., Role of Singlet Excited States of Molecular Oxygen in the Quenching of Organic Triplet States. *The Journal of Chemical Physics* **1967,** *46* (5), 1842-1853.

47. Kearns, D. R., Physical and chemical properties of singlet molecular oxygen. *Chemical Reviews* **1971,** *71* (4), 395-427.

48. Kearns, D. R.; Khan, A. U., SENSITIZED PHOTOOXYGENATION REACTIONS AND THE ROLE OF SINGLET OXYGEN†,‡. *Photochemistry and Photobiology* **1969,** *10* (3), 193-210.

49. Bodesheim, M.; Schütz, M.; Schmidt, R., Triplet state energy dependence of the competitive formation of O2(1Σ+g), O2(1Δg) and O2(3Σ−g) in the sensitization of O2 by triplet states. *Chemical Physics Letters* **1994,** *221*, 7-14.

50. Schmidt, R., Photosensitized Generation of Singlet Oxygen. *Photochemistry and Photobiology* **2006,** *82* (5), 1161-1177.

51. Bankhead, P.; Loughrey, M. B.; Fernández, J. A.; Dombrowski, Y.; McArt, D. G.; Dunne, P. D.; McQuaid, S.; Gray, R. T.; Murray, L. J.; Coleman, H. G.; James, J. A.; Salto-Tellez, M.; Hamilton, P. W., QuPath: Open source software for digital pathology image analysis. *Scientific Reports* **2017,** *7* (1), 16878.

52. Zhu, Y.-Y.; Lan, G.; Fan, Y.; Veroneau, S. S.; Song, Y.; Micheroni, D.; Lin, W., Merging Photoredox and Organometallic Catalysts in a Metal–Organic Framework Significantly Boosts Photocatalytic Activities. *Angewandte Chemie International Edition* **2018,** *57* (43), 14090-14094.

53. Lu, K.; He, C.; Guo, N.; Chan, C.; Ni, K.; Weichselbaum, R. R.; Lin, W., Chlorin-Based Nanoscale Metal–Organic Framework Systemically Rejects Colorectal Cancers via Synergistic Photodynamic Therapy and Checkpoint Blockade Immunotherapy. *Journal of the American Chemical Society* **2016,** *138* (38), 12502-12510.

54. Lu, K.; He, C.; Guo, N.; Chan, C.; Ni, K.; Lan, G.; Tang, H.; Pelizzari, C.; Fu, Y.-X.; Spiotto, M. T.; Weichselbaum, R. R.; Lin, W., Low-dose X-ray radiotherapy–radiodynamic therapy via nanoscale metal–organic frameworks enhances checkpoint blockade immunotherapy. *Nature Biomedical Engineering* **2018,** *2* (8), 600-610.